INFORMATION TO USERS

This manuscript has been reproduced from the microfilm master. UMI films the text directly from the original or copy submitted. Thus, some thesis and dissertation copies are in typewriter face, while others may be from any type of computer printer.

The quality of this reproduction is dependent upon the quality of the copy submitted. Broken or indistinct print, colored or poor quality illustrations and photographs, print bleedthrough, substandard margins, and improper alignment can adversely affect reproduction.

In the unlikely event that the author did not send UMI a complete manuscript and there are missing pages, these will be noted. Also, if unauthorized copyright material had to be removed, a note will indicate the deletion.

Oversize materials (e.g., maps, drawings, charts) are reproduced by sectioning the original, beginning at the upper left-hand corner and continuing from left to right in equal sections with small overlaps. Each original is also photographed in one exposure and is included in reduced form at the back of the book.

Photographs included in the original manuscript have been reproduced xerographically in this copy. Higher quality 6" x 9" black and white photographic prints are available for any photographs or illustrations appearing in this copy for an additional charge. Contact UMI directly to order.

UMI

A Bell & Howell Information Company
300 North Zeeb Road, Ann Arbor MI 48106-1346 USA
313/761-4700 800/521-0600

Surface Chemistry of
Iodine on Platinum(111)

by

Scott Anthony Furman
B.Sc., University Of Victoria, 1991

A Dissertation Submitted in Partial Fulfillment of the
Requirements for the Degree of

DOCTOR OF PHILOSOPHY

in the Department of Chemistry

We accept this dissertation as conforming
to the required standard

Dr. D.A. Harrington, Supervisor (Department of Chemistry)

Dr. A.D. Kirk, Departmental Member (Department of Chemistry)

Dr. C.X.W. Qian, Departmental Member (Department of Chemistry)

Dr. A. Watton, Outside Member (Department of Physics and Astronomy)

Dr. E.M. Stuve, External Examiner (Department of Chemical Engineering, University of Washington)

Supervisor: Dr. D.A. Harrington

ABSTRACT

The adsorption of iodine on a platinum(111) single-crystal surface has been investigated using LEED, Auger spectroscopy, and work function measurements. The phase transformations and work function changes have also been measured during desorption. Mass spectroscopy shows that above 300 K the main desorption product is atomic iodine with a small amount of molecular iodine detected as well. The desorption kinetics at these temperatures were studied by different techniques to extract the kinetic parameters and the orders of the desorption reactions. There are two main desorption features, one displaying zero-order desorption kinetics typical of a phase transition and the other displaying first-order kinetics with a coverage-dependent activation energy. The work function changes during adsorption and desorption were shown to be a function of coverage rather than having a site dependence. The adsorption of iodine at temperatures below 200 K was also studied. Multilayers of molecular iodine are formed that desorb with essentially zeroth order kinetics. Two multilayer desorptions were observed with thermal desorption spectroscopy. One of the multilayer desorptions had a significant work function change associated with it. The work function changes were modelled by calculating the hybridization dipole moment using extended-Hückel theory with Bloch wavefunctions. The calculations are sensitive to the atomic position of the adsorbate and require further refinement. Due to the protective nature of the iodine layer and its high polarizability, the iodine layers were used to study the ambient pressure adsorption of fluorinated carbosilane dendrimers. These dendrimers are stable in vacuum but do not form an ordered structure at ambient temperature. Heating the adsorbed dendrimer in vacuum to 1100 K produced a new ordered structure on the platinum surface.

This structure was shown not to be an intact dendrimer molecule as two different dendrimers with similar structural moieties produced the same ($\sqrt{19}x\sqrt{19}$)R23.4° LEED pattern. The ordered structure was studied by Auger spectroscopy to determine the carbon coverage. This structure is proposed to be islands of a coincidental lattice of graphite.

Examiners:

Dr. D.A. Harrington, Supervisor (Department of Chemistry)

Dr. A.D. Kirk, Departmental Member (Department of Chemistry)

Dr. C.X.W. Qian, Departmental Member (Department of Chemistry)

Dr. A. Watton, Outside Member (Department of Physics and Astronomy)

Dr. E.M. Stuve, External Examiner (Department of Chemical Engineering, University of Washington)

TABLE OF CONTENTS

LIST OF TABLES

LIST OF FIGURES

Page

Page

ACKNOWLEDGMENTS

The author would like to gratefully acknowledge Dr. David A. Harrington for his help in the preparation of this thesis. I would also like to thank him and the University of Victoria for providing me with the opportunity to do this research.

DEDICATION

This thesis is dedicated to

my loving wife Sarah

and my parents, Don and Marion.

1

Introduction

Electrochemical processes are fundamental parts of our technological world, and there has been much scientific study into all aspects of electrochemical systems. As a result, electrochemistry is a well-developed science with direct applications in industry. Most studies concentrate on the exchange of electrons at interfaces, such as the solid-liquid interfaces of electrodes immersed in an electrolyte. The detailed study of the surfaces of electrodes, and of other materials, has produced a new field of study called electrochemical surface science. This new scientific branch is an amalgamation of electrochemistry, solid-state physics, and materials engineering. Surface science attempts to probe surfaces on a microscopic and atomic level by using advanced instrumental techniques. These difficult experiments yield detailed information about the nature of surfaces. Indeed, the scanning tunnelling microscope (STM) provides subnanometer resolution, allowing us to actually see individual atoms on surfaces.

The adsorption of iodine on the (111) surface plane of a single crystal of platinum is the main focus of the investigations described in this thesis. This system has been well-characterized by several electrochemical and UHV techniques, including STM. These studies are briefly reviewed in Chapter 2. The experiments described in Chapters 4 and 5 examine the behaviour of the work function during the iodine adsorption and desorption. There are several structural phase transitions of the adsorbed iodine layer that occur on the surface. These phase transitions have been studied with LEED, Auger spectroscopy, and work function measurements. Chapter 4 focuses on the adsorption experiments and the structural

transformations of the adsorbate layer that occur on the surface. Chapter 5 discusses the desorption experiments and the methods used to extract kinetic information. Desorption above 300 K occurs mostly as atomic iodine while at 200 K the main desorption is molecular iodine. The kinetics of these desorptions have been studied using mass spectroscopy. The two main desorption features above 300 K both display first-order kinetics with one of them also having a coverage-dependent activation energy. An attempt is made to simulate these desorption spectra from the experimentally-determined kinetic parameters. At 200 K, the molecular iodine desorbs with essentially zeroth order kinetics.

The work function change during adsorption and desorption is studied to determine whether it is a function of iodine coverage or a function of the surface sites the iodine occupies. The sign of the change in work function during iodine adsorption is opposite to that expected based on electronegativity arguments. As described in Chapter 6, the work function is the energy required to extract an electron from the metal and remove it to the vacuum. It has both a surface and bulk component but only the surface component is modified by adsorbates. The change in work function is modelled using an extended-Hückel molecular orbital calculation that includes the translational symmetry of the repeating structure on the surface. A set of FORTRAN computer programs was written to perform these types of calculations.

In the final chapter we attempt to exploit the protective nature of the iodine layer to do ambient-pressure adsorption experiments using fluorinated carbosilane dendrimers. These dendrimers are stable in vacuum when adsorbed on the iodine layer. Heating these dendrimers forms an ordered structure with a $(\sqrt{19}\times\sqrt{19})R23.4°$ LEED pattern. This structure is likely to be islands of graphite rotationally oriented to have a coincidental lattice

match with the platinum substrate.

As this is the first set of experimental results to be generated using this vacuum system, the experimental details for all of the techniques are discussed extensively in Chapter 3. The computer interfacing of the equipment and the software used to process the experimental data are also described as these computer programs were also written by the author. Procedures are laid out for the attaining UHV pressures and the operation of most of the electrical components. Details for cleaning the platinum surface are also described.

2

Background To Iodine Adsorption On Platinum Electrodes

2.1 Iodine Structures on Platinum

Iodine and other halogens are known to adsorb strongly on the surfaces of many transition metals [2.1-2.5]. Studies of halogen adsorption on metals are well known in the literature [2.6]. On platinum electrodes, iodine forms a stable layer that creates a barrier to further adsorption of other potential adsorbates. The structure and electronic nature of these iodine layers have been investigated using several surface-sensitive techniques. On single-crystal surfaces of platinum, the iodine atoms arrange themselves into ordered monolayers that are commensurate with the metal surface. These overlayers are the main focus of this thesis.

Iodine will adsorb spontaneously if platinum is put into an aqueous solution containing iodide ions (KI, for example) [2.7]. Adsorption at open-circuit potential is accompanied by the transfer of an electron and the evolution of hydrogen gas:

$$\begin{aligned} I^- + H^+ &\rightarrow I_{ads} + \tfrac{1}{2} H_2 \qquad (pH<7) \\ I^- + H_2O &\rightarrow I_{ads} + OH^- + \tfrac{1}{2} H_2 \qquad (pH>7) \end{aligned} \tag{2.1}$$

Of the face-centered cubic (fcc) low-index crystal faces, the (111) surface is the most thermodynamically stable as it provides the highest coordination number for the surface atoms. The top three layers of the (111) surface are shown in figure 2.1. Three different

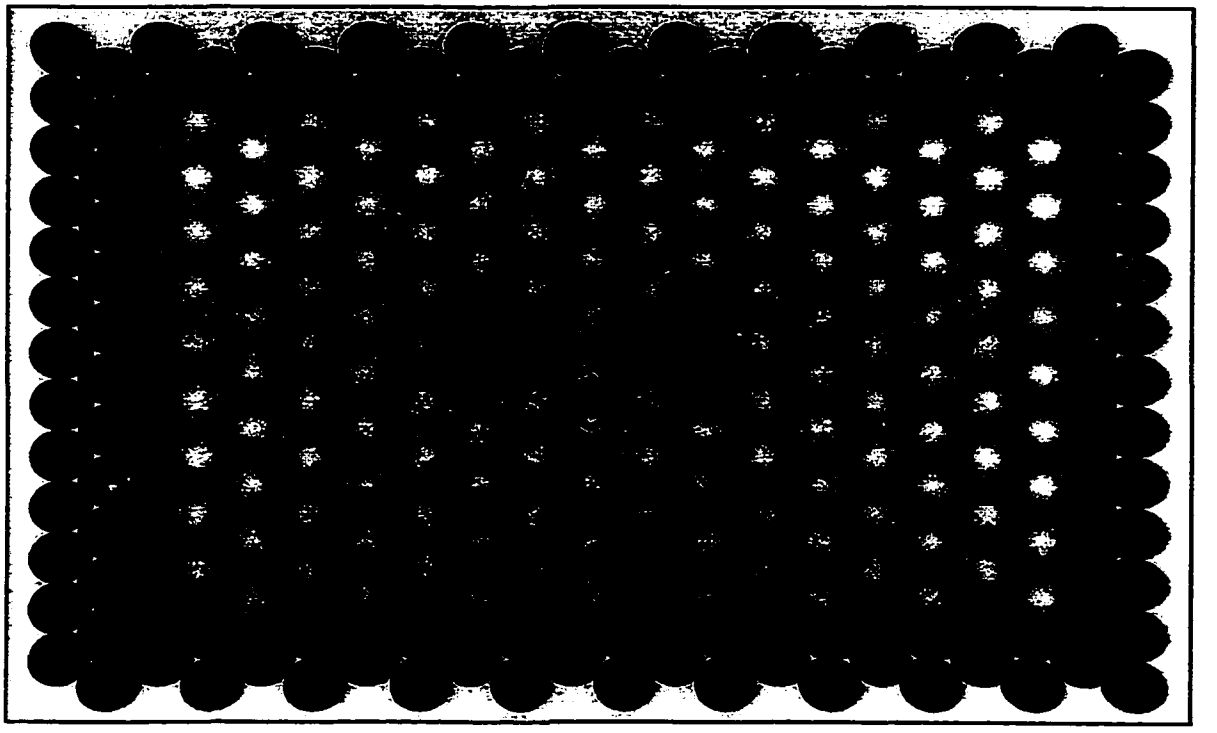

Figure 2.1-Top Three Layers of Platinum Surface Showing fcc and hcp Threefold Sites

iodine structures are observed when single-crystal platinum(111) electrodes are emersed from solutions containing iodine. These structures have all been studied by Auger electron spectroscopy (AES), low-energy electron diffraction (LEED), and scanning tunneling microscopy (STM). The adsorbed iodine atoms were found to occupy specific sites on the platinum(111) surface. There are three common adsorption sites on fcc (111) surfaces. The atop site is directly above a first layer platinum atom. The bridged site is a site that bridges two platinum atoms. The three-fold site is a site where the adsorbate binds to three platinum atoms. There are two types of three-fold sites on fcc (111) surfaces. Both are identical in the top layer but differ in the second layer of atoms. As shown in figure 2.1, using semi-transparent atoms in the top layer, one three-fold site (hcp site) has a second layer atom directly beneath it. The other three-fold site (fcc site) is above a hollow and has an atom in the third layer directly beneath it. The radius of the platinum atoms in this figure (and other

figures in this chapter) represents the metallic radius of 1.39 Å.

The lowest coverage structure, shown in figure 2.2, has a ($\sqrt{3}$x$\sqrt{3}$)R30° unit cell and a coverage of 1/3. All of the adsorbed iodine atoms occupy three-fold sites on the surface [2.8]. These figures were created with the Persistence Of Vision (POV) raytracing program [2.9] and are meant to represent three-dimensional models of the structures. At the centre of figure 2.2 is a semi-transparent iodine atom to show the bonding site. The three-fold site is expected to be the most energetically favoured bonding site as the adsorbate coordinates to three platinum atoms. Although there is little difference in binding energy between the fcc and hcp three-fold sites, the iodine atoms are thought to occupy the fcc three-fold sites [2.8]. At present, there is no experimental evidence to support this conclusion.

Another iodine structure formed has a ($\sqrt{7}$x$\sqrt{7}$)R19.1° unit cell and is shown in figure 2.3. This structure has a coverage of 3/7 with two three-fold sites and one atop site

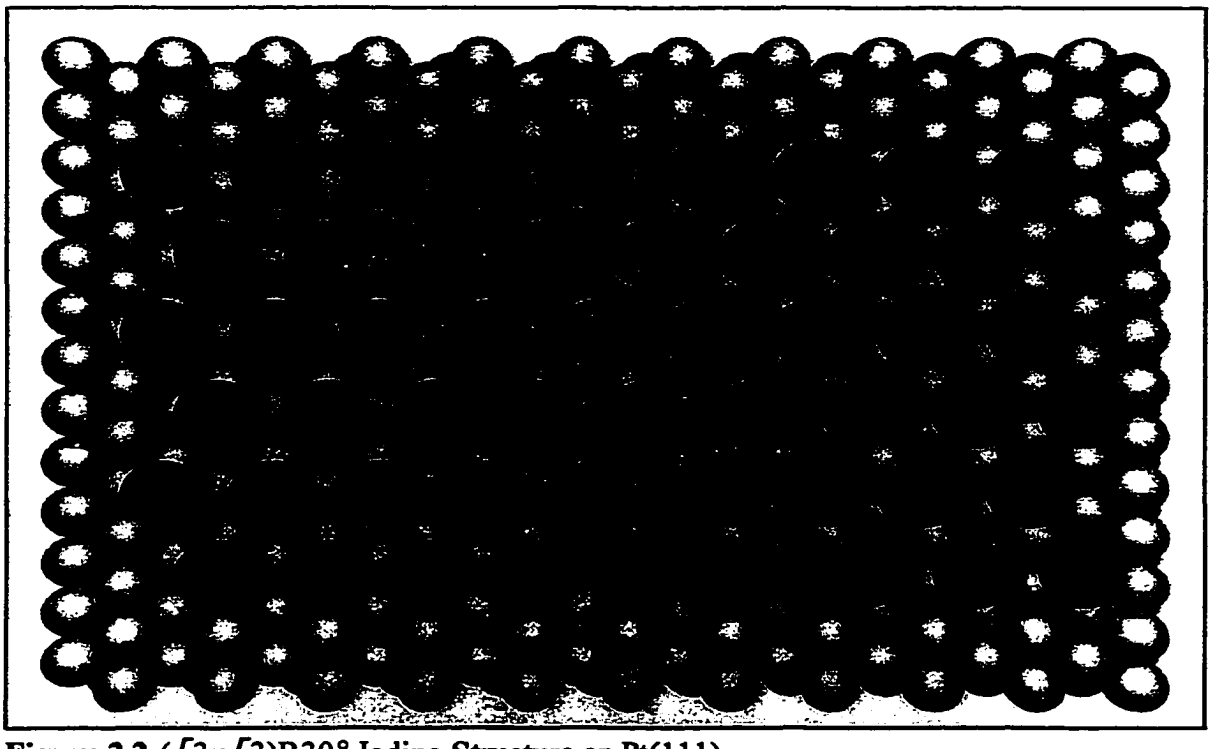

Figure 2.2-($\sqrt{3}$x$\sqrt{3}$)R30° Iodine Structure on Pt(111)

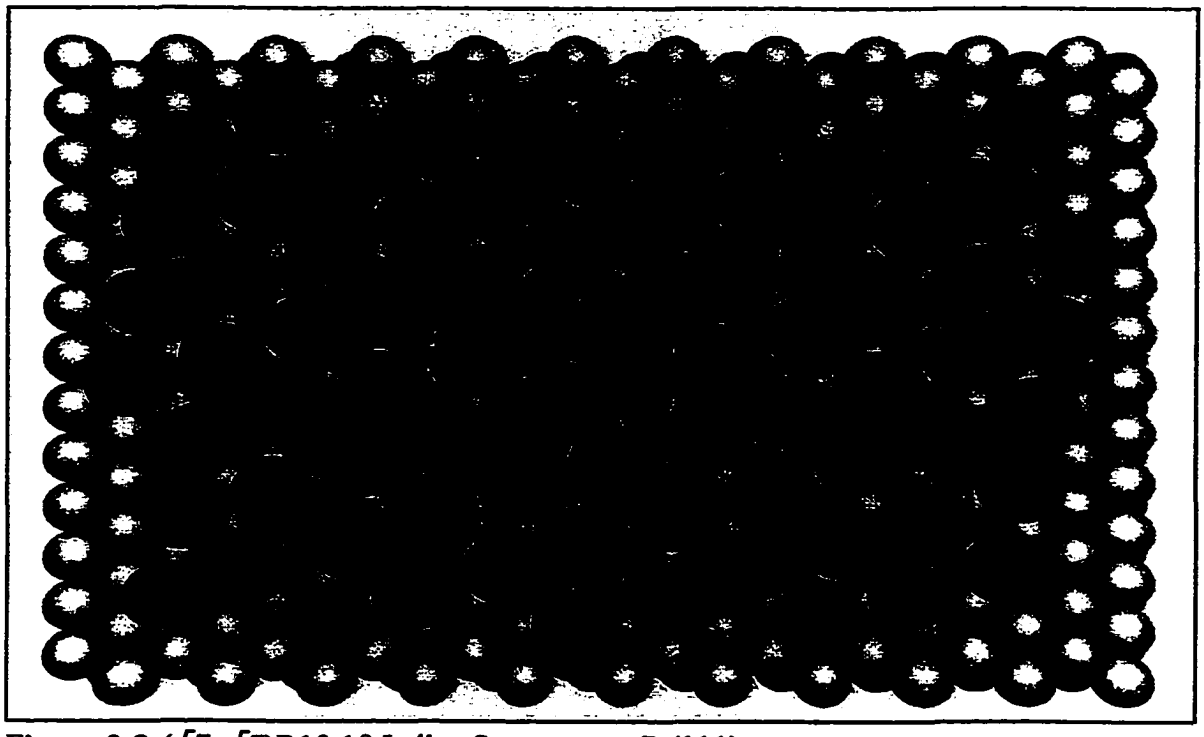

Figure 2.3-($\sqrt{7}$x$\sqrt{7}$)R19.1° Iodine Structure on Pt(111)

being occupied. There are two rotational domains of this structure that coexist in equal amounts on the surface. STM showed that these domains do not coexist on the same atomic terrace and that the terraces are equally populated by one or the other of the ($\sqrt{7}$x$\sqrt{7}$)R19.1° domains [2.10].

At a slightly higher coverage of 4/9, a (3x3) unit cell is observed. STM studies of this structure provided an unexpected result [2.11]. There are two structures that coexist on the surface, each of which has a (3x3) unit cell (shown in figures 2.4 and 2.5). One is the expected structure when all the iodine atoms occupy symmetric sites (one atop site and three bridged sites). This is labelled the symmetrical (3x3) structure. In the other (3x3) structure, (labelled the asymmetrical (3x3) structure) one three-fold site is occupied and three asymmetrical atop sites are occupied. Unlike the rotational domains of the ($\sqrt{7}$x$\sqrt{7}$)R19.1° structure, the two (3x3) structures do coexist on the same atomic terraces and boundaries

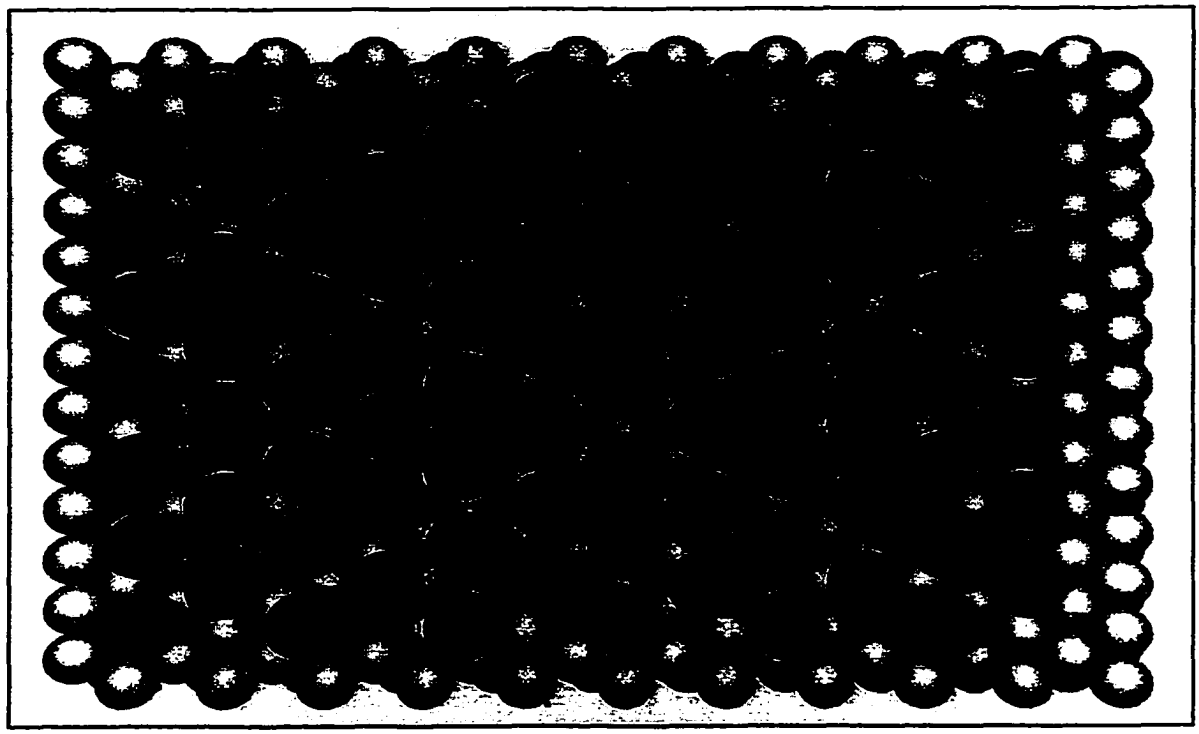

Figure 2.4-Symmetrical (3x3) Iodine Structure on Pt(111)

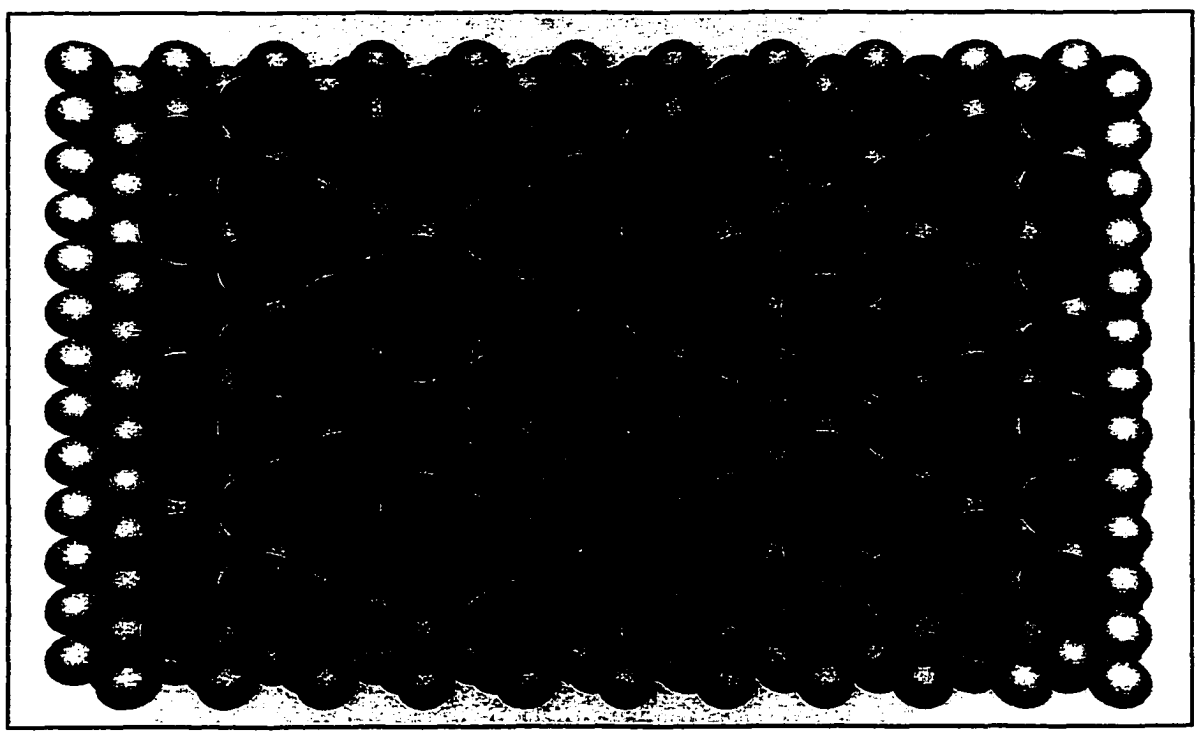

Figure 2.5-Asymmetrical (3x3) Iodine Structure on Pt(111)

between them have been observed with STM.

At a higher coverage of 0.64 (52/81), another iodine phase has been observed [2.12]. This structure has a $(3\sqrt{3}x9\sqrt{3})R30°$ unit cell that forces the iodine atoms into a densely packed state. The apparent iodine interatomic distance (3.3Å) is considerably less than the van der Waals radius (4.3Å). This phase is less stable than the other phases and readily converts to the (3x3) structure.

2.2 Electrochemical Studies of Iodine on Platinum

Most studies concerning the adsorption of iodine on platinum have been electrochemical in nature. The initial studies assumed that in solution, iodide ions adsorb on platinum electrodes similarly to chloride ions. It was soon realized that iodide ions adsorb as neutral iodine atoms with an electron being transferred, as shown in equation 2.1 [2.13, 2.14]. The amount of iodine adsorbed on the surface can be measured coulometrically by oxidizing the adsorbed iodine to the iodate ion by:

$$I_{ads} + 3H_2O \rightarrow IO_3^- + 6H^+ + 5e^- \qquad (2.2)$$

Coverages estimated from the charge (assuming a five electron process) indicated an iodine surface concentration of $1.14x10^{-9}$ mol/cm^2 ($6.87x10^{14}$ atoms/cm^2). If the polycrystalline platinum is mostly Pt(111) (with a surface packing density of $1.5x10^{15}$ atoms/cm^2), the iodine coverage is estimated to be 0.46. This result is very close to the coverages of the (3x3) structure (0.44) and $(\sqrt{7}x\sqrt{7})R19.1°$ structure (0.43).

The coverages of the iodine structures on Pt(111) were determined as a function of

electrode potential by emersion of the electrode and measurement of the iodine's X-ray fluorescence intensity (at 28.6 keV) [2.15]. These results showed that in the potential region where the $(\sqrt{7}x\sqrt{7})R19.1°$ is the stable phase (-0.3 V vs Ag/AgCl at pH 6.7), the coverage is $6.6x10^{14}$ atoms/cm^2 (θ=0.44). This coverage is in very good agreement with the proposed structures. At potentials more positive than this, the iodine coverage decreases to zero with increasing potential. The results also show that a coverage of 1/3 (the coverage of the $(\sqrt{3}x\sqrt{3})R30°$ structure) occurs at a potential of -0.5 V (vs Ag/AgCl) at pH 6.7.

The evidence for a neutral iodine adsorbate comes from coulometrically measuring the interfacial excess of Fe^{2+} when halogen-coated platinum electrodes are emersed from FeX_2 solutions [2.16]. If halogen anions are adsorbed on the surface, and the platinum is left uncharged, the Fe^{2+} ion would be needed at the surface to preserve electroneutrality after emersion. For Br^-, Cl^-, and F^- adsorption, an excess of Fe^{2+} ions was observed. The amount of Fe^{2+} associated with the adsorbed layers was half the amount of halogen present, as expected from the iron oxidation state. No Fe^{2+} was observed to be associated with the emersed iodine layer. This suggests that the Pt-I system is electrically neutral, though the Pt and I could be oppositely charged.

Cyclic voltammetry studies of iodine-coated platinum electrodes showed several interesting features. The under-potential deposition (UPD) of hydrogen that occurs on bare platinum electrodes is completely blocked by the presence of adsorbed iodine [2.17]. Iodine desorption does occur at more negative potentials (-0.5V vs. Ag/AgCl at pH 7) and is accompanied by evolution of hydrogen gas. The potential where iodine desorption occurs is a function of pH, changing from -0.3 V (vs. Ag/AgCl) at pH 4 to -0.6 V (vs Ag/AgCl) at pH 10.

The structure of the iodine on the platinum surface is also dependent on the electrode potential [2.18]. At high pH and positive potentials, the iodine exists as the $(\sqrt{7}x\sqrt{7})R19.1°$ structure. As the electrode potential is made more negative, the iodine coverage steadily drops and goes through an intermediate stage of having a mixed $(\sqrt{7}x\sqrt{7})R19.1°$ $(\sqrt{3}x\sqrt{3})R30°$ structure. As the iodine coverage decreases further, only the $(\sqrt{3}x\sqrt{3})R30°$ structure is observed on the surface.

At low pH, the (3x3) and $(\sqrt{7}x\sqrt{7})R19.1°$ structures are prevalent over a wide range of electrode potentials (+0.85 V to -0.3 V vs Ag/AgCl). At potentials more negative than -0.3 V, the $(\sqrt{3}x\sqrt{3})R30°$ structure is formed and the iodine coverage rapidly decreases. It is interesting to note that at high pH the (3x3) structure is not observed. It only forms at positive potentials (>0.5 V vs Ag/AgCl) at pH 7.

During these studies, where the platinum electrode was emersed from the iodide solution and transferred into vacuum for study, it was noticed that the (3x3) and $(\sqrt{7}x\sqrt{7})R19.1°$ structures are very hydrophobic, while the $(\sqrt{3}x\sqrt{3})R30°$ structure is hydrophilic [2.18]. This observation led to a series to experiments involving the competitive adsorption of solvents with iodine. It was found in all cases studied that the adsorbed iodine layers were completely stable to the solvents [2.19, 2.20]. The iodine could also displace preadsorbed solvent molecules, demonstrating the strength of the interaction between the iodine and the platinum electrode.

The stability of the iodine layers led to a procedure for preparing clean platinum single-crystal surfaces outside the UHV environment [2.21,2.22]. The procedure involves heating the platinum electrode in hydrogen and then cooling it in the presence of iodine vapor. Surfaces that have been purposely disordered by electrochemical cycling or by high-energy

ion bombardment can be reordered by adsorbing iodine at 700 K, which is 500 K below the usual annealing temperature for platinum. The iodine layer protects the platinum surface from contamination and allows the platinum to be transferred at ambient pressure to an electrochemical cell. The adsorbed iodine can be replaced by CO by bubbling the gas through the electrolyte. The adsorbed CO is then easily oxidized off the surface at potentials where the surface remains unreconstructed. This procedure yields a well-ordered platinum surface that is free of contaminants.

2.3 Vacuum Studies of Iodine on Platinum

UHV studies also showed that it was possible to create the $(\sqrt{3}x\sqrt{3})R30°$ and the $(\sqrt{7}x\sqrt{7})R19.1°$ iodine structures by exposing a clean platinum (111) surface to iodine vapor or to HI [2.23]. The I_2 and HI molecules dissociate to form atomic iodine that arranges into structures identical to those formed from solution. When HI adsorbs onto the surface, no hydrogen can be detected once the adsorption is complete. The (3x3) structure was not formed by gas-phase dosing in UHV even though the (3x3) structure prepared electrochemically, or by cooling at atmospheric pressure with iodine vapor (see above), is completely stable in vacuum.

The $(\sqrt{3}x\sqrt{3})R30°$ and $(\sqrt{7}x\sqrt{7})R19.1°$ structures have been studied by LEED and AES [2.14]. The structures formed are identical to those created electrochemically. Heating the iodine-covered platinum in vacuum causes the iodine to desorb. This can be measured with a mass spectrometer to identify the desorbing species. Only atomic iodine was observed desorbing from the surface over a wide temperature range (500-1000 K). Starting with the $(\sqrt{7}x\sqrt{7})R19.1°$ structure, iodine begins to desorb at 565 K. At this point the LEED pattern

changes from the ($\sqrt{7}$x$\sqrt{7}$)R19.1° pattern to a diffuse pattern. At 645 K, more iodine desorbs and the LEED pattern changes from a diffuse pattern to a ($\sqrt{3}$x$\sqrt{3}$)R30° pattern. At higher temperatures the LEED pattern becomes diffuse again. Above 1000 K, all of the iodine has been removed and the LEED pattern shows only the (1x1) pattern from the platinum substrate. At each phase transition, a peak is observed in the desorption spectrum of mass 127. All four peaks match the desorption spectra obtained from the experiments described in this thesis. Auger analysis during the desorption process showed an essentially linear drop in iodine coverage over this temperature range.

During the thermally-induced transitions, no molecular iodine is observed desorbing from the surface. However, during the conversion of the (3$\sqrt{3}$x9$\sqrt{3}$)R30° structure to the (3x3) phase, both mass 127 and mass 254 are observed. The formation of molecular iodine is likely due to the high packing density where the iodine atoms are being forced together.

Although STM conclusively showed where the iodine atoms are sitting on the surface for the various structural phases, no information was provided about the actual distance between the iodine and the platinum. A Surface-extended X-ray-absorption fine structure (SEXAFS) study of iodine adsorbed on Pt(111) gave a bond length of 2.64Å [2.24] for a surface with a coverage of 0.43. This is approximately the sum of the covalent radii for platinum and iodine (1.29Å and 1.33Å respectively).

Adsorption of iodine onto the 6(111)x(111) stepped platinum surface [2.25] produced several different LEED patterns, as expected. These could all be rationalized by considering that the surface consists of small terraces of Pt(111) separated by atomic steps. The thermal desorption of iodine showed that although there were several more binding sites (due to the steps), the iodine desorbs in essentially the same fashion as from the (111) surface.

To probe the difference between the iodine adsorbed in atop sites and those adsorbed in three-fold sites on the Pt(111) surface, the core-electron ($4d_{5/2}$) binding energy of the iodine was measured as a function of coverage [2.26]. At coverages below 1/3, where only three-fold sites are occupied, the binding energy decreases slightly (0.2 eV) with increasing coverage. This shift in binding energy is assumed to be due to repulsive interactions between the adsorbed iodine atoms. Once the $(\sqrt{3}x\sqrt{3})R30°$ is completed, increasing the coverage causes the atop sites to become occupied and the structure converts to the $(\sqrt{7}x\sqrt{7})R19.1°$ phase. A new binding state is observed, shifted by 0.95 eV from the binding state associated with the three-fold sites. This binding state is due to iodine atoms populating the atop sites. These atop iodine atoms are not as strongly bound to the surface as those iodine atoms in the three-fold sites. The energy of the three-fold iodine binding state continues to be shifted as the atop sites are filled, but the increase is the same as for coverages below 1/3. This suggests that the repulsive interaction between the iodine atoms is the same, regardless of whether the iodine atoms sit in three-fold or atop sites.

There is one other UHV study of iodine adsorption on platinum(111) where the iodine structures are prepared by thermally decomposing adsorbed methyl iodide rather than gas-phase iodine dosing [2.27]. Their XPS data shows that the adsorption of iodine causes a decrease in the work function of the platinum. However, their thermal desorption data of atomic iodine does not agree with the desorption behaviour described above (or the desorption data obtained in this thesis). The UHV system used to collect the XPS data was not equipped to perform LEED studies and so the structures of the adsorbed iodine could not be confirmed.

3

Experimental

3.1 Introduction

The experiments described in this thesis were performed using a stainless-steel ultra-high vacuum (UHV) chamber with an operating base pressure of $2x10^{-10}$ mbar. The UHV system has facilities for Auger electron spectroscopy (AES), low-energy electron diffraction (LEED), electron-stimulated desorption ion-angular distribution (ESDIAD), thermal desorption mass spectroscopy (TDS), and measurement of work function changes ($\Delta\Phi$). It is also possible to transfer the sample from the main UHV chamber to a high-pressure (HP) chamber that can easily cycle between vacuum conditions (10^{-8} mbar) and atmospheric pressure. The HP chamber allows the sample to be brought into contact with liquid and be made the working electrode in a standard electrochemical cell. This allows a wide variety of non-vacuum experiments to be performed. There are facilities to rapidly pump out the HP chamber after such experiments so the sample can be quickly transferred back into vacuum for ex-situ analysis using the methods mentioned above.

Before describing the details of the experiments, it seems appropriate to justify the need for such drastic experimental conditions. The UHV environment is difficult to achieve and the apparatus is prone to malfunction due its complexity. The reason for creating the UHV environment is that it allows one to prepare and study clean, atomically-flat surfaces. Such surfaces are quite reactive and molecules contacting the surface may stick or decompose. Such contaminants, carbon monoxide in particular, block sites on the surface and

can alter the outcome of any experiment. How long the surface remains clean is determined by the pressure inside the UHV system. At atmospheric pressure, the surface would remain clean for less than 10^{-9} s. At 10^{-6} mbar, the surface would remain clean for approximately one second. Pressures below 10^{-9} mbar are required to perform experiments that take tens of minutes.

The experiments available in the UHV can provide detailed atomic-level information about the surface of the sample. AES provides an elemental analysis of the surface layers, while LEED provides information about the structure, symmetry, and order of the surface layers. Work function measurements are very sensitive to changes in the electronic density at the surface, and can detect changes in surface coverages (θ) below 0.001 monolayers (ML). The mass spectrometer is used to detect species desorbing from the surface of the sample and can be used to determine kinetic information about the desorption process.

3.2 UHV System Overview

Attaining pressures in the UHV regime requires special pumping arrangements as shown in figure 3.1 and 3.2. The main chamber is pumped by a Balzers 510 l/s turbomolecular pump backed by a 2-stage Varian rotary-vane mechanical pump. There is also a Varian titanium-sublimation pump (TSP) in this chamber, located below the electron optics. This combination gives a base pressure inside the main chamber of 1.5×10^{-10} mbar. Both the mass spectrometer and the high-pressure analysis chamber are pumped by Balzers 60 l/s turbomolecular pumps backed by 2-stage Edwards rotary-vane mechanical pumps (5 m^3/h). The base pressure in the mass spectrometer is 6×10^{-10} mbar while the base pressure in the high-pressure analysis chamber is 6×10^{-9} mbar.

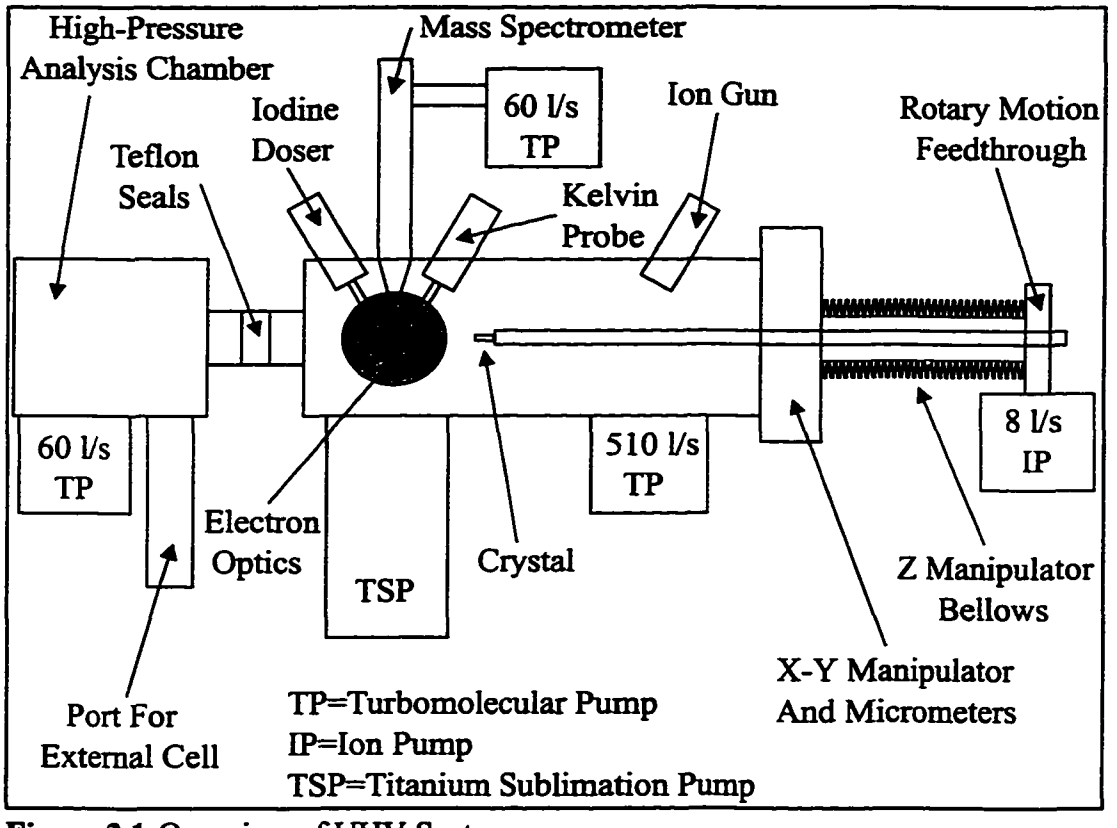

Figure 3.1-Overview of UHV System

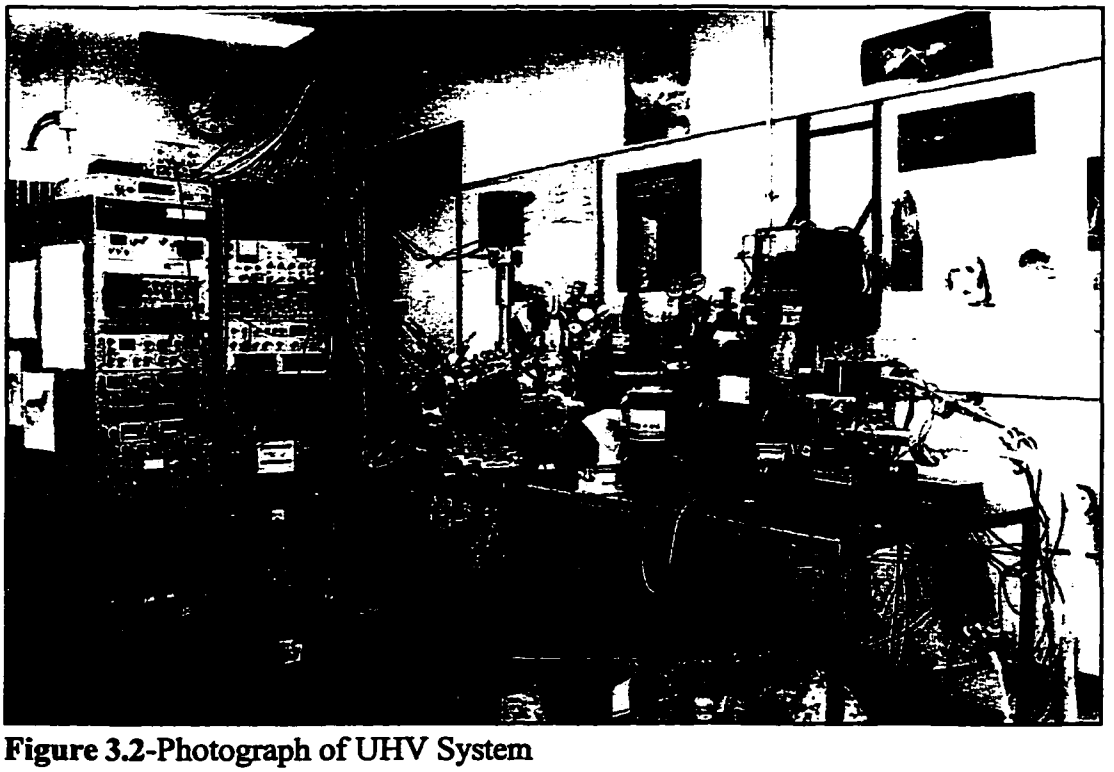

Figure 3.2-Photograph of UHV System

A doubly differentially-pumped rotary-motion feedthrough (RNN-150 from Thermionics Northwest Inc.) is mounted at the end of the sample manipulator to allow rotation of the crystal around the instrument's main axis (z-axis). The three seals inside the feedthrough create a constant leak that is unavoidable but has been minimized by the use of appropriate pumping. The first stage of differential pumping on the rotary seals is a low-vacuum ($\sim 10^{-3}$ mbar) connection to the roughing line of the mass spectrometer's turbomolecular pump. The second stage on the seals is pumped by a Varian 8 l/s Vacion ion pump ($<10^{-8}$ mbar). Pressure bursts during rapid sample rotation are below 10^{-9} mbar, and are barely detectable ($<2\times10^{-10}$ mbar) when the sample is rotated slowly.

Two molecular-sieve sorption pumps, cooled with liquid nitrogen, are used to quickly pump out the HP analysis chamber after it has been exposed to atmospheric pressure. There are also connections from the sorption pumps to a gas manifold used for the controlled introduction of gases into the vacuum.

During operation when liquid nitrogen is being used to cool the sample, the entire manipulator arm becomes cold and behaves like a cryopump. This lowers the ultimate base pressure from 1.5×10^{-10} mbar to 6×10^{-11} mbar. This effect also keeps the operating base pressure during experiments at 2×10^{-10} mbar. Two liquid nitrogen 'cold fingers', located close to the ion gun, also act like small cryopumps. A third 'cold finger' is located on the HP analysis chamber to help pump away excess solvent vapours during transfer experiments.

The pressure in the UHV chamber is measured by a Bayard-Alpert type ion gauge. A second ion gauge is located in the HP analysis chamber. The pressures in the three backing lines of the turbomolecular pumps are measured by thermocouple gauges. All of these pressure gauges are connected to a Varian Multigauge control unit. A Faraday cup inside the

mass spectrometer can measure the total pressure inside its chamber.

A custom-built system monitor was constructed at UVic to constantly monitor the pressures at various places in the UHV system. It has complete control over the power distribution, which is divided from a 3-phase 90 A electrical source. If the pressure levels are above certain setpoints, the system monitor will turn off certain electrical components to prevent damage to sensitive components inside the vacuum. To prevent catastrophic failure, the system monitor will cut power to the pumps if the pressure rise is large enough. If such an event takes place, a failure analysis card in the system monitor provides information about what caused the system shutdown. Other events, such as a disruption of the cooling water for the turbomolecular pumps, can also cause a complete system shutdown. The system is equipped with an uninterruptable power supply (Alpha Technologies UPS 600) to supply temporary power to critical components during power outages. At the present time, the UHV system can withstand power outages of less than thirty seconds without losing vacuum integrity.

3.3 Establishing and Maintaining a UHV Environment

Creating a vacuum in the 10^{-10} mbar range proceeds in several stages. Starting from atmospheric pressure, with all pumps stationary, the system monitor takes care of the initial startup. The roughing and turbomolecular pumps are powered, and the roughing pumps evacuate the chamber while the turbomolecular pumps accelerate up to operating speed. This part of the startup procedure takes approximately 15 minutes. The final operating speeds of the turbomolecular pumps are 60,000 RPM for the 510 l/s pump and 90,000 RPM for the 60 l/s pumps.

The ion pump is not automatically started by the system monitor as it cannot be operated at atmospheric pressure. Once the roughing line on the first stage of the rotary feedthrough has reached ~10^{-2} mbar, it is used to evacuate the main body of the ion pump. A liquid nitrogen cold trap in the roughing line helps to decrease the amount of oil contamination in the ion pump. Once the roughing line is back below 10^{-2} mbar, it is disconnected and the ion pump is switched on. The ion pump will usually start to actively pump within 20 seconds and quickly drop to the 10^{-5} mbar range.

After several hours of pumping, the pressure in the main chamber will usually be below 10^{-6} mbar. At this point, the system is baked, using three 1000 W heaters and a large insulating shroud that covers the entire UHV system. Baking the system causes gas molecules on the walls of the chamber, particularly water, to desorb so they can be pumped away. This step is essential to obtain UHV pressures. The heaters are regulated by a temperature programmer that reads the temperature of two thermocouples connected to the main body of the UHV chambers. The system is heated to 140 °C for a minimum of 12 hours as it takes 8 hours for the temperature of the metal chamber to reach 140 °C. Higher bakeout temperatures cannot be used because of a set of Teflon seals mounted in the system. The system monitor ensures that the pressure inside the chambers does not go above 10^{-5} mbar during the bake out. Power to the heaters will be cut if the pressure does go too high and baking will only resume after the pressure has dropped back below 10^{-5} mbar.

It is possible to bake the turbomolecular pumps with band heaters that heat the main body of the pumps. However, to avoid overheating the pumps, the baking temperature must then be decreased to 90°C. It is not recommended to bake the turbomolecular pumps on a routine basis as the heating degrades the oil lubricating the rotor bearings. The only time

when it is necessary to bake the pumps is after they have been cleaned (using isopropanol) or in cases where there is a large amount of water contamination.

After letting the system cool for at least 12 hours, the pressure in the system is typically below 10^{-9} mbar. All the filaments inside the vacuum chamber must then be degassed for several hours to desorb unwanted contaminants. After this, the system is baked again for another 12 hours. Upon cooling, the pressure is in the low 10^{-10} mbar range. After more filament degassing, the system should be ready for experiments to begin. After heavy use, where the system may become contaminated, it may be necessary to bake the UHV system again to regain a low operating base pressure. It should be noted that 12 hours is the minimum baking time and that baking the system longer (2-3 days) will, in general, improve the quality of the vacuum.

The titanium sublimation pump also aids in reestablishing a good working base pressure and can be used intermittently to 'clean up' the main UHV chamber. Operating the TSP for approximately one minute at 43 A will cause the base pressure to temporarily increase into the 10^{-8} mbar range. Once the power to the TSP is turned off, the pressure will drop as the titanium filaments cool down. Although the system may take several hours to reach a new base pressure, the ultimate pressure will be lower than before the TSP was switched on. The nipple where the TSP is mounted is cooled with water flowing through a copper jacket to prevent the hot titanium from warming the metal of the system.

3.4 Sample Mounting

The sample used for the experiments described in this thesis is a 1 cm diameter single-crystal of platinum. The surface was oriented to the (111) plane within 0.5° by Laue

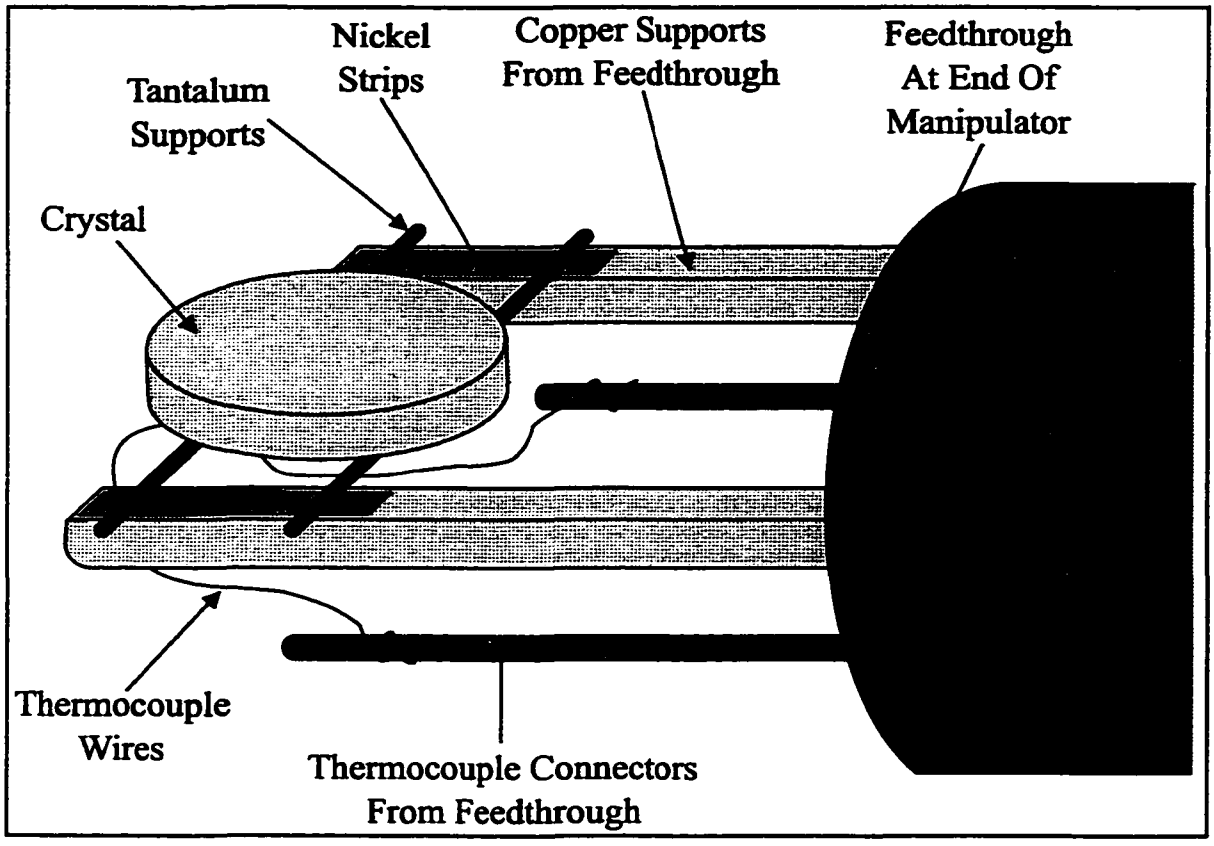

Figure 3.3-Crystal Supports and Thermocouple Connections

back diffraction. The sample is mounted at the end of a large manipulator arm, as shown in figures 3.3 and 3.4. In figure 3.4, the sample is located beneath the inlet to the mass spectrometer. The tip of the Kelvin probe can be seen just above the crystal.

The feedthrough (from ISI Insulated Seal Inc.) the end of the arm has a K-type thermocouple feedthrough and two copper electrical feedthroughs. These copper wires act as the main support for the crystal. Two 0.010" tantalum wires are spot welded across the back of the crystal. The tantalum wires are then spot welded to nickel strips that are silver-brazed to the copper electrical feedthroughs. Thermocouple wires (0.003") are spot welded to the back of the crystal and are connected to the thermocouple feedthroughs.

The copper electrical feedthrough allows the sample to be heated resistively up to

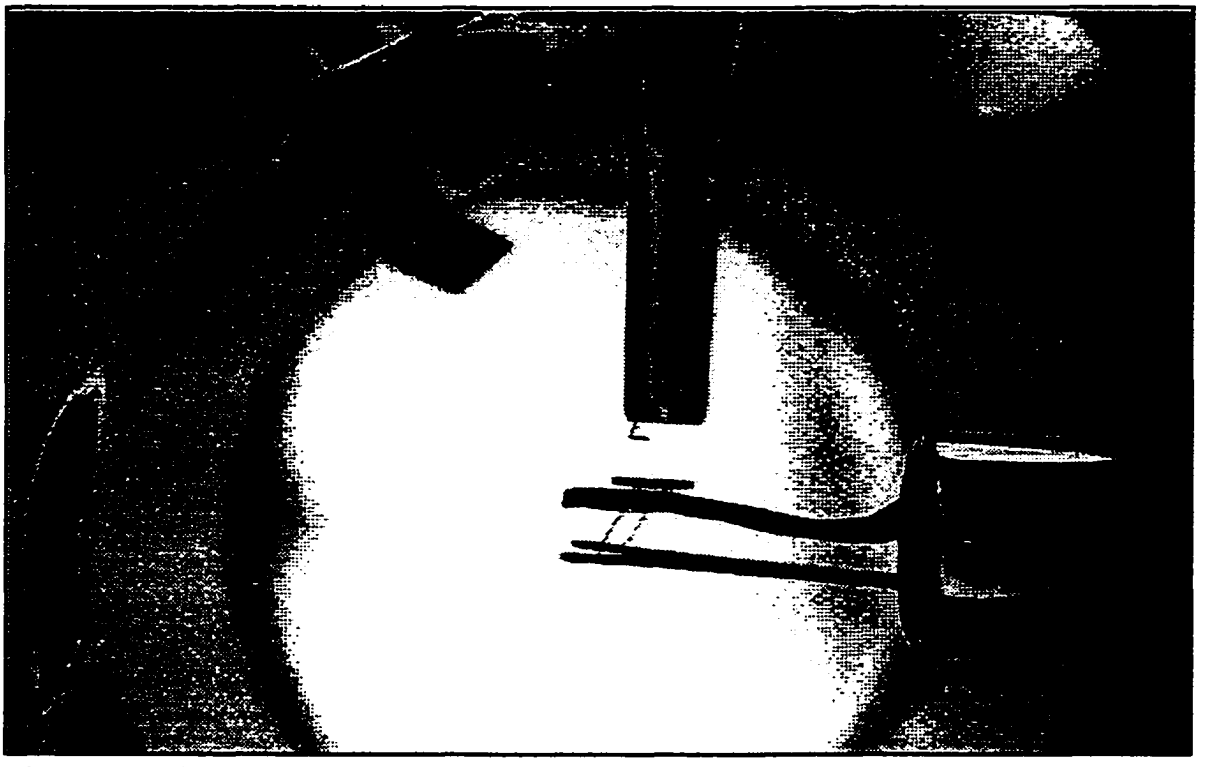

Figure 3.4-Photograph of Sample Supports

1300 K. An external power supply (model LK350-FMOV from Lambda Electronics Corp.), provided up to 35 A to heat the crystal. This regulated power supply is connected to a temperature control unit (built at UVic) that measures the sample temperature with the K-type thermocouple. The temperature controller allows the sample to be heated at a constant a rate, usually 1-10 K/s. The sample can also be cooled to 90 K as the copper electrical feedthroughs are cooled with a constant stream of liquid nitrogen. The flow of liquid nitrogen is shown in figure 3.5. When the sample is being heated, it is important to have sufficient cooling (liquid nitrogen or cold nitrogen gas) as the feedthrough for the sample mounting will become stressed at elevated temperatures. Cooling with liquid nitrogen also reduces the desorption of contaminants from the copper supports during thermal desorption experiments. Outside the vacuum, the copper and thermocouple wires are protected with teflon sleeves that also provide electrical insulation.

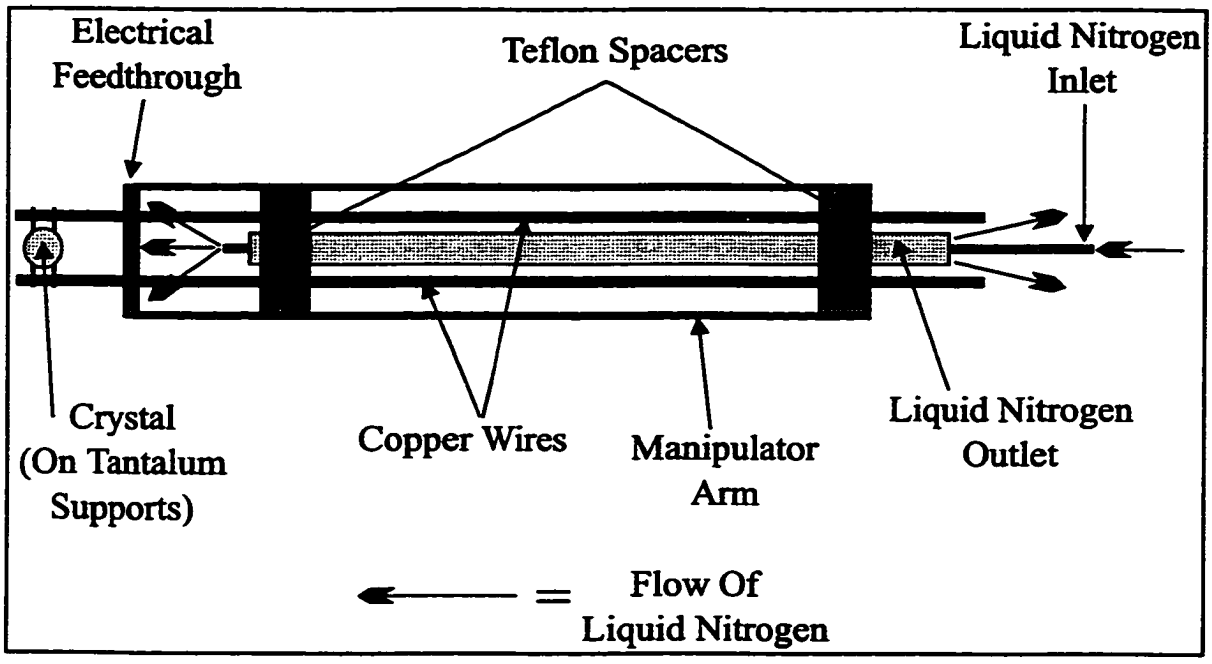

Figure 3.5-Flow of Liquid Nitrogen For Sample Cooling

The sample arm is mounted on an XYZ manipulator and has a rotary motion feedthrough to allow the sample to be rotated around the Z axis. The rotary seals inside the feedthrough are adventitiously cooled by the flow of liquid nitrogen and must be warmed with a heater fan to stay at room temperature. The micrometers on the manipulator allow precise and reproducible positioning of the sample for the various experiments.

3.5 Sample Preparation and Cleaning

The main reason for performing experiments in a UHV environment is the ability to do experiments on atomically-clean surfaces. Although the low pressures used ensure that surface contamination is minimized, it is critical that the surface is clean at the start of the experiment. There are several methods for cleaning the sample to obtain a surface that is reproducible on the atomic scale. The exact method used depends on the severity of the contamination and the type of contaminant present on the surface. The procedures described

here are specifically for cleaning platinum crystals and will change for other materials.

The platinum crystal used was cut from a single crystal stub grown by Metal Oxides and Crystals Ltd (99.999%). The crystal sample was cut with a diamond wafering saw. After cutting, the surface was polished with successive grades of Beuhler Ltd. diamond paste and then oriented by Laue back diffraction. After orienting the crystal to within 0.5° of the (111) plane, the crystal was polished further, using a 0.05 μm aluminum oxide slurry as the final polishing stage.

The sample was then mounted at the end of the manipulator arm, as described in the previous section. After establishing UHV conditions inside the vacuum chamber, the sample was ready to be cleaned.

There are two main cleaning stages used in the production of well-ordered, clean surfaces. The first stage is to bombard the surface with high energy (3 keV) argon ions using a Varian ion-bombardment gun (model 981-2043) at normal incidence. Using an argon pressure of $3x10^{-5}$ mbar and a filament current of 20 mA, a current of approximately 30 μA flows through the crystal to ground. The gun is rastered over the entire crystal surface and removes the contaminants by sputtering off several atomic layers from the surface. This treatment leaves the surface highly disordered. Heating the surface to a high temperature (1200 K) allows the surface atoms to move to their thermodynamically favoured positions and a well-ordered surface is produced when the sample is cooled. Annealing usually follows ion bombardment and together they form the basis of all cleaning procedures.

One of the problems encountered when annealing the crystal is the segregation of contaminants from the bulk metal to the surface [3.1]. The most common contaminants inside platinum crystals are silicon, sulfur, phosphorus, aluminium, and carbon [3.2]. Repeated

annealing can cause large amounts of these impurities to diffuse to the surface where they can significantly alter the chemistry of the surface being studied. The detection and elimination of these contaminants, particularly silicon, was the subject of a series of studies [3.3]. It was shown that, prior to 1981, most studies using platinum contained significant silicon contamination [3.4].

Most contaminants, such as carbon and phosphorus, are easily detectable by Auger electron spectroscopy (AES), which provides an elemental analysis of the surface layers of a sample. Characteristic Auger transitions (see section on AES) occur for each element at particular energies. Carbon, phosphorus, and aluminium have Auger transitions well separated from the platinum transitions and are therefore easily detected. Auger transitions from sulphur and silicon, however, overlap with platinum transitions and it is difficult to distinguish a clean sample from a sample contaminated with these elements.

The cleaning procedures developed are designed to eliminate these contaminants and ensure the cleanliness of the platinum samples. All of the common contaminants react with oxygen at high temperatures. Carbon and sulfur, for example, form gases that are easily pumped out of the UHV system. Other contaminants, such as aluminium and silicon, form stable oxides that do not diffuse back into the bulk metal. Platinum also reacts with oxygen to form platinum oxide but above 1000 K the oxygen desorbs leaving platinum metal.

The first step in the cleaning procedure is to heat the platinum sample to 1200 K in the presence of oxygen (5×10^{-7} mbar) for one hour. At this temperature the diffusion rate of contaminants through the metal is sufficiently high that the impurities will quickly segregate to the surface. Once at the surface, the contaminants will react with oxygen to form either volatile gases, which desorb, or stable compounds that remain fixed at the surface. After

heating, the sample can be ion-bombarded at 300 K to remove these oxides at the surface. Repeating the procedure will eventually deplete the contaminants in the crystal to the point where annealing the crystal no longer contaminates the surface.

One of the methods used to test for a clean crystal is to heat the sample to 1200 K in $5x10^{-7}$ mbar of oxygen for one hour and then to turn the oxygen off while the crystal is still hot. After all the residual oxygen has been pumped away, the sample is allowed to cool. Platinum oxide cannot form at 1200 K and so the presence of oxygen in the Auger spectrum (which is well separated from the platinum transitions) indicates surface contamination. If no other elements are present in the Auger spectrum, the contaminant is most likely to be silicon. The platinum sample must be able to pass this test before it can be considered clean.

The sample used in the studies here was put through the oxygen/ion bombardment cycle for two weeks before all of the silicon was depleted. No other contaminants were observed in the Auger spectrum, shown in figure 3.6. This spectrum compares well with published spectra of clean platinum surfaces.

The cleaning procedure currently used is to bombard the sample for 5 minutes using a 3 keV beam of argon ions ($3x10^{-5}$ mbar argon/20 μA emission current). During the bombardment it is important to raise a stainless-steel shield to cover the electron optics as the high-energy ions can damage the microchannel plate inside the optics. After the bombardment, the crystal is turned to face the throat of the 510 l/s turbomolecular pump. The flux of gas molecules (mostly hydrogen) coming from the pump is significantly less than the flux entering the pump. This reduces the amount of contaminants hitting the crystal while the pressure in the main chamber recovers from the argon bombardment. Once the pressure has reached $2x10^{-9}$ mbar, the crystal is heated at 10 K/s to 1200 K and held at that

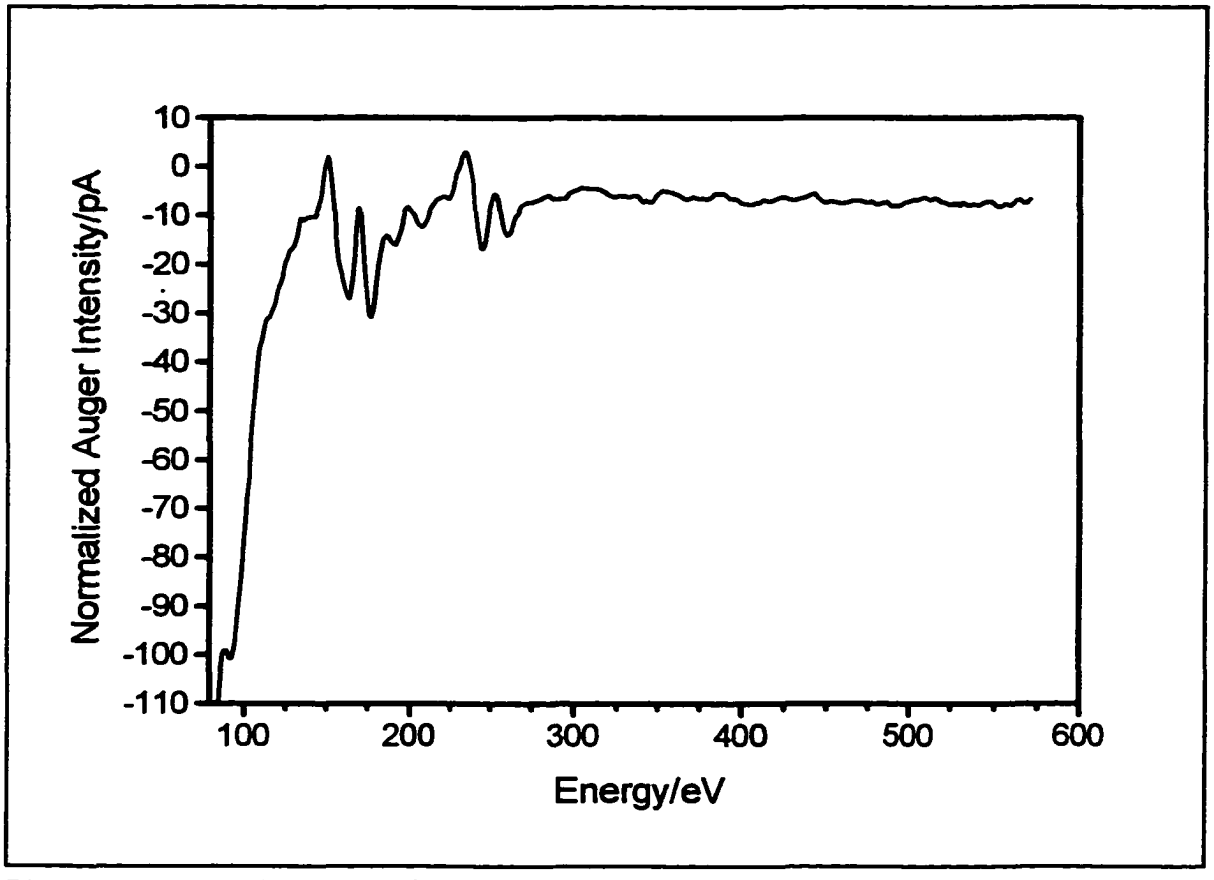

Figure 3.6-Auger Spectrum of Clean Platinum

temperature for one minute. After this, the sample is allowed to cool and is ready for use. After cooling to ambient temperature, the pressure is usually $6x10^{-10}$ mbar. At weekly intervals the crystal is heated in oxygen for one hour and then bombarded for ten minutes to ensure reproducible surface conditions.

3.6 Low-Energy Electron Diffraction

Two of the most common surface analysis methods used today are Auger electron spectroscopy (AES) [3.5] and low-energy electron diffraction (LEED) [3.6]. Both of these techniques are performed using the same set of electron optics on our UHV system.

Although using the same hardware, the types of information obtained from the two methods are quite different, and yet complementary. AES provides an elemental analysis of the surface layers, with no information about the organization of the elements present. LEED provides structural information but contains no information about the chemical composition of the structures. Although there are many other surface techniques, AES and LEED form the basis for most surface investigations.

The wavelength of electrons, from the de Broglie relationship, is related to their kinetic energy by $\lambda=(150\text{eV}\text{Å}^2/E)^{1/2}$. This relationship shows that electrons below 500 eV have the correct wavelength to interfere with atomic structures that are a few angstroms in size. Electron diffraction can be carried out with electrons that have higher kinetic energies, but low-energy electrons (<500 eV) have the added advantage that their penetration depth is only a few angstroms. Therefore, LEED only provides structural information about the

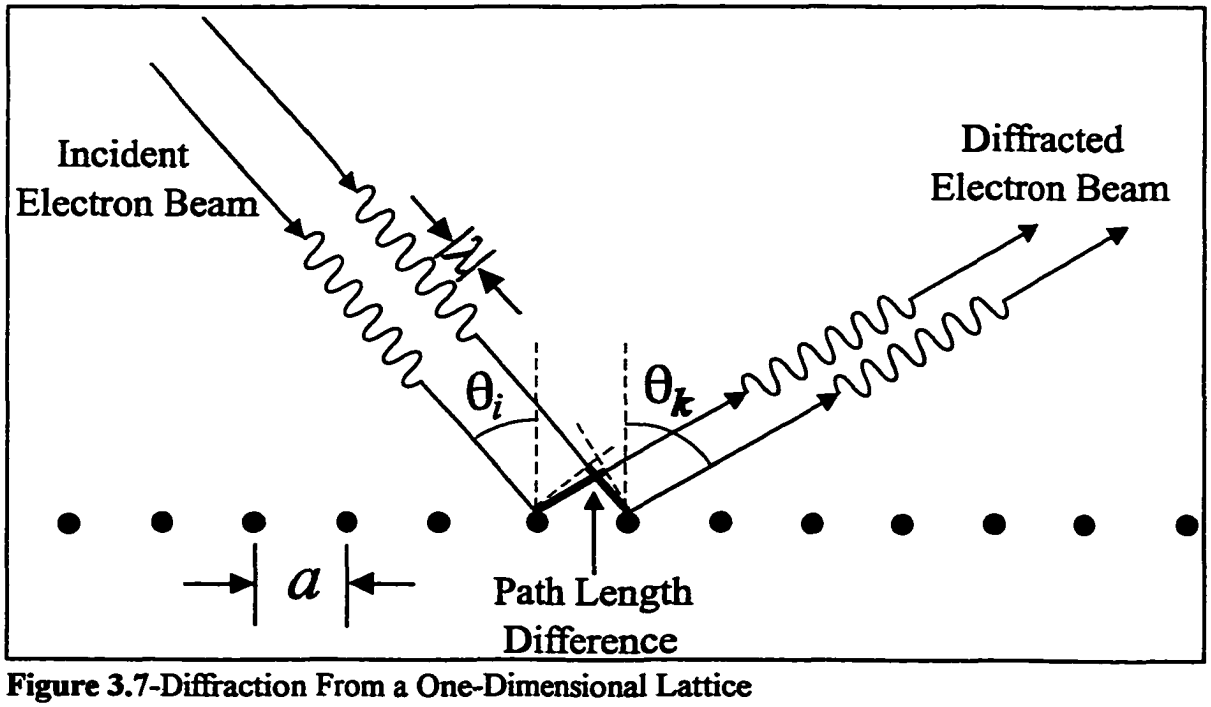

Figure 3.7-Diffraction From a One-Dimensional Lattice

atoms in the surface region.

The diffraction of electrons can be understood by considering a one-dimensional array of atoms, as shown in figure 3.7. The incident electrons have a wavelength (λ) that is comparable to the interatomic spacing (a). Only elastically scattered electrons that have the same kinetic energy as the incident electrons are detected in the LEED experiment. These electrons scatter in all directions but constructive interference only occurs when the difference in the path length of the scattered electrons is an integer multiple of the incident wavelength. The angles at which these diffraction beams will occur are given by the well-known formula:

$$k\lambda = a(\sin\theta_k - \sin\theta_i) \qquad k = 0, \pm 1, \pm 2, \ldots \tag{3.1}$$

A similar argument can be made for diffraction from a two-dimensional lattice to produce diffraction beams. The angle of incidence (θ_i) is usually zero (normal incidence) so that $k\lambda = a\cdot\sin\theta_k$. If a hemispherical, phosphorescent screen is placed a distance d away from the sample, the diffracted electron beams will appear as visible spots on the screen. The distance between diffraction spots will be $d\sin\theta_k$, which is equivalent to $d\lambda/a$. This conveniently introduces the concept of 'reciprocal space', so named because the distance between diffraction spots is proportional to $1/a$ with units of Å^{-1}.

All real-space lattices have a corresponding reciprocal lattice. If the real-space lattice has unit cell vectors $\boldsymbol{a}$ and $\boldsymbol{b}$, the reciprocal lattice will be defined by $\boldsymbol{a}^*$ and $\boldsymbol{b}^*$ such that:

$$\begin{aligned} \boldsymbol{a}\cdot\boldsymbol{a}^* &= \boldsymbol{b}\cdot\boldsymbol{b}^* = 1 \\ \boldsymbol{a}\cdot\boldsymbol{b}^* &= \boldsymbol{b}\cdot\boldsymbol{a}^* = 0 \end{aligned} \tag{3.2}$$

Measurement of the reciprocal space unit cell vectors $\boldsymbol{a}^*$ and $\boldsymbol{b}^*$, together with a

knowledge of the distance between the sample and the screen, provides a convenient way of calculating the real space unit cell vectors $\boldsymbol{a}$ and $\boldsymbol{b}$.

Besides determining the size and symmetry of the real-space unit cell, LEED also gives an indication of the long range order of the surface structure. The distance over which the surface structure is regular must be larger than the coherence width of the incident electron beam. If this condition is not met, the normally sharp diffraction spots will become diffuse spots. Therefore, the regularity of the surface can be gauged by observing the sharpness of the diffraction spots. If a significant amount of non-coherent elastic scattering occurs, the pattern on the screen will have a diffuse background between the diffracted beams. This indicates an even lower degree of regularity on the surface.

Once the diffraction pattern of a particular surface structure is known, it is possible to use this LEED pattern as a fingerprint for identification. Phase transformations between structures that have different diffraction patterns can be followed using LEED. The cleanliness of the surface can also be estimated using LEED, although this is always done in conjunction with AES.

The electron optics used for LEED and AES were supplied by Omicron Vakuumphysik, as shown in figure 3.8. This is a retarding-field analyzer using three energy selection grids with a microchannel plate (MCP) replacing the fourth grid that is present in many other LEED optics. The optics are fitted with a fringe-field plate that corrects the path of electrons travelling between the third grid and the MCP. This is necessary as the MCP is flat while the grids are hemispherical in shape. The fringe-field correction ensures that there is a linear relationship between the radial distance of the diffraction beams seen on the screen and the radial distance of the diffraction beams entering the optics.

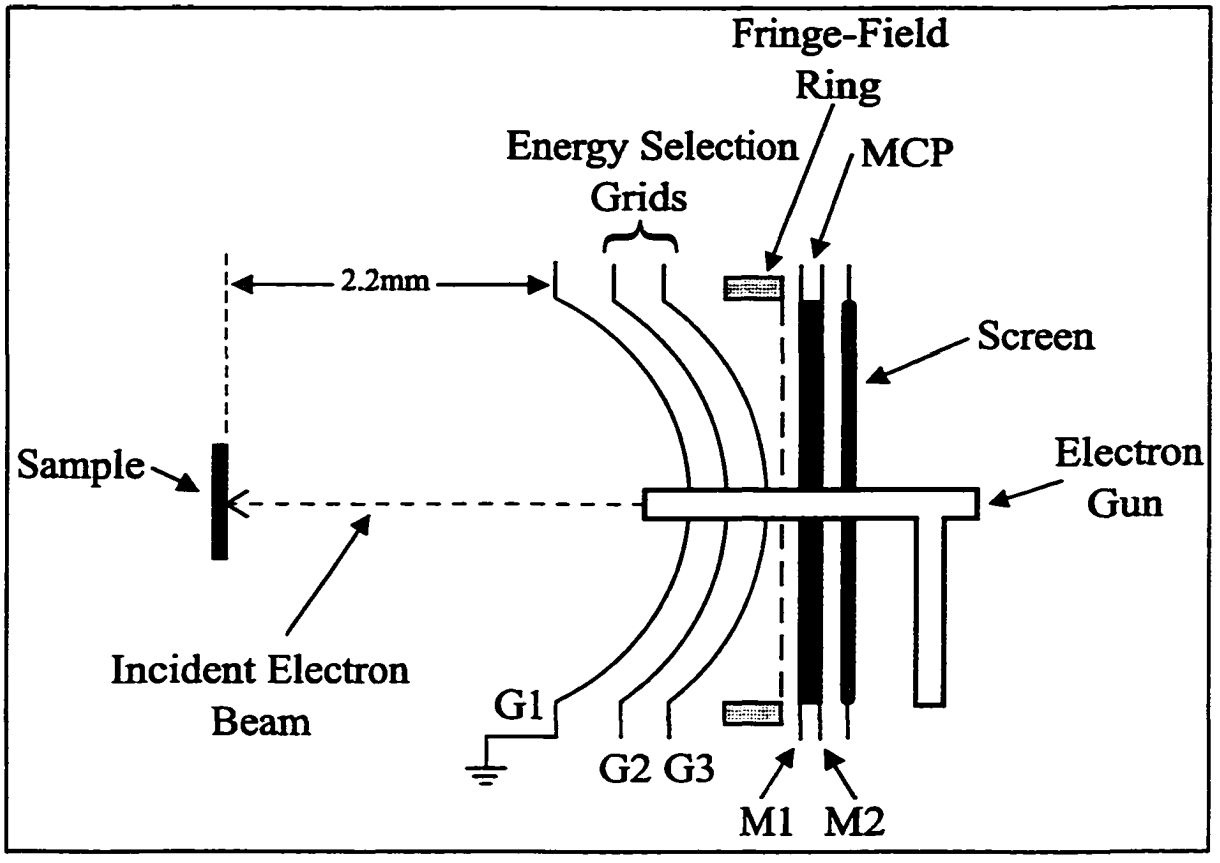

Figure 3.8-LEED and Auger Electron Optics

Unfortunately, the fringe field plate sometimes causes a bright ring to appear around the outside edge of the LEED patterns, as seen in figure 3.9. This ring is due to diffraction beams that have been folded back by the electric field of the fringe-field plate. As the beam energy decreases, diffraction beams should move away from the centre of the diffraction pattern. When they first travel through the region where the bright ring occurs, the beams appear to behave as expected. As the beam energy is lowered further, the beams should move off the screen and disappear. Instead the beams will reappear, travelling inwards briefly (only in the region of the bright ring) and then move back out again. In cases where there are a large number of beams near the edge of the diffraction pattern, this causes a bright ring to appear around the outside edge of the screen. This bright ring can complicate the LEED

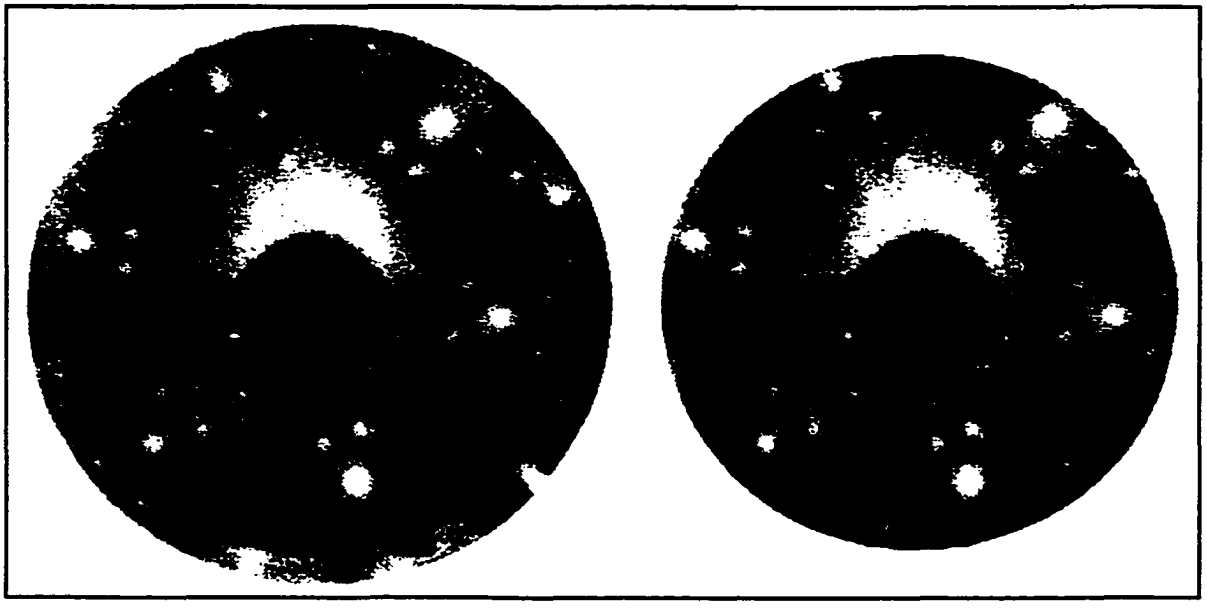

Figure 3.9-Removal of Ring Due to Fringe-Field Plate (Photo Taken at 135 eV)

pattern, and in some cases, such as those in Chapter 7, it has been artificially removed.

The electron gun is located in the centre of the electron optics and produces a beam of electrons by heating a lanthanum hexaboride single-crystal filament to ~1700 K. It can produce beam currents from below 0.01 μA to 30 μA at energies up to 3500 eV. This flexibility allows both LEED and AES to use the same electron gun.

Although the exact settings for each LEED experiment vary, the following are a complete set of parameters used to obtain a diffraction pattern of the clean platinum surface. The sample is located 2.2 cm from the optics, normal to the electron gun. The beam current is set to 0.01 μA (at 70 eV beam energy) by using a filament current of 0.93 A. The first grid (G1), closest to the sample, is held at ground to prevent deflection of the electrons from any stray electric fields. The second and third grids (G2 and G3) are held at a negative bias of 10 V from the primary beam energy. This ensures that only elastically scattered electrons pass through these grids. The front of the MCP (M1) is held at 1 kV while the back of the MCP (M2) is held at 1.8 kV (using a MCP bias of +800 V). This provides an electron gain of

approximately 10^4 across the MCP. The screen is held at 7 kV to accelerate the electrons to a sufficient velocity to produce visible spots on the phosphorescent screen.

The electron gun is focussed using an offset on lens 1/3 (L1/3) of 1 V (at 0 eV beam energy) while the lens 2 (L2) offset is set to 18 V (at 0 eV beam energy). At a beam energy of 70 eV, the gain on L1/3 is adjusted to 187 V and the gain on L2 is set to 29 V. The Wehnelt voltage is set to 37 V. Changing the focussing using L1/3 and L2 will change the beam current at a fixed beam energy. The focussing parameters will need to be changed slightly when the beam energy is changed, especially at energies below 60 eV.

The diffraction patterns formed on the phosphorescent screen are photographed using a Minolta SLR camera with a macro lens attached. Using an f-stop of f5.6, three photographs are taken of the screen using 2 s, 8 s and 32 s exposure times using 3200 ASA black and white film. The camera is mounted on an adjustable aluminum support that bolts directly to the UHV apparatus to minimize vibrations.

3.7 Auger Electron Spectroscopy

Auger electron spectroscopy (AES) is perhaps the most common technique used for the analysis of surfaces. It provides an elemental analysis of the surface and is essential for the detection of surface contaminants. Quantitative analysis is possible, but is complicated by scattering effects. However, for submonolayer coverages, it has been generally found that Auger intensities do increase linearly with surface coverage.

Auger spectroscopy is named after Pierre Auger who first observed the Auger effect in a cloud chamber [3.7]. Auger electrons are produced when a sample is irradiated with a suitable excitation source. As shown in figure 3.10, an incident beam of electromagnetic

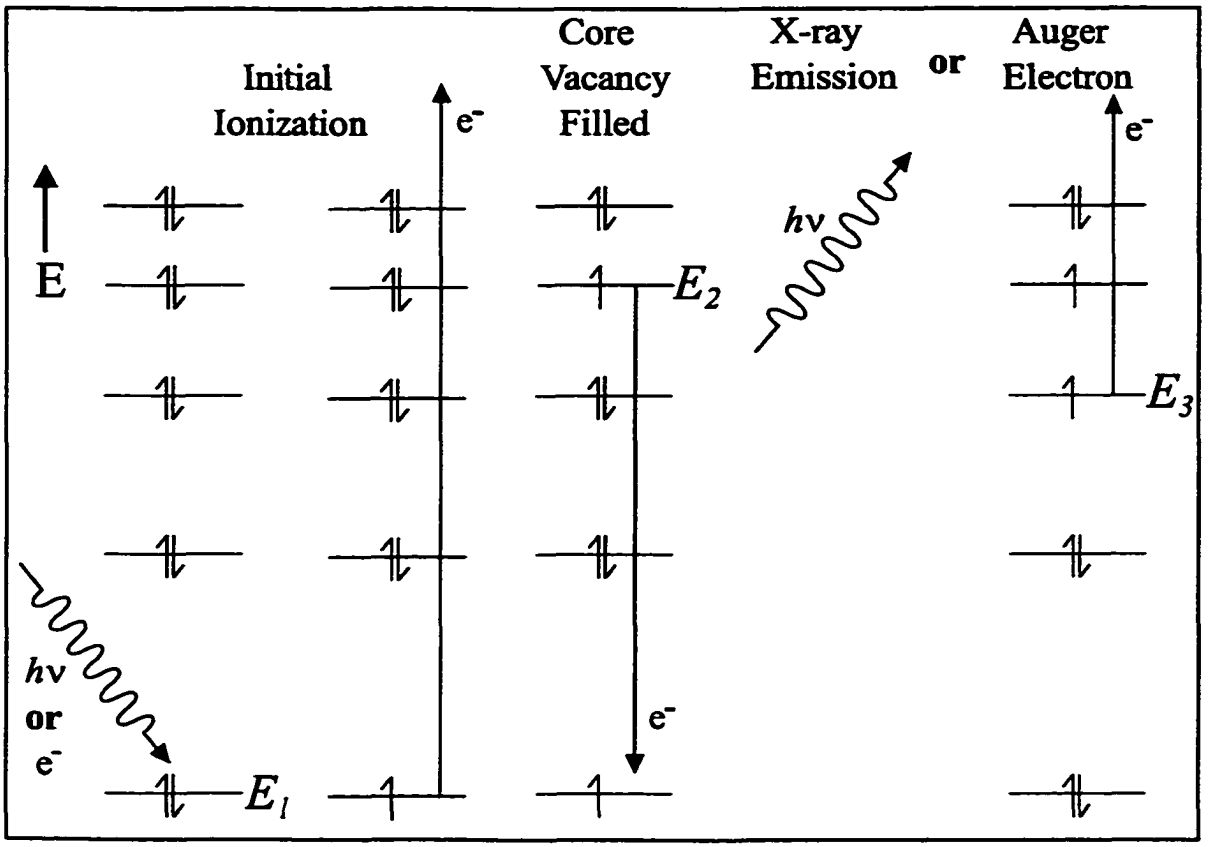

Figure 3.10-Production Of Auger Electrons

radiation ionizes an atom by ejecting a core-level electron. This ionization can be accomplished with either electrons or photons, provided the incident radiation has an energy (E_p) greater than the binding energy (BE) of the electron to be ejected. Electrons are primarily used as the excitation source as they are produced more easily than photons of the appropriate wavelength. Any excess energy (E_p-BE) is transferred to the ejected electron as kinetic energy.

The core level vacancy is filled by an electron from a higher level (E_2= -BE_2) dropping in energy to E_1 (-BE_1). There is an excess of energy (E_1-E_2) that must be liberated to conserve energy. Two mechanisms are possible: the energy can be emitted as a photon (X-ray) or the energy can be transferred to another electron, which will be ejected from the atom.

The second process is known as the Auger effect, producing an Auger electron and leaving the atom doubly ionized.

The kinetic energy of the Auger electron is dependent on the energies of the three electronic levels involved but is independent of the energy of the incident radiation. The kinetic energy of the Auger electron will be equal to E_2-E_1-E_3. It should be noted that the energy of levels 2 and 3 (E_2 and E_3) will be different from the atomic energy levels as the initial ionization shifts the positions of the levels.

All elements, except hydrogen and helium, can produce Auger electrons. The energies of the Auger electrons from a particular element are characteristic for that element. Energy overlaps between elements do occur, but in general most elements have a unique set of Auger transition energies that can be used for both qualitative and quantitative analysis. Table 3.1 lists the Auger energies of elements relevant to this thesis.

Table 3.1-Relevant Auger Transitions

Element	Auger Electron Energies/eV
Platinum	64, 92, 150, 158, 168, 238, 245
Aluminium	68
Silicon	93
Phosphorus	121
Sulfur	152
Carbon	275
Nitrogen	363, 383
Oxygen	510
Iodine	528
Fluorine	670

Auger electrons constitute only a small fraction of the electrons scattered by a surface (<0.1%) [3.8]. The detection of Auger electrons is made difficult by the large number of secondary electrons produced by the incident electron beam. Although more sensitive detectors exist, such as the cylindrical mirror analyzer (CMA), the detection system used here is a retarding-field analyzer (RFA). This conveniently allows Auger experiments to be done using the same electron optics used for LEED. The electronics used to control the optics are slightly different, as discussed below.

The RFA repels electrons below a certain energy E by biasing the grids (G2 and G3 in figure 3.8) to a negative voltage V that is equal to $-E/e$. Only electrons that possess a higher kinetic energy than E will pass through the grid system. The front of the microchannel plate (M1) is held at +300V and acts as the collector to count the electron current $I(E)$. The back of the MCP (M2) and the screen are held at 0 V to ensure that all electrons are counted at M1. The first grid (G1) is held at 0 V, as in the LEED experiment, to make sure there are no electric fields present to deflect the electrons before entering the optics system.

Due to the low yield of Auger electrons, it is not possible to detect Auger electrons using the retarding-field analyzer in this configuration. However, if the bias voltage V on G2 and G3 is modulated by a small voltage (1-10 V), the current $I(E)$ at the collector will also be modulated. As the current is proportional to the number N of electrons passing through the grids, the first and second derivatives of the current become:

$$\begin{aligned} I(E) &\propto \int_{E}^{\infty} N(E)\,dE \\ I'(E) &\propto N(E) \\ I''(E) &\propto N'(E) \end{aligned} \tag{3.3}$$

The first derivative of the current is therefore proportional to the number of electrons at a particular energy ($N(E)$).

The first and second derivatives of the current can be easily measured using a lock-in amplifier (LIA) that uses the modulation frequency as a reference. The usual method for displaying Auger spectra is to use the second derivative of the current, $I''(E)$ which is proportional to $dN(E)/dE$. There are many reasons why this is chosen, particularly for retarding-field analyzers. Auger peaks in an $N(E)$ curve have a low energy tail (due to energy losses) making the position of the peak easier to observe in a $dN(E)/dE$ curve. Both the first ($1f$) and second ($2f$) derivatives are easily measured using a LIA so measurement of the $2f$ signal does not require any extra electronics. The use of the $2f$ signal also eliminates any capacitive coupling that can occur between the modulating grids (G2 and G3) and the collector (M1). The front of the microchannel plate was biased to +300 V and used as the collector. Attempting to use the microchannel plate as an electron multiplier (and using the screen as the collector) scrambles the modulated Auger currents and no Auger signals are seen with the LIA.

Unless otherwise stated, a modulation voltage of 10 V (peak to peak) at 4.7 kHz was used for all of the experiments in this thesis. The effect of the modulation amplitude is shown in figure 3.11. The modulation amplitude was varied from 8 V (p-p) to 30 V (p-p). As the modulation amplitude increases, both the Auger current and the background current increase. Unfortunately, the resolution decreases as the modulation amplitude increases and the small signals can be lost in the noise. 10 V is a standard modulation amplitude for retarding-field analyzers.

The modulation signal was supplied by a built-in oscillator in a Stanford Research

System lock-in amplifier (model SR530). This LIA was also used to monitor the 2*f* signal from the collector. The modulated Auger current reaching the collector is converted to an oscillating voltage using a current follower with a gain of 2.2×10^6 V/A. All Auger intensities given in this thesis have been converted back to the magnitude of the oscillating Auger current. A constant phase shift of 41.1° was used to maximize the Auger signal on the X channel of the LIA. A beam energy of 3 keV was used as the excitation source with a beam current of approximately 20 μA. The usual range of beam currents used was between 17 and 23 μA. All Auger spectra in this thesis have been normalized to a 20 μA beam current. All Auger intensities are peak-to-peak heights in the normalized second-derivative spectra. A constant scan rate of 1 eV/s was used throughout the experiments.

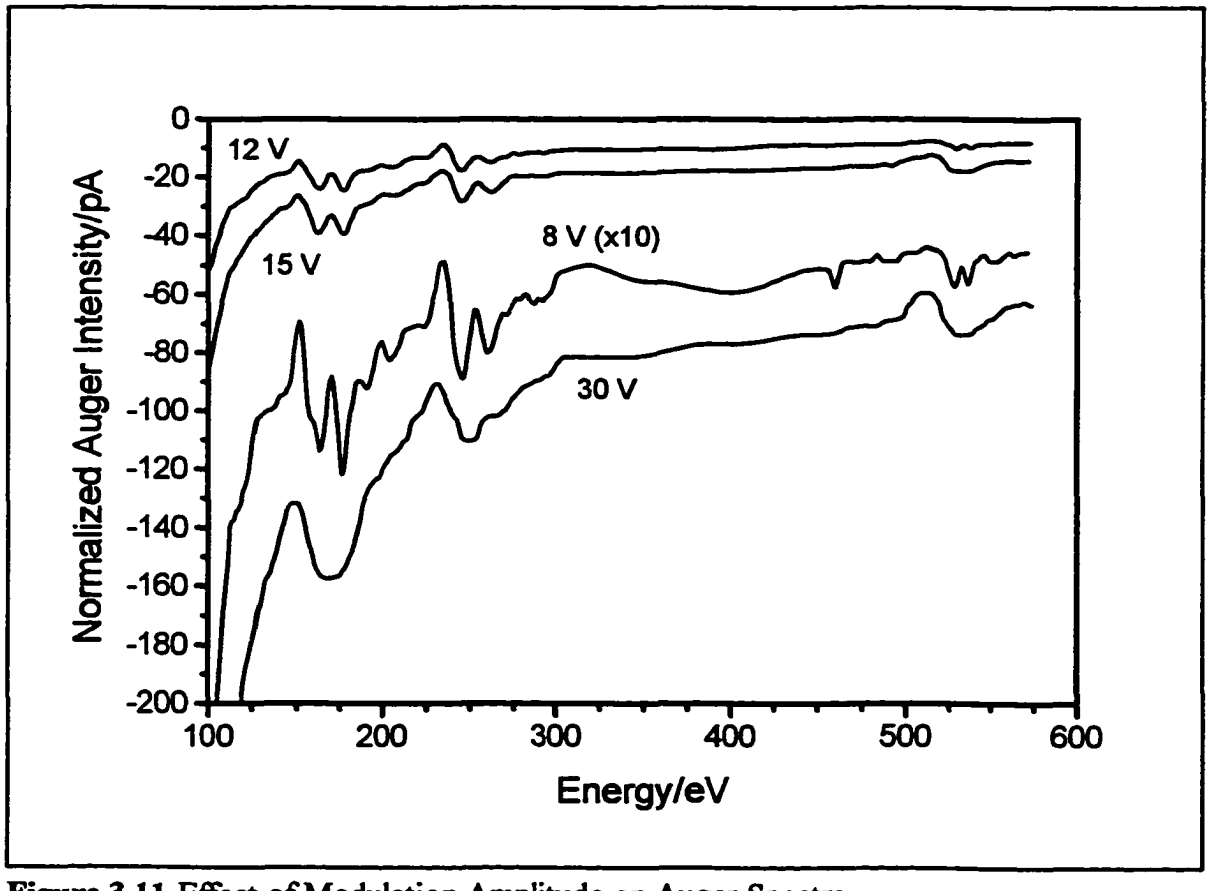

Figure 3.11-Effect of Modulation Amplitude on Auger Spectra

3.8 Mass Spectroscopy

The UHV system is equipped with a HAL 321 series quadrupole mass spectrometer manufactured by Hiden Analytical Ltd. The spectrometer can detect masses up to 320 amu and is equipped with both a Faraday cup and a secondary-electron multiplier (SEM) detector. The spectrometer is interfaced to a 66 MHz 80486 computer via a GPIB communications port. Several computer programs for data acquisition were written in QuickBasic to allow a number of different experiments to be performed using the mass spectrometer.

The mass spectrometer is located in a vertical position on the UHV chamber and is differentially pumped, as shown in figure 3.1, by a 60 l/s Balzers turbomolecular pump. A small 1 cm ID conical inlet (shown in figure 3.2) connects the spectrometer to the main chamber. Although the poor conduction through this inlet reduces the ability of the mass spectrometer to analyze the residual gases inside the main chamber, this inlet is essential for doing thermal desorption experiments.

When the platinum crystal is placed immediately below (~ 1 mm) this inlet, only species desorbing from the crystal surface will enter the spectrometer. As the tantalum and copper support wires are not within line-of-sight of the inlet, any material desorbing from them will not be able to directly enter the spectrometer. Material desorbing from the back of the crystal and the manipulator arm will also be excluded.

The spectrometer has three main modes of operation. In the first mode, the spectrometer scans over a range of masses, producing a standard mass spectrum. This is generally used for residual gas analysis when checking the composition of the background gases in the vacuum. For all of the experiments described in this thesis, one of the two operating modes described below was used.

The mass spectrometer allows specific masses to be monitored as a function of time, rather than scanning a range of masses. Up to 16 masses can be monitored in this multiple ion detection (MID) mode. It should be mentioned that when the spectrometer is operating in MID mode, the maximum data acquisition rate is determined by the dwell time of the spectrometer. The dwell time is the time the spectrometer spends collecting data on each mass. After the dwell time, the spectrometer produces a single, averaged result for the specific mass. The length of the dwell time depends on the sensitivity range and which detector is being used. Using the SEM detector on a typical 10^{-12} mbar range, data is collected approximately once every second for each mass. Collecting data for 16 masses takes approximately 20 seconds.

For several desired experiments, this sampling rate is too slow. Therefore, the mass spectrometer was modified to allow a much faster sampling rate using a modulation technique. The spectrometer still operates in MID mode (usually with a single mass channel) but the ions detected by the spectrometer are modulated at a fixed frequency (47 Hz), as described below. Most of the thermal desorption experiments described in this thesis use this modulated operating mode.

Neutrals entering the spectrometer are ionized before entering the quadrupoles for mass selection. The electronic circuitry controlling the voltage on the ionization source was modified to allow the ion source to be modulated. The mass-selected ions hitting the detector will then be modulated at the same frequency as the ion source. The modulated ion current is converted to a modulated voltage using a current follower with a gain of 10^{10} V/A. The amplitude of this modulated signal is measured by an SR530 lock-in amplifier (LIA) (Stanford Research Systems). The amplitude of the modulated signal is proportional to the number of

neutrals entering the spectrometer.

The ion source was modulated using the circuit shown in figure 3.12. The circuit uses a standard 555 timing chip to generate an astable modulating signal. Variable resistors allow the frequency of the modulation to be varied from 15 Hz to 2 kHz. The modulated signal from the timing chip is not symmetrical and is therefore sent into a D-type flip-flop. This produces a symmetrical square wave at half the frequency of the timing chip. The ion source is connected to the flip-flop output by a FET to allow for fast switching. The ion source can

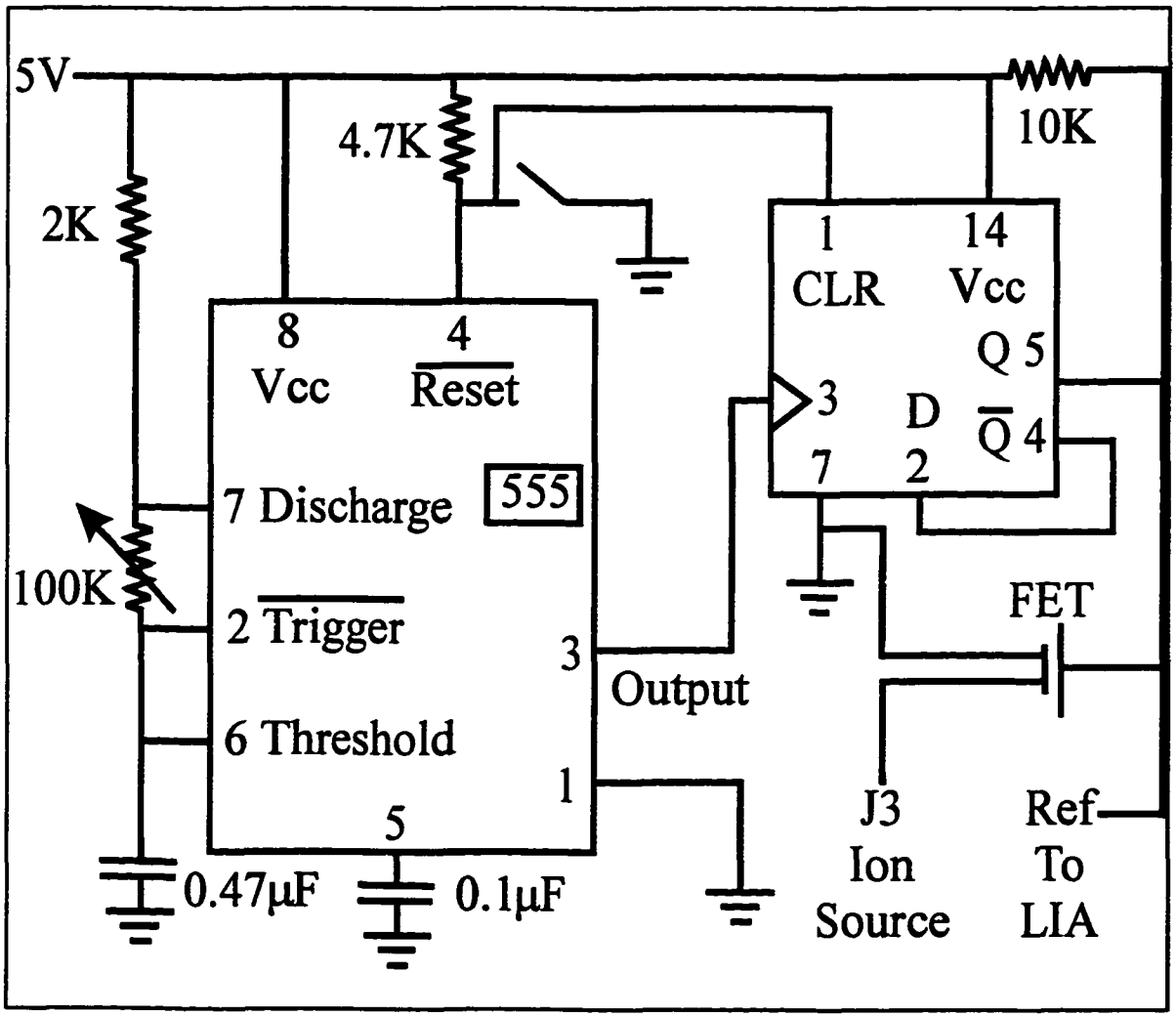

Figure 3.12-Modulation Circuit For Mass Spectrometer Ion Source

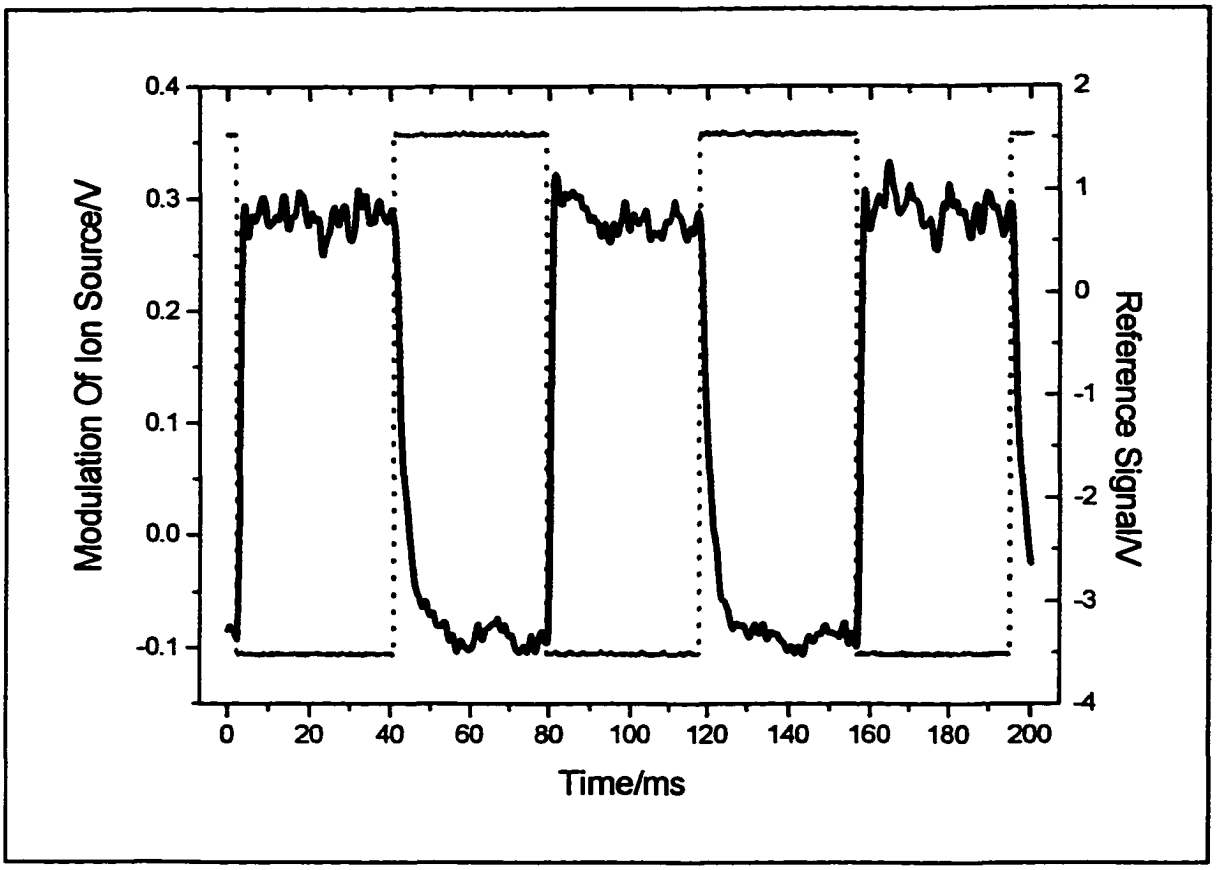

Figure 3.13-Modulation of Ion Source In Mass Spectrometer

therefore be modulated at frequencies between 7.5 Hz and 1000 Hz.

A modulation frequency of 47 Hz was chosen as the optimum frequency for a number of reasons. The modulated signal from the detector does not exactly follow the modulation of the ion source. There is a finite rise and fall time (τ_{rf}) of the detector signal of approximately 3 ms, as shown in figure 3.13. At frequencies higher than $1/\tau_{rf}$ (>200 Hz), a significant proportion of the signal is lost. At frequencies below $1/\tau_{rf}$, a larger portion of the signal is retained.

Signal loss due to the rise time of the detector can be virtually eliminated by modulating the ion source at low frequencies. However, the output from the LIA has a sine wave superimposed on it that is twice the modulation frequency. This is unavoidable in analog

lock-in amplifiers. This sine wave can be removed by Fourier transform filtering but this will produce a 'ringing' effect on any real signals that occur at frequencies close to the sine wave frequency. The sine wave can also be removed by the built-in filters on the LIA, but for low frequencies (-10 Hz), the time constant required for such filtering (>100 ms) limits the response time of the LIA.

The maximum time constant used in the experiment should be approximately the same as the maximum sampling rate. In the current configuration, data is collected at a sampling rate of 50 points per second. Therefore, a time constant up to 30 ms can be safely used at these sampling rates. A 30 ms time constant can effectively remove a sine wave at three times this frequency (~100 Hz). A modulation frequency of 47 Hz was chosen as the sine wave from the LIA will be at 94 Hz and will be removed using a 30 ms time constant. The 47 Hz modulation frequency is also just outside the range of the 60 Hz line notch filters used by the LIA to remove 60 Hz signals due to 120 VAC power connections.

This modulation technique offers two main advantages over the normal MID mode operation. The time resolution is much higher and the lock-in technique is very good at detecting small changes in large signals. The main disadvantage is that it is difficult to sort the signal when several masses are being monitored. This is not a concern if only one or two masses are being monitored but the data becomes confusing if more mass channels were used. However, the mass spectrometer does perform an automatic amplifier offset adjustment at the end of each cycle through a series of masses. This creates a small spike in the LIA output as the signal from the mass spectrometer temporarily becomes incoherent with the reference modulation signal. This spike is quite brief and can be used as a reference point for determining the starting positions for each cycle through a series of masses. However, the

spike is easily lost if the time constant of the LIA is set too high (>30 ms) and does not always appear even with low time constants.

3.9 Kelvin Probe

The work function (Φ) is a fundamental property of solids simply defined as the minimum work required to extract an electron from a solid. It is central to the explanations of the photoelectric effect and thermionic emission and is discussed extensively in Chapter 6. The work function is intimately affected by changes in electron density at the surface of the solid and measuring changes in work function provides a convenient way to study shifts in electron density that occur during adsorption and desorption. There is often a simple relationship between the change in work function and adsorbate coverage that can be easily utilized to measure coverage if the relationship is known.

There are several methods for measuring both the absolute value of the work function and changes in the work function [3.8]. The technique described here measures changes in work function and does not provide an absolute value of the work function. This is not a serious limitation as the method is nondestructive, can be done in-situ during adsorption and desorption, and has a precision below 5 meV.

The Kelvin probe, or vibrating capacitor method, uses the contact potential difference (CPD) between the sample and a reference to measure changes in work function. The reference, a tantalum loop mounted at the end of a vibrating stainless steel reed, has an unknown, but constant, work function. Assuming that both the sample and the reed are at the same potential, there will be a potential difference in the vacuum between the two that is equal to the difference in their work functions ($V_{SR}=\Phi_{Ref}-\Phi_{Sample}$). The distance between the

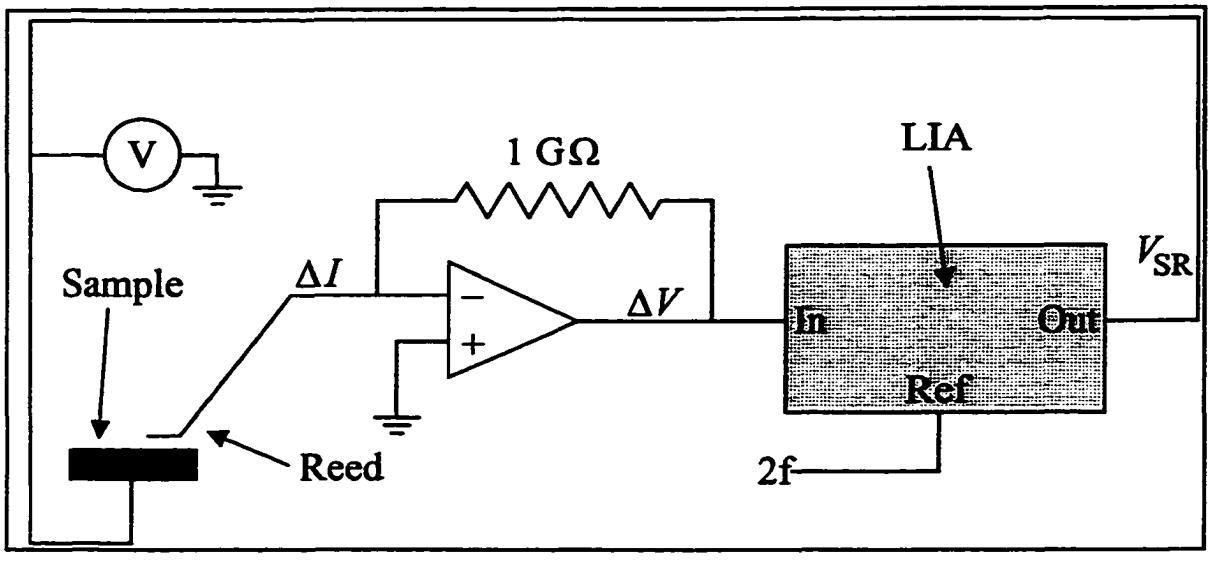

Figure 3.14-Feedback Loop in Kelvin Probe

sample and the reference is small (~1 mm) and there is a capacitance (C) between them. As the reed is vibrating, the capacitance is modulated at the frequency of the reed. As the potential difference V_{SR} remains constant, the oscillating capacitance must arise from oscillating charges on the sample and reference as $Q(t)=C(t)\ V_{SR}$.

This oscillating charge causes an oscillating current (ΔI) that is measured using the feedback loop shown in figure 3.14. This feedback loop converts the oscillating current to an oscillating voltage and uses a lock-in amplifier (LIA) to measure the amplitude of the oscillation. The potential of the sample can then be adjusted to compensate for the difference in work function between the sample and the reference. If the potential of the sample is adjusted by V_{RS}, there will no longer be an electric field between the sample and the reference and consequently no current will flow through the reed.

This feedback loop continually adjusts the voltage on the sample to ensure that a field-free region exists between the sample and the reference. Any change in the work function of the sample results in an equal compensating voltage on the sample to maintain the field-free

region. This compensating voltage is easily measured and corresponds exactly to the change in the sample's work function.

A schematic diagram of the Kelvin probe is shown in figure 3.15. The tantalum (0.05") pickup loop (10 mm diameter) that vibrates next to the sample is mounted at the end of a stainless steel reed. This reed is constructed of two segments of stainless steel tubing (47 mm, 1.6 mm OD and 31 mm, 0.9 mm OD) spot welded together. The reed is spot welded to a stainless steel plate spring (4 mm x 11 mm x 0.5 mm) held in place with a locating pin. A thin plate of conetic metal (0.5 mm x 11 mm) is spot welded to the bottom of the reed. An electromagnetic coil driven by an oscillating square wave (at a frequency f) attracts the conetic plate regardless of the magnet's polarity. Therefore, the reed vibrates at a frequency of $2f$.

The resonant frequency of the vibration is specific for each reed and changes with the temperature of the reed. For this reason, the Kelvin probe operates in a phase-locked mode rather than a frequency-locked mode. A ceramic piezoelectric crystal, mounted in the support

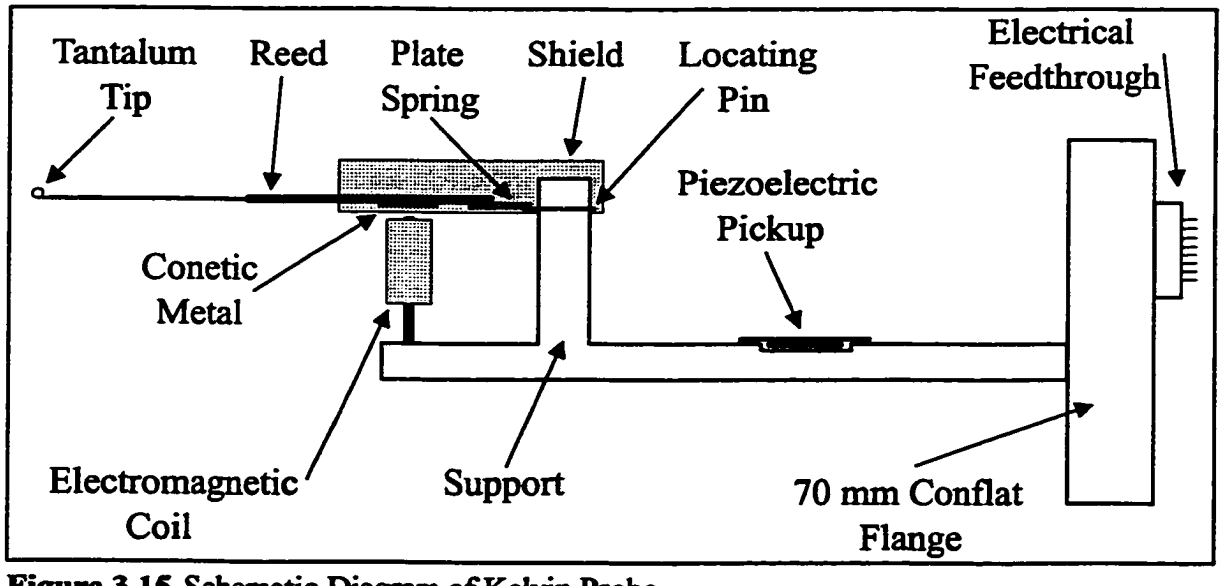

Figure 3.15-Schematic Diagram of Kelvin Probe

that holds the reed assembly, measures the frequency of the reed vibration. A phase-locked loop ensures that the phase relationship between the piezoelectric signal and the coil drive frequency is constant. If the reed frequency starts to drift, this is detected as a phase shift and the coil frequency is adjusted to maintain the correct phase relationship. Operating in this mode, the resonant reed frequency can drift by up to 20 Hz from its initial value and the coil frequency will be adjusted to ensure that the reed continues to vibrate.

Part of the reed assembly is surrounded by an aluminum shield, shown in figure 3.15. The potential of this shield can be altered to try to compensate stray electric fields. When properly adjusted, small changes in the distance between the reed and sample (<1 mm) do not change the measured work function. This ensures that small distance fluctuations, such as those due to sample heating or mechanical vibration, do not alter the measured work function of the sample.

3.10 Iodine Doser

The main focus of the experiments described in this thesis is the adsorption of iodine on platinum surfaces. Conventionally, iodine dosing experiments involve leaking iodine vapour into the UHV chamber through a variable leak value. The partial pressure of iodine vapour in the chamber is typically increased to 5×10^{-8} mbar. However, iodine is a reactive gas that corrodes sensitive vacuum components, particularly after extended exposure.

The need for a new method of dosing iodine, and other halogens, led to the development of solid-state dosers. These dosers produce halogens in vacuum by electrolyzing a solid material, usually a silver halide. A collimator is then used to direct the halogen beam at the target. As the flux of halogens is localized, the contamination of the UHV system is

greatly reduced. However, silver halides are poor conductors at room temperature and must be heated above 550 K to increase the mobility of the silver ions. Only at elevated temperatures do the silver halides become conductive enough to allow a reasonable current to pass through them. Heating the solid electrolyte is known to cause some evaporation of the silver halide and outgassing from the hot components requires extensive degassing before use.

Ag_4RbI_5 was chosen as an alternative to AgI as it is an ambient-temperature fast-ion conductor. This material has a high conductivity (0.124 $\Omega^{-1}cm^{-1}$ at 20 °C [3.9]) as the silver ions are very mobile, presumably moving along grain boundaries. With one of the highest ionic conductivities known for a solid, Ag_4RbI_5 has been used in superconductor studies as a solid electrolyte [3.10]. Ag_4RbI_5 is hygroscopic and light-sensitive and must be stored in a desiccator inside an opaque container. Unfortunately, other fast-ion conductor materials are not known for the other halogens and the doser design described here cannot be extended to other halogens.

As the Ag_4RbI_5 solid electrolyte does not require heating, the construction and operation of the doser is less complicated than other dosers [3.11]. Operation at ambient temperature also reduces the possibility of evaporation of unwanted contaminants onto the target.

The Ag_4RbI_5 (supplied by All-Chemie Ltd.) is powdered using a high-speed amalgamator (Wig-L-Bug) for one minute and then 0.5 g is placed into a hardened-steel die sandwiched between two stainless steel disks. As shown in figure 3.16, a section of platinum mesh is placed between the Ag_4RbI_5 and the bottom stainless steel disk. The platinum mesh will act as part of the anode once the pellet is placed in the doser. A hydraulic press of the

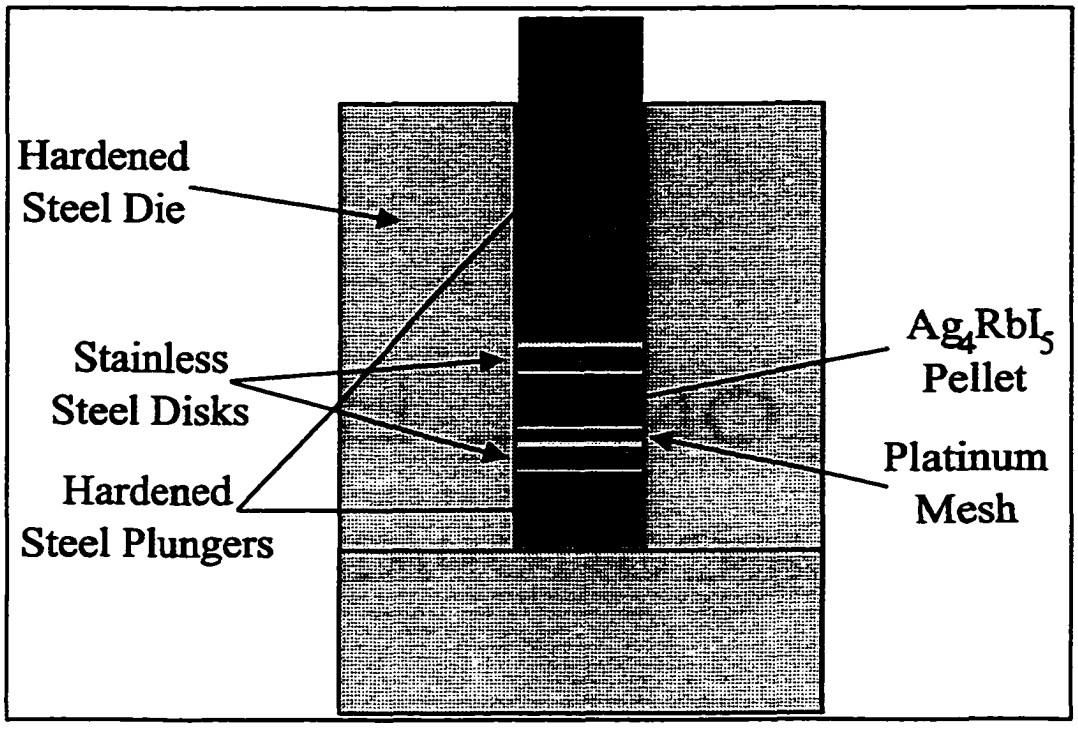

Figure 3.16-Hardened Stainless-Steel Press For Making $RbAg_4I_5$ Pellet

type used for making alkali-halide infrared windows is used to press the Ag_4RbI_5 at a pressure of 600 MPa for five minutes. This produces a disk 7.5 mm in diameter and approximately 3 mm thick.

Once the Ag_4RbI_5 pellet is prepared, the doser is assembled as shown in figure 3.17. The pellet is sandwiched between two stainless-steel electrodes (1 cm diameter) that are electrically isolated from the supports with ceramic spacers. The anode has a 6 mm hole in its centre to allow the iodine to travel down the collimator (9.5 cm long, 6 mm ID). The platinum mesh embedded in the pellet is in direct contact with the stainless steel anode to ensure that the iodine is produced evenly from the surface of the pellet.

A photograph of the doser is shown in figure 3.18. The doser's cell is connected to a Hewlett-Packard variable-voltage power supply. The flux of iodine can be easily regulated

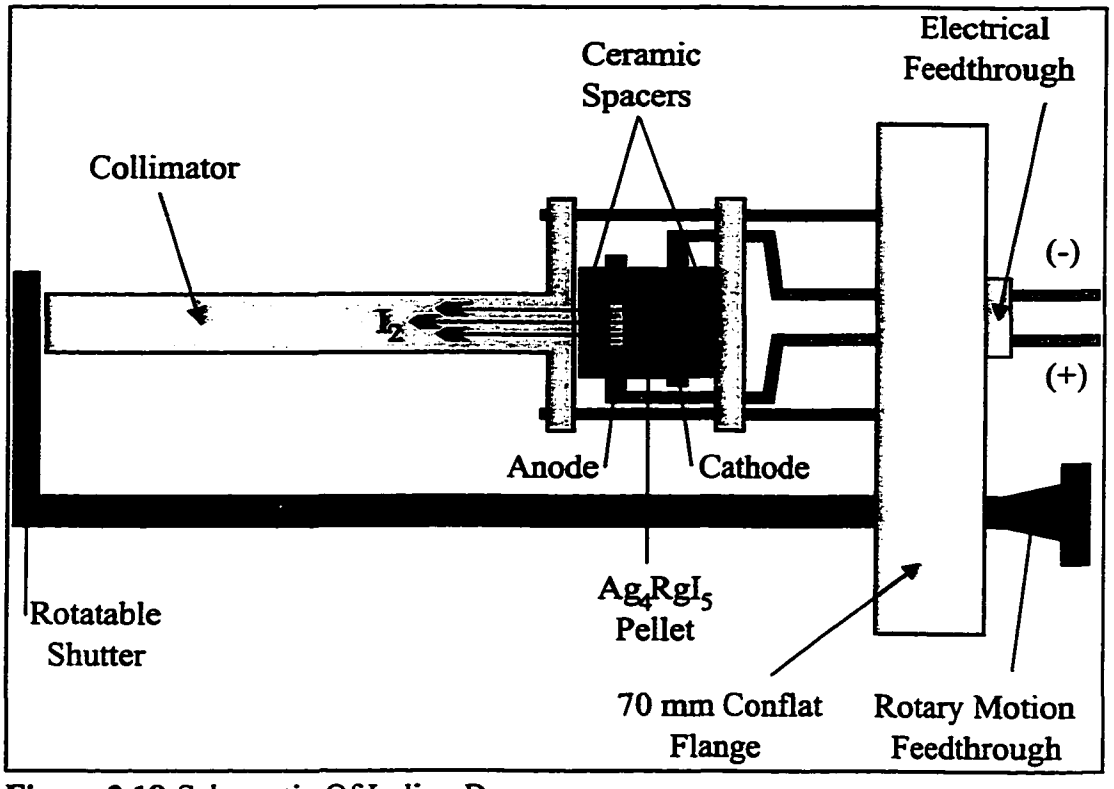

Figure 3.18-Schematic Of Iodine Doser

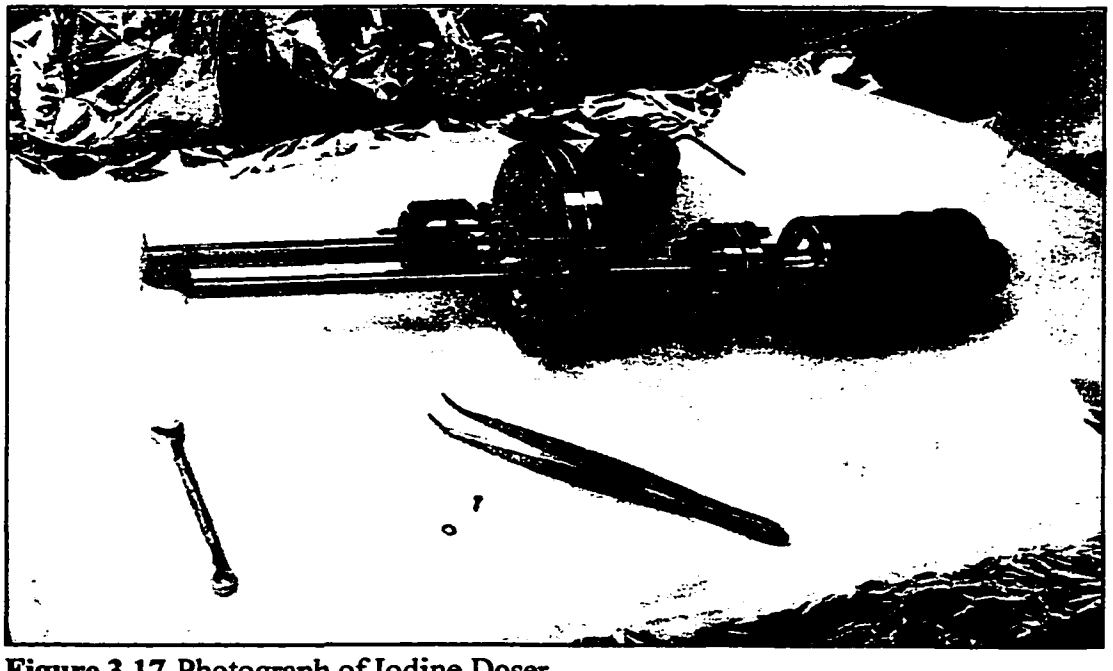

Figure 3.17-Photograph of Iodine Doser

by changing the current flowing through the cell. The current passing through the cell is

monitored by measuring the voltage drop across a 50 kΩ resistor connected in series with the cell. The cell typically has a resistance of 2.5 kΩ and is operated with a current of 200 μA during most dosing experiments.

Although switching the cell off stops the production of iodine, there is always a residual flux from the collimator. A stainless steel shutter is used to block the collimator exit once the cell current has been shut off. This completely stops the flux of iodine and allows for precise dosing of the sample.

3.11 Dendrimer Transfer Experiments

One of the unique features of the UHV system described here is its ability to transfer the mounted sample from the vacuum environment to the ambient pressure environment. This type of transfer allows the sample to be treated or analyzed by more conventional chemical methods. The sample can be brought into contact with solutions or be used as the working electrode in an electrochemical cell. This feature greatly enhances the versatility of the UHV system. The sample can be transferred back into the vacuum environment for analysis by the UHV techniques previously described. In all of the experiments described here, the platinum crystal is contacted with solutions but is not used as part of an electrochemical cell.

The transfer is accomplished by moving the sample from the UHV chamber into a second chamber that is also under vacuum. This high pressure (HP) chamber is connected to the UHV chamber by a tube containing a pair of spring-loaded teflon rings (Furon AR103-216AH from Fluorocarbon Mechanical Seal Division) that are differentially pumped. These teflon rings press against the sample manipulator arm, as shown in figure 3.19. The tip of the manipulator arm is polished to help form a seal with the teflon rings. Once the sample is in the

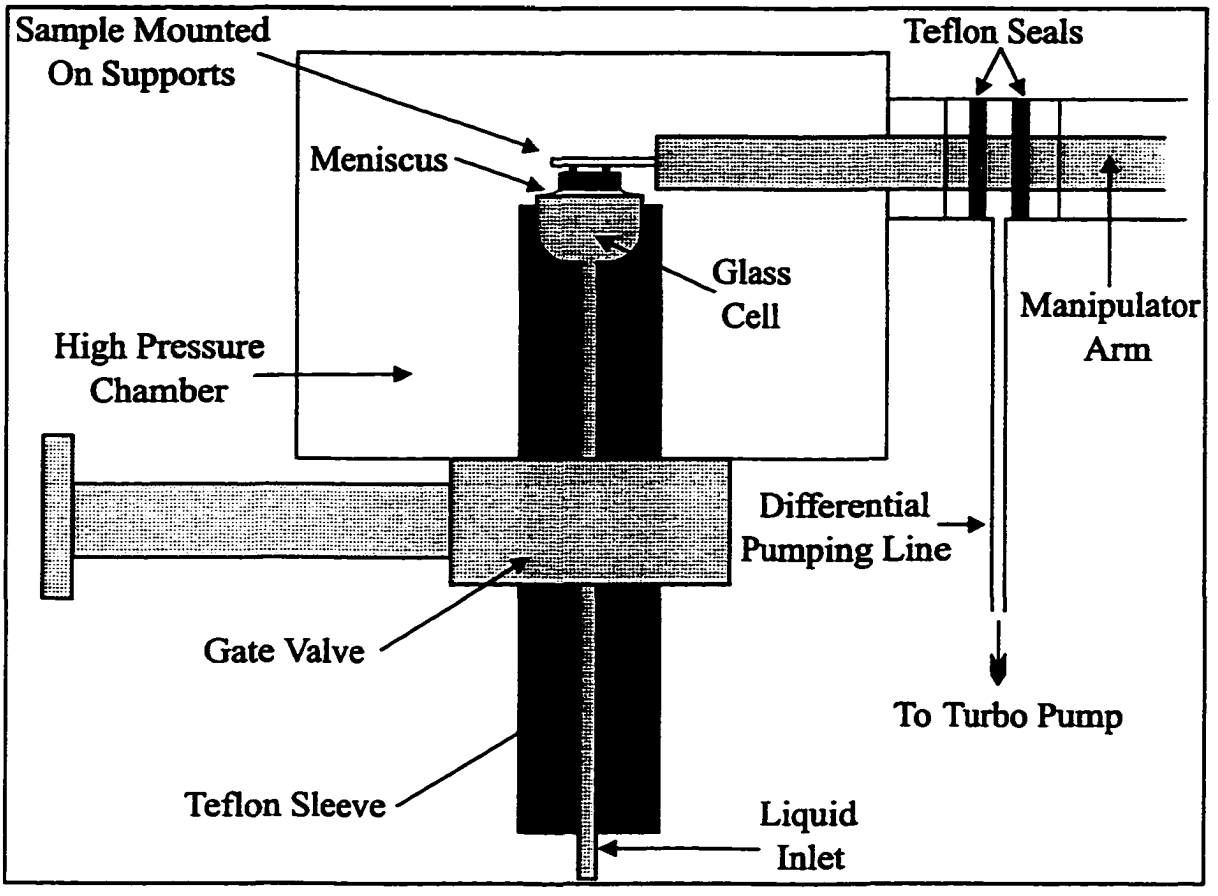

Figure 3.19-Transferring Sample To High-Pressure Analysis Chamber

HP chamber, the chamber is isolated from its turbomolecular pump and then filled with argon. The argon used for this is purified by a Centorr getter furnace (model 2B-2O-Q) that uses a hot titanium filament to remove contaminants from the argon. The pressure in the UHV chamber does not rise above $3x10^{-10}$ mbar while the HP chamber is at atmospheric pressure.

Once the HP chamber is at atmospheric pressure, a gate valve is opened to allow a teflon sleeve containing a glass cell to be brought into the transfer chamber. At this point, a variety of experiments can be performed to study or modify the sample surface. During such experiments, a constant flow of argon maintains a positive pressure in the HP chamber to ensure that no air enters. After the completion of the ambient pressure experiments, the cell is removed, the gate valve is closed, and the argon flow is stopped. Two zeolite-filled sorption

pumps, cooled with liquid nitrogen, are used to evacuate the HP chamber to below 10^{-3} mbar. After this initial evacuation, the turbomolecular pump is used to lower the pressure in the HP chamber to below 10^{-7} mbar. A liquid nitrogen cold finger helps to reduce the partial pressure of water in the transfer chamber.

After 2-5 minutes, the sample is brought back into the UHV chamber. There is always a pressure burst in the UHV chamber when the sample is transferred back from the HP chamber. This is unavoidable and the magnitude of the pressure burst depends on the solvent used in the ambient pressure experiments. Water produces pressure bursts in the 10^{-7} mbar range while volatile solvents, such as hexane, produce pressure bursts in the 10^{-8} mbar range. The UHV chamber can be isolated from the HP chamber by a gate value once the sample has been transferred back.

The time needed for the HP chamber to recover to its base pressure of 1×10^{-8} mbar also depends on the solvent used. In some cases, the entire system needs to be baked before the base pressure in the transfer chamber is reestablished.

The cleaning procedure for the platinum crystal is slightly different to that used for studies carried out only in vacuum. As the manipulator arm forms the seal between the UHV chamber and the HP chamber, it is not possible to transfer the sample if the arm has been cooled with liquid nitrogen. The thermal contraction of the metal arm would likely interfere with the seal formation. The teflon seals would also become cold and would likely harden around the arm during the time the sample is in the transfer chamber. Hardened seals could potentially scratch the manipulator arm during the transfer back to the UHV chamber, causing the seal to leak during future transfer experiments.

More significantly, the copper support wires and the thermocouple wires would

condense large quantities of ice if cold. Therefore, cleaning the crystal before transfer experiments uses liquid nitrogen only during the annealing stage of the cleaning. Starting the flow of liquid nitrogen immediately before the start of the temperature ramp and stopping it once the sample is no longer being heated ensures that the problems described above do not occur. At all other times during the cleaning and transfer, a flow of dry air is used in place of the liquid nitrogen.

All of the transfer experiments described in this thesis involve the adsorption of dendrimers on the platinum surface. All of the dendrimers used for the experiments described were prepared by members of the Stobart group at this University. The details of their synthesis will therefore not be discussed. After preparation, the dendrimers were purified by dissolving them in hexane and passing them down a silica gel column. The purified dendrimers were stored in glass vials covered with aluminum foil to prevent photodegradation.

The glassware used in the UHV experiments was first cleaned in warm chromic acid and then washed with 18 MΩ·cm water from a Millipore Milli-Q purification system. The glassware was then rinsed with 95% ethanol, wrapped in aluminum foil, and placed in a 110°C oven for at least 6-12 hours. The ethanol used is the same quality as that used for the cleaning of all vacuum components on the UHV system and was found to have a very low residual content. After baking the glassware, it was removed from the oven and allowed to cool to room temperature before use.

The teflon components were not cleaned in chromic acid as some discoloration was observed. Instead, they were washed with 18 MΩ·cm water, rinsed with 95% ethanol, and given a final rinse with HPLC grade (99.9% purity) hexane (from Baxter Healthcare Corp). The teflon components were then wrapped in aluminum foil and placed in a 110°C oven for

one hour. After removal from the oven, the teflon components were allowed to cool to room temperature under a constant flow of purified argon gas.

The experimental setup for contacting the dendrimer solutions with the platinum crystal is shown in figure 3.19. All components have a constant flow of purified argon passing through them at all times. The dendrimer solutions were degassed with purified argon for one hour before contact with the platinum crystal.

3.12 Data Acquisition and Processing

All of experimental techniques described, excluding LEED, use a general purpose interface bus (GPIB) to transfer data to a digital computer (66 MHz 80486) for storage. A series of computer programs were created using QuickBASIC (written by Scott A. Furman) that would interface with a Nicolet 310 oscilloscope, the Stanford Research Systems lock-in amplifier (LIA), and the Hidden Analytical Ltd. (HAL) mass spectrometer. These three devices are all equipped with a GPIB port and can be controlled remotely with a computer.

The Nicolet oscilloscope displays 4000 points on each of two channels with variable time and voltage ranges. The computer program interfaced with the oscilloscope transfers both channels as well as information on the time and voltage ranges used. A simple ASCII data file is created that contains the time and the two voltage channels. Note that the oscilloscope must be in 'hold' mode before data transfer can occur. Once the transfer is complete, the program will prompt the user for a file name and the oscilloscope can be put back into 'live' mode.

The HAL mass spectrometer has two modes of operation, as described previously in section 3.8. When operating in the modulated mode, all data acquisition is done through the

lock-in amplifier (see below). When operating in MID mode, data is transferred directly from the mass spectrometer. The spectrometer enters a 'local' mode and remains 'locked out' during data collection and acquisition. During this time, the spectrometer's main keyboard is not functional. The computer program selects the appropriate operating mode and reads a data stream coming from the spectrometer that is sent after the completion of each scan. This data stream is decoded immediately after the data has been received to convert it to a series of partial pressures for each of the masses being scanned. The time, sample temperature, and UHV pressure are recorded along with the partial pressures of the mass being monitored in a simple ASCII data file. At the termination of the experiment, the mass spectrometer is returned to 'local' mode and the front keyboard becomes operational again.

The SRS lock-in amplifier has a built-in 4-channel analog to digital (A/D) converter and a 2-channel digital to analog (D/A) converter. These are fully accessible through the GPIB interface. The four A/D converters are currently configured to read the Auger electron energy (channel X1), the sample temperature (channel X2), the work function (channel X3), and the pressure in the main UHV chamber from the ion gauge (channel X4). One of the D/A convertors (channel X5) is used to select the Auger modulation frequency. The output of X5 is used as the frequency input of an oscillator circuit that is also inside the LIA. This configuration allows data from all of the various experiments to be acquired easily as no cables need to be switched for the various experiments.

The X and Y channels of the LIA can also be read through the GPIB interface. For both the AES and modulated mass spectrometer experiments, the phase on the LIA is adjusted to provide maximum signal on the X channel. The phase of the LIA, the LIA time constants, and the voltage ranges are all set to the appropriate values by the data acquisition software.

Unlike the mass spectrometer, the LIA is not 'locked-out' during data acquisition and all of the keys on the front panel are fully operational.

Once the data has been stored on the computer, it may need to be processed before it can be analyzed. Four FORTRAN computer programs (written by Scott A. Furman) were developed to perform commonly used functions. All four programs will prompt the user for the input (file names and parameters) but they also can be used with command line codes. This allows batch files to be used to process files. An addition program (written in QuickBasic) will execute a single command on a number of different files. This allows the processing of large numbers of data files without any need for the user to be present. This program was developed because of the long time (several hours) it takes to process the data from a single day of experiments.

The four processing programs perform different types of functions on data files. They all automatically detect the type of data file (header lines, number of columns, column separators) and can be used on almost any data file that is in an ASCII format. The first program (SMOOTH.EXE) smooths the data in selected columns by one of three methods. Both boxcar and FFT smoothing routines are available as well as a spike removal routine. This routine was designed to remove the spikes in modulated mass spectral data files (see section 3.8).

Many of the data files generated are quite large (>5000 lines) and a program (FILTER.EXE) was written to reduce the size of these files. The file can be filtered by averaging a set number of data points into a single data point, or it can be filtered by selecting a interval range on a particular column.

Common math functions (add, subtract, multiply, divide, integrate) can be performed

on data files using MATH.EXE. The last program (BACKGRND.EXE) is used to subtract a background baseline from a column of data. The program subtracts a polynomial (up to forth order) from the desired data and allows the user to select a range where no background subtraction will occur. This is useful in thermal desorption spectra where the background only increases when the sample temperature goes above 600K.

All of the data files used to create the figures in this thesis were processed in some way before plotting. Care was taken to make sure that information was not lost from the smoothing. Figure 3.20 demonstrates a typical smoothing of some thermal desorption data. The smoothed data has been offset for clarity.

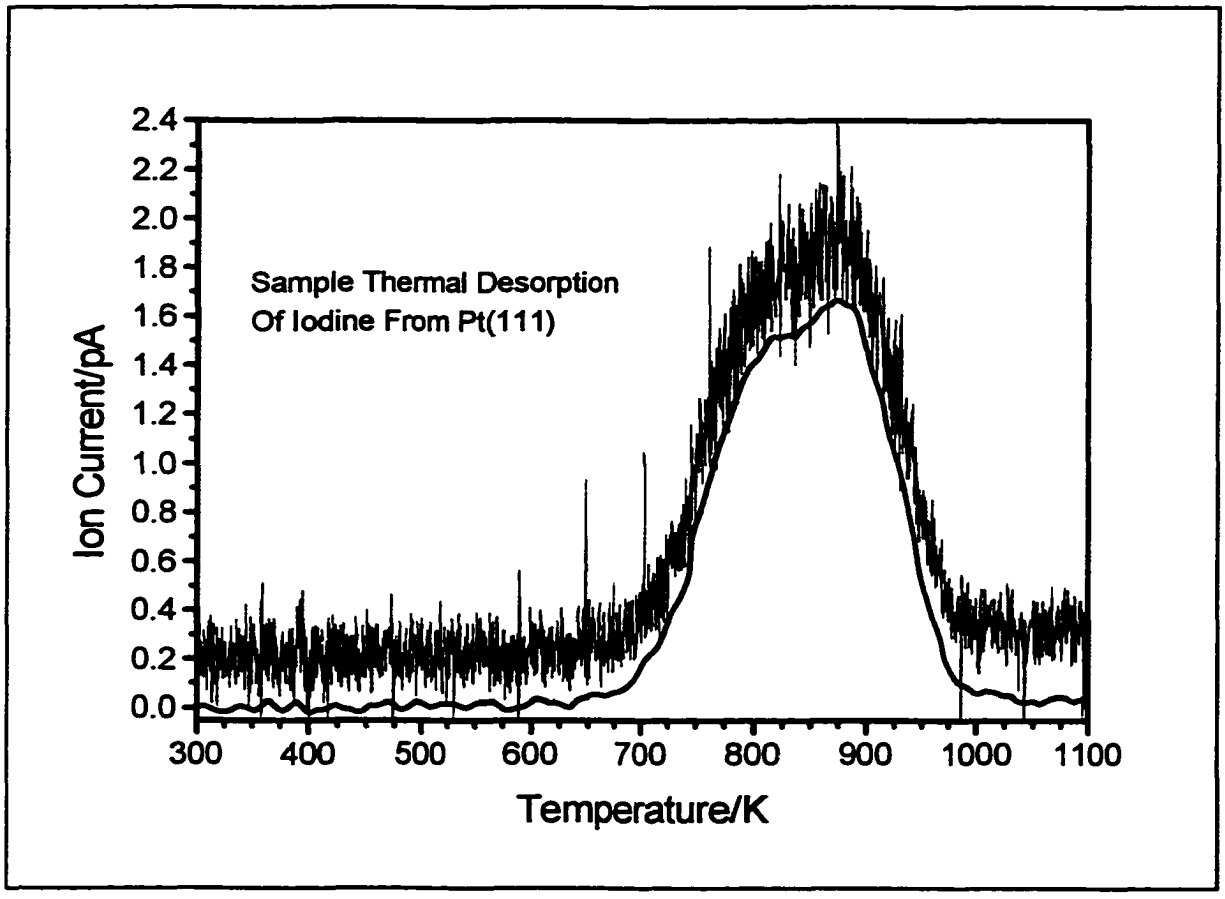

Figure 3.20-Comparison Of Raw and Smoothed Thermal Desorption Data

4

Iodine Adsorption On Platinum(111)

4.1 Introduction

Iodine gas readily adsorbs on platinum(111) at ambient temperature to form a stable layer that has been characterized by several electrochemical and UHV techniques. The surface structures formed are known, and there is some UPS data suggesting that the work function decreases during adsorption. The details of the structures formed at 300 K and 150 K will be investigated. The work function of the platinum as a function of iodine coverage will be determined and the sticking coefficient will also be studied as a function of adsorption temperature.

4.2 Structure of Adsorbed Layers

There are four structural phases of iodine that have been previously observed. These are the $(3\sqrt{3}x9\sqrt{3})R30°$ structure (θ=0.64), the (3x3) structure (θ=4/9), the $(\sqrt{7}x\sqrt{7})R19.1°$ structure (θ=3/7) and the $(\sqrt{3}x\sqrt{3})R30°$ structure (θ=1/3). The three lower coverage structures have been prepared electrochemically [4.1] while the (3x3) structure has not been previously prepared in vacuum. Little is known about the $(3\sqrt{3}x9\sqrt{3})R30°$ structure as it has only been prepared using iodine vapour at atmospheric pressures [4.2].

The unit cells of the three low coverage iodine structures are given in figures 4.1-4.3. In the (3x3) structure, both unit cells (symmetrical and asymmetrical) are shown. Only one of the rotational domains of the $(\sqrt{7}x\sqrt{7})R19.1°$ structure is shown.

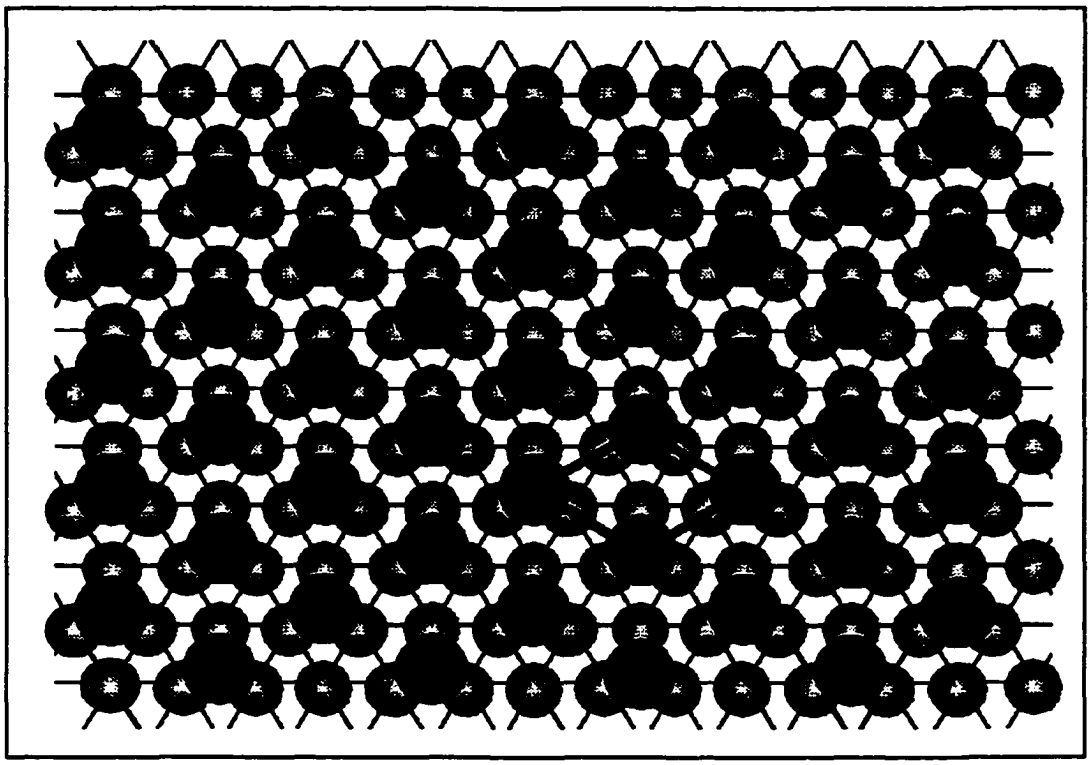

Figure 4.1-($\sqrt{3}$x$\sqrt{3}$)R30° Structure of Iodine on Pt(111)

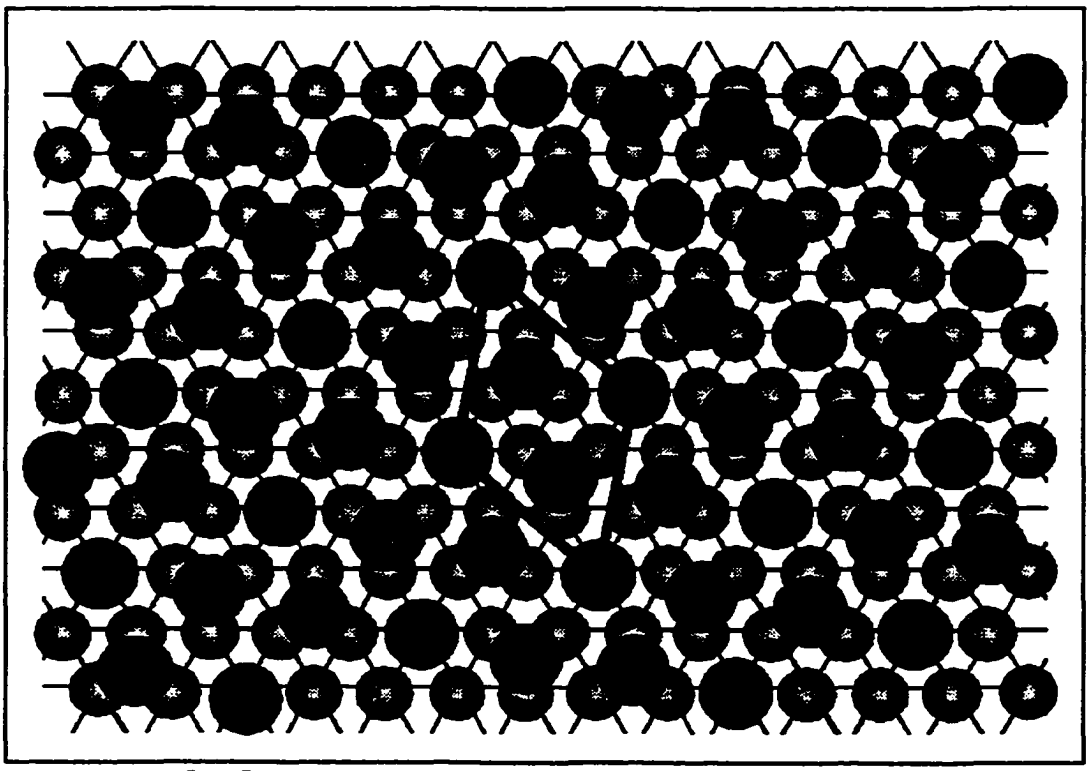

Figure 4.2-($\sqrt{7}$x$\sqrt{7}$)R19.1° Structure of Iodine on Pt(111)

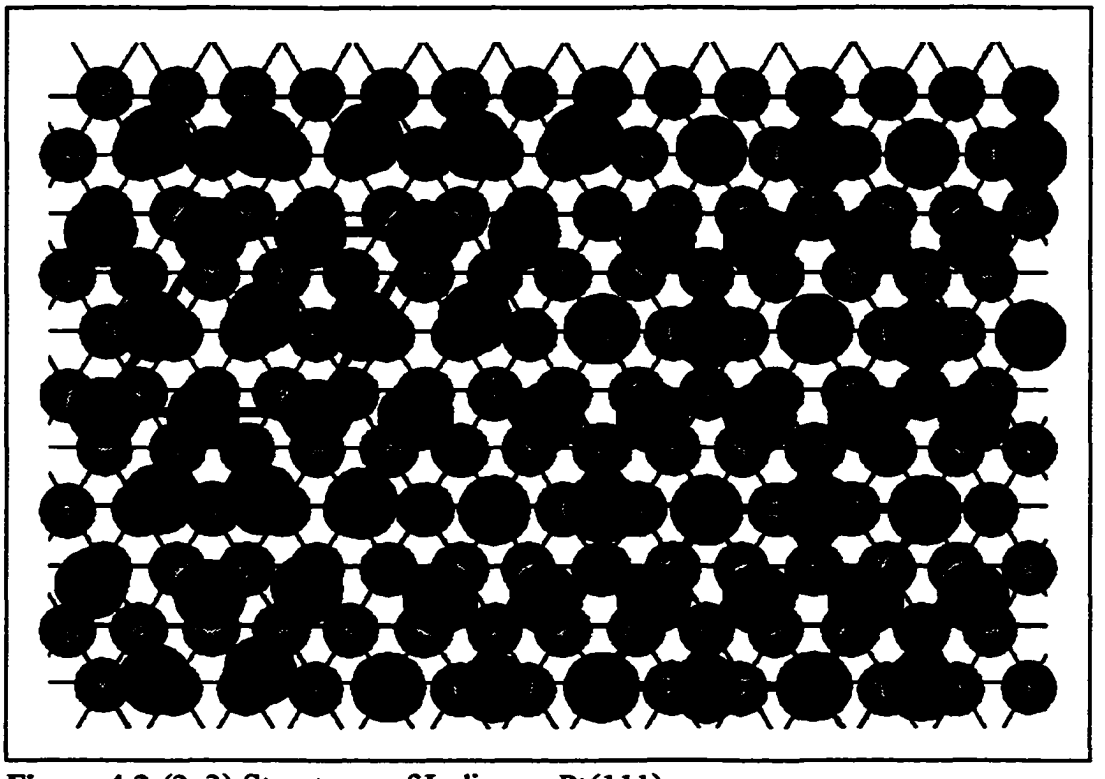

Figure 4.3-(3x3) Structures of Iodine on Pt(111)

4.3 Iodine Adsorption

Monitoring the LEED pattern of the platinum surface provides a detailed picture of the adsorption process. Starting with a clean platinum surface, only the (1x1) pattern is observed with LEED (shown in figure 4.4). At no point during any of the experiments described here did the platinum (1x1) pattern change or disappear. This confirms the hypothesis that the positions of the surface platinum atoms are unaffected by the adsorption of iodine. When iodine first begins to adsorb onto the surface, the LEED pattern changes very little. The ($\sqrt{3}$x$\sqrt{3}$)R30° pattern forms first, although the diffraction beams are broad and diffuse when the pattern first appears. As more iodine is adsorbed, the ($\sqrt{3}$x$\sqrt{3}$)R30°

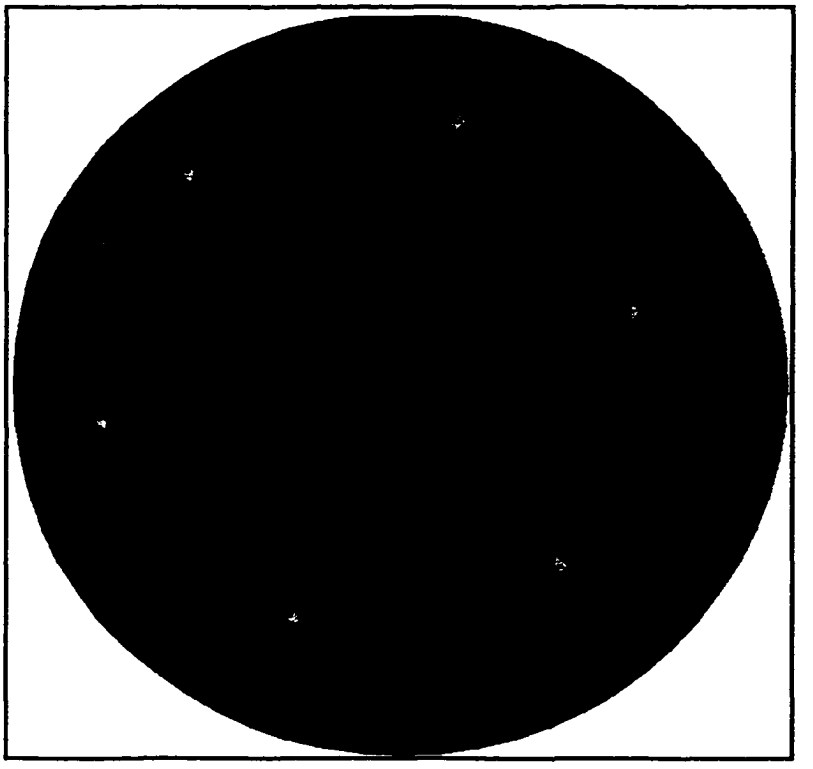

Figure 4.4-Pt(111) (1x1) LEED Pattern at 135 eV

pattern becomes sharper. After this, the ($\sqrt{7}$x$\sqrt{7}$)R19.1° pattern begins to appear and both diffraction patterns are visible on the surface. Eventually the ($\sqrt{7}$x$\sqrt{7}$)R19.1° diffraction beams are always observed to be sharp when visible. The addition of more iodine causes the ($\sqrt{3}$x$\sqrt{3}$)R30° pattern to fade and only the ($\sqrt{7}$x$\sqrt{7}$)R19.1° pattern is visible. The ($\sqrt{3}$x$\sqrt{3}$)R30° and ($\sqrt{7}$x$\sqrt{7}$)R19.1° LEED patterns are shown in figures 4.5 and 4.6. The (3x3) pattern is shown in figure 4.7.

Using LEED to following the adsorption of iodine is useful as it provides clear information about the structures on the surface. This is made easier when the coverages and bonding geometries of the structures have previously determined (see Chapter 2). The coverage can be determined using AES but both techniques require the dosing procedure to be interrupted before the coverage and structure can be determined.

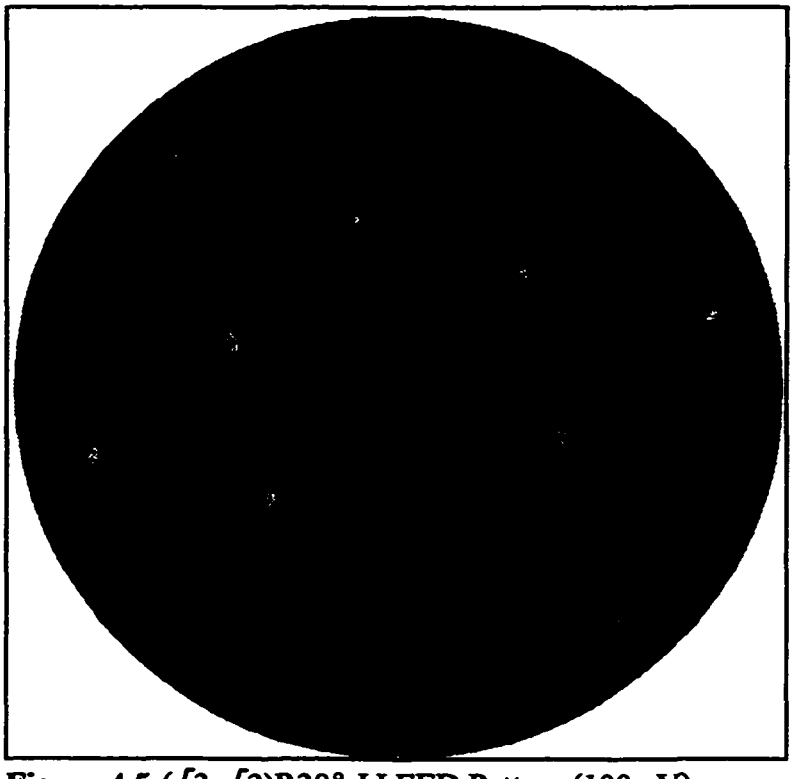

Figure 4.5-($\sqrt{3}$x$\sqrt{3}$)R30°-I LEED Pattern (100 eV)

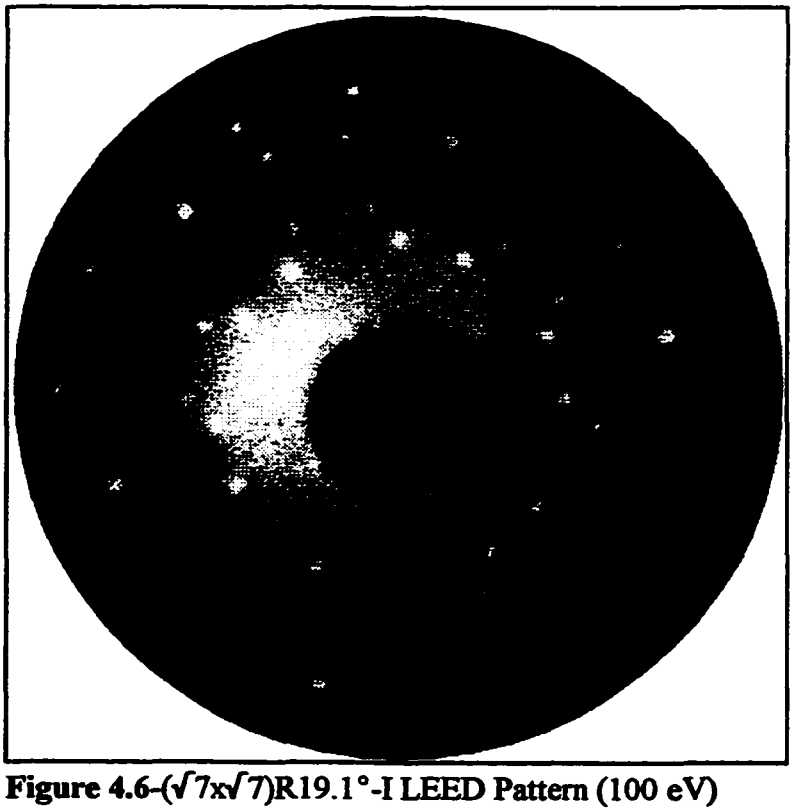

Figure 4.6-($\sqrt{7}$x$\sqrt{7}$)R19.1°-I LEED Pattern (100 eV)

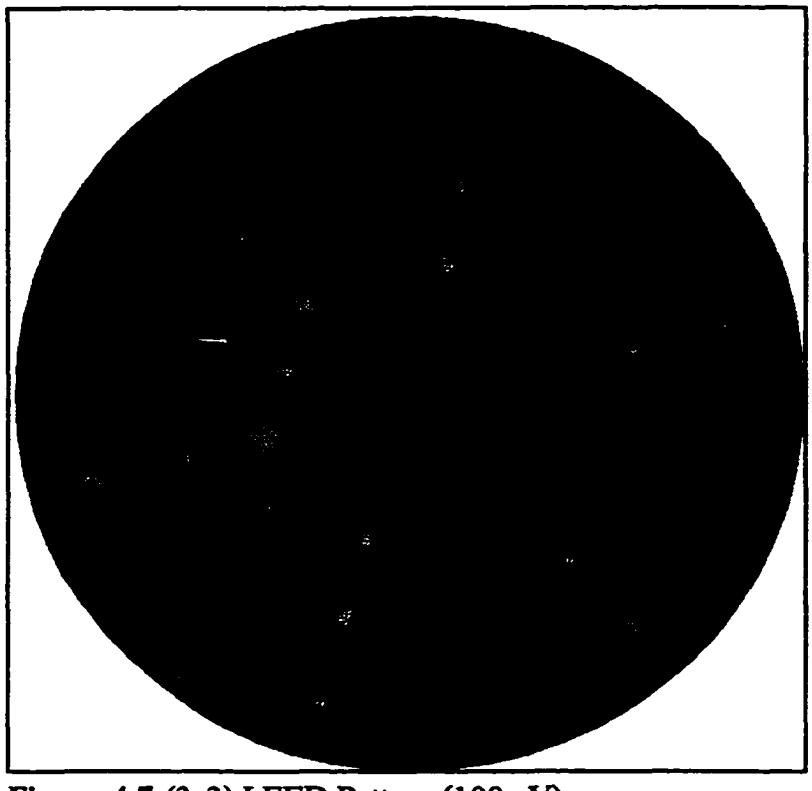

Figure 4.7-(3x3) LEED Pattern (100 eV)

Another convenient way to monitor the adsorption process is to measure the change in work function. The geometry of the Kelvin probe and the iodine doser allow the work function to be continuously monitored during the iodine dosing. Once the relationship between the work function and coverage has been established, the coverage can be easily estimated using the change in work function.

As seen in figure 4.8, the work function initially decreases when iodine adsorbs on the surface. After a minimum value is reached, the work function increases. Once the surface is saturated, the work function levels off at a constant value. Extended dosing after saturation produces no further change in the work function.

The iodine doser used for these experiments allows the flux of iodine to be turned off at any point during the experiment. This was done at several different times to study the

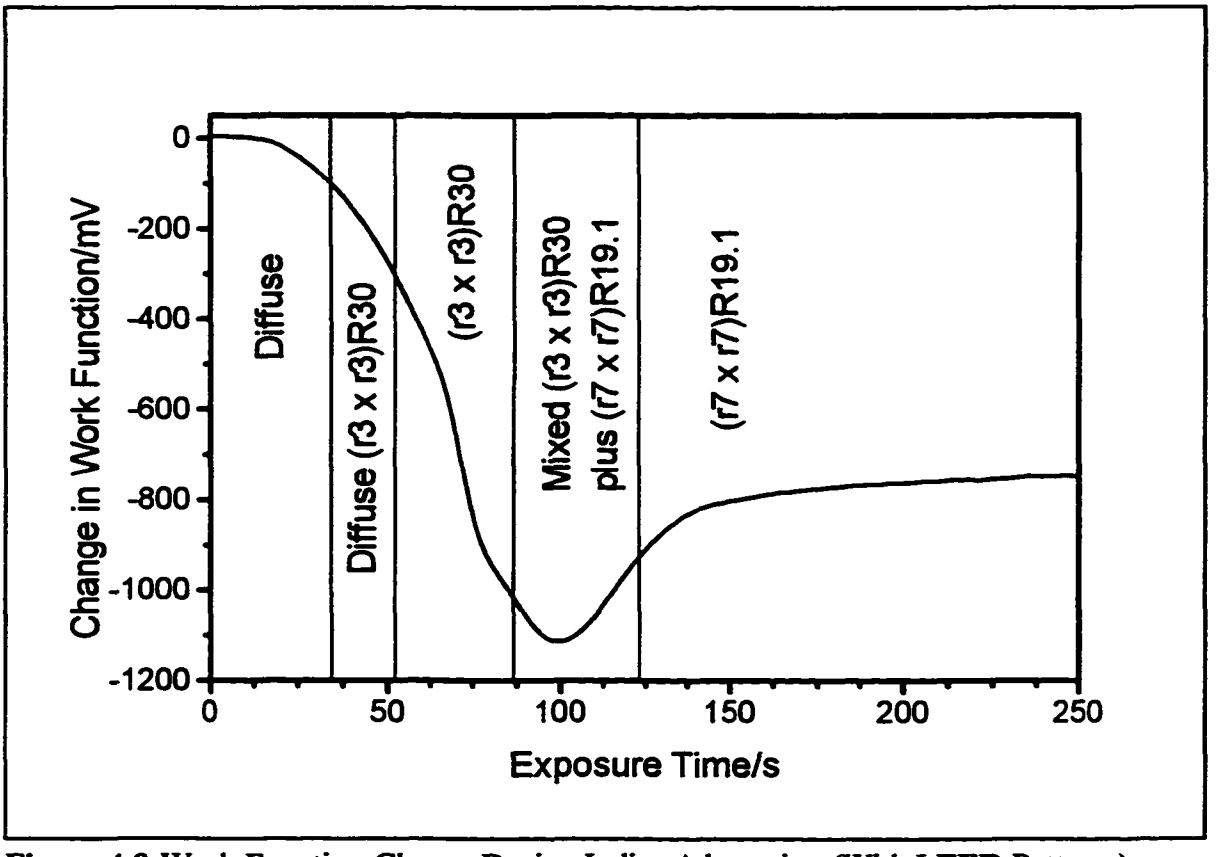

Figure 4.8-Work Function Change During Iodine Adsorption (With LEED Patterns)

surface with LEED and AES. The LEED transformations during adsorption are also shown in figure 4.8.

The peak-to-peak height of the iodine Auger signal at 530 eV (see figure 4.9) was used to calculate the coverage. This was done by assuming that the Auger signal obtained once the adsorption was complete corresponded to a coverage of 3/7. The variation of the work function with coverage is shown in figure 4.10. Two data sets were combined to construct this graph, each using a different modulation amplitude for the energy analyzer. Using a 30 V modulation increases the Auger current detected but decreases the resolution (see examples in Chapter 3). Using the standard 10 V modulation provides good resolution but the Auger current decreases. The intensity of the iodine signal, particularly at low

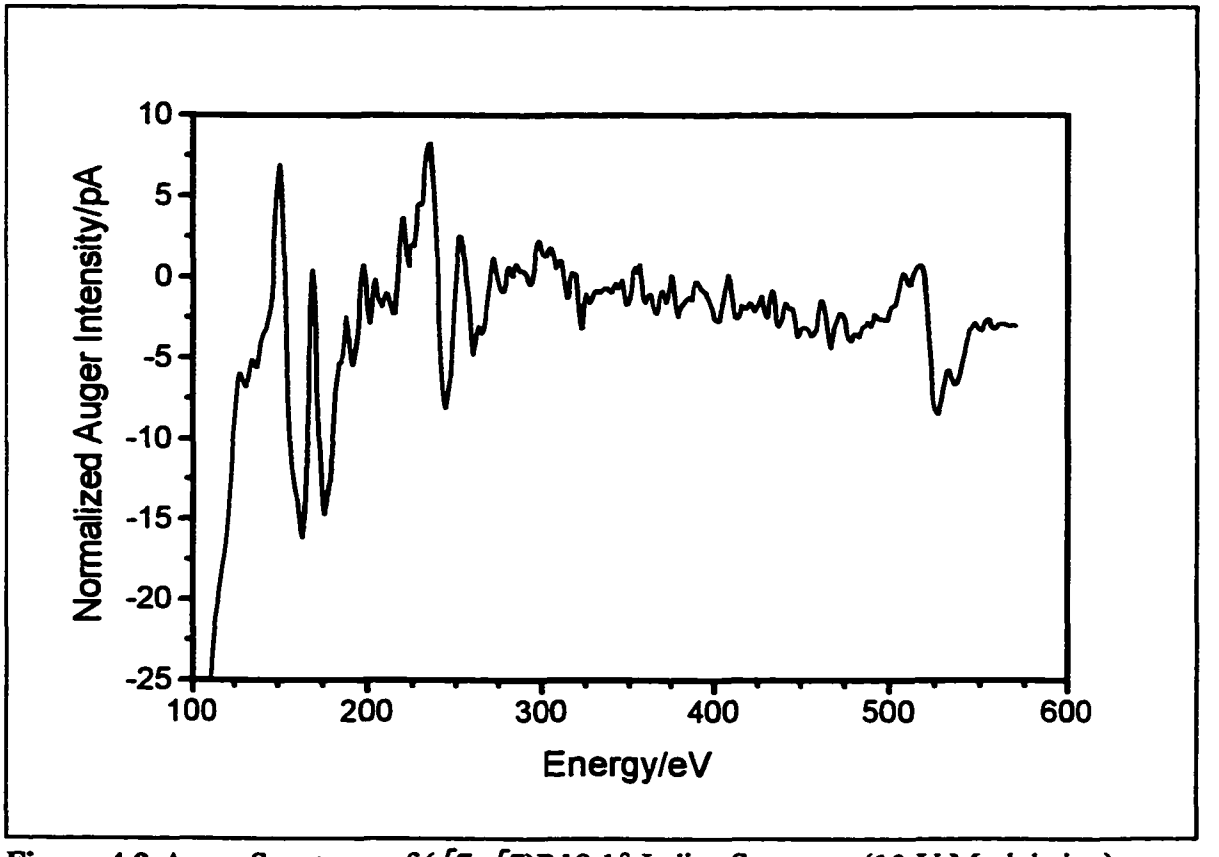

Figure 4.9-Auger Spectrum of ($\sqrt{7}$x$\sqrt{7}$)R19.1° Iodine Structure (10 V Modulation)

coverages, becomes difficult to determine due to the noise in the spectra. The error bars were estimated from the amount of noise present in the spectra compared to the intensity of the iodine Auger signals.

From this data, the minimum in the work function corresponds to a coverage of 1/3. This is the expected coverage of the ($\sqrt{3}$x$\sqrt{3}$)R30° structure. Upon scanning the entire crystal face with the electron beam, it was found that there were patches of a mixed ($\sqrt{3}$x$\sqrt{3}$)R30° and ($\sqrt{7}$x$\sqrt{7}$)R19.1° LEED pattern. However, most of the surface only showed the ($\sqrt{3}$x$\sqrt{3}$)R30° pattern.

The fact that the work function increases during the formation of the ($\sqrt{7}$x$\sqrt{7}$)R19.1° structure at coverages greater than 0.33 is interesting. While adsorption in the threefold sites

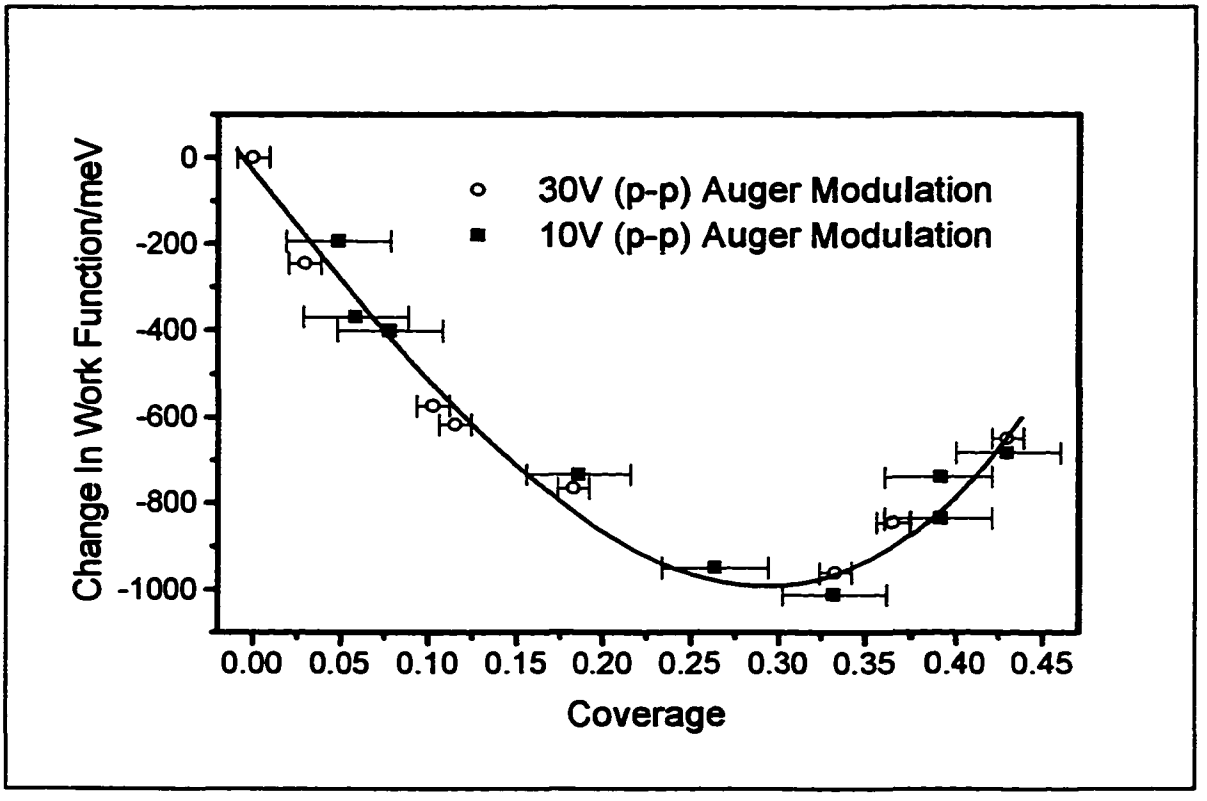

Figure 4.10-Coverage Dependence of Change in Work Function at 300 K

is accompanied by a decrease in work function, adsorption in the atop sites seems to increase the work function. This issue will be addressed in Chapter 5 to determine if the reversal of the work function is due to a coverage dependence or a site dependence.

Iodine adsorption at 150 K produces an almost identical change in work function, as shown in figure 4.11. The difference is that the adsorption of iodine does not stop once the coverage has approached 0.44. The work function continues to increase and actually becomes positive (relative to the bare surface value) before levelling off. At this point, it is believed that molecular iodine is simply condensing on the surface.

Once again the flux of iodine was interrupted at different stages of the dosing (at 150 K) and the surface was studied with LEED and AES. At low coverages (<0.3), all three

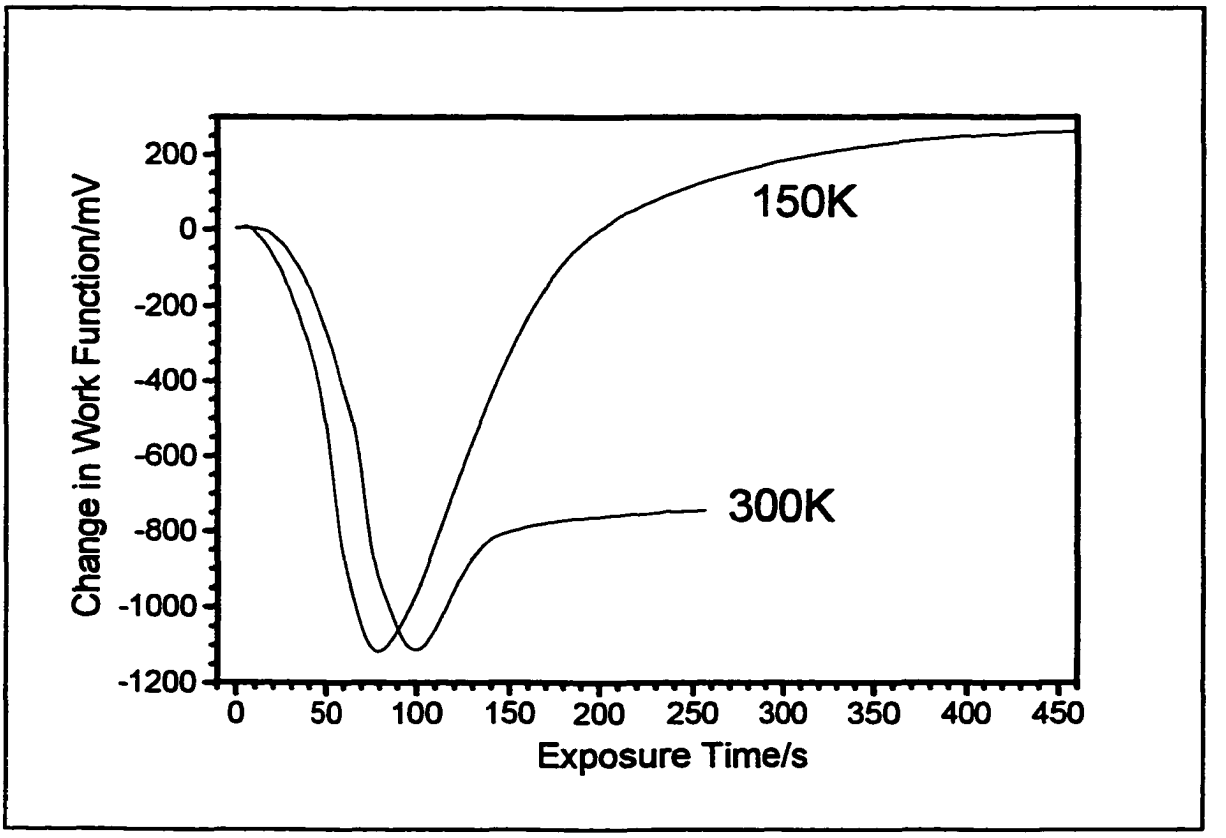

Figure 4.11-Comparison of Changes in Work Function at 300 K and 150 K

structures are visible in the LEED pattern. Moving the sample to obtain a diffraction pattern from different regions of the crystal produced various combinations of the three diffraction patterns. As more iodine is added to the surface, the ($\sqrt{3}$x$\sqrt{3}$)R30° pattern disappears and only the (3x3) (see figure 4.7) and ($\sqrt{7}$x$\sqrt{7}$)R19.1° patterns are visible. Once the coverage increases beyond 0.44, the LEED pattern begins to develop a diffuse background. Eventually, all the diffraction beams from the surface fade completely as the background becomes dominant. The LEED pattern after extensive dosing at 150 K usually did not show any extra diffraction beams that could not be assigned to the three structures discussed above. However, the LEED pattern shown in figure 4.12 was photographed after the dosing shown in figure 4.11 (at 150 K). Although it is difficult to see the pattern clearly, this appears to match the diffraction patten from the (3$\sqrt{3}$x9$\sqrt{3}$)R30° structure discussed in Chapter 2. Most

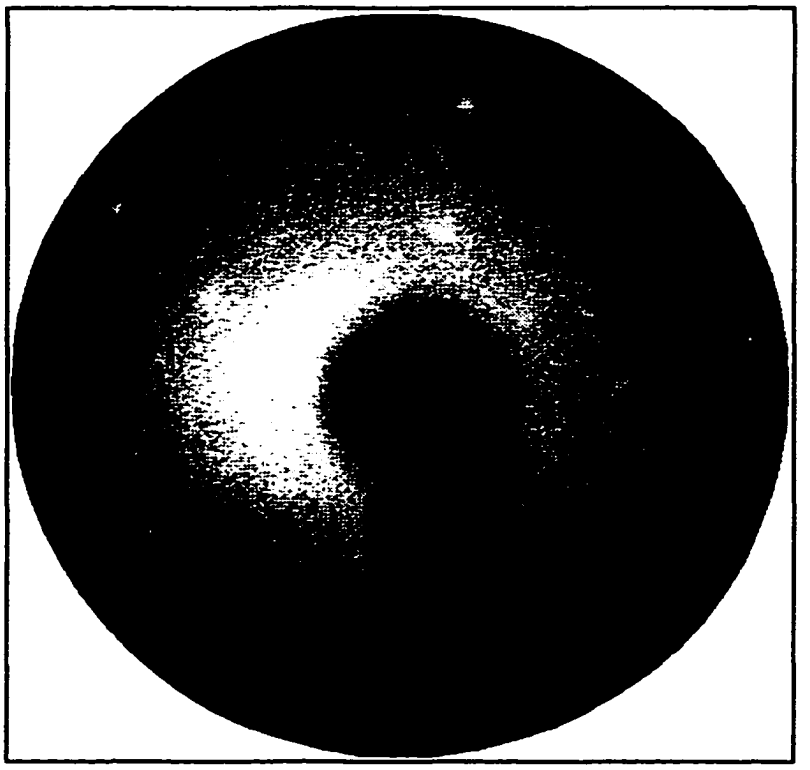

Figure 4.12-(3√3x9√3)R30° LEED Pattern (84 eV)

of the less intense diffraction beams that are present in the reference pattern [4.2] are missing from this pattern but all spots present here match those previously seen. The background in this LEED pattern is very intense and is likely due to the (3√3x9√3)R30° structure being covered in condensed molecular iodine.

Although the changes in work function at 300 K and 150 K are very similar, this does not mean the iodine coverage for a particular value of the work function is the same. The relationship between work function and coverage must be determined for adsorption at 150 K. The sample was analyzed by AES but since the surface does not become saturated at a known coverage, it is not possible to calibrate the Auger intensities by the same method that was used at 300 K.

The ratio of the iodine Auger intensity to the platinum Auger intensities changes as

a function of iodine coverage. For the ($\sqrt{7}$x$\sqrt{7}$)R19.1° iodine structure (created at 300 K) the ratio of the iodine (530 eV) to the platinum (150 eV) Auger intensities is 1:2.5. The Auger spectrum of the surface (at 150 K) when the work function had decreased by 850 mV had a similar ratio (1:2.38). This means the coverage at this point is approximately 2.38/2.51=0.95 times the ($\sqrt{7}$x$\sqrt{7}$)R19.1° saturation coverage (0.95x0.43=0.408). Using this a calibration point for the other Auger spectra taken at 150 K, figure 4.13 was constructed.

Comparing figures 4.13 and 4.10 shows that the coverage for a given value of the work function is higher at 150 K than it is at 300 K. This suggests that some of the iodine adsorbed onto the surface at 150 K does not to contribute the change in work function. Given the similarity of the adsorption curves in figure 4.10, it seems that the observed change

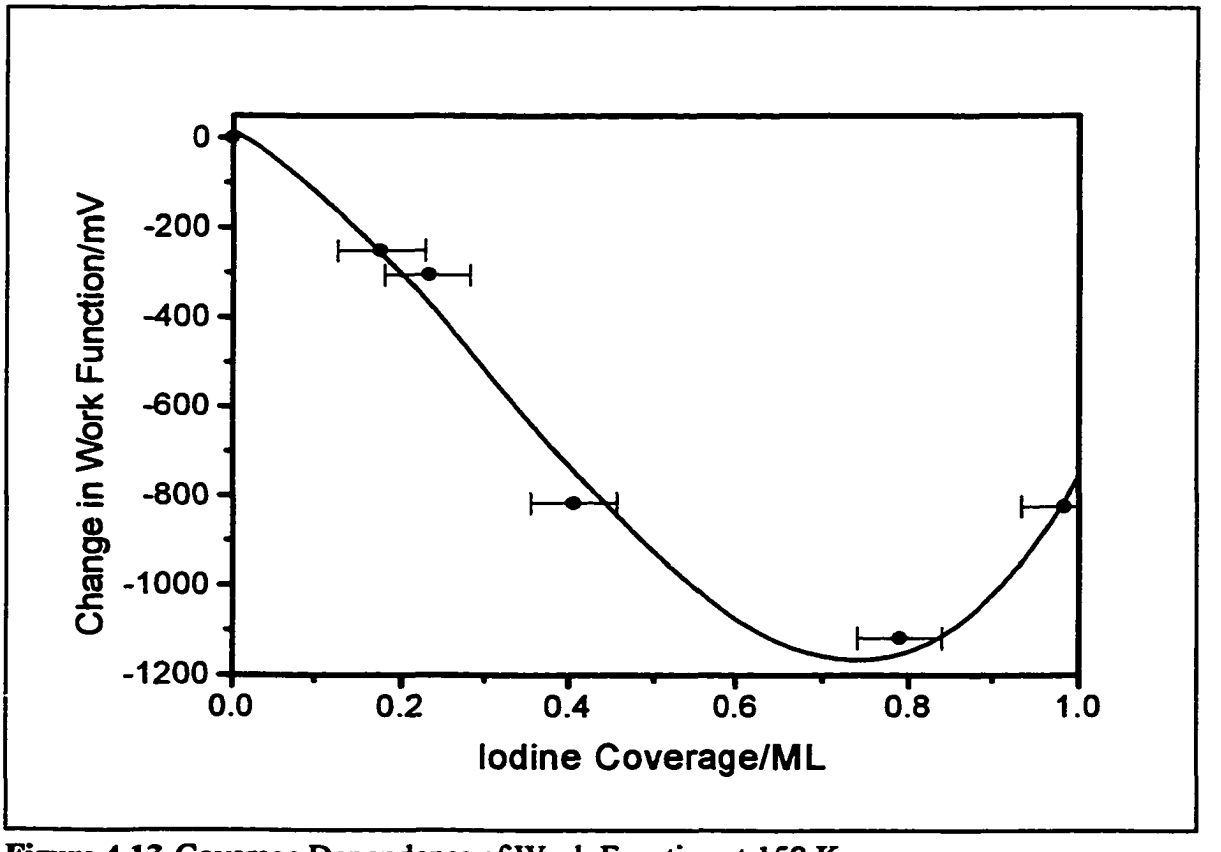

Figure 4.13-Coverage Dependence of Work Function at 150 K

in work function has very little dependence on the surface sites being occupied. At 300 K, only the $(\sqrt{3}x\sqrt{3})R30°$ structure is observed at low coverages while at 150 K, the $(\sqrt{7}x\sqrt{7})R19.1°$ and the (3x3) structures are also seen at low coverages. If the different adsorption sites had different effects on the work function, the adsorption curve at 150 K would be expected to be different from the adsorption curve at 300 K.

The higher coverage observed in the adsorption curve at 150 K can be explained by assuming that some of the iodine adsorbed at that temperature does not contribute to the work function. Assuming that any iodine that comes in direct contact with the surface (forming patches of the three known structures) makes a contribution to the work function, the difference in coverage between figures 4.13 and 4.10 should be the amount of condensed molecular iodine on the surface. At the minimum in the work function, the coverage at 300 K was 0.33 ML while at 150 K it was 0.75 ML. This means there was 0.21 ML of molecular iodine on the surface at this point.

If we assume that at 150 K, the sticking coefficient of the iodine is unity (all iodine hitting the surface sticks to the surface), the data from figures 4.13 and 4.10 should provide a reasonable estimate of the sticking coefficient at 300 K. Taking into account the slightly different initial induction period, the time to reach the minimum in the work function was 94 seconds at 300 K and 79 seconds at 150 K. This assumes that the iodine doser was producing an identical flux in both cases. As these experiments were performed successively (300 K dosing first), and given the error in the coverages, this assumption seems reasonable. The sticking coefficient at 300 K is then estimated to be (0.33/94 ML/s)/(0.75/79 ML/s)=0.37.

5

Thermal Desorption Of Iodine

5.1 Introduction

Thermal desorption spectroscopy (TDS) is a very useful tool for probing the nature of adsorbates at the surface. The strength of the chemical bond between the adsorbate and the surface can be roughly calculated by measuring the temperature where the adsorbate desorbs. Since the adsorption of gas onto a surface is usually not activated, the energy of desorption can be equated with the adsorption energy. The kinetics of the desorption process provide information about the nature of different binding sites and can probe the effects of interactions between adsorbates. The most common method for studying the desorption process is to use a mass spectrometer to identify the species as they desorb from the surface. The UHV system described in this thesis allows the simultaneous measurement of the changes in work function along with the mass analysis to provide extra information about the desorption process.

One of the pitfalls of thermal desorption spectroscopy is that the desorption process reflects the nature of the surface only at the desorption temperature. Heating the surface to cause desorption may also cause other reactions, decompositions, or structural rearrangements. Thus, the state of the surface at the desorption temperature may not accurately represent the state of the surface at the temperature of adsorption. However, it is still a powerful technique and, like LEED and AES, is an essential method for probing the nature of adsorbates.

5.2 Overview of Iodine Desorption

Before describing the details of the desorption kinetics and the changes in work function, the general features of the iodine desorption spectra should be reviewed. Iodine was adsorbed onto the platinum surface at 300 K and 150 K (see Chapter 4) and studied at different coverages. Adsorption at 300 K results in saturation at the (√7x√7)R19.1°-I structure while at 150 K, the growth of multilayer iodine is observed. Previous studies at 300 K [5.1] showed that when the surface is heated, four distinct phase transitions are seen. The thermal desorption spectrum shown in figure 5.1 shows these different transitions, as observed by LEED. The work function change during the desorption is also shown.

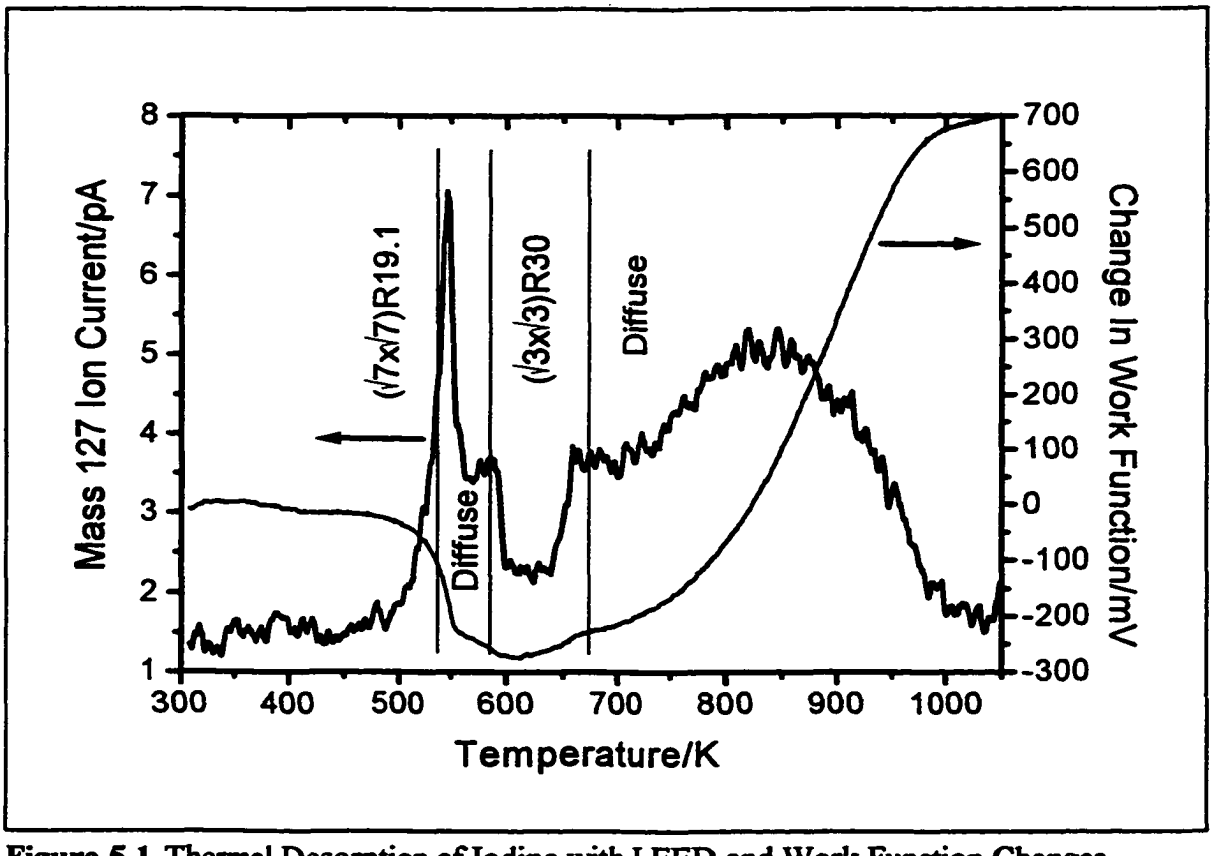

Figure 5.1-Thermal Desorption of Iodine with LEED and Work Function Changes

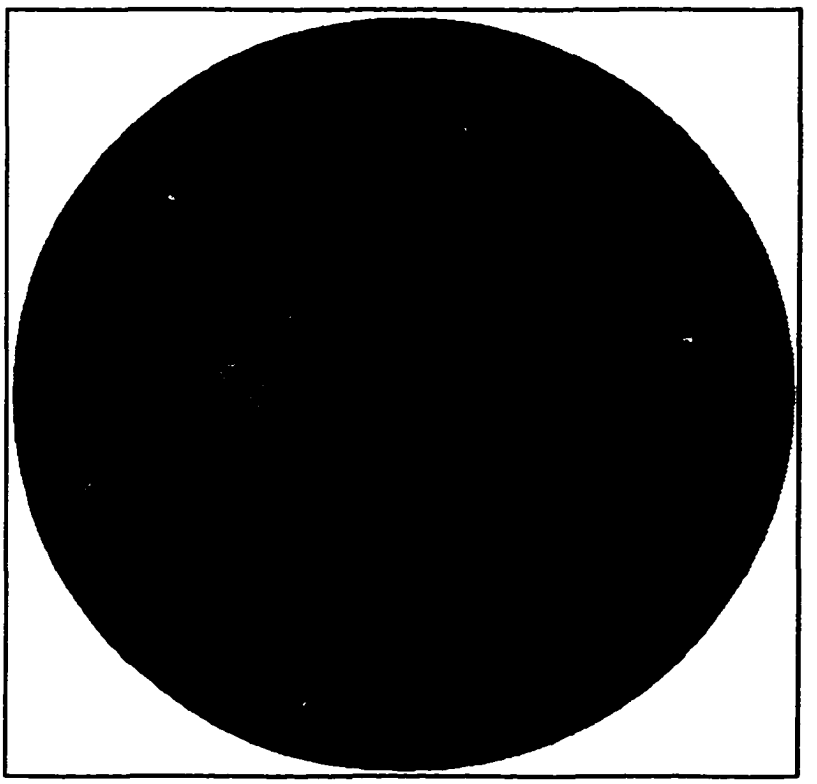

Figure 5.2-Diffuse ($\sqrt{3}x\sqrt{3}$)R30° LEED Pattern (100eV)

The first LEED transformation is from the ($\sqrt{7}x\sqrt{7}$)R19.1° pattern to a diffuse background at 530 K. When passing through this transition slowly (1 K/s), the diffuse background develops into a diffuse ($\sqrt{3}x\sqrt{3}$)R30° structure (shown in figure 5.2) where the fractional beams from the iodine layer are spread out. The diffuse pattern must come from structural disorder (rather than disorder from surface diffusion) as continued heating causes the ($\sqrt{3}x\sqrt{3}$)R30° pattern to become sharp (at 570 K). Above 670 K, LEED shows only a diffuse pattern, presumably due to thermally-induced surface diffusion where the iodine atoms no longer have fixed positions. Above 1000 K, LEED only shows the (1x1) pattern of the platinum substrate as all of the iodine has desorbed.

The change in work function during desorption is essentially the reverse of the work function change during adsorption. The minimum value of the work function corresponds to

the ($\sqrt{3}$x$\sqrt{3}$)R30° structure. The coverage at this point is expected to be 0.33, the same coverage where the minimum occurs during adsorption. In general, desorption from the atop sites (at 530 K) causes the work function to decrease while desorption from the threefold sites causes the work function to increase. This suggests that the two sites have a different contribution to the work function, as mentioned in Chapter 4. However, in section 5.4, it will be shown that the work function changes are related to coverage rather than specific sites.

Dosing at 150 K produces a variety of mixed LEED patterns. Dosing until the work function has become positive (relative to the bare surface value) produces a diffuse pattern with other patterns (mostly ($\sqrt{7}$x$\sqrt{7}$)R19.1° and (3x3)) visible, but obscured by the diffuse

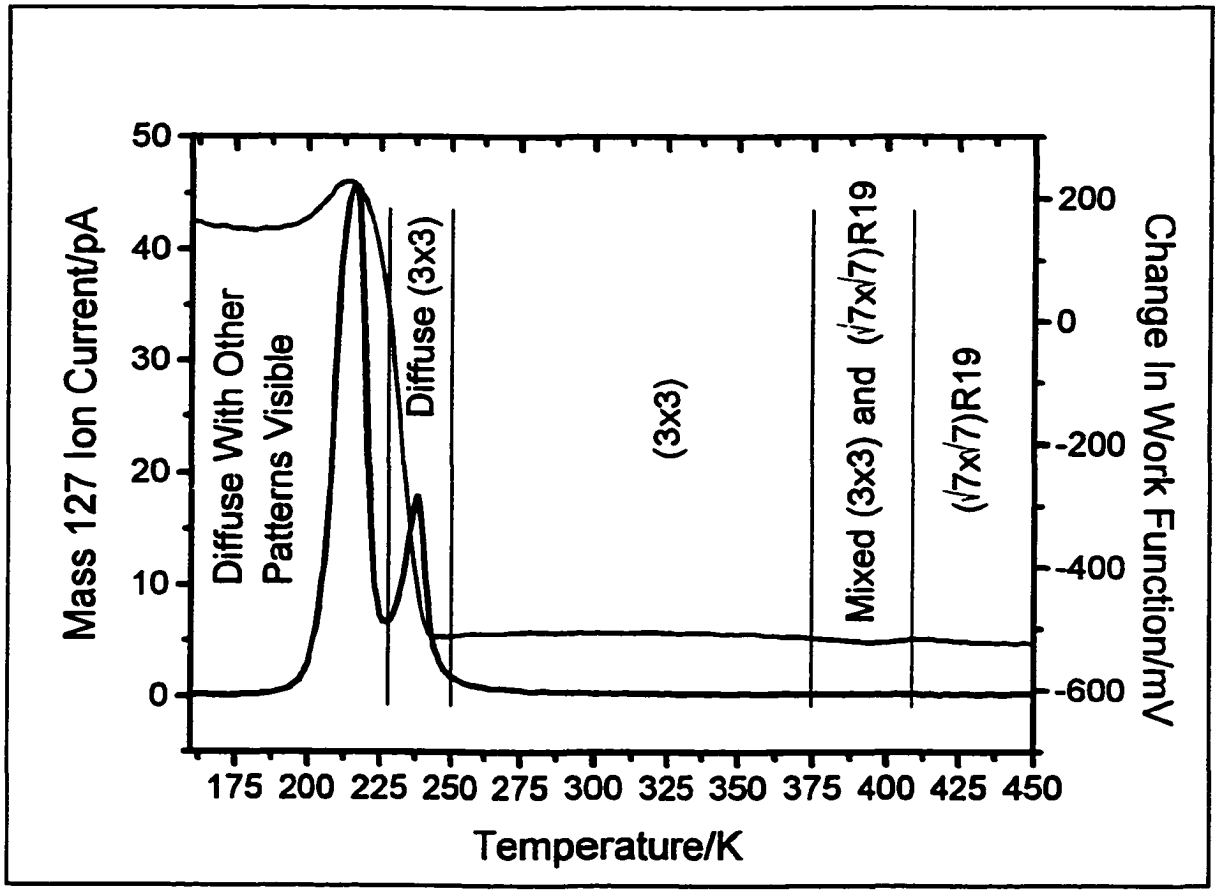

Figure 5.3-Low-Temperature Thermal Desorption with LEED and Work Function Changes

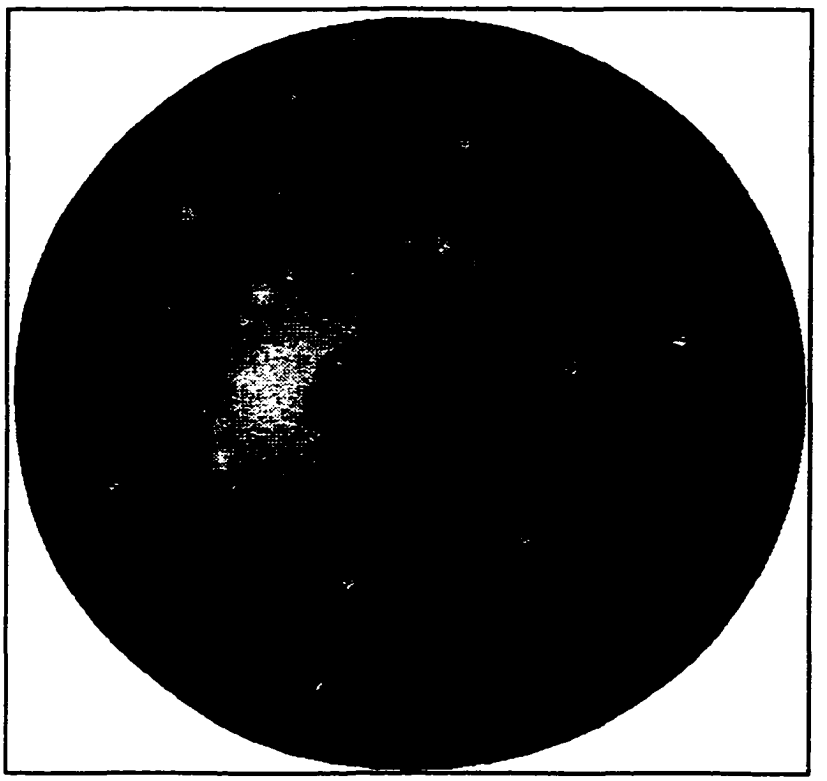

Figure 5.4-Mixed (3x3) and ($\sqrt{7}$x$\sqrt{7}$)R19.1° LEED Pattern (100eV)

background. Heating to 300 K produces a series of phase transitions that were observed by LEED (shown in figure 5.3). There is no notable difference in the LEED pattern observed during the first phase transition at 215 K. At 230 K, the diffuse pattern changes to a (3x3) pattern that noticeably sharpens at 245 K. The (3x3) pattern is stable up to 375 K, where it transforms to a mixed (3x3)/($\sqrt{7}$x$\sqrt{7}$)R19.1° pattern (shown in figure 5.4). This mixed pattern is stable up to 425 K where the (3x3) disappears completely. After this, the phase transitions are identical to the phase transitions described above. Note that there is no work function change associated with the transformation from the (3x3) to the ($\sqrt{7}$x$\sqrt{7}$)R19.1° phase (as seen in figure 5.3).

The work function change during desorption shows that the multilayer structure (desorbing at 215 K) does not have a significant work function change associated with it. There is a small change during the desorption but this is small compared to the change associated with the desorption peak at 235 K. The work function change at this temperature is quite large, suggesting that unlike the multilayer structure, the iodine associated with this desorption process is in much more intimate contact with the platinum surface.

These two low temperature peaks both appear to be molecular iodine desorbing from the surface. A signal due to mass 127 (atomic iodine) is seen in the spectrometer due to the ionization-induced division of the iodine molecule. The dissociation ratio (127:254) was

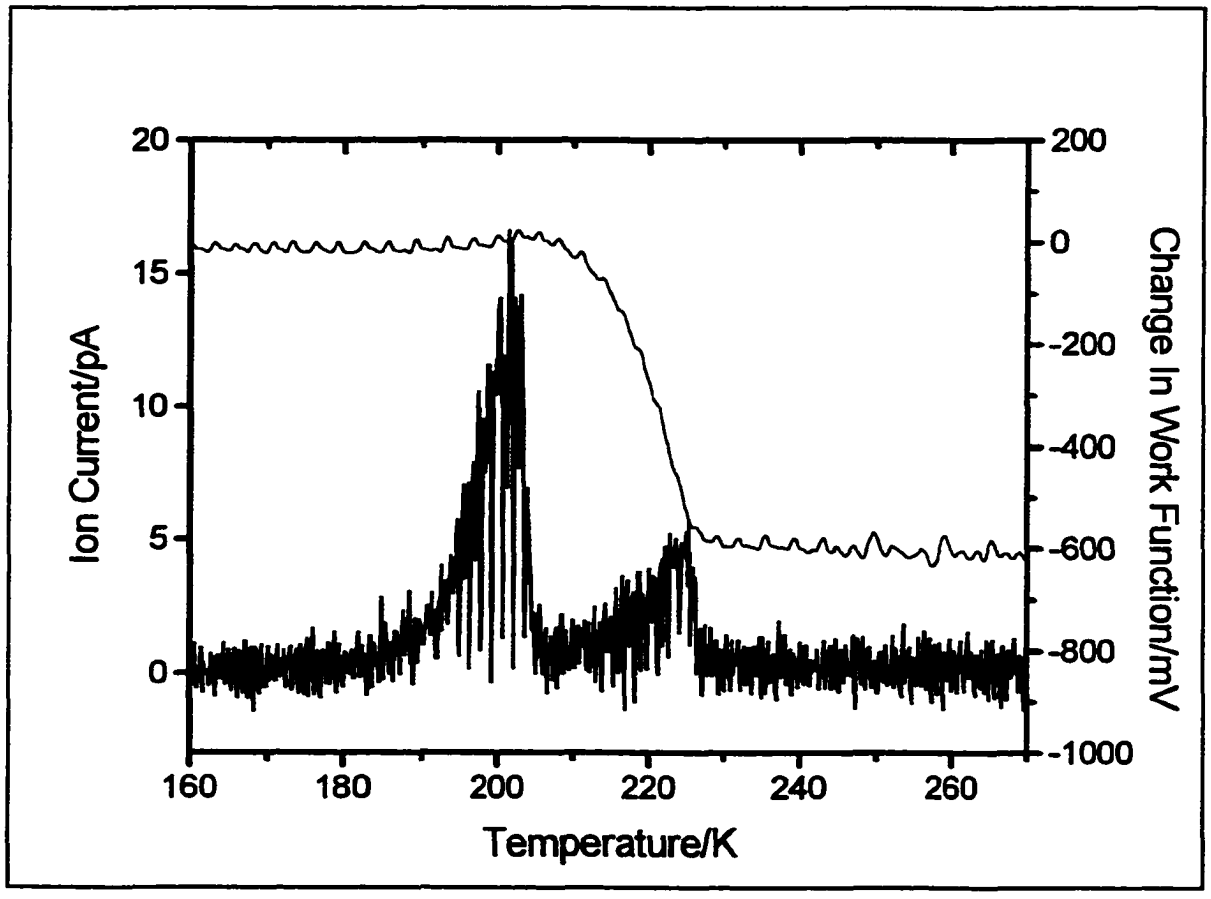

Figure 5.5-Double-Mass Modulation Desorption Spectrum with Work Function Changes

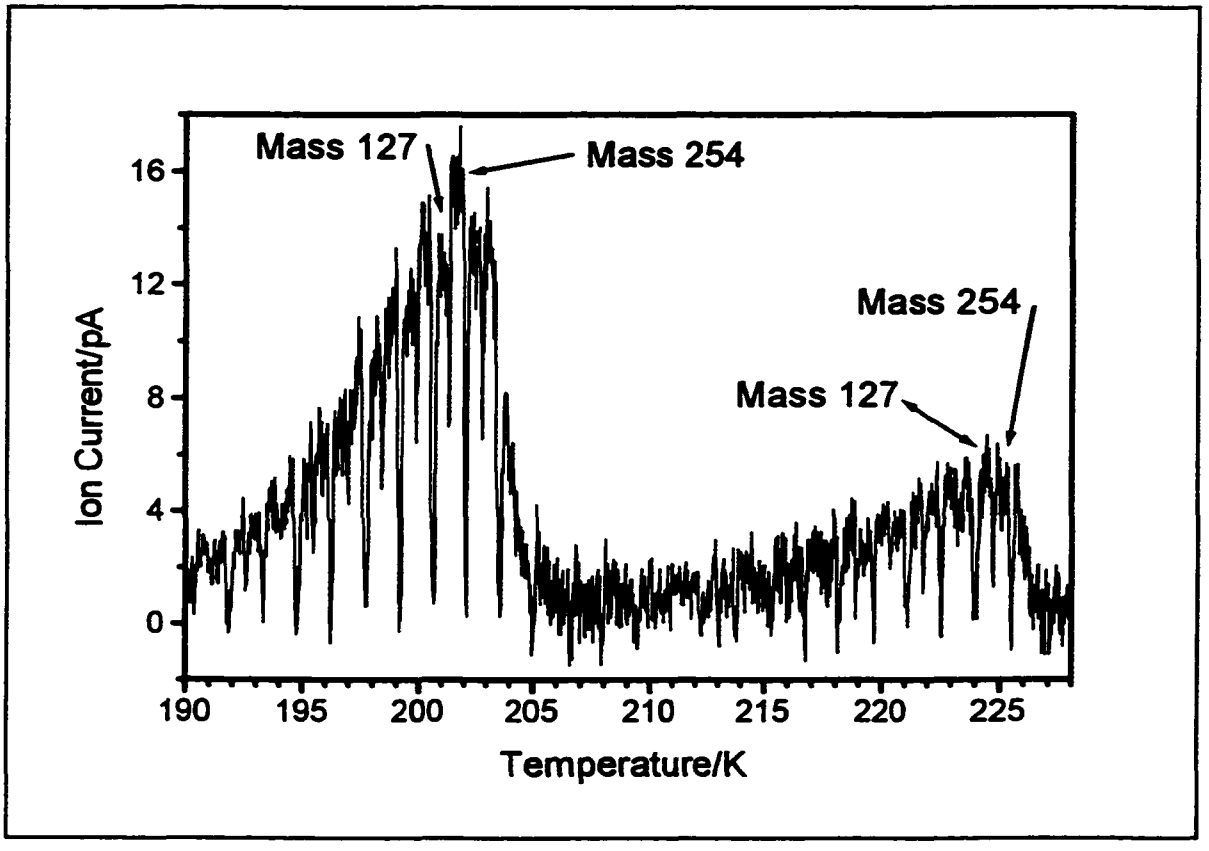

Figure 5.6-Expanded View of Double Mass Modulation Desorption

measured by operating the mass spectrometer in its modulated mode using both of these masses. The resulting desorption spectrum is shown in figure 5.5. The spectrum is complicated by the fact that the mass spectrometer is continually switching between the two masses. Careful examination of the two peaks, shown in figure 5.6, clearly indicates that both atomic and molecular iodine are being detected. If we assume that all of the iodine desorbing at 215 K is molecular iodine, the dissociation ratio (127:254) is measured to be 0.8:1. At 235 K, the measured ratio of mass 127 to mass 254 is 1.0:1. This suggests that there is some atomic iodine desorbing from the surface, although most of the desorbing material is molecular iodine.

It was previously thought that desorption above 300 K produced only atomic iodine.

Heating the sample at 15 K/s did show some evidence of mass 254, although the amount observed is near the detection limit of our instrument. The results from three separate experiments were averaged to produce the desorption spectrum shown in figure 5.7. Also shown is the mass 127 signal (15 K/s).

The desorption spectrum shows that molecular iodine is desorbing from the surface in a similar fashion to the atomic iodine. Currently, there is no way to calibrate the amount of iodine that this desorption represents. However, it is possible to determine how much of the mass 127 signal is due to the dissociation of molecular iodine. The maximum intensity of the mass 254 signal (at 540 K) K is 0.16 pA. At the same temperature, the mass 127 ion current is 4.6 pA. If we assume that the cracking ratio is the same as that determined above

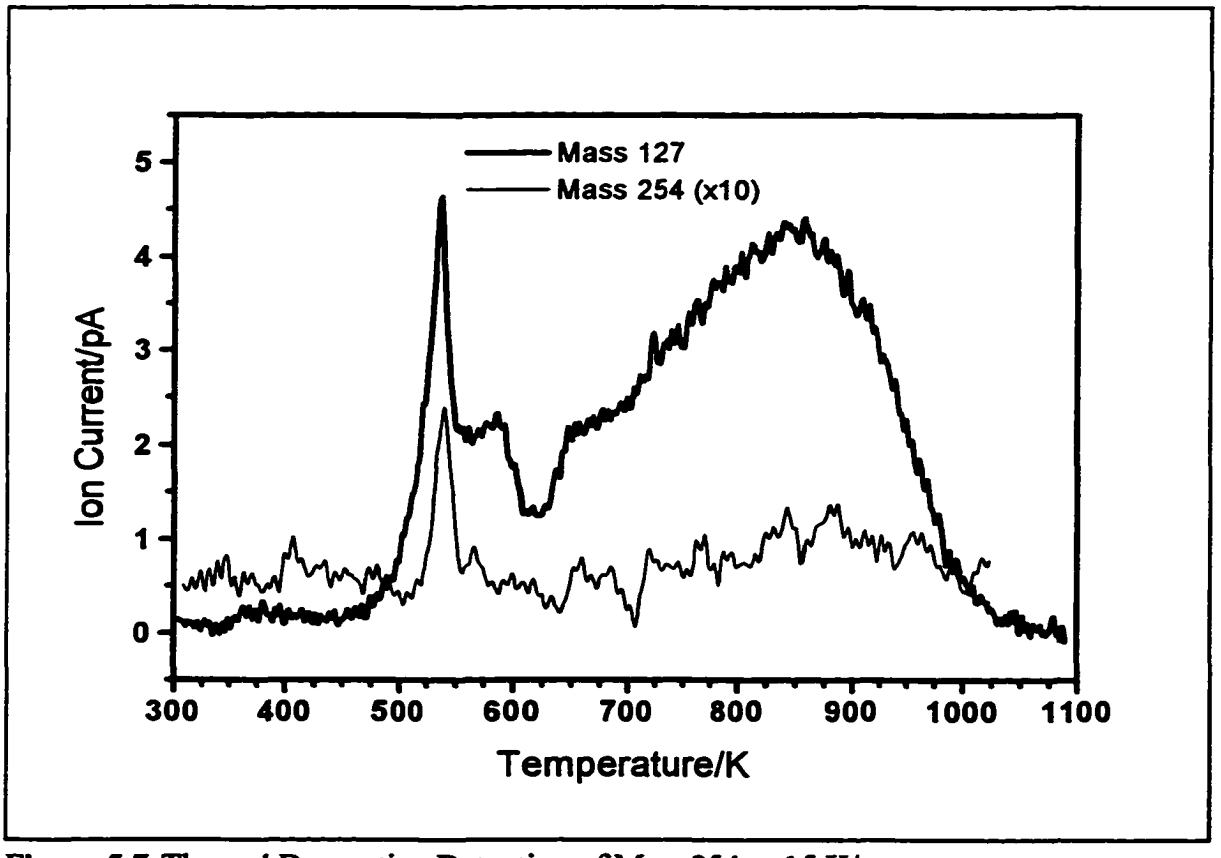

Figure 5.7-Thermal Desorption Detection of Mass 254 at 15 K/s

(127:254=0.84:1) then approximately 3% of the 127 mass signal (at 540 K) is due to the dissociation of molecular iodine.

Although the general shape of the desorption spectra of mass 254 and mass 127 is similar, the intensity of the broad mass 254 desorption peak at 840 K is lower. Comparison of the intensities of masses 127 and 254 at 840 K (4.2 pA and 0.6 pA respectively) shows that only 1% of the mass 127 signal is due to the dissociation of molecular iodine at this temperature.

5.3 Reversibility of Thermally-Induced Phase Transitions

Some thermally-induced phase transitions described here have been found to be reversible, while others are essentially irreversible. This has been explored by heating the sample to various temperatures while monitoring the LEED pattern. Once a phase transition has occurred, the sample is cooled and the LEED pattern is monitored for any changes.

The low temperature transitions (<250 K) are irreversible. Once an ordered structure has been formed on the surface, cooling to 150 K does not cause the LEED pattern to become diffuse. Cooling usually improves LEED patterns as the lower amount of thermal energy reduces the atomic motions of the adsorbate.

The transformation from the (3x3) phase to the $(\sqrt{7}x\sqrt{7})R19.1°$ phase proved to be almost irreversible. This is surprising given the small difference in coverage (0.016 ML) between the two structures. Once this phase transition begins (at 375 K), and a mixed LEED pattern is observed, the transition can be stopped by simply stopping the temperature ramp. Once the heating has stopped, no further LEED transformations occur. Cooling the mixed structure does not cause the $(\sqrt{7}x\sqrt{7})R19.1°$ pattern to disappear. Heating the sample to 425

K causes the entire surface to be converted to the ($\sqrt{7}$x$\sqrt{7}$)R19.1° structure. Cooling the sample to 300 K just after the (3x3) pattern has disappeared partially restores a blurry (3x3) pattern, with the sharp ($\sqrt{7}$x$\sqrt{7}$)R19.1° pattern being dominant. However, in most cases, the transformation to the ($\sqrt{7}$x$\sqrt{7}$)R19.1° structure is irreversible.

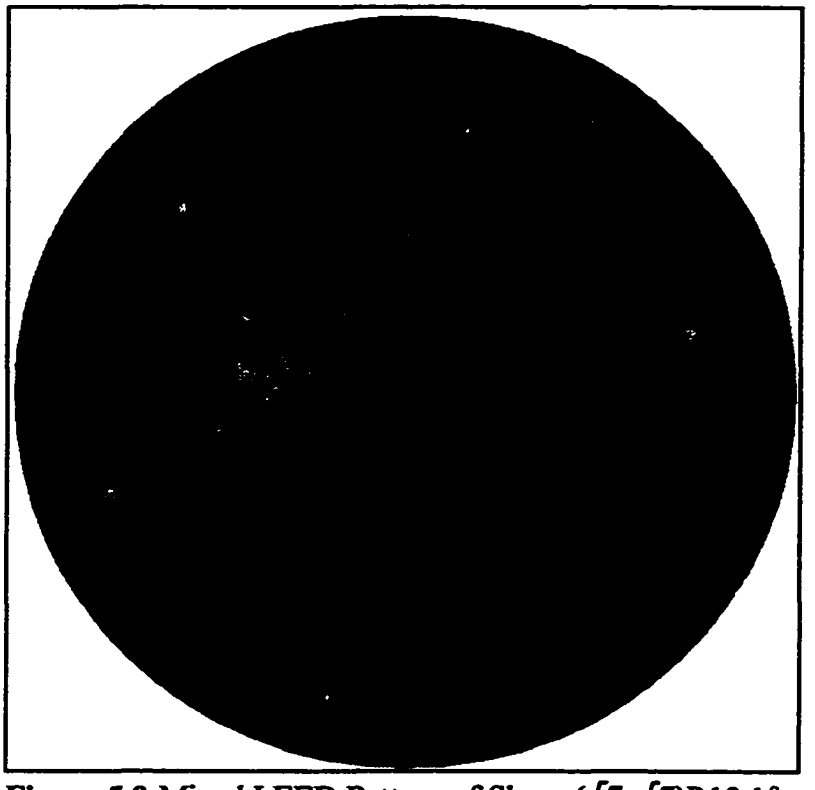

Figure 5.8-Mixed LEED Pattern of Sharp ($\sqrt{7}$x$\sqrt{7}$)R19.1° and Diffuse ($\sqrt{3}$x$\sqrt{3}$)R30°

Heating the sample to 530 K causes the ($\sqrt{7}$x$\sqrt{7}$)R19.1° LEED pattern to disappear leaving only a diffuse pattern with a diffuse ($\sqrt{3}$x$\sqrt{3}$)R30° sometimes visible. Once this phase transition begins, it does not stop until all of the ($\sqrt{7}$x$\sqrt{7}$)R19.1° structure is gone (even at constant temperature). If the sample is cooled, both the ($\sqrt{7}$x$\sqrt{7}$)R19.1° and ($\sqrt{3}$x$\sqrt{3}$)R30° patterns become visible, although the ($\sqrt{3}$x$\sqrt{3}$)R30° is poorly defined (shown in figure 5.8). Interestingly, if the sample is heated back to 480 K, the ($\sqrt{3}$x$\sqrt{3}$)R30° pattern disappears, leaving only the ($\sqrt{7}$x$\sqrt{7}$)R19.1° pattern visible.

Heating the sample to 600 K forms a sharp ($\sqrt{3}$x$\sqrt{3}$)R30° LEED pattern. Cooling the sample from this temperature causes a mixed ($\sqrt{7}$x$\sqrt{7}$)R19.1° and ($\sqrt{3}$x$\sqrt{3}$)R30° pattern to develop. Once again, the ($\sqrt{3}$x$\sqrt{3}$)R30° pattern is slightly diffuse.

Heating the sample (from saturation coverage) to 700 K caused the ($\sqrt{3}$x$\sqrt{3}$)R30° pattern to disappear as the LEED pattern became diffuse. Cooling from this temperature restores the ($\sqrt{3}$x$\sqrt{3}$)R30° pattern. Heating to 750 K and cooling does not restore the ($\sqrt{3}$x$\sqrt{3}$)R30° pattern. At this point, it seems that too much iodine has desorbed from the surface to reform an ordered structure. Based on the results of integrated desorption spectra (see section 5.5), this corresponds to a coverage of 0.2.

5.4 Work Function Changes During Desorption

The work function changes during desorption provide another means of following the desorption process. As previously mentioned, the threefold sites and atop sites appear to have different contributions to the work function. However, no change in work function is observed when the iodine changes from the (3x3) structure to the ($\sqrt{7}$x$\sqrt{7}$)R19.1° structure. It is difficult to assess what would be expected during this transition if the work function changes are site dependent. The (3x3) structure is a mixture of two surface structures (the symmetric and asymmetric forms) with atop, threefold, bridged and asymmetric sites being populated. We will therefore concentrate on the work function changes associated with the ($\sqrt{3}$x$\sqrt{3}$)R30° and ($\sqrt{7}$x$\sqrt{7}$)R19.1° structures. The changes in work function at low temperature will also be investigated as one of the desorption peaks at low temperature has a significant work function change associated with it.

Starting from ambient temperature, thermally desorbing the iodine at low coverages

(<0.25) produces a change in work function that is essentially the reverse of the change observed during adsorption. The work function changes for some low coverage desorptions and a desorption from saturation coverage is shown in figure 5.9. As previously mentioned, desorption from a saturated surface produces a decrease in the work function at 530 K (where the $(\sqrt{7}x\sqrt{7})R19.1°$ structure transforms to the $(\sqrt{3}x\sqrt{3})R30°$ structure). At higher temperatures, the work function increases and returns to its bare surface value after all the iodine has desorbed.

Also shown is a desorption from the point where the work function reached its minimum during dosing. At 540 K, where the atop iodine atoms are expected to desorb, the work function increases. It seems that the atop sites can have both a positive and negative effect on the work function. LEED analysis after adsorption showed that at the work

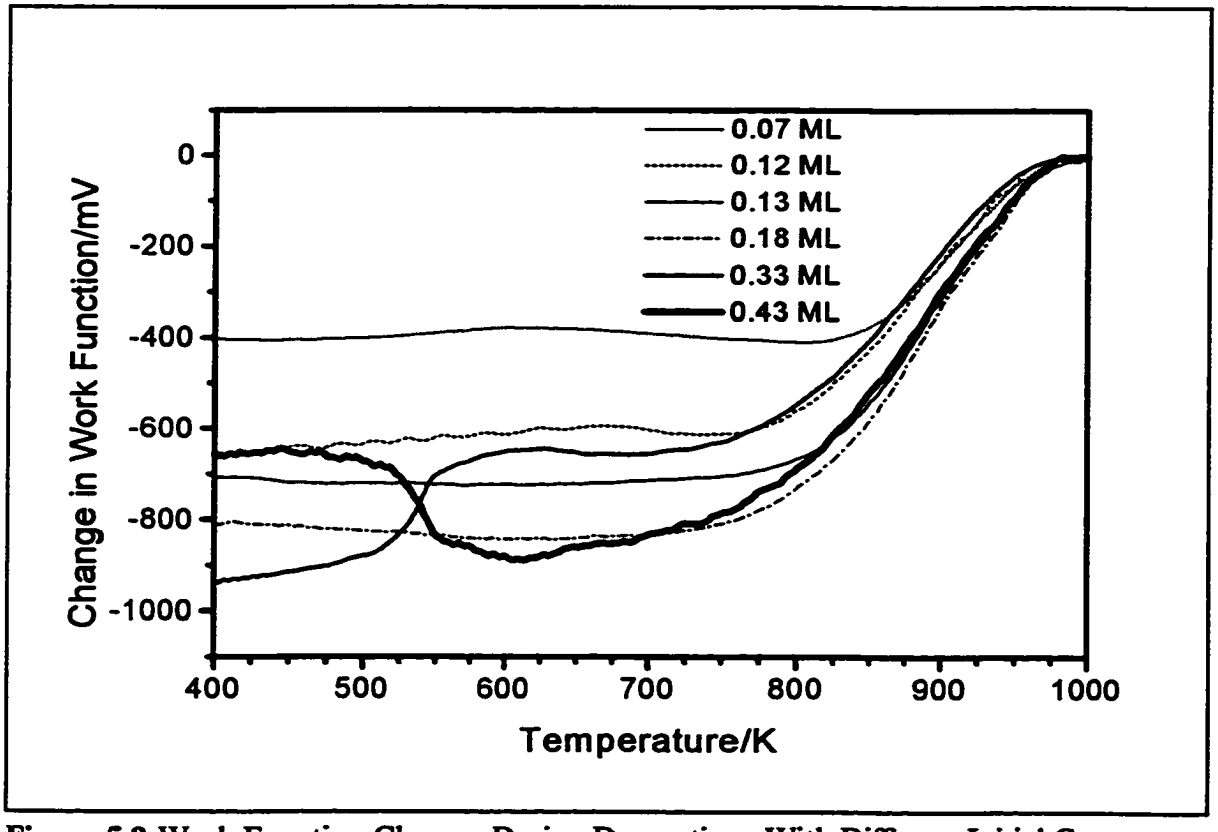

Figure 5.9-Work Function Changes During Desorptions With Different Initial Coverages

function minimum, there is some ($\sqrt{7}$x$\sqrt{7}$)R19.1° structure present. The desorption of mass 127 (shown in figure 5.10) shows that there is no significant desorption at 530 K where this unusual increase in work function occurs. Instead, there is continual increase in the desorption rate up to 800 K. This result shows that the change in work function is not due to the occupation of specific sites but is dependent on the coverage.

As mention before, heating the sample from saturation coverage causes the work function to decrease at 530 K. After this desorption, the coverage is approximately 1/3 as LEED analysis shows only the presence of a well defined ($\sqrt{3}$x$\sqrt{3}$)R30° structure. The work function at this point has almost gone back to the minimum value (~1000 mV) again showing

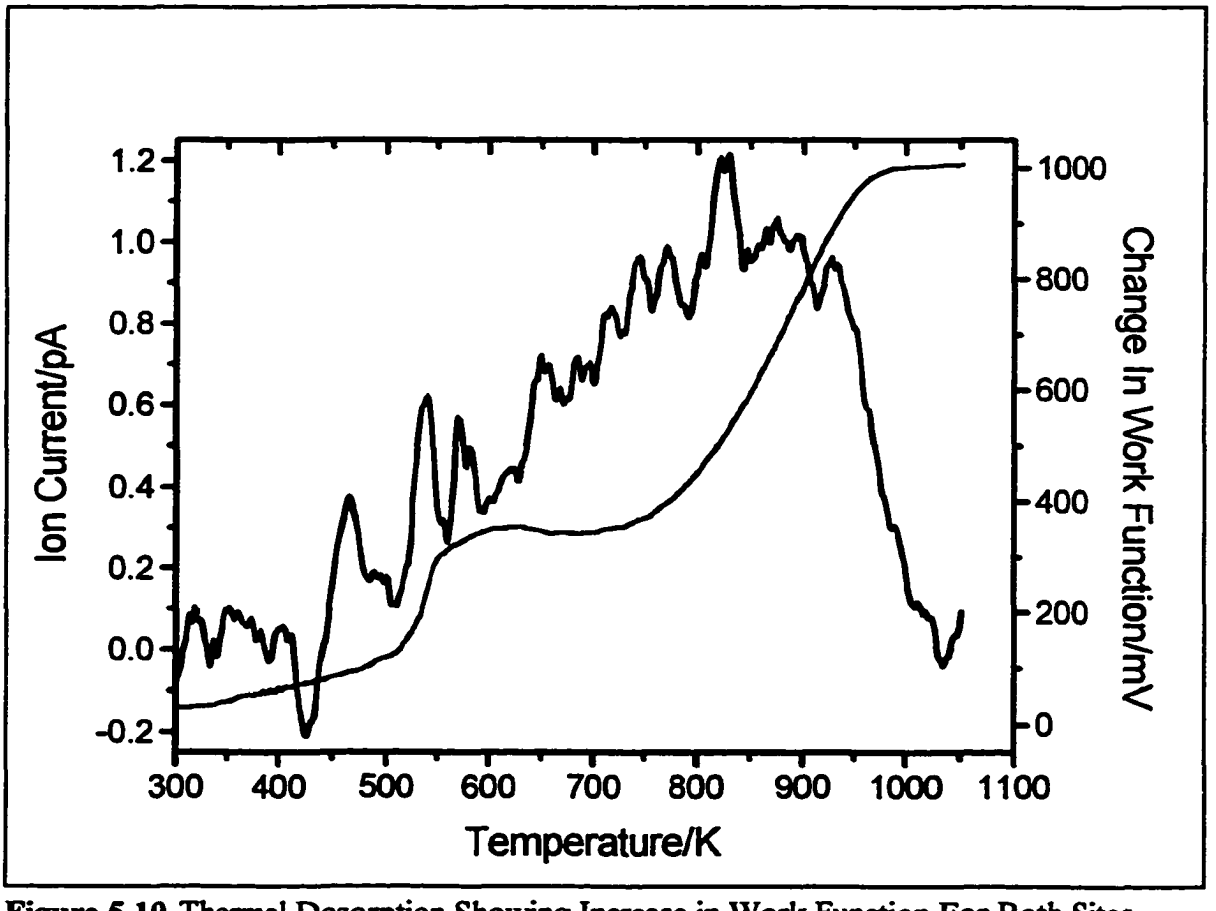

Figure 5.10-Thermal Desorption Showing Increase in Work Function For Both Sites

that the work function depends more on the coverage than it does on the specific site. It may be that different sites make a slightly different contribution per occupied site but clearly the sign of the contribution for each site is determined by the coverage.

A coverage-dependent work function, as opposed to a site-dependent work function, can be explained by the mutual depolarization of adjacent dipoles. Many systems exhibit this behaviour [5.2] and this has been the subject of several studies [5.3]. Bringing the dipoles closer together is expected to increase the amount of depolarization. This aspect of the work function studies will be addressed in Chapter 6.

The coverage-dependent work function helps to explain why no work function change is observed during the (3x3)→($\sqrt{7}$x$\sqrt{7}$)R19.1° transformation. As the difference incoverage

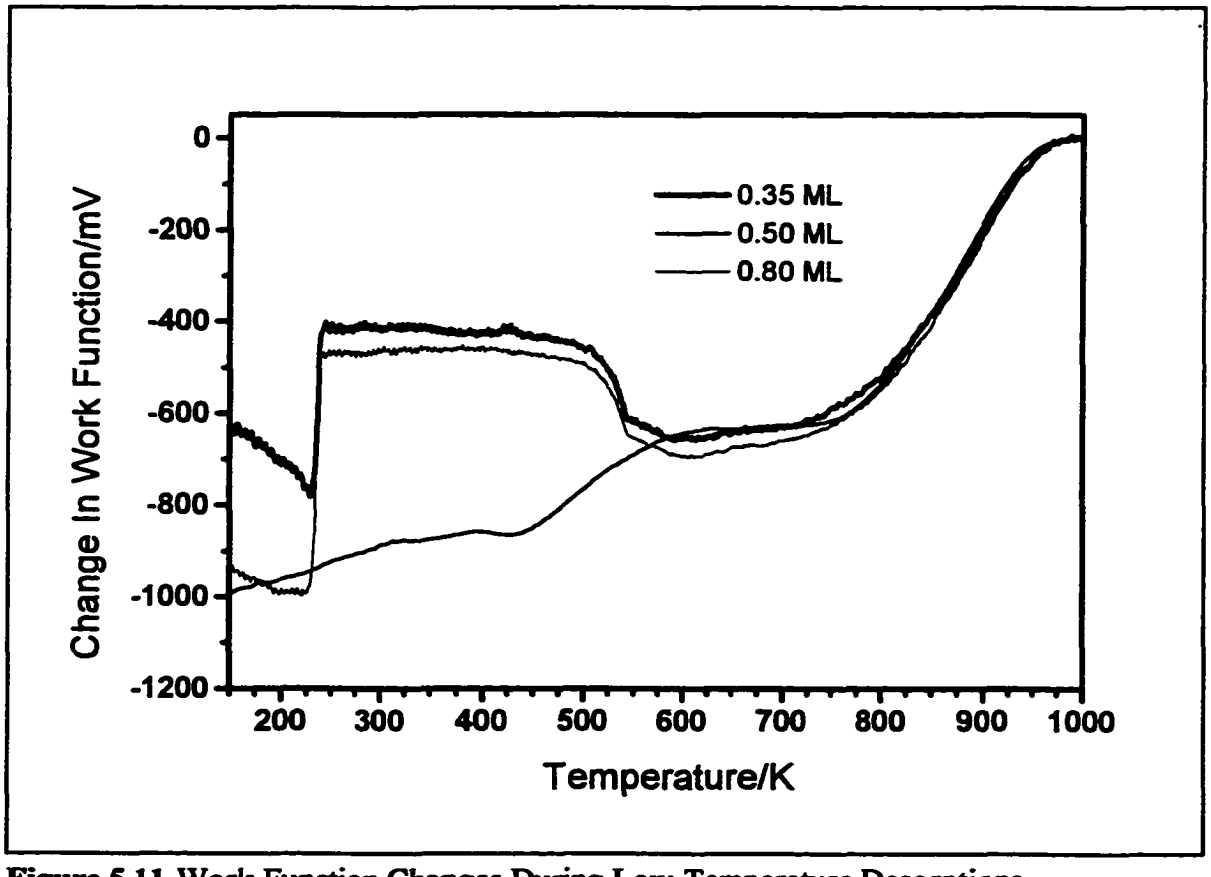

Figure 5.11-Work Function Changes During Low-Temperature Desorptions

is very small (0.016 ML), no change in work function is expected.

Dosing the sample at 150 K leads to the formation of molecular multilayers. Desorption of these multilayers showed two distinct binding states. The state associated with the desorption at 215 K does not produce a significant change in the work function. The state at 235 K , however, has a large work function change associated with it. As shown in figures 5.11 and 5.12 the work function associated with this desorption can be positive or negative, depending on the initial coverage. However, increasing the coverage by extended dosing at 150 K has an unusual effect on the high temperature desorptions (see figure 5.12). The amount of iodine on the surface in these cases is quite large and the work function changes at higher temperatures are not consistent. At present, we have no explanation for this behaviour.

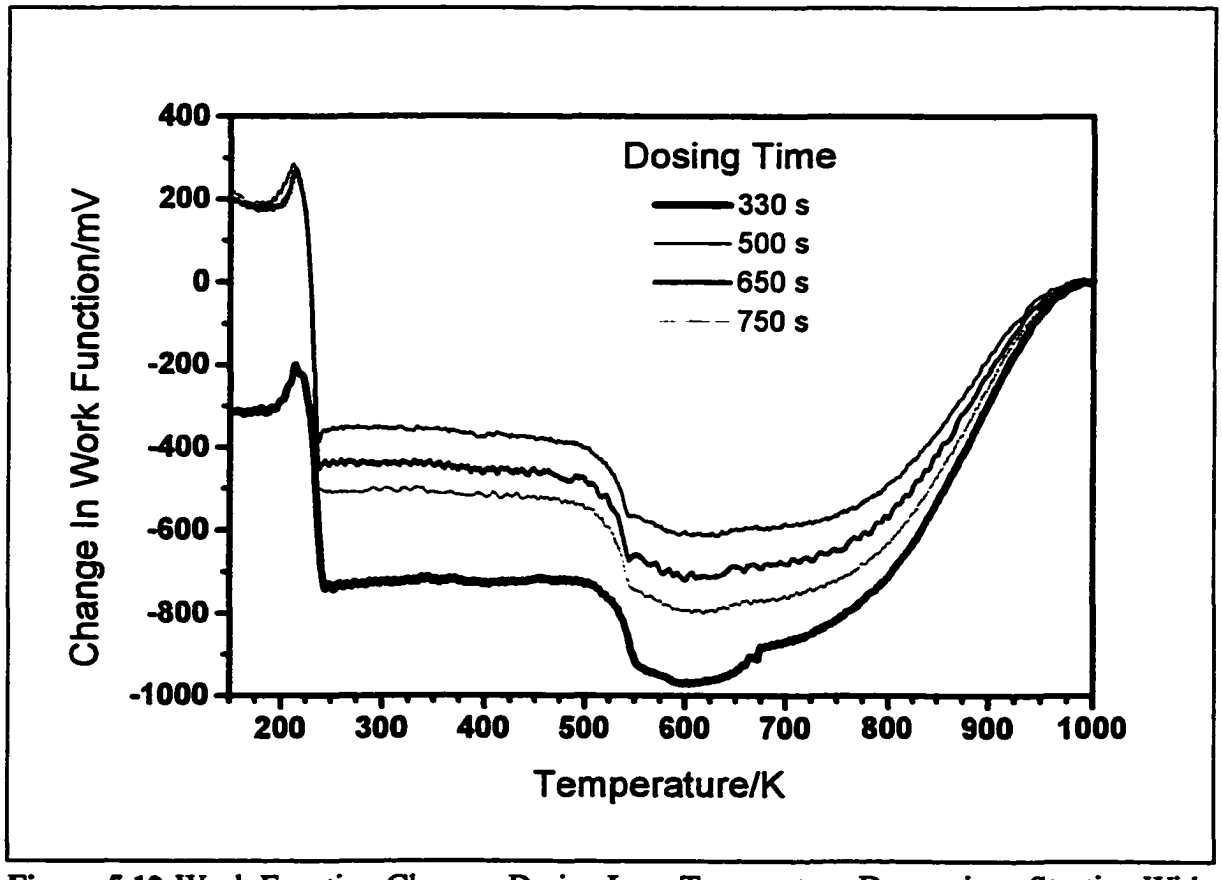

Figure 5.12-Work Function Changes During Low-Temperature Desorptions Starting With Multilayer

5.5 High-Temperature Desorption Kinetics

The desorption of atomic iodine at temperatures above 300 K has been studied extensively to obtain a clear picture of how iodine interacts with platinum. The kinetics of the desorptions also provide an insight into the interactions between adsorbates on the surface. The structural transformations during adsorption and desorption provide a solid foundation to construct a kinetic model.

The experimentally measurable quantity is the increase in partial pressure of the desorbing species. In situations where the mass spectrometer has continuous pumping (such as the system used here), the increase in partial pressure is equal to the rate of material desorbing from the surface times a proportionality constant (K). The following equation describes the change in surface concentration (Γ) with time for a reaction of order n.

$$K(P-P_0) = -\frac{d\Gamma}{dt} = k_i\theta^n = \nu_n(\theta)\theta^n \exp(-E_d(\theta)/RT) \qquad (5.1)$$

In this equation, E_d is the activation energy for desorption that may or may not be coverage dependent. ν_n is the frequency factor (or pre-exponential factor) that may also have a coverage dependence. Γ and θ are simply related as θ=1 correpsonds to 1.5×10^{15} atoms/cm^2 for Γ. There are several ways to determine these parameters and their coverage dependence. Most of the commonly used methods [5.4] rely on assumptions and simplifications of this equation. Those methods will not be used here. Three separate experimental approaches will be described to determine these parameters with no unjustified assumptions being made.

The most direct method is to heat the sample to a specific temperature where desorption occurs. Once at that temperature, the heating is adjusted to maintain that

temperature. During this isothermal desorption, the rate will steadily decrease until all of the adsorbate has desorbed. The rate constant (k_i) can be extracted directly from such a decay curve using the logarithmic form of equation 5.1. Measuring this rate constant at different temperatures allows one to construct an Arrhenius plot according to the equation:

$$\ln(k_i) = \ln(\nu_n(\theta)) - E_d(\theta)/RT \qquad (5.2)$$

A graph of ln(rate) vs. $1/T$ should give a straight line with a slope of $-E_d/R$ and an intercept of ln(ν). If the frequency factor or the desorption energy is coverage dependent, the analysis becomes more complex as the activation energy will change during the isothermal desorption.

There are two other experimental procedures that are better suited for extracting coverage-dependent rate parameters and can be used if a coverage dependence is observed. These procedures rely on extracting temperature and rate information at a specific coverage. The rate of desorption at a particular coverage will depend on how the system came to be at that coverage. For example, heating the sample at different heating rates will often change the position and size of the peaks in thermal desorption spectra. Changing the initial coverage will also cause the desorption rates to vary.

Extracting the rate and temperature where the system passes through a particular coverage allows one to obtain the desorption energy by using the following logarithmic form of equation 5.1:

$$\ln K + \ln(P - P_0) = \ln\left(\frac{-d\Gamma}{dt}\right) = \ln(\nu_n(\theta)) + n\ln(\theta) - E_d(\theta)/RT \qquad (5.3)$$

Therefore, a graph of ln $(P-P_0)$ vs. $1/T$ will have a slope of $-E_d(\theta)/R$. The y-intercept will be

equal to $(\ln(\nu_n(\theta))+n\ln(\theta)-\ln K)$. If this analysis is done at a series of coverages, the coverage dependence of the desorption energy can be measured directly. Furthermore, if a graph of the y-intercepts (from plotting equation 5.3) vs. $\ln(\theta)$ is linear, the frequency factor must be coverage independent and the slope of such a graph is equal to n (the order of the reaction).

5.5.1 Coverage-Dependent Desorption

The coverage dependence of the desorption spectrum allows one to easily make some preliminary statements about the desorption kinetics and what type of analysis should be done. The desorption spectra for a series of different initial coverages are shown in figure 5.13. The peak at 530 K appears to be zeroth order as all the desorptions at different coverages have a common leading edge [5.5]. This is typical of a phase transition [5.6]. In addition, the position of the peak increases with coverage, although only slightly. The broad peak centred around 800 K appears to be second order as the peak position moves to lower temperature with increasing coverage [5.7, 5.8]. However, the common trailing edge is not a feature of second order kinetics. Also, it is difficult to construct a valid second order mechanism for the desorption of atomic iodine. If the desorption produced molecular iodine, one could easily imagine a rate law that would be second order. As shown in section 5.2, less than three percent of the atomic iodine detected comes from the dissociation of molecular iodine. The other possibility is that the broad desorption at 800 K is actually first order but has a coverage-dependent activation energy for desorption.

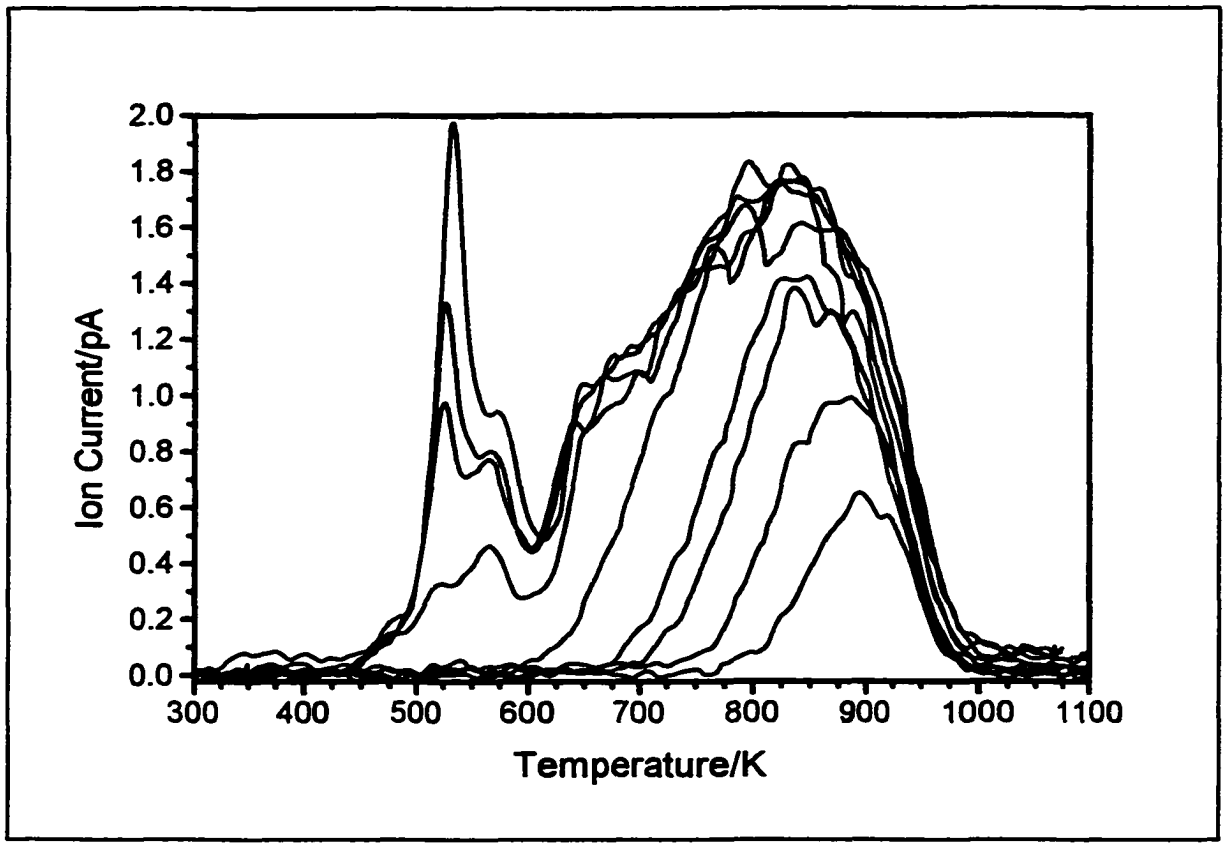

Figure 5.13-Iodine Desorption From Different Initial Coverage (6 K/s). Coverages equal 0.06, 0.11, 0.15, 0.18, 0.28, 0.36, 0.38, 0.39, 0.43 ML.

If the thermal desorption spectra in figure 5.13 are integrated and we assume that the highest coverage is 0.43, we can construct a graph of coverage as a function of temperature. This is shown in figure 5.14. Some desorption lines for different coverages appear to overlap at some points. Analysis of the desorption rates at constant coverage was unsuccessful because of these overlaps. However, measuring the coverage dependence of the desorption spectra did provide a qualitative picture of the desorption kinetics.

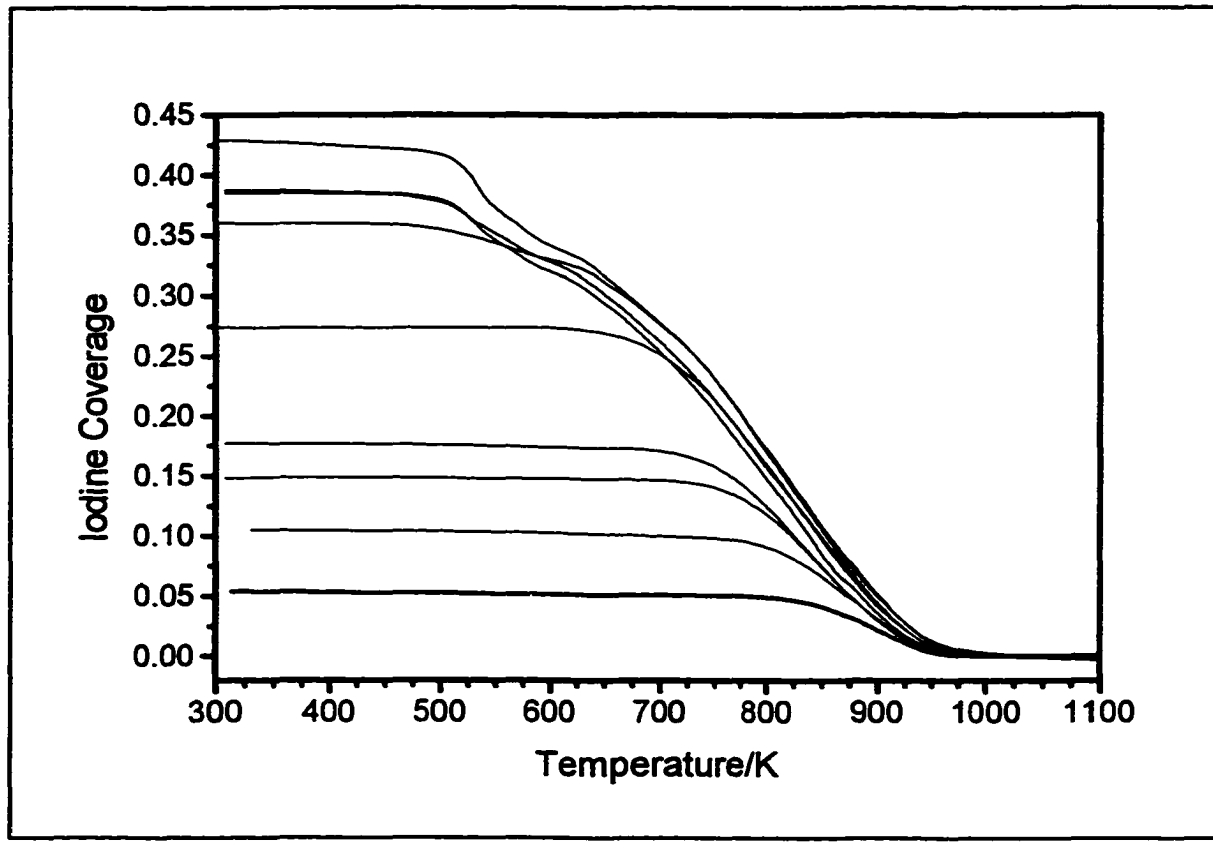

Figure 5.14-Iodine Coverage as a Function of Temperature During Desorption (6 K/s). Coverages as in Figure 5.13.

5.5.2 Kinetic Analysis at Different Heating Rates

Measuring the desorption spectra at different heating rates, starting with the same initial coverage, is another way of extracting kinetic data. Starting from the saturation coverage, the heating rate was varied from 3 K/s to 15 K/s, as shown in figure 5.15. These spectra were integrated and converted to coverage profiles. At 0.01 increments in coverage from 0.01 to 0.43, the rate and temperature corresponding to those coverages were determined at each heating rate. This allowed a series of graphs to be constructed for the determination of the desorption energy (using equation 5.3). A sample of those graphs is shown in figure 5.16. The different slopes indicate a different desorption energy.

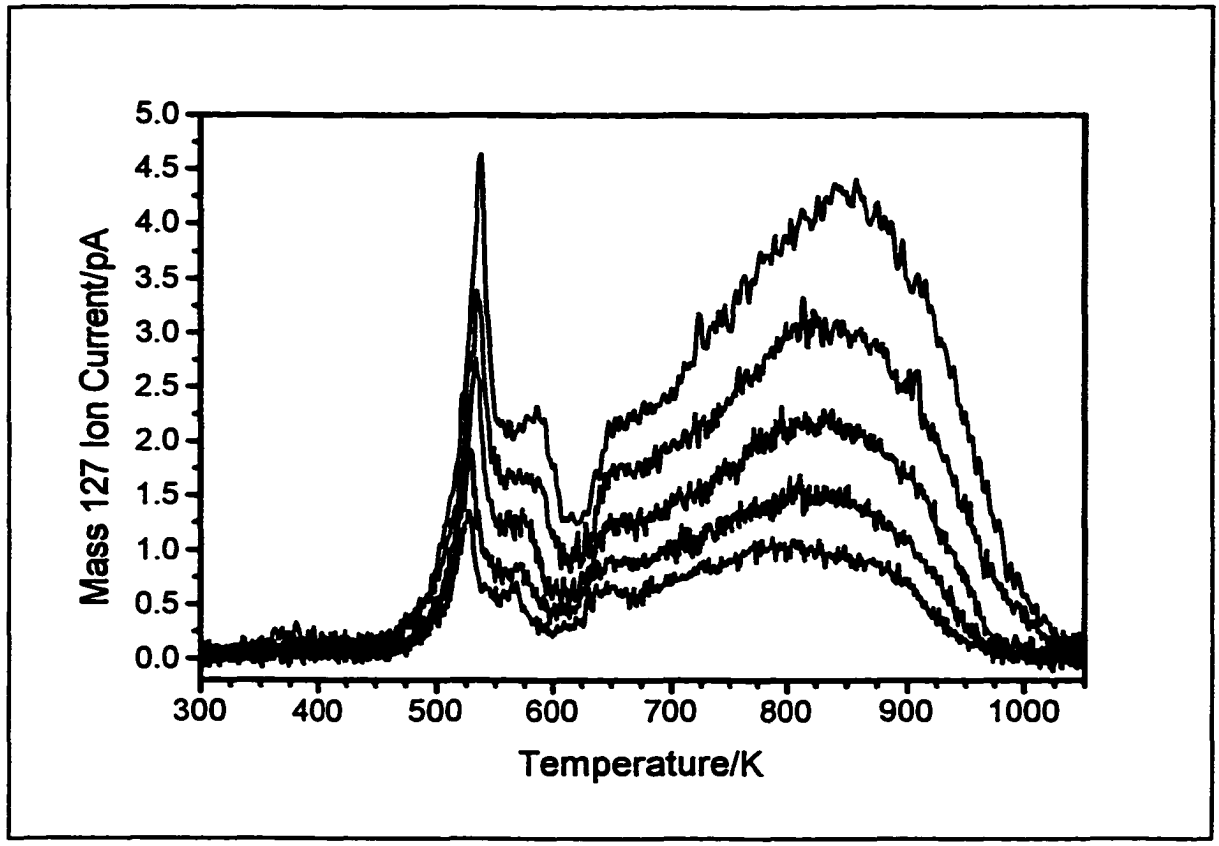

Figure 5.15-Variation of Desorption Spectrum With Heating Rate (3, 5, 7, 10, 15 K/s)

The change in the activation energy as a function of coverage is shown in figure 5.17. The y-intercepts are also shown. The error bars are taken from the calculated standard deviation of the linear graphs in figure 5.16. The activation energy steadily decreases from 253 kJ/mole (±4 kJ/mole) at zero coverage to 200 kJ/mole at a coverage of 0.3 ML. The change in activation energy with coverage is therefore -180 $kJ \cdot mol^{-1}ML^{-1}$ (±20 $kJ \cdot mol^{-1}ML^{-1}$). At a coverage of 0.33 ML, the activation energy would be expected to be 194 kJ/mole, having decreased by 59 kJ/mole. Each iodine on the surface will have three nearest neighbours per unit cell and so the interaction energy between iodine atoms can be estimated to be 20 kJ/mole. This interaction is repulsive, as the activation energy decreases with increasing coverage.

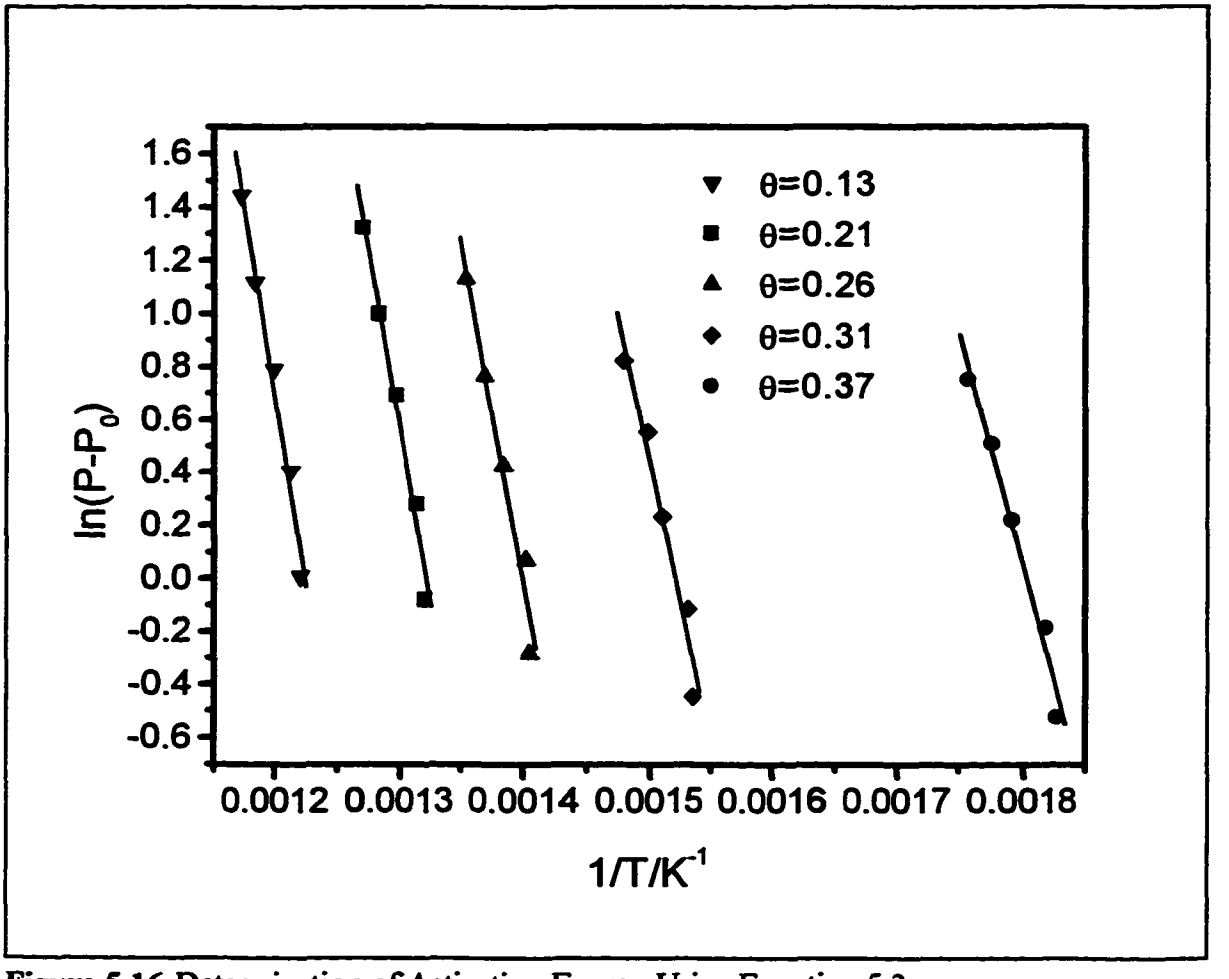

Figure 5.16-Determination of Activation Energy Using Equation 5.3

At higher coverage, the results begin to fluctuate. This is because different sweep rates are probing different desorption processes and the plots of equation 5.3 are not linear in this coverage range. However, at a coverage of 0.37, the desorption energy becomes stable again. The value for the activation energy at this point is 146 kJ/mole (±10 kJ/mole). This corresponds to the desorption of iodine from the atop sites. The desorption spectra at different coverages (figure 5.13) suggested that this desorption process is zeroth order and that the activation energy is not coverage dependent.

The frequency factors can be extracted from the y-intercept data in figure 5.17. If we assume that the frequency factor is independent of coverage, the y-intercept from plotting

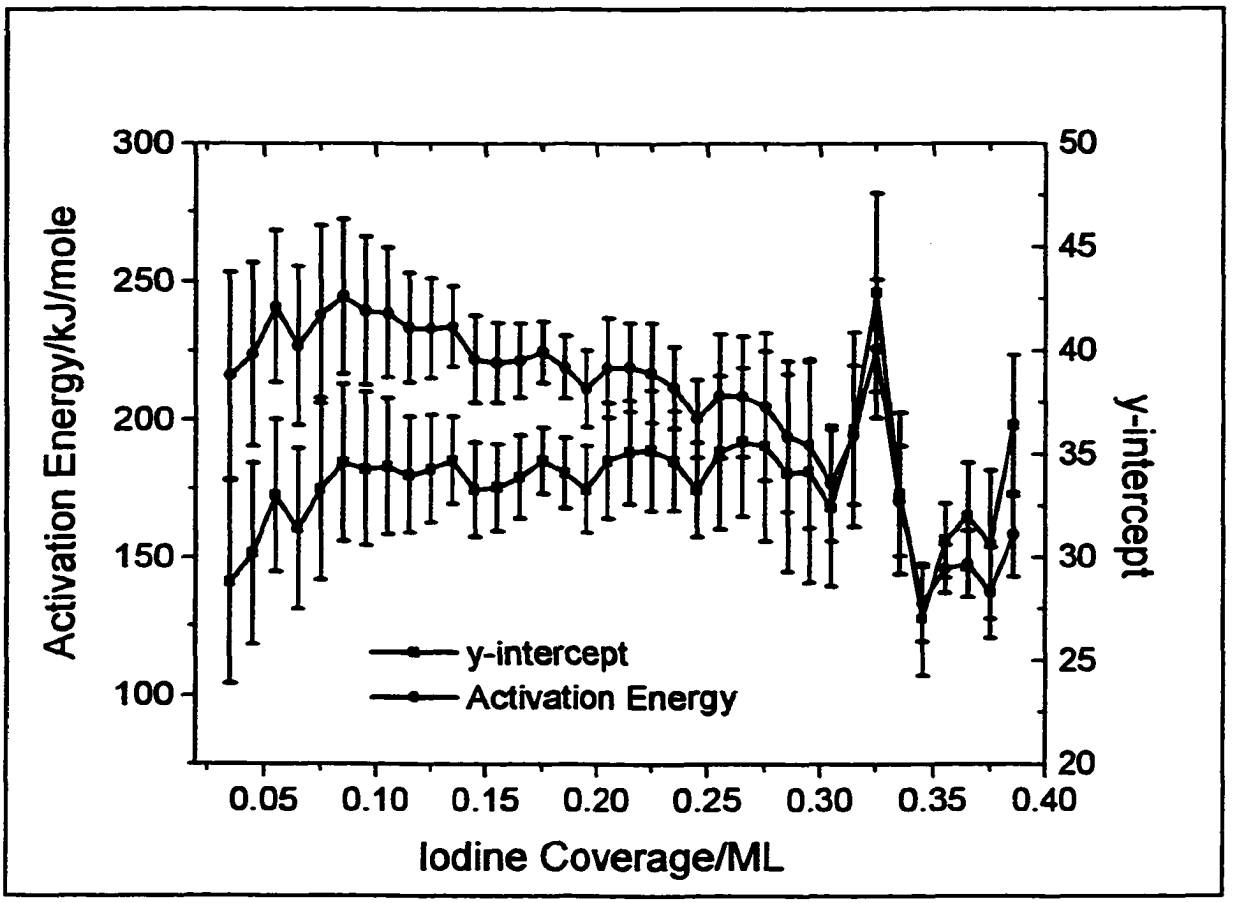

Figure 5.17-Determination of Coverage Dependence of Kinetic Parameters

equation 5.3 is equal to $\ln(v)+n\ln(\theta)-\ln(K)$. The proportionality constant K converts the measured ion current from the mass spectrometer to a desorption rate of iodine from the surface.

The value of the constant K is determined by integrating a thermal desorption spectrum and converting to surface concentration (with units of atoms/cm^2). Differentiating the coverage with respect to time gives the desorption rate from the surface (see figure 5.18). This can be compared with the ion current in figure 5.15 (5 K/s) to calculate K. Using the maximum desorption rate at 80 s, the value of K is calculated to be (1.4×10^{13} atoms cm^{-2} s^{-1}/1.9 pA) $=7.4\times10^{12}$ atoms cm^{-2} s^{-1} pA^{-1}.

For the desorption of the atop sites, the y-intercept from figure 5.17 is 31 (±2). If the

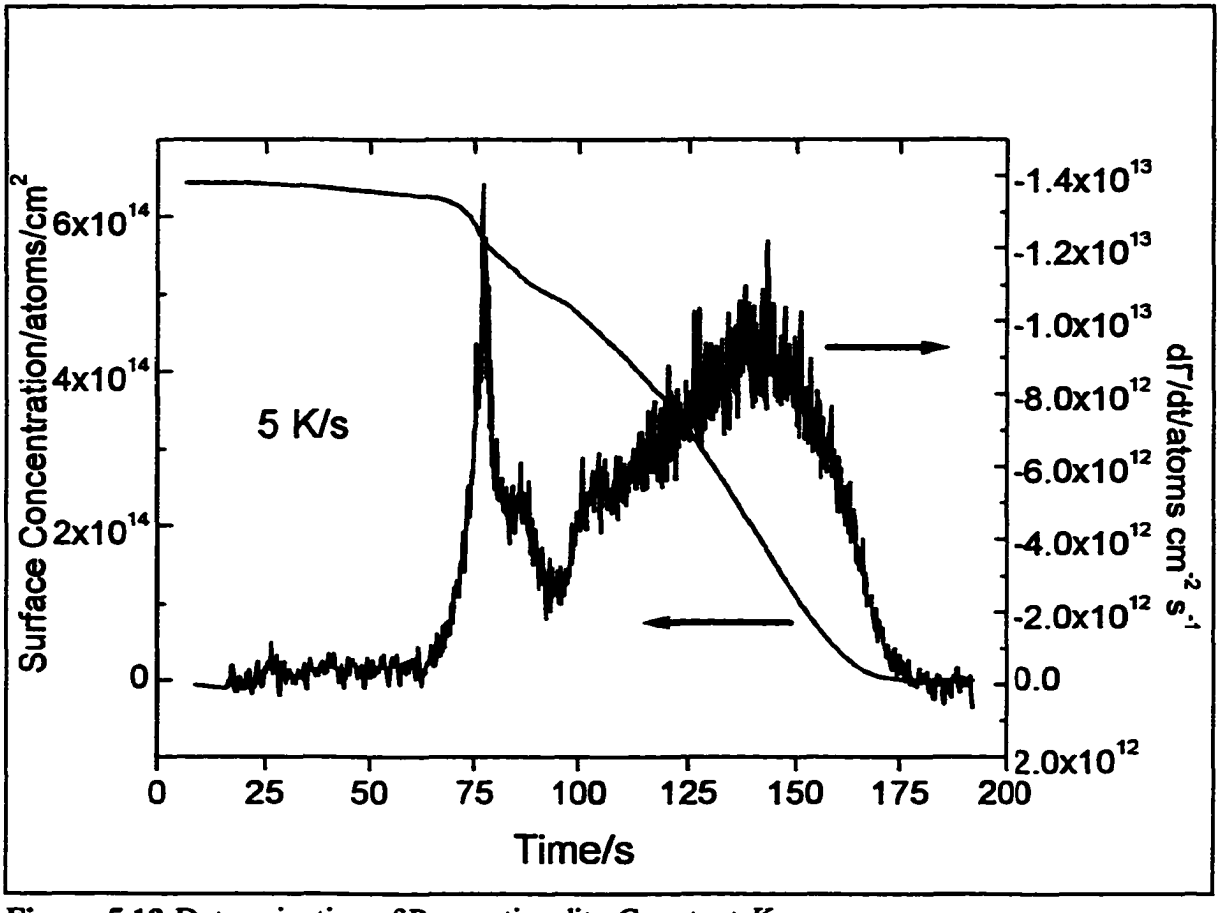

Figure 5.18-Determination of Proportionality Constant *K*

desorption process is assumed to be zeroth order, the y-intercept equals ln(v)-ln(*K*) and v is equal to 2.1×10^{26} atoms cm^{-2} s^{-1}.

The frequency factor for the desorption from the threefold sites can be determined by plotting the y-intercept against ln(θ) as shown in figure 5.19. The slope of this line is the reaction order *n*, and the y-intercept is ln(v)-ln(K). The y-intercept of 2.4 gives a value of the frequency factor to be 8.2×10^{13} s^{-1} and the slope yields a reaction order of 1.0 (±0.4). Given the large error in the slope, the order of the reaction may not be exactly unity.

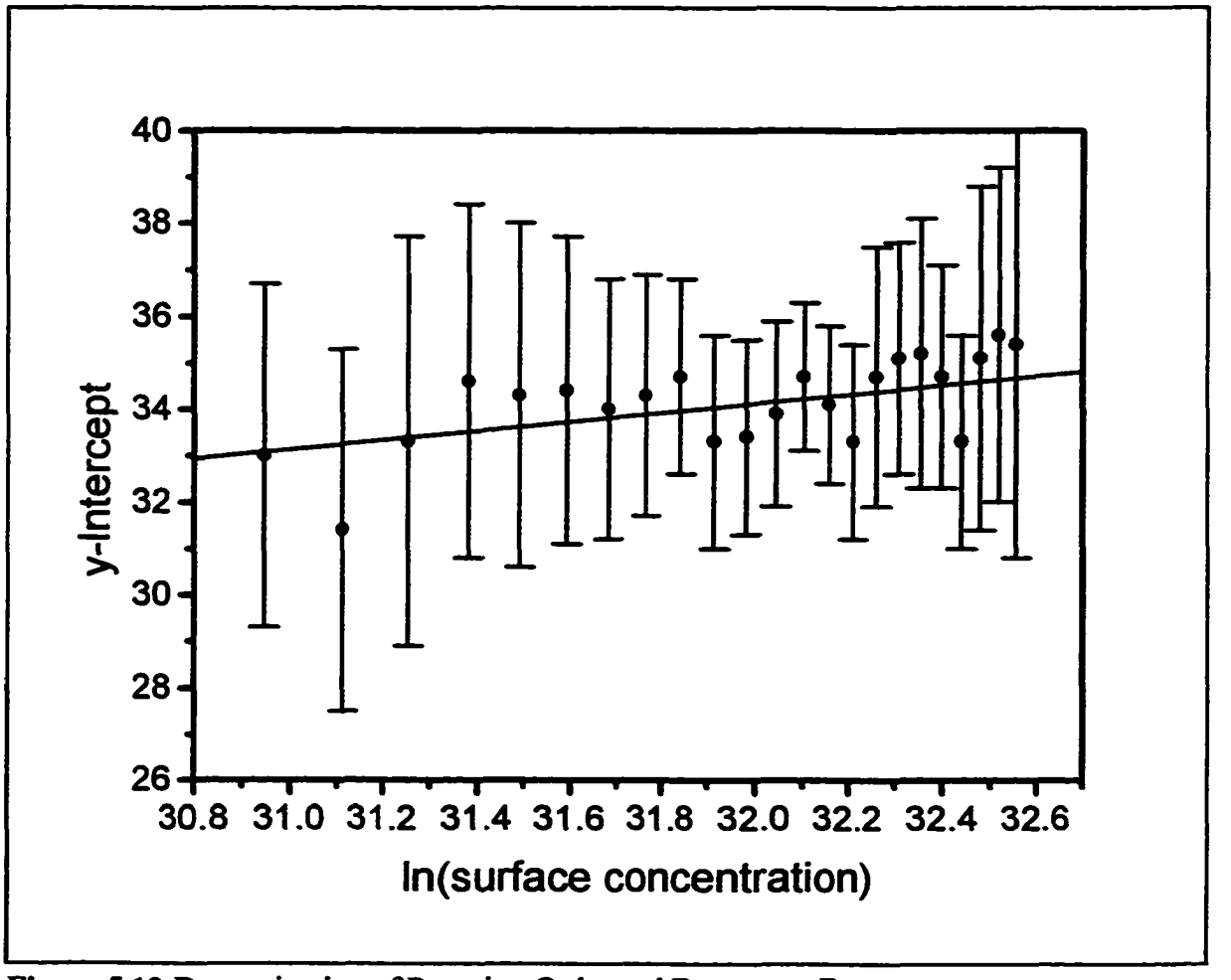

Figure 5.19-Determination of Reaction Order and Frequency Factor

5.5.3 Isothermal Desorptions

Isothermal desorptions also allow the calculation of the desorption activation energy and the frequency factor. This was done by starting from saturation coverage at 300 K and heating at 5 K/s. Attempts were made to probe all four of the desorption processes observed by TDS but only the results concerning the desorption at 530 K are meaningful. Probing the two small TDS features between 560 K and 700 K was made difficult by the low intensity of the desorption peaks and overlap with the larger desorption peaks.

The desorption of iodine from the threefold sites is coverage dependent. During the

isothermal desorption, the coverage is changing and therefore the activation energy is changing. Calculation of the coverage is difficult due to the high background present in the desorption spectra that makes integration of the desorptions inaccurate.

Efforts were concentrated on determining the rate constants for the atop desorption process. The isothermal data on the large desorption peak at 530 K is shown in figure 5.20. The temperature stability during the desorption is ±0.5 K. There is a constant increase in the background of the mass spectrometer signal that must be accounted for in the fitting procedure. All isothermal desorptions were fit to the following nonlinear equation:

$$y = y0 + b\,t + A\exp(-(t-t0)k) \qquad (5.4)$$

The mass intensity is y and the time (in seconds) is t. $y0$ and $t0$ are offsets values for the data. The value of b determines the slope of the linear background subtracted from the data while A is a constant. The rate constant k was determined by using a nonlinear least-squares curve fitting routine. The only parameter held constant during the curve fitting procedure was $t0$. The data was not processed in any way before the fitting procedure was used. After the fitting was complete, the quality of the fit was checked by subtracting equation 5.5 from the data and plotting the resulting residual data (lower traces in figure 5.20). This was always a straight line with a slope of zero and an average value of zero. Extracting the activation energy and frequency factor is done by plotting $\ln(k)$ vs. $1/T$, as shown in figure 5.21. The activation energy is 146 kJ/mole (±6 kJ/mole) and, assuming zero-order kinetics, the frequency factor is 4×10^{26} atoms cm^{-2} s^{-1} ($\pm2\times10^{26}$ atoms cm^{-2} s^{-1}).

The activation energy is in complete agreement with that obtained by varying the heating rate. The frequency factor calculated here is higher than that calculated from different

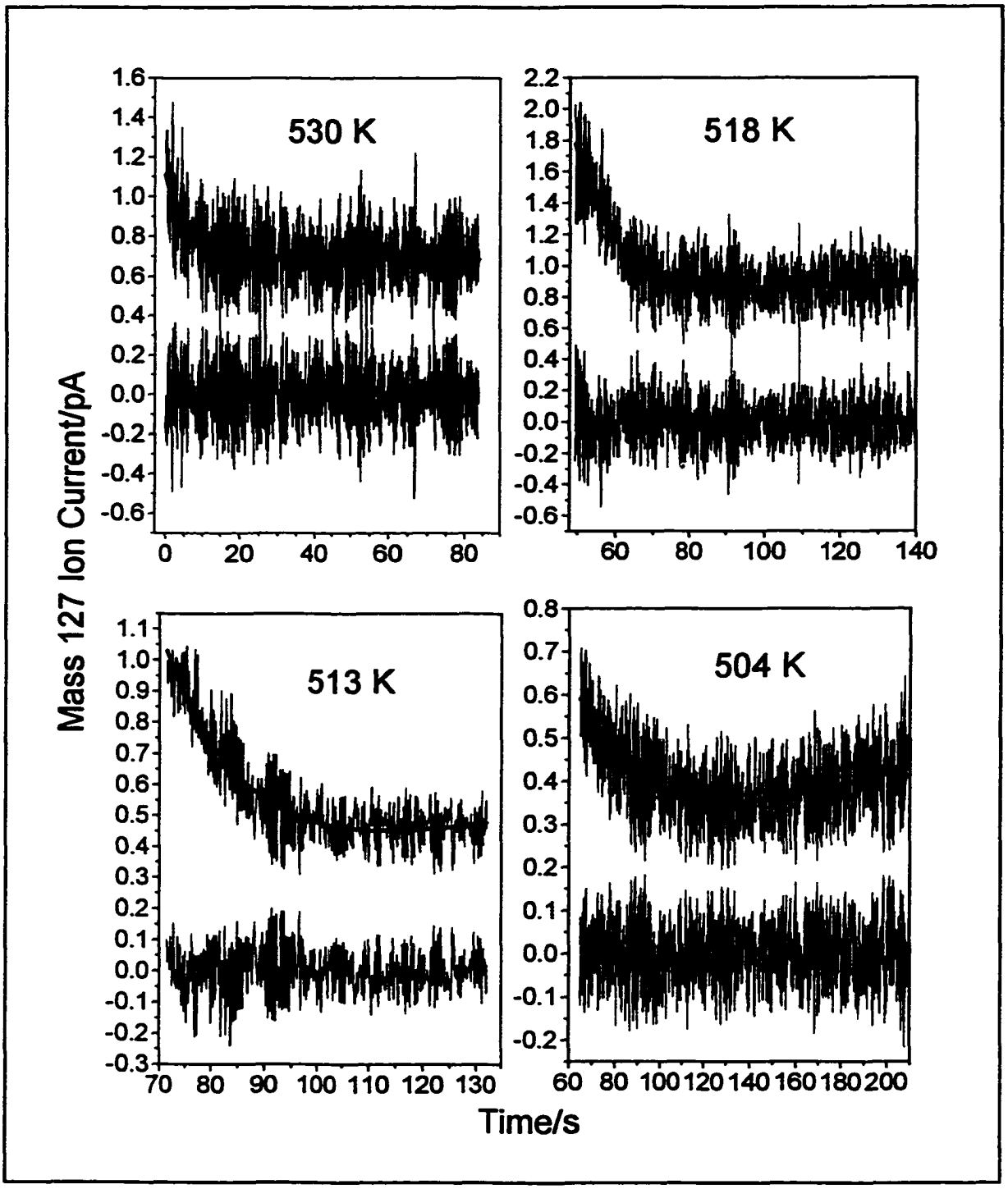

Figure 5.20-Isothermal Desorption of Atop Iodine Atoms With Residuals From Non-Linear Curve Fitting

heating rates but is within the measured error.

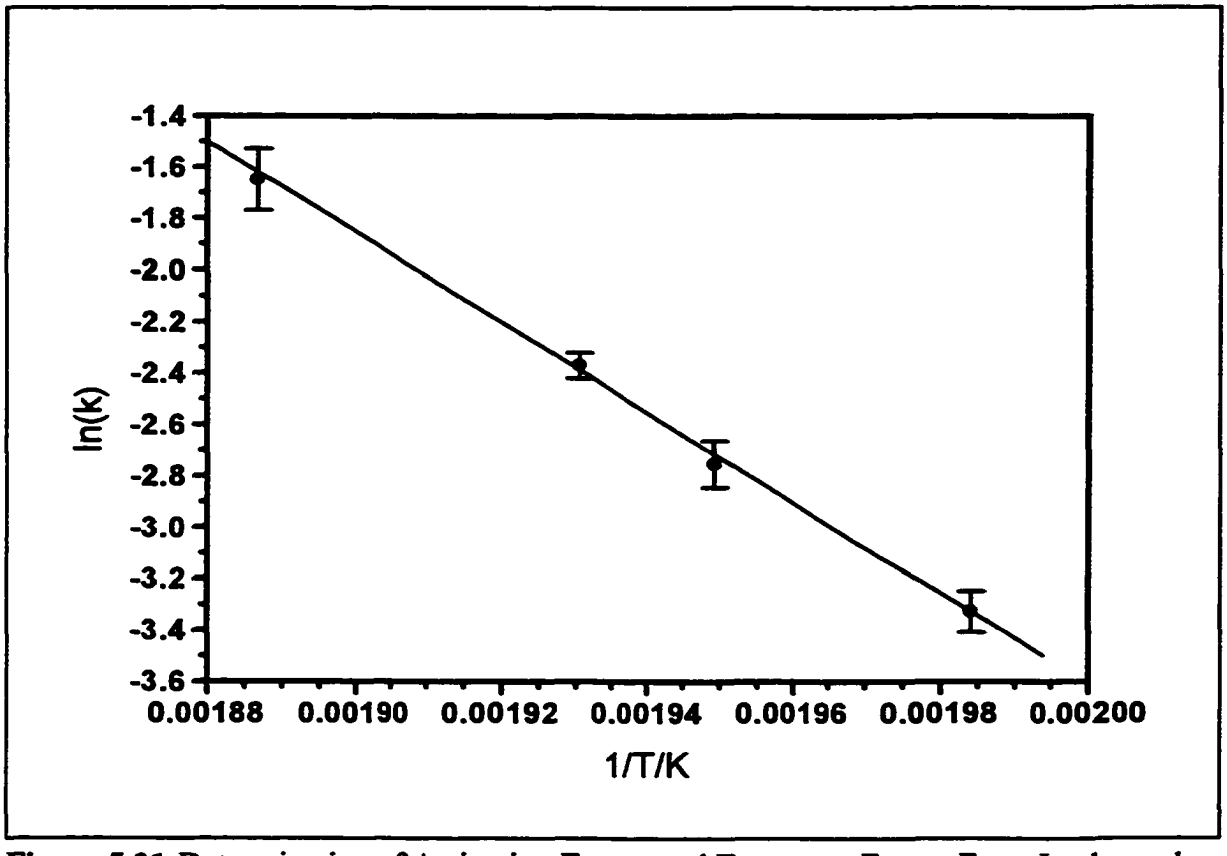

Figure 5.21-Determination of Activation Energy and Frequency Factor From Isothermal Desorptions of Atop Iodine Atoms

The desorption of molecular and atomic iodine at low temperatures was also studied isothermally. The results of these experiments, shown in figure 5.22 and 5.23, indicate that both of the low temperature desorptions are approximately zeroth order. Zeroth order reactions proceed at the the same rate at a given temperature regardless of the adsorbate coverage. In isothermal desorptions, once the reaction begins, the rate does not change until the reaction is complete. Both of the isothermal desorptions display this basic behaviour, although neither remains truly constant during the entire desorption process. Both exhibit the same gradual decrease in rate. It is interesting that the second desorption peak displays zeroth order kinetics as the work function results indicate that this phase is associated in some way with the platinum surface.

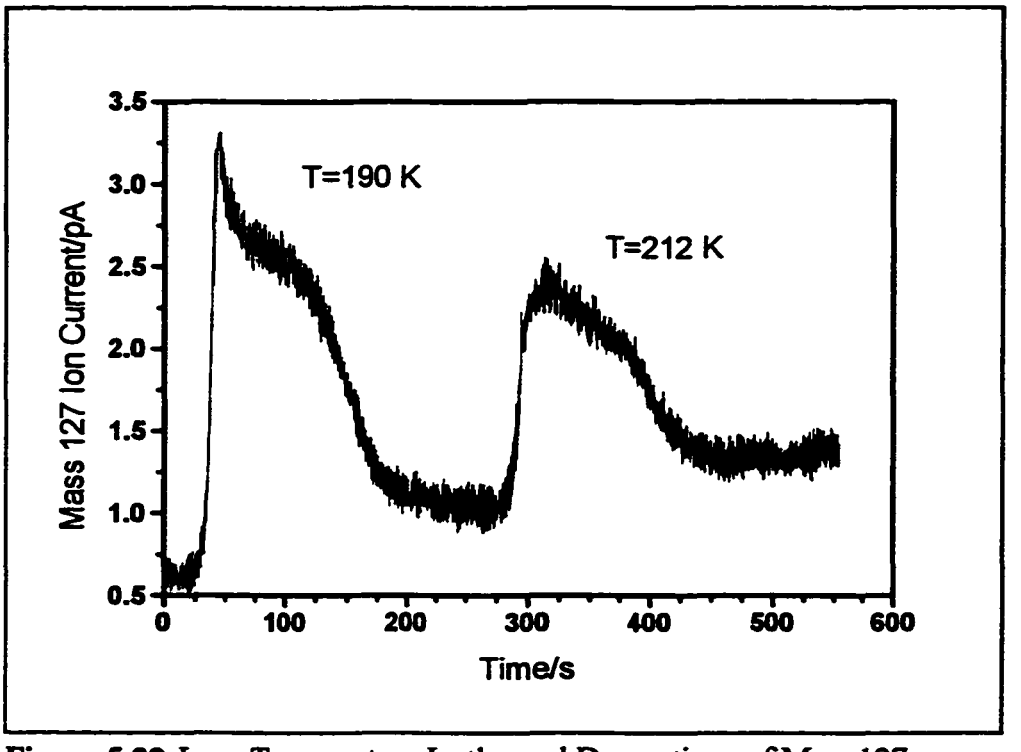

Figure 5.22-Low-Temperature Isothermal Desorptions of Mass 127

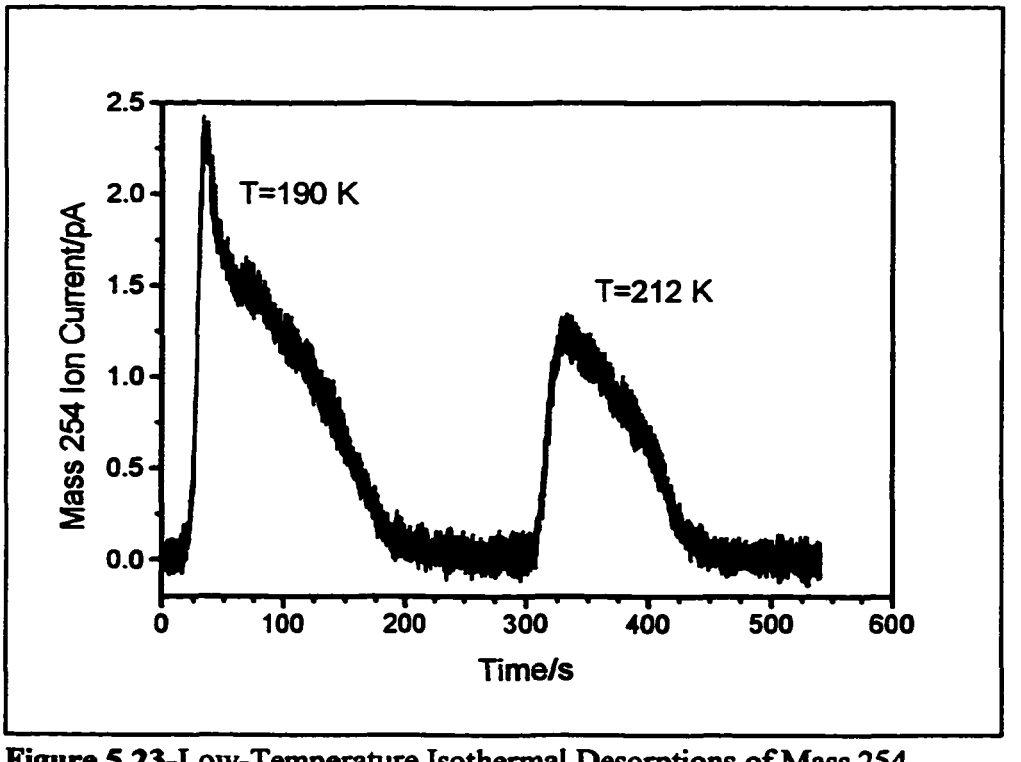

Figure 5.23-Low-Temperature Isothermal Desorptions of Mass 254

5.6 Kinetic Simulations

To determine if the rate parameters determined in the previous section are reasonable, the thermal desorption curves were simulated using those parameters. The two main desorption features, the desorption of the atop and threefold iodine atoms, were simulated using two different procedures as they follow two different types of mechanism. The desorption of the atop iodine atoms appeared to be zero order with no measurable coverage dependence. Thermal desorption spectra for this transition were simulated using a stochastic kinetic modelling program that is freely available from IBM Research [5.9]. This software, however, cannot simulate desorption spectra where the rate parameters are coverage dependent. For the simulation of the desorption of the threefold iodine atoms, the software package MAPLE was used. This program can provide numerical solutions of differential equations.

The desorption from the threefold sites was simulated using the following equation:

$$-\frac{d\theta}{dt} = \nu\theta\exp(-(E_d - w\theta)/RT) \qquad (5.5)$$

where w is a parameter that represents the coverage-dependent interaction between iodine atoms on the surface. The value of the activation energy was determined (in section 5.5.2) to be 253 kJ/mole at zero coverage and decreased by 60 kJ/mole at an iodine coverage of 5×10^{14} atoms/cm^2. This makes w=1.2×10^{-13} kJ mol^{-1}/atoms cm^{-2}. The frequency factor used in the calculation was 8×10^{13} s^{-1}, the experimentally determined value. The desorption spectra were simulated at a variety of inital coverages to compare with the experimental spectra.

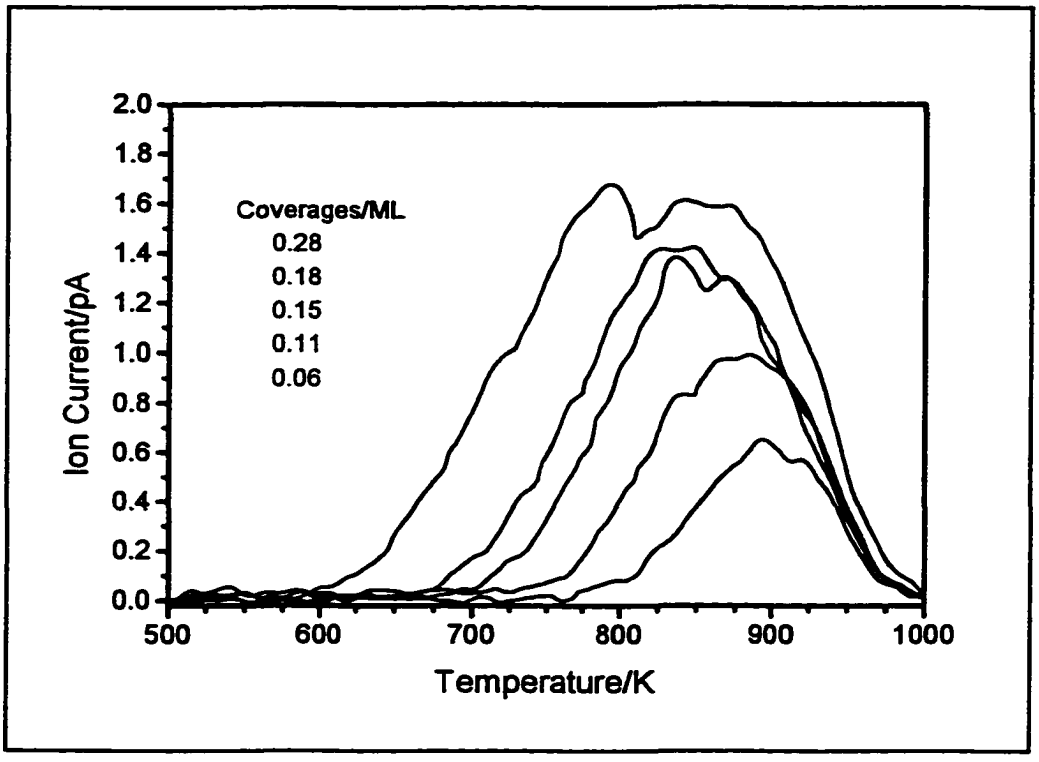

Figure 5.24-Experimental Iodine TDS From Threefold Sites

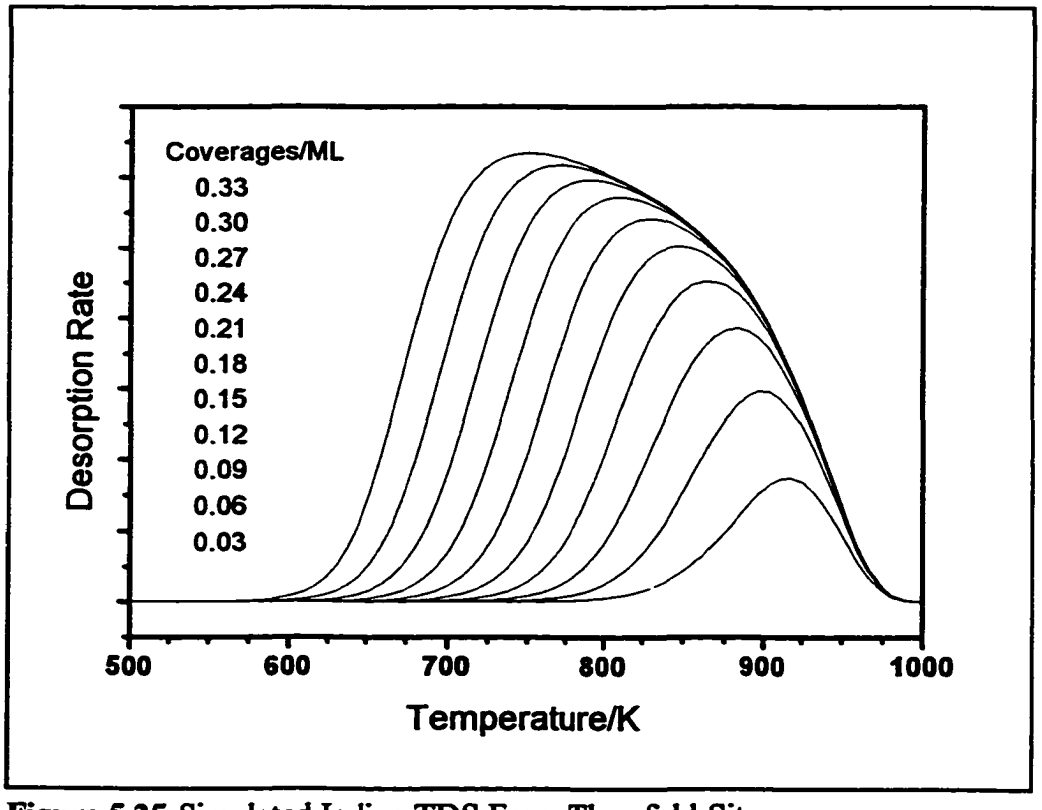

Figure 5.25-Simulated Iodine TDS From Threefold Sites

The overall shape of the simulated spectra (see figure 5.25) are similar to the experimental spectra (figure 5.24) but there are several significant differences between the two sets of spectra. The positions of the maxima in the desorption spectra are not the same, being slightly higher in the simulated spectra. The temperature where these maxima occur is quite sensitive to the kinetic parameters used and a small change of the frequency factor or activation energy could provide better agreement for the desorption maxima.

The most significant difference between these two sets of spectra is the shape of the desorption spectra, particularly at high coverages. In the experimental spectra, the peaks are symmetrical, except at high coverages where a small shoulder appears at 650 K. In the simulated spectra, the desorption peaks become asymmetrical at higher coverages. Clearly, the simple kinetic model used is not sophisticated enough to truly represent the actual desorption process.

The simulations do show that the parameter for interaction energy (w) is the correct order of magnitude, at least at low coverages, as the shift in peak position is approximately correct. It may be that the interaction energy is not constant with coverage, even though there is a constant shift in the binding energy of the iodine $4d_{3/2}$ electrons with increasing coverage [5.10]. The error bars in figure 5.17 leave room for different coverage dependencies to be explored.

The desorption of iodine from the atop sites was modelled with the experimental rate parameters using the IBM kinetic simulator. The activation energy was set to 146 kJ/mole and the frequency factor was 4×10^{26} atoms cm^{-2} s^{-1}. The iodine coverage was varied from 1.5×10^{14} atoms/cm^2 to 0.4×10^{14} atoms/cm^2.

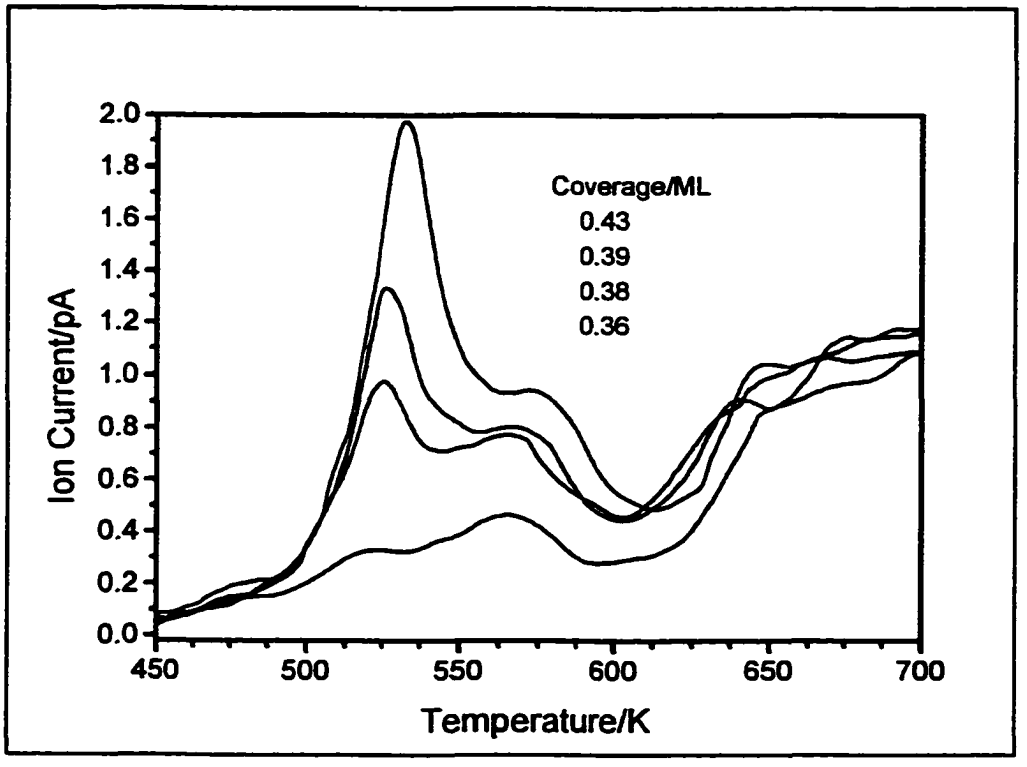

Figure 5.26-Experimental Iodine TDS From Atop Sites

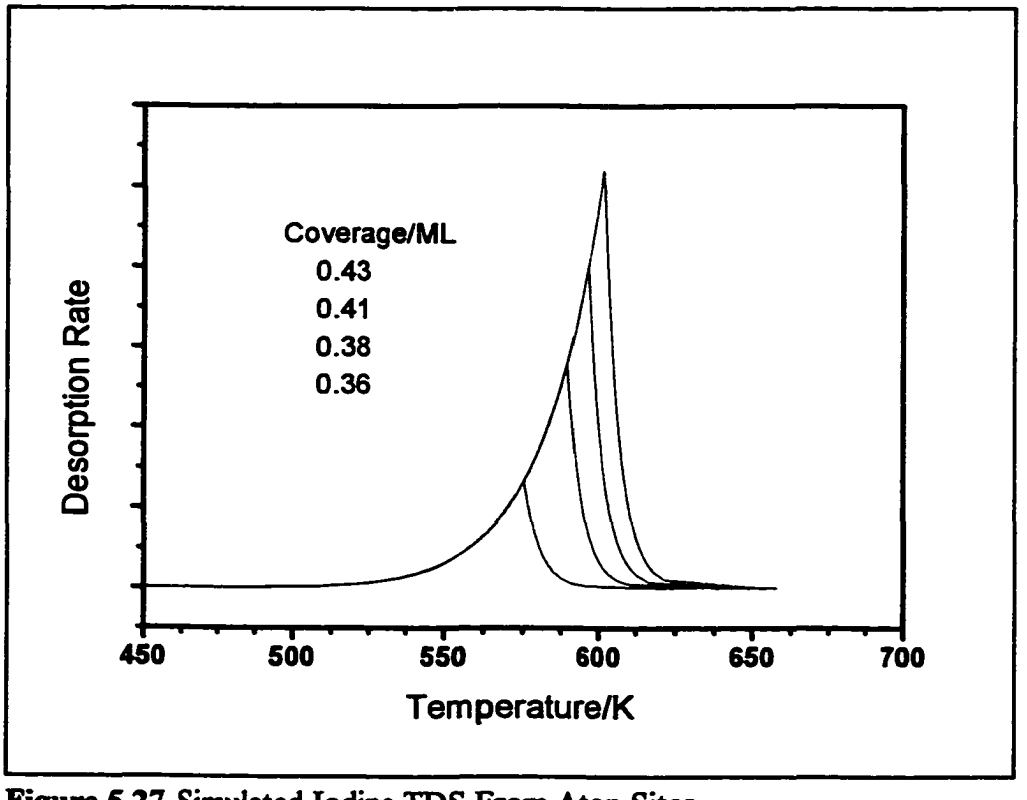

Figure 5.27-Simulated Iodine TDS From Atop Sites

Once again the exact positions of the desorption maxima in the simulated spectra (shown in figure 5.27) do not exactly match the peak maxima in the experimental spectra (shown in figure 5.26). Slight modification of the rate parameters could increase the correlation between the two sets of spectra.

The main difference between these two sets of spectra is that the leading edges of the experimental desorption peaks do not follow as expected for a zero-order reaction. However, their behaviour is close to the simulated spectra and the sharpness of the peaks also tends to indicate a zero-order phase transition.

5.7 Summary of Results

The results of the thermal desorption experiments showed that above 300 K, most of the material desorbing from the surface is atomic iodine. Some molecular iodine is also seen. The main desorption product at low temperatures is molecular iodine. Atomic iodine is also seen but most of this can be attributed to the dissociation of molecular iodine inside the mass spectrometer. Measurement of the dissociation ratio indicated that above 300 K, less than 3% of the atomic iodine observed is due to the dissociation of molecular iodine.

The work function behaviour during desorption was essentially the reverse of the change during adsorption. Dosing to the point where the work function is at a minimum value demonstrated several interesting points. The calculated iodine coverage is 0.33 but LEED analysis shows the presence of some $(\sqrt{7}x\sqrt{7})R19.1°$ structure. Heating the sample causes the iodine in the atop sites to desorb, although the amount observed is small. This desorption causes an increase in the work function. Desorption from the atop sites when the sample is saturated causes a decrease in the work function. This demonstrates that the work function

is dependent on the coverage, not the site occupied.

After removal of all the atop iodine atoms from a saturated surface, the work function is close to the value at the minimum (-1000 mV) as the coverage is approximately 0.33. A coverage dependent work function also explains the lack of work function change during the (3x3)→($\sqrt{7}$x$\sqrt{7}$)R19.1° structural transition. It also helps to explain why the work function changes during dosing at 300 K and 150 K are so similar.

The desorption kinetics above 300 K were studied by isothermal desorptions and by varying the heating rate. The broad desorption peak at 800 K was found to be a first order desorption with a coverage-dependent activation energy. At zero coverage, the activation energy is 253 kJ/mole while at a coverage of 0.33 ML (corresponding to the ($\sqrt{3}$x$\sqrt{3}$)R30° structure) the activation energy has dropped to 196 kJ/mole. The frequency factor was determined to be 8.2×10^{13} s^{-1}.

The activation energy of the desorption from the atop sites was determined to 146 kJ/mole (assuming zero order kinetics). Analysis of both heating-rate and isothermal data gave identical activation energies. The frequency factor was calculated to be 4×10^{26} atoms cm^{-2} s^{-1}.

The attempts to simulate the desorption spectra were mostly unsuccessful. The general temperature range for the desorptions was correct but the calculated peak shapes for both the atop and threefold site desorptions were different than the experimental shapes.

6

Theoretical Model Of The Work Function

6.1 Introduction

The work function (Φ) is a fundamental property of solids, and is simply defined as the minimum work needed to extract an electron from the Fermi level of the solid. It is a measure of the energy barrier that prevents electrons from physically leaving the solid. As a fundamental property, the work function has been the subject of many theoretical and experimental studies. It is central to the explanation of several physical phenomena, including thermionic emission, contact potentials, and the photoelectric effect.

The concept of the work function was first introduced in 1905 [6.1] when Einstein explained the photoelectric effect using Planck's newly developed quantum theory. Although many scientists at the time (including Planck and Einstein) did not believe that quantum theory could be correct, several experimental results could be explained using the ideas of quantization and the work function. As far back as 1839, A.C. Becquerel noticed that light could change the electrical properties of some materials [6.1]. In 1888, Hertz also noted an effect of light on his experiments into the propagation of electromagnetic waves [6.1]. That same year, Hallwachs showed that ultraviolet light could discharge a negatively charged electroscope but not a positively charged one [6.1]. Investigating the photoelectric effect, Lenard showed in 1900 [6.1] that the speed of the emitted photoelectrons was independent of the intensity of the light used. This result contradicted the accepted Newtonian model.

However, changing the intensity of the light did change the number of electrons being emitted. It was also found that the speed of the photoelectrons was dependent on the frequency of the light and there was a minimum energy required to cause electron emission. Later, in 1921[6.1], it was found that the work function barrier could be overcome by thermally exciting the electrons. Thermionic emission [6.2] is the basis on which the cathode ray tube (CRT) produces a beam of electrons. Many of the experimental techniques described in this thesis rely on electrons produced through this process.

As a fundamental property of metals, there have been many theoretical investigations into the work function. There have also been several attempts to correlate the work function with other physical properties such as electronegativity [6.3], potential of zero charge (pzc) [6.4], and hydrogen reduction rates [6.5]. One important outcome from these lines of investigations was that the worlds of solid-state physics and electrochemistry could finally communicate. The work function of the standard hydrogen electrode, which is the zero reference point on the electrochemical reduction scale, has been determined to be approximately 4.8 eV [6.6]. This allows electrochemical reduction potentials to be converted to absolute potentials, where zero energy is defined as an electron at rest at infinity. Absolute potentials are more often used in solid-state physics and quantum chemistry.

The work function can be theoretically considered as consisting of two parts, a bulk contribution, and a surface contribution. The bulk contribution is the chemical potential μ, and can be thought of as the energy holding an electron to its nucleus. The surface component is due to the ability of electrons to climb the potential barrier at the surface and escape the solid. As shown in figure 6.1, some electron density escapes beyond the confines of the solid leaving a partial positive charge in the metal. This separation of charge

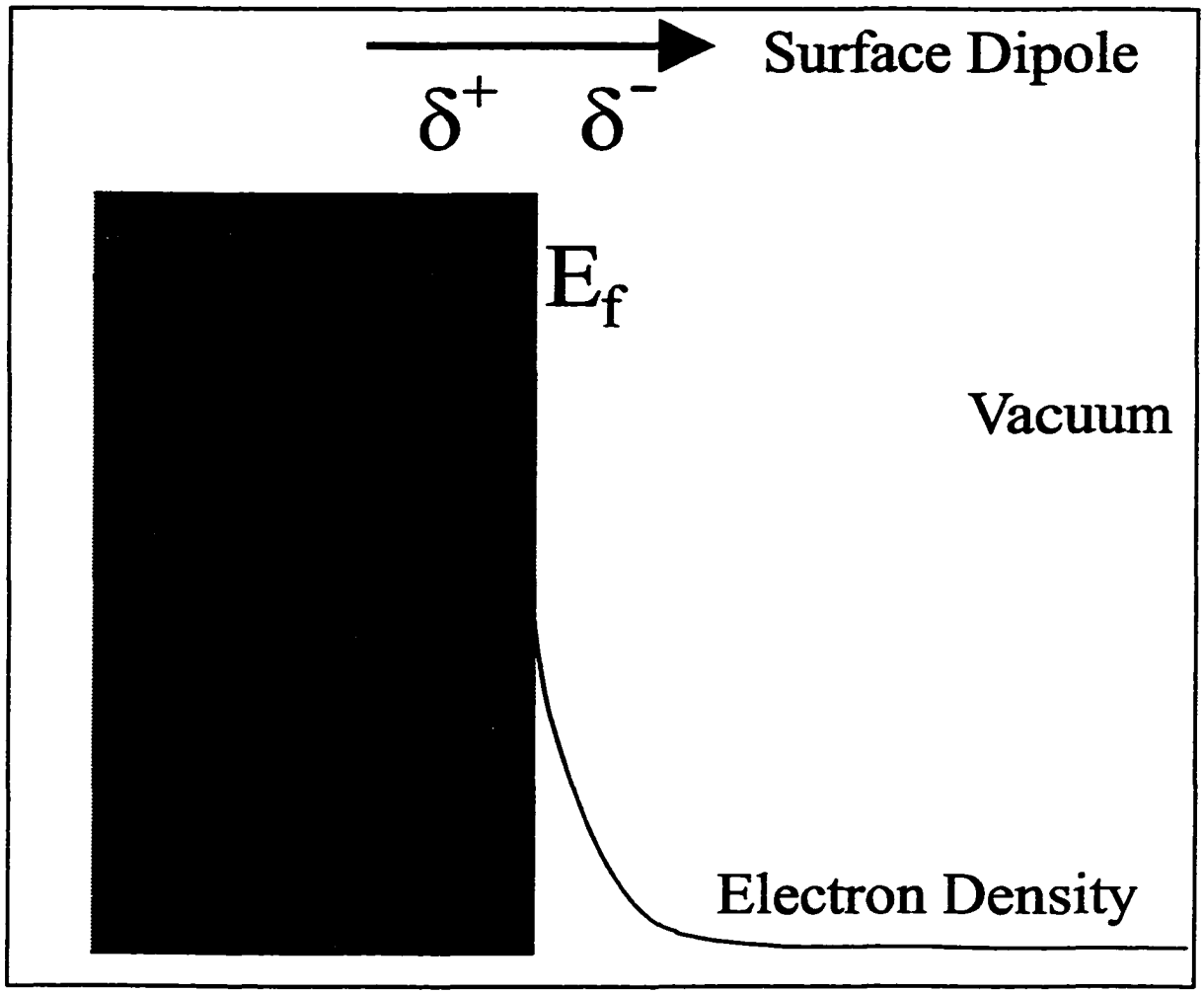

Figure 6.1-Creation of Surface Dipole by Electron Spillover Into Vacuum

constitutes a dipole, named the surface dipole, and makes a significant contribution to the work function in transition metals. The chemical potential is unaffected by adsorption at the metal surface and can be considered as a constant for a particular metal. The surface dipole, and the surface potential (χ) associated with the dipole, are intimately affected by adsorption. Therefore, any theoretical model used to predict changes in work function by adsorbates must deal with how the surface dipole is affected by adsorption.

The simplest models for how the work function is changed by adsorption are based on differences in electronegativity. Any difference in electronegativity causes some distortion

of the electron density at the surface, creating a new dipole moment. This dipole moment is added to the dipole moment already present at the surface of the metal, causing the work function to change. If the adsorbate is more electronegative than the metal, the adsorbate should withdraw electron density from the metal and increase the magnitude of the surface dipole. This should increase the work function. If the adsorbate is more electropositive than the metal, then the adsorbate will donate electrons to the metal. This should decrease the surface dipole and decrease the work function. This general model works well for many cases, such as alkali metal adsorption where the work function of transition metals decreases by several electron volts. Most electronegative adsorbates, such as oxygen and the halogens, cause an increase in the work function of transition metals. However, for several systems, electronegative adsorbates are found to decrease the work function [6.7]. Most of these anomalous work function changes are only of the order of a few hundred meV and do not represent a serious breakdown of the model outlined above.

Other behaviour is also observed where the work function will initially decrease and then later increase. Several adsorbate systems pass through a minimum work function value at a particular adsorbate coverage [6.8]. This type of behaviour is usually explained as a mutual depolarization of the dipoles that only occurs at higher coverages [6.9].

In the case of iodine adsorption on platinum(111), the work function was found to decrease by 1100 meV before increasing again. At a saturation coverage of 0.43, the work function is still negative by 600 meV. Iodine is considered to be more electronegative than platinum and should increase the work function. Both bromine and chlorine exhibit similar behaviour in that they both cause an initial decrease in the work function (less than 300 meV) [6.10, 611]. However, both of these halogens cause the work function to increase at higher

coverages and at saturation, the work function is higher than the bare surface value.

Iodine therefore represents a unique case where the model for adsorbate-induced work function changes does not predict the correct behaviour. Any extension of this model would need to be able to explain this anomalous case. It is clear that we must probe the characteristics of the surface in more detail than just considering differences in electronegativities. The nature of the electrons at the surface must be considered as these electrons are not only responsible for creating the surface dipole (by tunnelling into the vacuum) but they are also the electrons directly involved in bonding with adsorbates.

6.2 Electrons in Solids

There are several ways in which one can try to envisage the electrons in solid. There are electrons bound to the cores of the individual atoms that shield the valence electrons from the positive charge of the nucleus. These can be grouped in with the nuclear core to make a centre with an effective nuclear charge. The outer electrons present more of a problem in that the chemical bonding of the solid must be considered. As there are a variety of types of solids, there are a variety of theoretical models used to describe the electrons in the solid. Only the theories relevant to the discussion of transition metals will be presented here.

In metals with high electrical conductivity, the valence electrons are usually considered to be free electrons. These conduction electrons can travel freely throughout the solid and can be thought of as travelling electron waves. These electron waves travel in a periodic potential arising from the atomic cores and must adopt the same translational symmetry as the lattice. This fact was first formalized by Bloch in 1928 and is known as Bloch's theorem [6.12]. The resulting energy bands are well-known in solid-state physics and are very useful

for studying semiconductors [6.13].

But it is also known that the free electron model is not sufficient for describing the d bands. These d electrons are partially bound to the nucleus and are considered less free than electrons in the s and p orbitals. This is best demonstrated by looking at the general band structure of metals, such as platinum, which have s, p, and d orbitals involved in the conduction band. The band structure can be represented by the density of states (DOS) that shows the number of energy levels in a given energy range. A schematic of the DOS of a transition metal is shown in figure 6.2. The s and p bands are seen to be broad distributions while the d orbitals form a narrow band that is more well defined. In transition metals, the d bands are partially occupied while most of the s and p bands remain unfilled. In the case

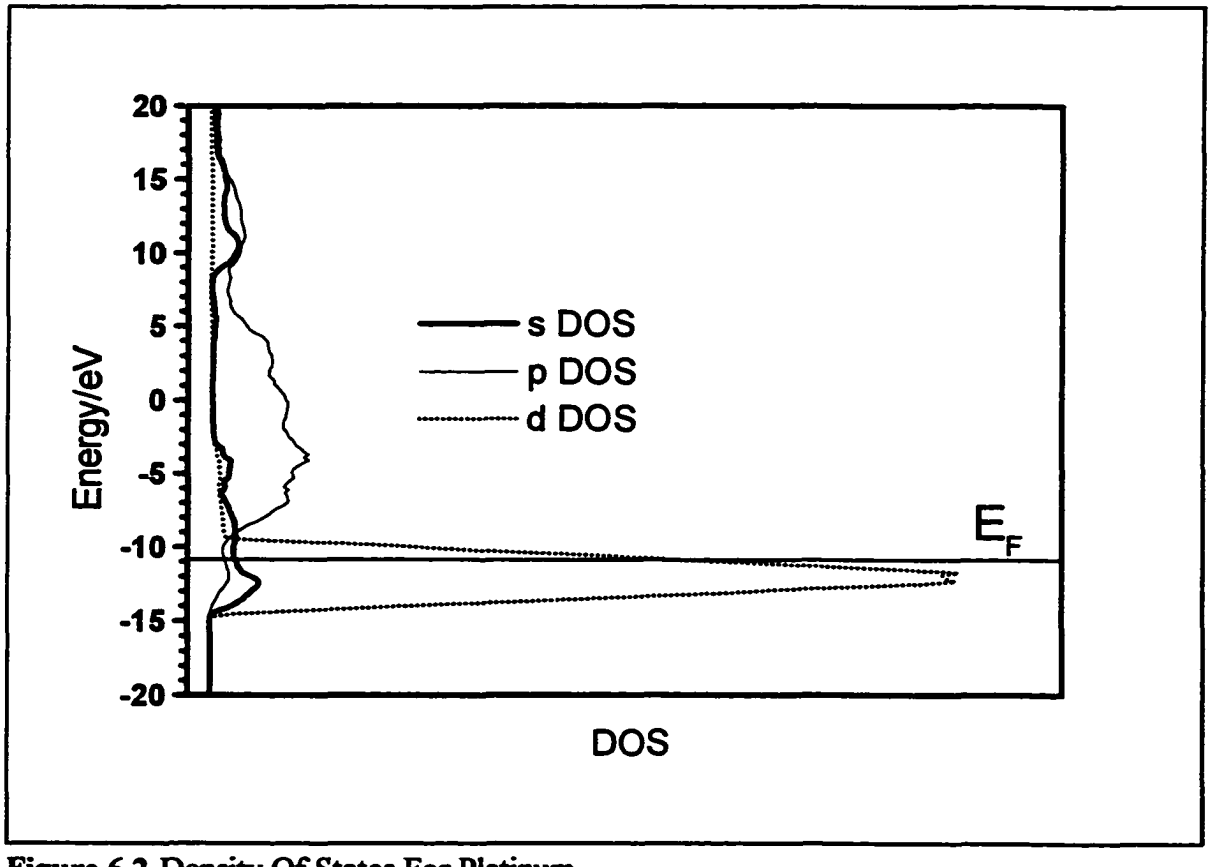

Figure 6.2-Density Of States For Platinum

of platinum, the d band is almost completely filled, as indicated by the position of the Fermi level in figure 6.2.

There are several methods that have been used to model the electrons in solids. The first type of calculations involve using density functional theory to model the profile of the electron tail that spills into the vacuum [6.14]. Once the functional form of the electron density profile has been determined, an adsorbate can added to the surface and this profile will be altered. Density functional calculations often do not contain any specific information about the arrangement of the atoms at the surface and appear to lack chemical information. More recent calculations do include site-specific information [6.15, 6.16].

The other common approach to modelling adsorption at surfaces is to construct molecular wavefunctions. These wavefunctions have various levels of sophistication ranging from simple Hückel theory to the Hartree-Fock method [6.17]. Calculations have been done using both clusters [6.18, 6.19, 6.20] and semi-infinite systems [6.21].

If good wavefunctions can be calculated, the electron distribution can also be calculated. It was proposed [6.22] that the changes in dipole moments calculated from the wavefunctions could be used to model work function changes. Using an extended-Hückel Hamiltonian, this approach was shown to be able to qualitatively describe some of the anomalous work function changes that occur during adsorption [6.23, 6.24]. Attempts have also been made to improve the extended-Hückel Hamiltonian by adding a repulsive energy term [6.25].

Other methods have been used to perform quantum calculations on surfaces. Using augmented plane waves in the basis set, the modification of the surface electronic structure by electronegative adsorbates has calculated [6.26]. The polarization of adsorbates at metal

surfaces has also been the topic of several theoretical studies [6.27, 6.28]. The adsorption of alkali metals demonstrates this polarization effect and has been studied extensively [6.29, 6.30, 6.31]

The method chosen here for studying the d bands is the tight-binding method using the extended-Hückel method for calculating matrix elements. This method assumes that the valence electrons are tightly bound to the nucleus and can be treated using chemical bonding arguments. This approach is different from the free-electron theory used for treating sp metals where the electrons are free to travel through the solid without interacting with the nuclear centres. Both methods explicitly use the translational symmetry of the crystal to predict electronic distributions but the tight-binding method produces results that are more chemical in nature.

6.3 Changes in the Surface Dipole Due to Adsorption

The electron density near the surface of metals can be strongly affected by adsorbates. There are several mechanisms by which the adsorbate can alter the surface electron distribution, depending on the type of interaction and the type of adsorbate. Some adsorbates will alter the atomic positions of the metal atoms by causing surface reconstructions or by the formation of surface compounds. Such drastic alterations in the surface will not be examined here and it will be assumed that the metal remains essentially unaltered by adsorption. Any changes in work function due to adsorption will be assumed to involve shifts in electron density rather than shifts in atomic positions.

One factor that complicates the study of adsorbate-induced work function changes is the dipole moment of the adsorbate. Many adsorbates, like water and ammonia, have

permanent molecular dipole moments. This dipole can change during adsorption and can also interact with the surface dipole. The orientation of the adsorbate's dipole with respect to the surface plays a large role in determining the overall effect an adsorbate will have on the metal's work function.

Fortunately, iodine adsorbs in an atomic state (except for multilayer adsorption) and has no molecular dipole. However, there is a dipole moment associated with the iodine atoms due to the polarization of the iodine atom by the electric field at the surface. This effect is very important for the adsorption of polarizable atoms (such as xenon) and will be analyzed in section 6.5.

The only other mechanism by which adsorbates can change the metal's work function is to alter the surface dipole directly. This is likely to occur in chemisorption when the electron density responsible for the creation of the surface dipole is directly involved in formation of the chemical bond. The alteration of the surface dipole by chemical bonding is the focus of the next section.

6.4 Molecular Orbital Calculations

Molecular-orbital (MO) theory is the most widely used approach for solving quantum-mechanical problems in chemistry and has been used to calculate many chemical and electronic properties of atoms and molecules. It is based on the variational theorem, minimizing the energies of a set of trial wavefunctions using some form of the Hamiltonian. This discussion will be restricted to the extended-Hückel, or Mulliken-Wolfsberg-Helmholz (MWH) type of MO calculations and how they apply to surface structures. Using a formalism first introduced by Bloch, the two-dimensional translational symmetry of the surface unit cell

can be explicitly used in the construction of the trial wavefunctions. The results of such calculations are used to estimate atomic-charge densities, dipole moments, and chemical bond strengths. We will then study the effect of adsorbates on the surface and compare this information with the experimental results.

6.4.1 MO Theory Of Molecules

Standard MWH-MO theory, as it relates to molecules, is based on using N linear combinations of N atomic orbitals (LCAO) to construct trial wavefunctions. The procedure for generating these trial wavefunctions (molecular orbitals), is well known in chemistry. Only brief details will be given here as a background to the more complex problem of generating trial wavefunctions for surface systems.

The energy (E) of a trial wavefunction (Ψ) is given by the Schödinger equation:

$$H\Psi = E\Psi \tag{6.1}$$

where H is the energy operator (the Hamiltonian) and:

$$\Psi = \sum_{j=1}^{N} c_j \chi_j \tag{6.2}$$

and χ_i is an atomic orbital. The coefficients (c_j) in the linear combination describe the relative contributions of each of the atomic orbitals to a particular molecular orbital. Expanding each of the molecular-orbital wavefunctions and rearranging the equation gives:

$$(H-E)\cdot\sum_{j=1}^{N} c_j\chi_j = \sum_{j=1}^{N} c_j\cdot(H-E)\chi_j = 0 \tag{6.3}$$

Following the variation method, we first multiply this equation by the complex conjugate of one of the atomic orbitals (χ_2^* for example):

$$\sum_{j=1}^{N} c_j\cdot\chi_2^*(H-E)\chi_j = \sum_{j=1}^{N} c_j\cdot(\chi_2^* H\chi_j - E\chi_2^*\chi_j) = 0 \tag{6.4}$$

Proceeding similarly with each of the complex atomic orbitals (χ_i^*) and then integrating yields a set of equations:

$$\sum_{j=1}^{N} c_j\cdot\left(\int_{-\infty}^{\infty}\chi_i^* H\chi_j d\tau - E\int_{-\infty}^{\infty}\chi_i^*\chi_j d\tau\right) = 0 \qquad i=1,2,3,..N \tag{6.5}$$

This set of linear equations can be rewritten as:

$$\sum_{j=1}^{N} c_j\cdot(H_{ij} - E\,S_{ij}) = 0 \qquad i=1,2,3..N \tag{6.6}$$

where (introducing the bra-ket notation):

$$\begin{aligned} H_{ij} &= \int_{-\infty}^{\infty}\chi_i^* H\chi_j d\tau = \langle\chi_i|H|\chi_j\rangle \\ S_{ij} &= \int_{-\infty}^{\infty}\chi_i^*\chi_j d\tau = \langle\chi_i|\chi_j\rangle \end{aligned} \tag{6.7}$$

Minimizing the energy with respect to the coefficients is done by solving the standard secular determinant:

$$\det|\boldsymbol{H}-\boldsymbol{ES}| = 0 \tag{6.8}$$

where $\boldsymbol{H}$ is the NxN matrix of H_{ij} integrals and $\boldsymbol{S}$ is the NxN matrix of S_{ij} integrals from equation 6.7

The determinant of the NxN matrix ($\boldsymbol{H}$-$\boldsymbol{ES}$) is a polynomial of degree N. Solving this polynomial expression yields N energy values and N sets of N coefficients (c_{jk}) that describe N linear combinations of the type in equation 6.2. This means there are actually N unique (linearly independent) molecular-orbital wavefunctions. The coefficients can be used to calculate other physical quantities, such as atomic charges and dipole moments.

6.4.2 Bloch Wavefunctions

The quantum-mechanical calculations used in this thesis combine the LCAO approach (described above) with Bloch's theorem, first proposed by Bloch in 1928. Bloch's theorem originates from the use of projection operators in group theory and allows one to construct symmetry-adapted wavefunctions. Any symmetry that exists in the system being studied can be projected onto the trial wavefunctions so they possess the same symmetry. In the case being studied here, the symmetry is the two-dimensional translational symmetry of the lattice.

As previously described, surfaces of single crystals are very well-ordered. The unit cell describes a subsection of the surface that is repeated continuously over the entire surface. This, of course, neglects the properties of real surfaces such as defects, dislocations, and atomic contaminations. However, STM studies have shown that on numerous single crystal

surfaces, including platinum, there are large terraces where the atomic structure is extremely regular.

Bloch's theorem states that the wavefunctions used to describe periodic structures (such as 2-D lattices) must possess the same symmetry as the periodic structure. A unit cell can be translated by any unit-cell vector, or combination of unit cell vectors, and the local chemical environment inside the unit cell remains unchanged. This translational symmetry must also apply to any wavefunction describing the unit cell. Bloch's theorem ensures that the wavefunction possesses the desired symmetry.

Again we start with a set of N atomic orbitals but these atomic orbitals are part of a unit cell rather than a molecule. As there are M unit cells, there will be a total of MxN atomic orbitals used as a basis set for the calculation. Rather than set up molecular orbitals that are linear combinations of all of the atomic orbitals from each of the unit cells (which could lead to a very large secular determinant) we construct the molecular orbitals from a set of N Bloch orbitals (φ_{jk}), defined as:

$$\varphi_{jk} = \frac{A}{\sqrt{M}} \sum_{p=1}^{\sqrt{M}} \sum_{q=1}^{\sqrt{M}} \exp(i\mathbf{k}\cdot(p\mathbf{a}_1 + q\mathbf{a}_2))\chi_j(p\mathbf{a}_1 + q\mathbf{a}_2) \qquad (6.9)$$

where $\chi_j(p\mathbf{a}_1+q\mathbf{a}_2)$ is an atomic orbital (χ_j) that has been translated by integer multiples of the real-space unit-cell vectors $\mathbf{a}_1$ and $\mathbf{a}_2$. A is a normalization constant that is approximately equal to one and $\mathbf{k}$ refers to a reciprocal lattice vector that is within the first Brillouin zone. The reciprocal lattice is defined by the unit cell vectors $\mathbf{b}_1$ and $\mathbf{b}_2$ which are related to the real-space unit-cell vectors by:

$$\begin{aligned} a_1 \cdot b_1 &= 2\pi \quad a_2 \cdot b_2 = 2\pi \\ a_1 \cdot b_2 &= 0 \quad\quad a_2 \cdot b_1 = 0 \end{aligned} \tag{6.10}$$

Note that there is a slight difference (a factor of 2π) between the reciprocal-lattice unit-cell vectors described here and those described in the section on LEED. Allowed values of k are given by:

$$\begin{aligned} k &= \frac{r}{\sqrt{M}} b_1 + \frac{s}{\sqrt{M}} b_2 \\ r &= \frac{-\sqrt{M}-1}{2}, .. -1, 0, 1, .. \frac{\sqrt{M}-1}{2} \qquad s = \frac{-\sqrt{M}-1}{2}, .. -1, 0, 1, .. \frac{\sqrt{M}-1}{2} \end{aligned} \tag{6.11}$$

providing that k is actually inside the first Brillouin zone.

The first Brillouin zone is a special region in reciprocal space that is a Wigner-Seitz unit cell of the reciprocal lattice. As shown in figure 6.3, the first Brillouin zone contains a

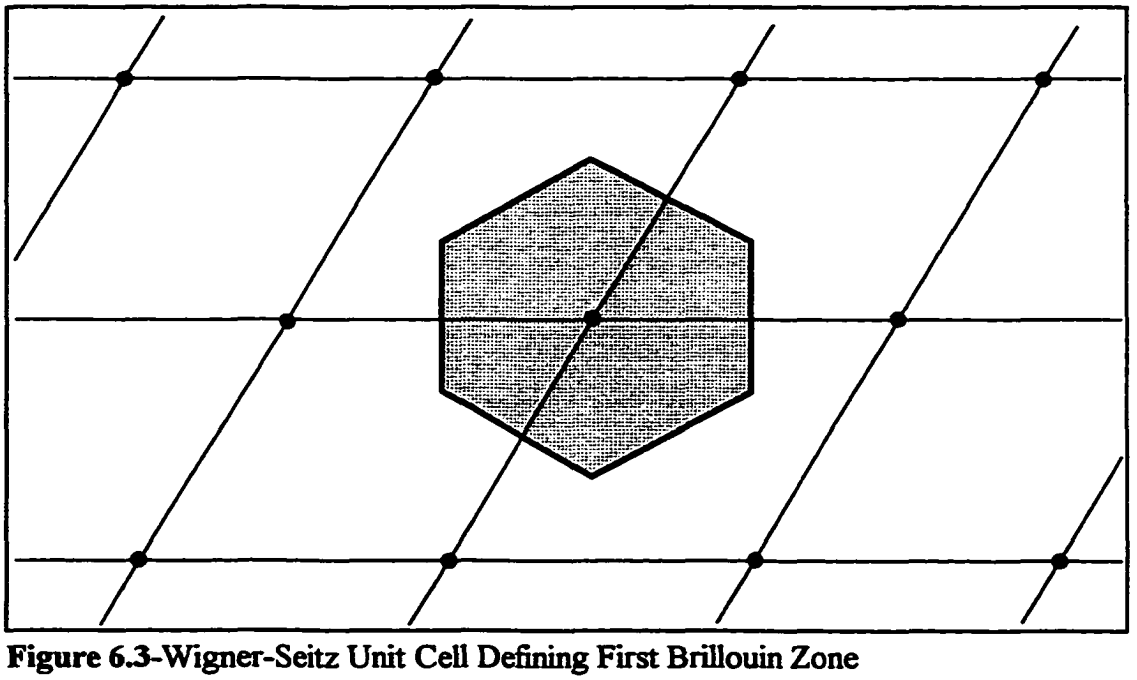

Figure 6.3-Wigner-Seitz Unit Cell Defining First Brillouin Zone

set of points in k-space that are closer to the central lattice point than to any of the other lattice points. The molecular orbitals (Ψ) can now be constructed from Bloch orbitals, rather than atomic orbitals. There are NxM Bloch orbitals used in the linear combination:

$$\Psi = \sum_{j=1}^{N} \sum_{k=1}^{M} c_{jk} \varphi_{jk} \tag{6.12}$$

that leads to a very large secular determinant. Fortunately, Bloch orbitals with different values of k are guaranteed to be orthogonal and so:

$$\int_{-\infty}^{+\infty} \varphi_{jk}^{*} \varphi_{ik'} \, d\tau = 0 \qquad for \; k \neq k' \tag{6.13}$$

This block-diagonalizes the secular matrix into M blocks of NxN matrices. These NxN matrices can be solved individually, and the results of the M calculations can be combined after the energies and coefficients have been found.

The first step is to set up the NxN blocks of k-dependent matrix elements:

$$\begin{aligned} H_{ijk} &= \int_{-\infty}^{+\infty} \varphi_{ik}^{*} H \varphi_{jk} \, d\tau \\ S_{ijk} &= \int_{-\infty}^{+\infty} \varphi_{ik}^{*} \varphi_{jk} \, d\tau \end{aligned} \tag{6.14}$$

We begin with the overlap matrices as the energy matrices are slightly more complicated and (as we shall see later) are related to the overlap matrices. Using Dirac's bra-ket notation, the overlap of two Bloch orbitals is given by:

$$\langle\varphi_{ik}|\varphi_{jk}\rangle=\frac{AB}{M}\langle\sum_{p=1}^{\sqrt{M}}\sum_{q=1}^{\sqrt{M}}\exp(ik\cdot(pq)\chi_i(pq)|\sum_{r=1}^{\sqrt{M}}\sum_{s=1}^{\sqrt{M}}\exp(ik\cdot(rs)\chi_j(rs)\rangle \quad (6.15)$$

where (pq) represents the real-space vector pa_1+qa_2 and (rs) represents the real-space vector ra_1+sa_2. Expansion of this expression yields M terms:

$$\begin{aligned}\langle\varphi_{ik}|\varphi_{jk}\rangle &= \frac{AB}{M}\sum_{\text{all values of}}^{p,q,r,s}\langle\exp(ik\cdot(pq))\chi_i(pq)|\exp(ik\cdot(rs))\chi_j(rs)\rangle \\ &= \frac{AB}{M}\sum_{\text{all values of}}^{p,q,r,s}\exp(-ik\cdot(pq))\exp(ik\cdot(rs))\langle\chi_i(pq)|\chi_j(rs)\rangle\end{aligned} \quad (6.16)$$

If we explicitly expand the exponential terms, the overlap expression becomes:

$$\begin{aligned}{}_{ik}|\varphi_{jk}\rangle &= \frac{AB}{M}\sum_{\text{all values of}}^{p,q,r,s}\exp(-ik\cdot(pa_1+qa_2)\exp(ik\cdot(ra_1+sa_2)\langle\chi_i(pq)|\chi_j(rs \\ &= \frac{AB}{M}\sum_{\text{all values of}}^{p,q,r,s}\exp(-ik\cdot((p-r)a_1+(q-s)a_2)\langle\chi_i(pq)|\chi_j(rs)\rangle\end{aligned} \quad (6.17)$$

To simplify this expression, we can place limits on the values of r and s in terms of p and q:

$$\begin{aligned}r &= p, p+1, p-1 \\ s &= q, q+1, q-1\end{aligned} \quad (6.18)$$

This means that atomic orbitals in one particular unit cell can only interact with atomic orbitals in the same unit cell, or in unit cells immediately surrounding it.

As shown in figure 6.4, the central unit cell is surrounded by eight other unit cells. In standard molecular orbital theory, interactions beyond these distances are usually neglected as the overlap integrals are essentially zero. Even if the central unit cell only contains one atomic orbital, this assumption is usually valid as overlap integrals are not usually calculated

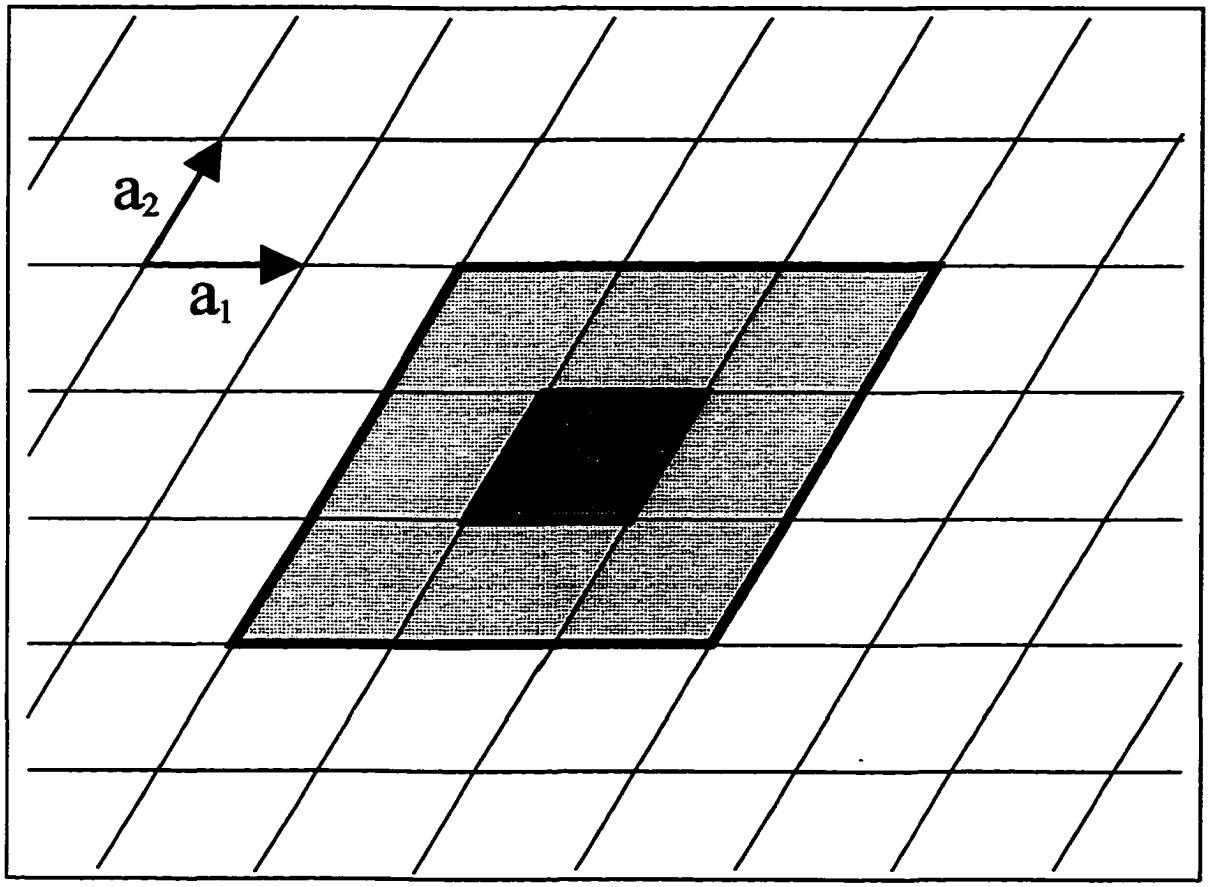

Figure 6.4-Limit On Interactions Between Different Unit Cells

beyond nearest neighbours. If one does wish to include longer-range interactions, one can simply choose a larger unit cell that makes the assumptions in equation 6.18 valid.

These restrictions on the range of interactions make many of the terms in equation 6.17 equal to zero. Replacing r and s with the values from equation 6.18, the overlap expression becomes:

$$\begin{aligned}
\varphi_{ik}|\varphi_{jk} \geq \frac{AB}{M}\sum_{p=1}^{\sqrt{M}}\sum_{q=1}^{\sqrt{M}}\Big[&\exp(-ik\cdot((p-p)a_1+(p-p)a_2)\langle\chi_i(pa_1+qa_2)|\chi_j(pa_1+qa_2)\rangle \\
&\exp(-ik\cdot((p-(p-1))a_1+(q-(q-1))a_2)\langle\chi_i(pa_1+qa_2)|\chi_j((p-1)a_1+(q-1)a_2)\rangle \\
&\exp(-ik\cdot((p-(p+1))a_1+(q-(q+1))a_2)\langle\chi_i(pa_1+qa_2)|\chi_j((p+1)a_1+(q+1)a_2)\rangle \\
&\exp(-ik\cdot((p-(p-1))a_1+(q-(q+1))a_2)\langle\chi_i(pa_1+qa_2)|\chi_j((p-1)a_1+(q+1)a_2)\rangle \\
&\exp(-ik\cdot((p-(p+1))a_1+(q-(q-1))a_2)\langle\chi_i(pa_1+qa_2)|\chi_j((p+1)a_1+(q-1)a_2)\rangle \\
&\exp(-ik\cdot((p-p)a_1+(q-(q-1))a_2)\langle\chi_i(pa_1+qa_2)|\chi_j(pa_1+(q-1)a_2)\rangle \\
&\exp(-ik\cdot((p-p)a_1+(q-(q+1))a_2)\langle\chi_i(pa_1+qa_2)|\chi_j(pa_1+(q+1)a_2)\rangle \\
&\exp(-ik\cdot((p-(p-1))a_1+(q-q)a_2)\langle\chi_i(pa_1+qa_2)|\chi_j((p-1)a_1+qa_2)\rangle \\
&\exp(-ik\cdot((p-(p+1))a_1+(q-q)a_2)\langle\chi_i(pa_1+qa_2)|\chi_j((p+1)a_1+qa_2)\rangle\Big]
\end{aligned} \tag{6.19}$$

There will be M terms in equation 6.19 that have the same differences involving p and q. There will be nine groups of these M terms, one for each of the restrictions in equation 6.18. Simplifying the exponential terms and gathering the M terms together into nine groups gives:

$$\begin{aligned}
\langle\varphi_{ik}|\varphi_{jk}\rangle = AB\Big[&\langle\chi_i(0a_1+0a_2)|\chi_j(0a_1+0a_2)\rangle \\
&+\exp(-ik\cdot(a_1+a_2)\langle\chi_i(0a_1+0a_2)|\chi_j(-a_1-a_2)\rangle \\
&+\exp(-ik\cdot(-a_1-a_2)\langle\chi_i(0a_1+0a_2)|\chi_j(a_1+a_2)\rangle \\
&+\exp(-ik\cdot(a_1-a_2)\langle\chi_i(0a_1+0a_2)|\chi_j(-a_1+a_2)\rangle \\
&+\exp(-ik\cdot(-a_1+a_2)\langle\chi_i(0a_1+0a_2)|\chi_j(a_1-a_2)\rangle \\
&+\exp(-ik\cdot(a_2)\langle\chi_i(0a_1+0a_2)|\chi_j(-a_2)\rangle \\
&+\exp(-ik\cdot(-a_2)\langle\chi_i(0a_1+0a_2)|\chi_j(a_2)\rangle \\
&+\exp(-ik\cdot(a_1)\langle\chi_i(0a_1+0a_2)|\chi_j(-a_1)\rangle \\
&+\exp(-ik\cdot(-a_1)\langle\chi_i(0a_1+0a_2)|\chi_j(a_1)\rangle\Big]
\end{aligned} \tag{6.20}$$

This expression gives the complete form of the overlap integral for Bloch-type wavefunctions. The exponential terms represent a k-dependent phase term and the overlap terms represent a k-independent overlap integral between orbitals in the central (0,0) unit cell and orbitals in surrounding unit cells (as shown in figure 6.2). If atomic orbital i does not interact with atomic orbital j in a particular unit cell, the term in equation 6.20 from that

interaction will be zero. If atomic orbital i does not interact with atomic orbital j in any other unit cells besides the (0,0) unit cell, equation 6.20 simplifies to a simple k-independent overlap integral as all terms except the first will be zero.

The energy matrix elements can be derived in a similar fashion to give:

$$\begin{aligned}
\langle\varphi_{ik}|H|\varphi_{jk}\rangle = AB\Big[&\langle\chi_i(0a_1+0a_2)|H|\chi_j(0a_1+0a_2)\rangle \\
&+ \exp(-ik\cdot(a_1+a_2)\langle\chi_i(0a_1+0a_2)|H|\chi_j(-a_1-a_2)\rangle \\
&+ \exp(-ik\cdot(-a_1-a_2)\langle\chi_i(0a_1+0a_2)|H|\chi_j(a_1+a_2)\rangle \\
&+ \exp(-ik\cdot(a_1-a_2)\langle\chi_i(0a_1+0a_2)|H|\chi_j(-a_1+a_2)\rangle \\
&+ \exp(-ik\cdot(-a_1+a_2)\langle\chi_i(0a_1+0a_2)|H|\chi_j(a_1-a_2)\rangle \\
&+ \exp(-ik\cdot(a_2)\langle\chi_i(0a_1+0a_2)|H|\chi_j(-a_2)\rangle \\
&+ \exp(-ik\cdot(-a_2)\langle\chi_i(0a_1+0a_2)|H|\chi_j(a_2)\rangle \\
&+ \exp(-ik\cdot(a_1)\langle\chi_i(0a_1+0a_2)|H|\chi_j(-a_1)\rangle \\
&+ \exp(-ik\cdot(-a_1)\langle\chi_i(0a_1+0a_2)|H|\chi_j(a_1)\rangle\Big]
\end{aligned} \tag{6.21}$$

Next the normalization constant (A) must be evaluated. For the case of $j=i$, where $\langle\varphi_i|\varphi_i\rangle=1$, equation 6.20 can be rearranged to give:

$$\begin{aligned}
A = \Big[&\langle\chi_i(0a_1+0a_2)|\chi_j(0a_1+0a_2)\rangle \\
&+ \exp(-ik\cdot(a_1+a_2)\langle\chi_i(0a_1+0a_2)|\chi_j(-a_1-a_2)\rangle \\
&+ \exp(-ik\cdot(-a_1-a_2)\langle\chi_i(0a_1+0a_2)|\chi_j(a_1+a_2)\rangle \\
&+ \exp(-ik\cdot(a_1-a_2)\langle\chi_i(0a_1+0a_2)|\chi_j(-a_1+a_2)\rangle \\
&+ \exp(-ik\cdot(-a_1+a_2)\langle\chi_i(0a_1+0a_2)|\chi_j(a_1-a_2)\rangle \\
&+ \exp(-ik\cdot(a_2)\langle\chi_i(0a_1+0a_2)|\chi_j(-a_2)\rangle \\
&+ \exp(-ik\cdot(-a_2)\langle\chi_i(0a_1+0a_2)|\chi_j(a_2)\rangle \\
&+ \exp(-ik\cdot(a_1)\langle\chi_i(0a_1+0a_2)|\chi_j(-a_1)\rangle \\
&+ \exp(-ik\cdot(-a_1)\langle\chi_i(0a_1+0a_2)|\chi_j(a_1)\rangle\Big]^{-\frac{1}{2}}
\end{aligned} \tag{6.22}$$

This shows that the complete form of the normalization constant for the Bloch wavefunctions is k-dependent. It can also be seen that if atomic orbital i in the central unit cell does not

interact with any other i atomic orbitals from the surrounding unit cells, the normalization constant is equal to one. Although it is customary to start with wavefunctions that are completely normalized, in the calculations performed here the Bloch wavefunctions used in the basis set will only be 'approximately' normalized (neglecting the constant A). The reasons for this will be discussed below when deriving the expressions used in the population analysis. However, the normalization constants A and B will be used appropriately to ensure that the wavefunctions behave as if they were completely normalized.

6.4.3 Calculating Matrix Elements

Up to this point in the discussion there have been no assumptions about how to calculate the matrix elements of H and S. There are many calculation methods currently in use and the selection criteria must be reviewed before continuing.

The overlap integral between two atomic orbitals is difficult to calculate using the one-electron hydrogen orbitals that are commonly used in chemistry. These wavefunction consist of a radial factor ($R(r)$) and an angular factor ($Y(\varphi,\theta)$):

$$\chi(r,\varphi,\theta)=Y(\varphi,\theta)R(r) \tag{6.23}$$

The angular factors are the well-known spherical harmonics that are used in a variety of quantum problems. This part of the wavefunction is retained for the calculation of overlap integrals. The radial part of the wavefunction makes solving the overlap integrals difficult. Although numerical methods can be used to attempt such calculations, another approach has been adopted.

In 1930 Slater proposed that the radial term be replaced with another expression that

would allow the overlap integrals to be more easily calculated. His solution was to construct Slater-type orbitals (STOs) that are a product of the spherical harmonics and a new radial function ($R'(r)$). This new radial function makes the Slater functions match the hydrogen-orbital functions in the region where overlap usually occurs (large values of r). In regions of r where the overlap does not usually occur (such as very small r), the Slater functions do not match the hydrogen functions very well. But for the purpose of calculating overlap integrals, this approach is very useful.

The Slater orbitals have the form of:

$$R'(r) = (2\zeta)^{n+1/2} (1/2n!)^{1/2} e^{-\zeta r} \qquad (6.24)$$

where n is the effective principal quantum number and ζ is the Slater exponent. STOs are used extensively in quantum chemistry and are used for all the calculations described here.

There is another approach to finding a replacement function for $R(r)$ that will be mentioned for the sake of completeness although it is not used in this thesis. Gaussian functions can replace the radial part of the atomic orbital (χ) as this leads to overlap integrals that are very easy to solve. However, the Gaussian orbitals do not match the hydrogen functions very well and so linear combinations of Gaussian orbitals are used rather than a single Gaussian function. Using approximately ten Gaussian orbitals matches the quality of one Slater orbital and the computational savings become less significant. But Gaussian orbitals are also extensively used for quantum calculations and are favoured when three and four-centre integrals need to be calculated.

A significant improvement can be made by using double-ζ STOs. These are linear combinations of two single-ζ Slater orbitals and are available for most transition metals. The

orbitals used for platinum in the calculations described here are of this type.

The atomic orbitals (χ_i, χ_j) on the same atom are assumed to be orthogonal so that:

$$\langle\chi_i(pa_1+qa_2)|\chi_j(pa_1+qa_2)\rangle = \delta_{ij} \tag{6.25}$$

Atomic orbitals on different atoms (χ_i, χ'_j) are assumed to be non-orthogonal as are atomic orbitals on the same atoms that are in different unit cells:

$$\begin{aligned}
&\langle\chi_i(pa_1+qa_2)|\chi_i(pa_1+qa_2)\rangle = S_{ii}\equiv 1\\
&\langle\chi_i(pa_1+qa_2)|\chi_i(ra_1+sa_2)\rangle = S'_{ii}\\
&\langle\chi_i(pa_1+qa_2)|\chi_j(pa_1+qa_2)\rangle = S_{ij}\\
&\langle\chi_i(pa_1+qa_2)|\chi'_j(ra_1+sa_2)\rangle = S'_{ij}
\end{aligned} \tag{6.26}$$

where S'_{ii}, S_{ij}, and S'_{ij} are overlap integrals calculated using Slater orbitals.

Once the atomic orbital overlaps have been evaluated, the Bloch overlap integrals can be readily calculated (using the 'approximately' normalized wavefunction):

$$\begin{aligned}
\langle\varphi_{ik}|\varphi_{jk}\rangle &= \langle\chi_i(0a_1+0a_2)|\chi_j(0a_1+0a_2)\rangle\\
&+ \exp(-ik\cdot(a_1+a_2)\langle\chi_i(0a_1+0a_2)|\chi_j(-a_1-a_2)\rangle\\
&+ \exp(-ik\cdot(-a_1-a_2)\langle\chi_i(0a_1+0a_2)|\chi_j(a_1+a_2)\rangle\\
&+ \exp(-ik\cdot(a_1-a_2)\langle\chi_i(0a_1+0a_2)|\chi_j(-a_1+a_2)\rangle\\
&+ \exp(-ik\cdot(-a_1+a_2)\langle\chi_i(0a_1+0a_2)|\chi_j(a_1-a_2)\rangle\\
&+ \exp(-ik\cdot(a_2)\langle\chi_i(0a_1+0a_2)|\chi_j(-a_2)\rangle\\
&+ \exp(-ik\cdot(-a_2)\langle\chi_i(0a_1+0a_2)|\chi_j(a_2)\rangle\\
&+ \exp(-ik\cdot(a_1)\langle\chi_i(0a_1+0a_2)|\chi_j(-a_1)\rangle\\
&+ \exp(-ik\cdot(-a_1)\langle\chi_i(0a_1+0a_2)|\chi_j(a_1)\rangle
\end{aligned} \tag{6.27}$$

The calculation of the H matrix elements is simplified by using empirical relationships to estimate them from the overlap integrals. The energy matrix elements for Bloch orbitals ('approximately' normalized) is given by:

$$
\begin{aligned}
\langle\varphi_{ik}|H|\varphi_{jk}\rangle = &\langle\chi_i(0a_1+0a_2)|H|\chi_j(0a_1+0a_2)\rangle \\
&+ \exp(-ik\cdot(a_1+a_2)\langle\chi_i(0a_1+0a_2)|H|\chi_j(-a_1-a_2)\rangle \\
&+ \exp(-ik\cdot(-a_1-a_2)\langle\chi_i(0a_1+0a_2)|H|\chi_j(a_1+a_2)\rangle \\
&+ \exp(-ik\cdot(a_1-a_2)\langle\chi_i(0a_1+0a_2)|H|\chi_j(-a_1+a_2)\rangle \\
&+ \exp(-ik\cdot(-a_1+a_2)\langle\chi_i(0a_1+0a_2)|H|\chi_j(a_1-a_2)\rangle \\
&+ \exp(-ik\cdot(a_2)\langle\chi_i(0a_1+0a_2)|H|\chi_j(-a_2)\rangle \\
&+ \exp(-ik\cdot(-a_2)\langle\chi_i(0a_1+0a_2)|H|\chi_j(a_2)\rangle \\
&+ \exp(-ik\cdot(a_1)\langle\chi_i(0a_1+0a_2)|H|\chi_j(-a_1)\rangle \\
&+ \exp(-ik\cdot(-a_1)\langle\chi_i(0a_1+0a_2)|H|\chi_j(a_1)\rangle
\end{aligned}
\tag{6.28}
$$

Hamiltonian terms involving one atomic orbital on the same atom in the same unit cell (Coulomb integrals) are calculated from spectroscopic data. All other Hamiltonian terms (resonance integrals) are calculated semi-empirically. We will use the following notation for discussing these Hamiltonian terms:

$$
\begin{aligned}
C_{ii} &= \langle\chi_i(pa_1+qa_2)|H|\chi_i(pa_1+qa_2)\rangle \quad \textit{sameorbital/sameunitcell} \\
R_{ij} &= \langle\chi_i(pa_1+qa_2)|H|\chi_j(pa_1+qa_2)\rangle \quad \textit{differentorbital/sameunitcell} \\
R'_{ij} &= \langle\chi_i(pa_1+qa_2)|H|\chi_j(ra_1+sa_2)\rangle \quad \textit{differentorbital/differentunitcell}
\end{aligned}
\tag{6.29}
$$

where C_{ii} are Coulomb integrals and R_{ij} and R'_{ij} are resonance integrals.

The Coulomb integrals are assigned to the negative value of the valence orbital ionization energy (*VOIE*). This energy depends on the electronic configuration of the valence electrons which in turn depends on the charge (whole or partial) that resides on the atom. The *VOIE* is therefore assumed to be a function of charge according to:

$$VOIE(q) = Aq^2 + Bq + C \tag{6.30}$$

where q is the atomic charge, and A,B, and C are constants.

A number of methods have been developed for calculating the resonance integrals and

although the Wolfsberg-Helmholz formula has become the most popular method used, several are available. All of these semi-empirical methods relate the Hamiltonian terms to the overlap integral. A larger overlap integral should lead to more mixing of orbitals and this intuitive expectation is reflected in the formulae given below.

The Wolfsberg-Helmholz formula is based on an equal contribution from both atomic orbitals:

$$R_{ij} = \kappa S_{ij}(C_{ii}+C_{jj})/2 \tag{6.31}$$

where κ is a parameter with a value between 1.5 and 2.0 (usually 1.75). Other variations for the calculation of the resonance integrals are:

$$\begin{aligned} R_{ij} &= -\kappa S_{ij}(C_{ii}C_{jj})^{1/2} && \kappa \approx 1.5 \\ R_{ij} &= \kappa S_{ij}(2C_{ii}C_{jj})/(C_{ii}+C_{jj}) && \kappa \approx 1.5 \\ R_{ij} &= S_{ij}((C_{ii}+C_{jj})/2+\kappa) && \kappa \approx 1.5 \\ R_{ij} &= (\kappa-|S_{ij}|)S_{ij}(C_{ii}+C_{jj})/2 && \kappa \approx 2 \end{aligned} \tag{6.32}$$

A weighted variation of the Wolfsberg-Helmholz formula can also be used when dealing with diffuse orbitals (with high principal quantum numbers):

$$\begin{aligned} R_{ij} &= (1/2)(\kappa-(\kappa-1)\Delta^2)S_{ij}((1+\Delta)C_{ii}+(1-\Delta)C_{jj}) \\ \Delta &= (C_{ii}-C_{jj})/(C_{ii}C_{jj}) \qquad \kappa \approx 1.75 \end{aligned} \tag{6.33}$$

The energy matrix elements for the Bloch orbitals can be easily constructed once the Coulomb and resonance integrals have been calculated.

Once all of the integrals have been calculated, the secular determinant (equation 6.8) can be solved. The procedure for solving this equation will be discussed below. As both the

energy matrix H and the overlap matrix S are block diagonalized, a set of eigenvalues (energies) and eigenvectors (MO coefficients) can be found separately for each block. These groups of solutions must be combined to yield average molecular properties such as atomic charge and dipole moments. Before this can done, the procedure for calculating the desired physical quantities from the eigenvectors must be described.

6.4.4 Population Analysis

The eigenvectors from solving the secular determinant are the coefficients for constructing the molecular orbitals from the atomic (or Bloch) orbitals in equations 6.2 and 6.12. The two quantities we wish to extract from these coefficients are the electronic distribution and the dipole moment associated with that distribution. The electronic distribution will be mapped by calculating total electronic populations (using a Mulliken population analysis) associated with each atom and the overlap population associated with the chemical bond between the atoms. The dipole moment of each atom will be calculated using the method of hybridization dipole moments discussed in the next section. Both these calculations will be discussed for molecular systems and then extended using Bloch wavefunctions.

The molecular orbitals produced by solving the secular equation are normalized:

$$<\Psi_g|\Psi_g> = 1 = <\sum_{i=1}^{N} c_{gi}\chi_i|\sum_{j=1}^{N} c_{gj}\chi_j> \qquad (6.34)$$

Each molecular orbital can contain two electrons, although the population of the molecular orbital depends on its energy relative to the highest-occupied molecular orbital (HOMO) and

the lowest-unoccupied molecular orbital (LUMO). If n_g represents the molecular orbital's occupation, the total electron population will be given by:

$$POP_g = n_g \langle \sum_{i=1}^{N} c_{gi}\chi_i | \sum_{j=1}^{N} c_{gj}\chi_j \rangle = n_g \sum_{i=1}^{N}\sum_{j=1}^{N} c_{gi}^* c_{gj} \langle \chi_i | \chi_j \rangle \qquad (6.35)$$

This molecular orbital population can be divided into contributions from each atomic orbital by dividing the total population into two fractions:

$$POP_g = n_g \sum_{i=1}^{N} (c_{gi}^* c_{gi} + \sum_{j=1(j\neq i)}^{N} c_{gi}^* c_{gj} \langle \chi_i | \chi_j \rangle) \qquad (6.36)$$

The first term ($c^*_{gi}c_{gi}$) represents the population contribution purely from the i^{th} atomic orbital. The second term represents the overlap population that resides in the chemical bond between two atomic centres. The overlap population between two atomic orbitals in a molecular orbital is given by:

$$OV\ POP_{gij} = n_g \left(c_{gi}^* c_{gj} \langle \chi_i | \chi_j \rangle + c_{gj}^* c_{gi} \langle \chi_j | \chi_i \rangle \right) \qquad (6.37)$$

Mulliken proposed that this overlap population be equally divided between the two atomic centres. Therefore, the overlap population associated with the i^{th} atomic orbital in the g^{th} molecular orbital is:

$$OV\ POP_{gi} = \frac{1}{2} n_g \sum_{j=1(j\neq i)}^{N} \left(c_{gi}^* c_{gj} \langle \chi_i | \chi_j \rangle + c_{gj}^* c_{gi} \langle \chi_j | \chi_i \rangle \right) \qquad (6.38)$$

The charge on the atom (q_v) is the difference between the total electronic population

and the number of electrons (n_v) on the isolated atom:

$$
\begin{aligned}
{}_{v} &= n_{v} - \left(\sum_{i=AOs}^{on\ Atom\ v} \sum_{g=1}^{N} n_g \left(c_{gi}^{*} c_{gi} + OV\ POP_{gi} \right) \right) \\
&= n_{v} - \left(\sum_{i=AOs}^{on\ Atom\ v} \sum_{g=1}^{N} n_g \left(c_{gi}^{*} c_{gi} + \frac{1}{2} \sum_{j=1(j\neq i)}^{N} \left(c_{gi}^{*} c_{gj} \langle \chi_i | \chi_j \rangle + c_{gj}^{*} c_{gi} \langle \chi_j | \chi_i \rangle \right) \right) \right)
\end{aligned}
\tag{6.39}
$$

The extension of population analysis using Bloch wavefunctions simply involves the use of more molecular orbitals. At each of the M points in k-space there are N normalized molecular orbitals of the form in equation 6.9. Molecular orbitals with energies below the Fermi level will usually contain two electrons. MO's with energies that are close to the Fermi level may be only partially occupied (following a Boltzmann distribution), depending on the temperature.

Once the molecular-orbital occupations are known, the overlap populations between the various Bloch orbitals in the unit cell can be calculated at each point in k-space by:

$$
POP_{gk} = n_{gk} \sum_{i=1}^{N} \left(c_{gik}^{*} c_{gik} \langle \varphi_{ik} | \varphi_{ik} \rangle + \sum_{j=1(j\neq i)}^{N} c_{gik}^{*} c_{gjk} \langle \varphi_{ik} | \varphi_{jk} \rangle \right) \tag{6.40}
$$

The overlap between the same Bloch orbitals may not be equal to one if the atomic orbital associated with the Bloch orbital interacts with the same atomic orbital in a different unit cell.

The overlap population between two Bloch orbitals is given by:

$$
OV\ POP_{gijk} = n_{gk} \left(c_{gik}^{*} c_{gjk} \langle \varphi_{ik} | \varphi_{jk} \rangle + c_{gjk}^{*} c_{gik} \langle \varphi_{jk} | \varphi_{ik} \rangle \right) \tag{6.41}
$$

This quantity is called the crystal-orbital overlap population (COOP) and will be discussed

below in more detail. Unlike the molecular case, there may exist an overlap population between a Bloch orbital and itself. To calculate this, we use:

$$OV\ POP_{gik} = 2n_{gk}\left(c^{*}_{gik}c_{gik}(<\varphi_{ik}|\ \varphi_{ik}> - 1)\right) \qquad (6.42)$$

In cases where the atomic orbital associated with the Bloch orbital does not interact with itself in other unit cells, the overlap ($<\varphi ik|\varphi ik>$) will be one (as they are normalized). If the overlap integral is not equal to one, any difference is due to the overlap with the same atomic orbital in a different unit cell. Any such contribution must be associated with the overlap population as it represents electron density associated with a chemical bond.

The COOP is equally divided between the two Bloch orbitals and an expression for the population of a particular Bloch orbital is just a sum of all the COOP terms with all other Bloch orbitals:

$$POP_{gik} = \frac{1}{2}n_{gk}\sum_{j=1}^{N}\left(c^{*}_{gik}c_{gjk}<\varphi_{ik}|\ \varphi_{jk}> + c^{*}_{gjk}c_{gik}<\varphi_{jk}|\ \varphi_{ik}>\right) \qquad (6.43)$$

Note that this expression contains both the overlap populations and the population associated with an orbital localized on an atomic centre.

The charge on each atom can be calculated at each point in k-space:

$$q_{vk} = n_{v} - \sum_{i=AOs\ on\ Atom\ v} n_{gk}\sum_{g=1}^{N} POP_{gik} \qquad (6.44)$$

The charge on each atom is then an average of all the charges calculated at different points in k-space. In calculating the atomic charges, two other useful quantities are calculated.

These are the density of states (DOS) and the crystal-orbital overlap population (COOP). These are the band theory equivalents of the molecular energy levels and the molecular bond order.

6.4.5 Calculating The Dipole Moment

A dipole moment is created by the separation of charges and is proportional to the magnitude of the charges and the distance of separation. In systems that contain distributions of charges, it is the distance between the barycentres of the positive and negative charge distributions that determine the magnitude of the dipole. For molecular systems (containing K atoms), the barycentre of the positive charge distribution is:

$$D_{nuclear} = \sum_{K} R_K Q_K \Big/ \sum_{K} Q_K \qquad (6.45)$$

where R_K is the atomic position and Q_K is the charge on the nucleus. The electronic barycentre of an electronic distribution described by a wavefunction (ψ) is given by:

$$D_{electronic} = \langle \psi | er | \psi \rangle \qquad (6.46)$$

If the barycentres of the positive and negative charges do not coincide, a dipole moment exists.

The evaluation of the nuclear barycentre is trivial, while the evaluation of the electronic barycentre can be very tedious. Within the LCAO-MO approximation, each wavefunction (ψ) is a linear combination of N atomic orbitals. The electronic barycentre becomes:

$$D_{electronic} = \sum_{i=1}^{N} \langle \psi_i | er | \psi_i \rangle = \sum_{i=1}^{N} \langle \sum_{j=1}^{N} c_{ij}\chi_j | er | \sum_{k=1}^{N} c_{ik}\chi_k \rangle \tag{6.47}$$

This expression yields numerous terms that have the form:

$$c_{ij}^{*} c_{ik} \langle \chi_j | er | \chi_k \rangle = e c_{ij}^{*} c_{ik} \langle \chi_j | r \chi_k \rangle = e c_{ij}^{*} c_{ik} \langle \chi_j | \chi_k' \rangle \tag{6.48}$$

where the last term is actually an overlap integral between an atomic orbital (from the basis set) and a modified atomic orbital (χ). This modified atomic orbital is a linear combination of atomic orbitals that have higher n quantum numbers (and possibly different l values as well). The number of overlap integrals needed to perform a dipole calculation on even a small molecule can be quite large. For this reason, approximation methods have been developed to simplify the calculation.

Some of the terms in equation 6.47 have a special meaning as they are terms that contain atomic orbitals on the same atomic centre. When one of the atomic orbitals is a p orbital and the other is either an s or a d orbital, a significant dipole moment can be produced. This is the hybridization dipole moment and is due to the occupation of hybridized orbitals whose barycentre does not coincide with the atomic centre. The mixing that occurs to form the various hybridization dipoles is shown in figure 6.5.

If one analyses all of the terms (from equation 6.48) in the complete dipole analysis, it becomes clear that the dipole contributions can be divided into three separate categories. The main contribution to the dipole moment is the electron density associated with each atomic centre. Between the atomic centres are chemical bonds that also contribute to the dipole

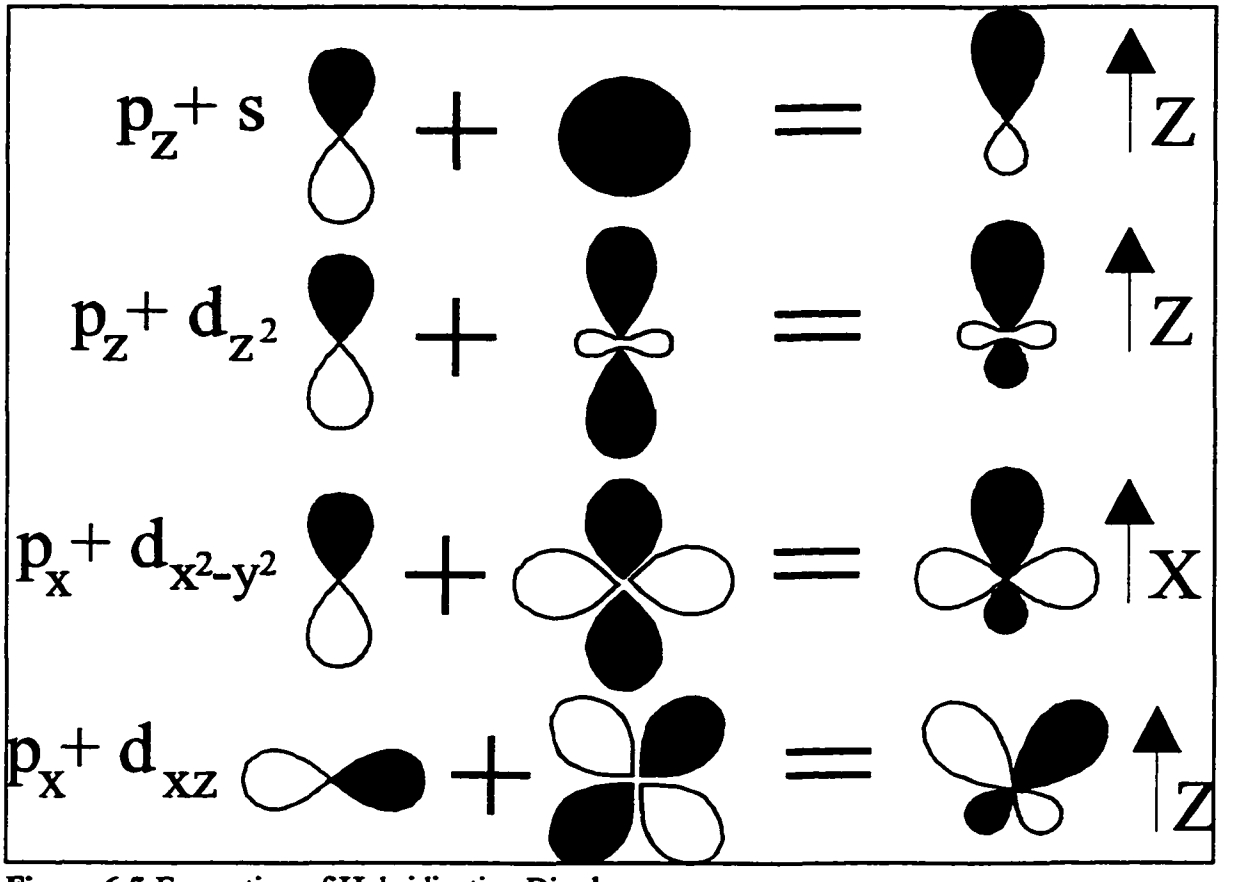

Figure 6.5-Formation of Hybridization Dipoles

moment. The last contribution is the hybridization dipole that is usually associated with an occupied 'lone pair' of electrons.

This is most clearly demonstrated with the water molecule as it has two occupied lone pairs of electrons (formed from the hybridization of the 2s and 2p orbitals). These lone pairs make a significant contribute to the dipole moment of the water molecule. The hybridization dipole is also used to explain why the dipole moment of CO places the positive end of the dipole on the more electronegative oxygen atom [6.32].

Using a Mulliken population analysis allows one to calculate the electron density on the atomic centres. The bond's electron density is simply divided up between the two atomic centres sharing the bond. This simplification is poor for the description of polarized bonds but

works well in cases where the difference in electronegativity between the two bonding atomic centres is small.

This division of the complete dipole moment into smaller components helps to reduce the complexity of the problem of calculating a dipole moment from electronic wavefunctions. The total dipole then becomes a sum of the hybridization dipole and the dipole arising from the atomic charge distribution. Unfortunately, the extended-Hückel procedure is known to overestimate atomic charges. We will therefore concentrate on calculating changes in the hybridization dipole and qualitatively look at the atomic charge distribution.

For the late transition metals (like platinum) that have an almost filled d band, the surface can be considered as being electron rich. The surface can be envisaged as having 'dangling bonds' that are actually occupied hybrid orbitals. These hybridized orbitals make a large contribution to the work function of these metals, which have some of the largest work functions of the transition metals. Chemical bonding between the adsorbate and the surface metal atoms is likely to involve these hybrid orbitals and will likely change the degree of hybridization. Changes in hybridization should result in a change in the work function, although there are other effects to consider. The adsorbate can form its own hybridization dipole upon adsorption and if it is polarizable (like iodine), it can form a polarization dipole that will tend to oppose the surface dipole. This is the reason why xenon adsorption on platinum decreases the work function by 1 V [6.33].

6.5 Molecular Orbital Computer Programs

A series of computer programs were written (by Scott A. Furman) to perform the molecular orbital calculations described above. The programs take the atomic coordinates of

a surface (or molecule) and use the unit cell's translational symmetry to construct the Bloch wavefunctions. The computer programs uses single and/or double ζ Slater orbitals to calculate the overlap integrals between the atoms. Calculation of the energy matrix (***H***) elements can be done by several methods, as described in section 6.4.3. Once the essential matrix elements have been computed, the energy calculation is done at a series of points within the first Brillouin zone. At each ***k***-vector, a set of molecular wavefunctions is generated. Once the energy calculation is complete, a population analysis is done using the eigenvalues and eigenvectors from all the points sampled in the first Brillouin zone. After all of the eigenvalues (MO energies) have been sorted, all of the electrons are 'dumped' into the molecular orbitals (filling lowest energy states first) to determine the Fermi level. Once the orbital occupations are known, the charge at each point sampled in ***k***-space can be calculated from the eigenvectors using a Mulliken population analysis. The atomic charge calculated by the program is an average of the charges from each ***k***-vector. The density of states (DOS) and crystal-orbital overlap populations (COOP) are generated as intermediate steps during the population analysis and can be analyzed once the calculation is complete.

The hybridization dipole is then calculated from the coefficients of the molecular orbitals. The computer program that does this calculation contains a series of routines to calculate the individual single-centre hybridization terms that have the form:

$$\langle p_i | \boldsymbol{r}_j | s, d_l \rangle \tag{6.49}$$

for all combinations of i, j, and l. This provides the hybridization dipole for the **x**, **y**, and **z** directions. The expressions for the single-centre overlaps were determined using the software package MAPLE for all possible orbital combinations. Obviously, only single-centre overlap

integrals that involve p orbitals need to be calculated.

All of the information calculated by these programs (atomic charges, atomic hybridization dipoles, DOS, and COOP) is stored in simple ASCII data files. Charges are calculated as the partial electronic charges while dipole moments are calculated in atomic units of length (1 a.u. = 2.541 D). Dipole moments will be reported here will be converted to Debye.

There are several extra programs to process the information from the calculations and to help generate the data file that contains the initial parameters (atomic coordinate, orbital exponents) for the calculation. A typical calculation using 500 orbitals in the basis set and sampling 81 $\boldsymbol{k}$-vectors in the first Brillouin zone requires 12 hours of computational time (on a 200 MHz pentium computer), 350 Mbytes of disk space, and approximately 8 Mbytes of memory. There is no current limit to the size of the basis set or the number of $\boldsymbol{k}$-vectors that can be used for the calculation.

6.6 Calculation of Changes in Work Function

To investigate the effect of iodine adsorption on the work function of Pt(111), a simple model of the surface region was used. Seven layers of platinum atoms arranged in the fcc structure represent the surface region. 81 $\boldsymbol{k}$-vectors within the first Brillouin zone were sampled for the calculations, which is typical for such surface calculations [6.34].

The orbital parameters for the calculations are given in Table 6.1. The parameters for iodine are taken from the valence orbital ionization energy (VOIE) and the charge parameters are taken from a linear extrapolation of the VOIE of the first ionized state. The double-ζ parameters from platinum are taken from the literature where they have been used to calculate

energy differences in hydrocarbon bonding sites [6.35].

Table 6.1-Atomic Orbital Parameters For Calculations

Element	Orbital	Slater Exponent	Orbital Energy Charge Iteration Parameters $E/eV=-(A*q^2 + B*q + C)$		
			A	B	C
Platinum	5d	0.6334*6.013 + 0.5513*2.696	2.331	8.522	12.002
Platinum	6s	2.554	1.05	5.112	8.728
Platinum	6p	2.554	0.95	3.892	5.209
Iodine	5s	2.681	0	0	23.3
Iodine	5p	2.332	0	7.94	14.0

As shown in figure 6.6 for a series of bare platinum calculations, the hybridization dipole of the surface atoms does not change significantly with increasing the number of layers included in the calculation. The charge on the surface atoms converges reasonably well by the seventh layer. An attempt was made to determine the charges on the platinum atoms self-consistently. All attempts to do this were unsuccessful. For this reason, the charge distribution within the metal can only give a qualitative picture of shifts in electron density.

The density of states provides information about changes in the energy levels that occurs after adsorption. The density of states of the platinum surface before and after iodine adsorption in the threefold sites is given in figure 6.7. The change iteration for the iodine yielded a charge of -0.1 $|e|$. The charge iteration parameters indicate that the iodine level would be at approximately -14 eV and this is seen in the DOS curves.

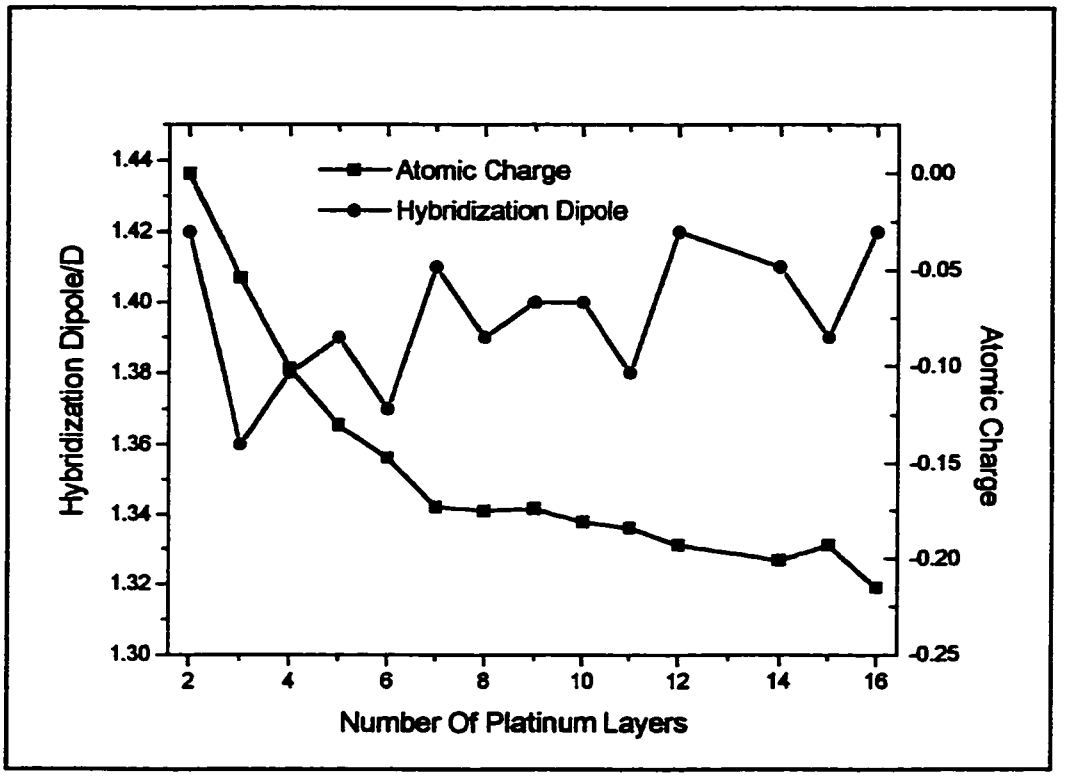

Figure 6.6-Variation of Charge and Dipole With Number of Platinum Layers

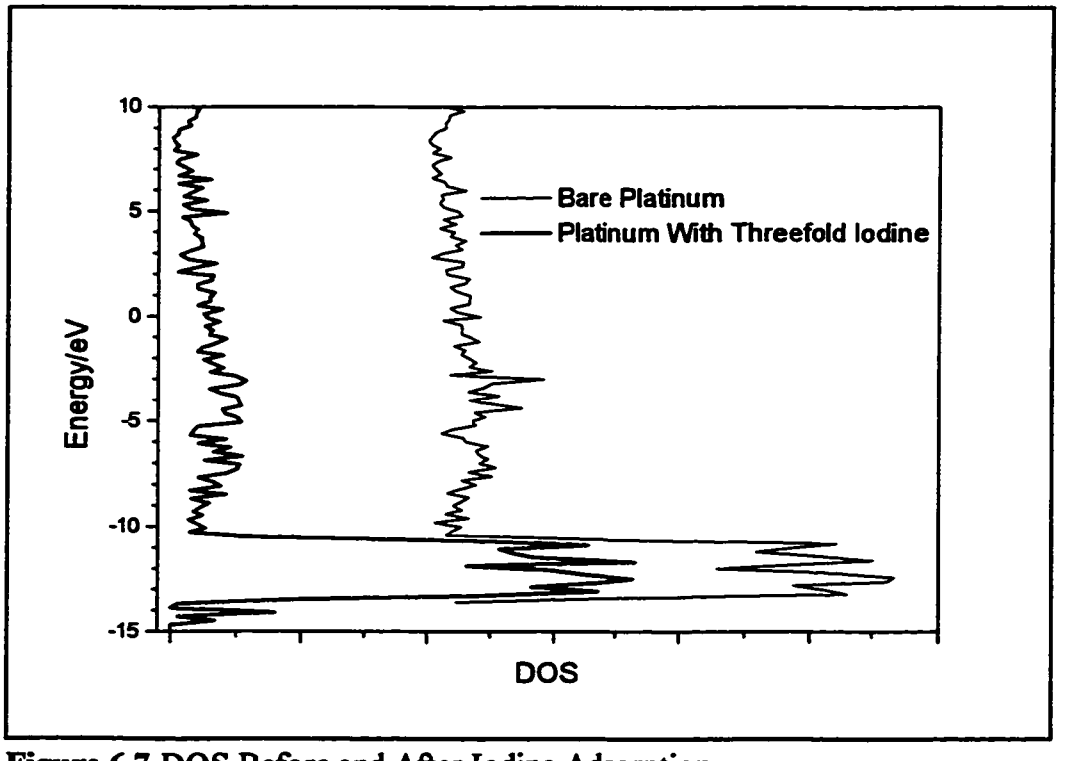

Figure 6.7-DOS Before and After Iodine Adsorption

In such a model there are actually two surfaces created and iodine atoms are only allowed to adsorb onto one of them. Preliminary calculations showed that for systems with more than five layers, adsorption at one surface did not affect the charge distribution at the other surface.

There are two fundamental questions to be addressed here. The first is whether or not this calculation can predict the correct sign and magnitude of the work function change observed during iodine adsorption. The other question to be answered is whether there is a difference in the predicted sign and magnitude of the work function change for the two different adsorption sites (atop vs. threefold). This is evaluated by doing the MO calculations on two ($\sqrt{3}x\sqrt{3}$)R30° structures where the iodine atom sits in either the threefold or atop site. In both cases the charge on the iodine atom was determined self-consistently by using charge dependent orbital energies. The charge calculated in both cases is the same as the charge used in the initial calculation parameters.

Dipoles calculated from the atomic charge distribution within the metal (using equation 6.45 for positive and negative atomic charges) were one to two orders of magnitude too large (~40 Debye within the metal). This is likely related to the fact that the metal charges were not determined self-consistently.

The hybridization dipole moment per bare-surface platinum atom was calculated to be 1.4 D. The surface contribution to the work function is equal to the negative of the potential drop ($\Delta\varphi$) across a two dimensional array of these dipoles. If the area per dipole (p) is A, the potential drop across the array of dipoles is:

$$\Delta\varphi = -\frac{ep}{A\varepsilon_0} \qquad (6.50)$$

For platinum, the area occupied per atom is 5.465 Å^2. This gives a potential drop across the interface of 2.4 V. This result is not meant to be an estimate of the actual work function of the platinum (which also contains a contribution from the chemical potential) but provides a reference point for the calculations.

As a comparison, the dipole moment can be calculated from the work function changes observed during iodine adsorption. The dipole moment at zero coverage (p_0) should not contain any effects due to depolarization and is easily calculated from the adsorption data. Using the adsorption data in Chapter 4 (figure 4.10) at a coverage of 0.07 ML ($1x10^{14}$ atoms/cm^2) the work function has changed by 0.380 V. As each adsorbate atom occupies an effective area of 78 Å^2 at this coverage, the dipole moment per adsorbate (from equation 6.50) is 3.1 D.

Placing an iodine in the threefold site and using a Pt-I bond distance of 2.64 Å, the hybridization dipole on the surface platinum atoms drops to 0.23 D. This would correspond to a decrease in the work function of 2 V. The fact that the iodine has such a large effect is encouraging but the magnitude of the work function change is actually too large. However, the iodine atom also develops a hybridization dipole equal to -5.2 D. This dipole tends to increase the work function. Given that in the $(\sqrt{3}x\sqrt{3})R30°$ structure the area per dipole is three times larger than in platinum, this makes a contribution to the work function (using equation 6.50) of +3 V. The sum of these two contributions is +1 V, indicating that the work function should increase.

When the iodine is moved from the threefold site to the atop site, the hybridization dipole of iodine drops to -3.7 D and the charge increases to -0.3 |e| from -0.1 |e|. As the dipole per unit area has not changed, the potential drop across this layer is 2.1 V. Again, this would tend to increase the work function, though not by as much as the threefold iodine. The platinum atom bonding with the atop iodine reduces its hybridization dipole by 1.1 D. This would lower the work function by only 0.7 V. This is lower than might be expected because the hybridization dipoles of the other two surface atoms in the $(\sqrt{3}x\sqrt{3})R30°$ unit cell do not change when the iodine is in the atop position. The overall work function would be expected to increase (by 1.4 V).

The charge on the platinum atoms after iodine adsorption is calculated to be positive (0.17 |e|). Before adsorption it is calculated to be negative (see figure 6.6). This suggests that iodine adsorption tends to push the electrons back into the metal. This is what is qualitatively expected for a decrease in the work function. However, the poor refinement of the charges on the metal centres makes it difficult to estimate how much this would alter the work function.

The distance between the iodine and metal surface is one of the parameters that has a large effect on the magnitude of the hybridization dipole changes. The distance used in the above calculations was obtained from a SEXAFS experiment and may actually represent an atomic height above the metal plane rather than an actual bond distance. If the iodine atom is placed 2.6 Å above the threefold site, the hybridization dipole of the metal only decreases by 0.5 D, which would lower the work function by 1.7 V. The hybridization dipole on the iodine is -2.84 D. This corresponds to a work function increase of 1.6 V. The overall result would be a lowering of the work function by 0.1 V.

From these results, two conclusions can be drawn. Firstly, the distance between the platinum and the iodine atoms must be determined accurately. This is currently being done in a joint project with the K. Mitchell group at the University of British Columbia using tensor LEED. This technique provides the three dimensional coordinates of the surface atoms and would allow a better model to be used for these calculations. The second conclusion is that there is a relationship between the strength of the platinum-iodine bond and the degree of hybridization. As the iodine moves closer to the surface, the bond becomes stronger. As the bond gets stronger, the hybridization dipole of the platinum decreases and that of the iodine becomes larger. Both hybridization dipoles point away from the surface so these two effects oppose each other and tend to cancel one another.

These calculations are not able to reproduce the observed change in the work function that occurs during iodine adsorption. The electron density of the surface metal atoms is pushed back into the bulk of the metal but the formation of a hybridization dipole on the iodine cancels these effects. It is tempting to simply remove the 5s iodine orbital from the basis set (eliminating the hybridization dipole on the iodine) but the calculated changes in the work function only based on the hybridization dipole of the metal are too large.

The formation of a polarization dipole can be used to qualitatively explain the decrease in the work function. The adsorbate becomes polarized by the surface electric field, which is quite high for platinum, and this dipole tends to oppose the surface dipole of the metal. Iodine is known to be quite polarizable but it is difficult to estimate the polarizability of a strongly chemisorbed adsorbate. Such polarization arguments are usually applied to adsorbates that are physisorbed where the adsorbate's electron cloud is not involved with chemical bonding. Xenon, which decreases the work function of platinum by 1 V [6.33], is considered to be more

polarizable than iodine. This suggests that the polarization effect alone cannot account for the decrease in work function caused by iodine adsorption.

7

Adsorption Of Dendrimers On Platinum

7.1 Introduction

Dendrimers are a unique class of molecules with a branched, tree-like structure and large, monodisperse molecular weights (500-10,000 g/mol). The synthesis and properties of such compounds have been the subjects of many recent studies [7.1-7.3]. One aspect of particular interest is the physical size of these molecules. The dendrimers studied here are not large enough to be measured by standard light-scattering experiments and do not readily form crystals, eliminating the possiblity of x-ray analysis.

As these dendrimers are essentially spherical in shape, it is possible that they could form close-packed monolayers on a well-ordered surface. If the dendrimer monolayer formed an ordered structure, and this structure were stable in vacuum, the dendrimer's size could then be investigated by LEED. The size of the unit cell determined by LEED could be used to estimate the size of the dendrimer molecules.

7.2 Chemical Structure of Dendrimers

The chemical structure of the three dendrimers under investigation is shown in figure 7.1 . All of these dendrimers are expected to have low vapor pressures and should be stable in vacuum. Dendrimers **2** and **3** are intended to be spherical, being symmetrical around the central silicon atom. These two dendrimers were specifically synthesized to contain silicon-fluorine bonds at the end of each branch. The reasons for this are explained in the next

section.

The chemical structures of the dendrimers were verified by, ^{1}H, ^{13}C, and ^{19}F NMR (for dendrimers 2 and 3), infrared spectroscopy, and refractive index (fror dendrimers 1 and 2). Although difficult to interpret due to the complexity of the molecules, all of these analytical techniques confirmed the structures given.

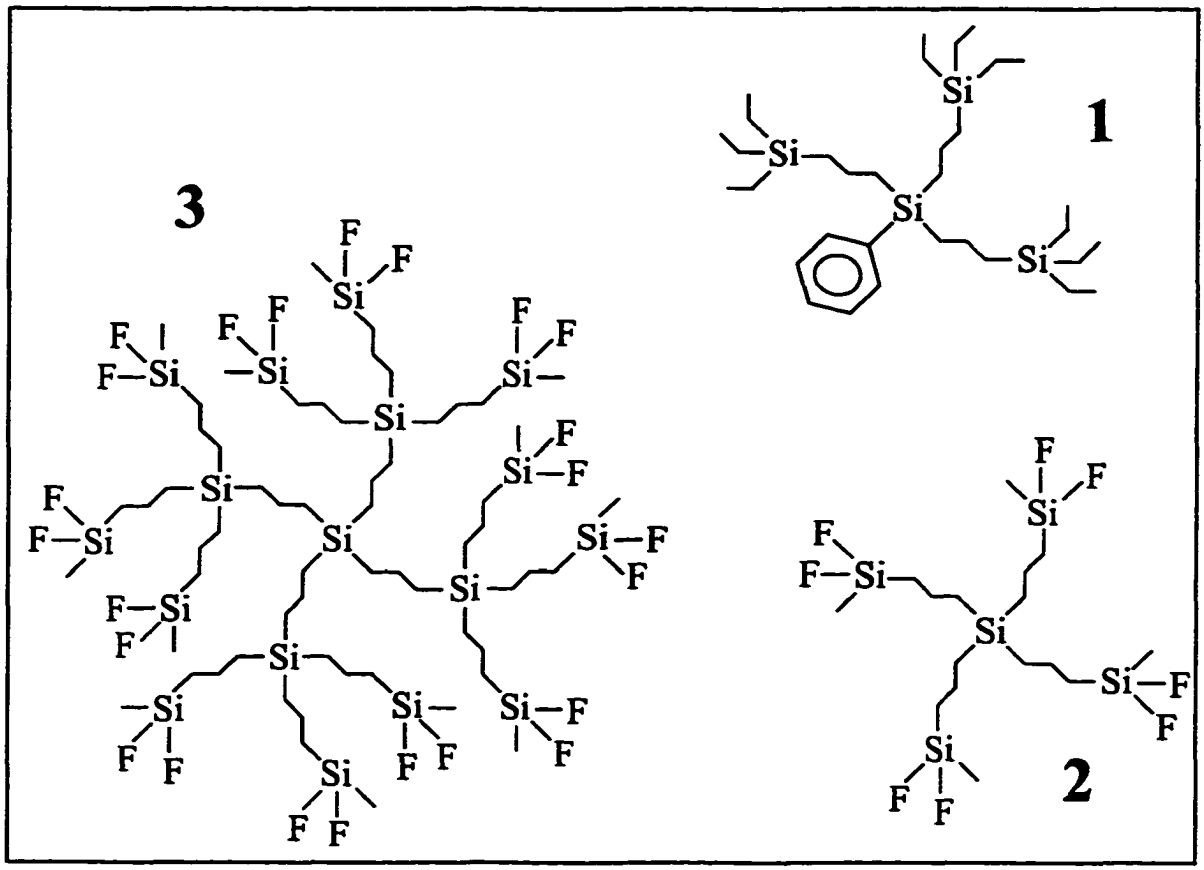

Figure 7.1-Chemical Structure Of Dendrimers

7.3 Use of Iodine AdLayer as Adsorption Substrate

The $(\sqrt{7}x\sqrt{7})R19.1°$-I adlayer was chosen as the substrate for the dendrimer adsorption experiments for a number of reasons. Perhaps the most important feature of this iodine adlayer is its chemical stability. Iodine has been shown to form a number of well-ordered and chemically-inert structures on Pt(111). The $(\sqrt{7}x\sqrt{7})R19.1°$ structure is

unaffected by most solvents and interacts only weakly with common contaminants. A blank transfer experiment, where the (√7x√7)R19.1°-I structure was placed in direct contact with liquid hexane for 30 seconds, showed very little contamination, as measured by the carbon intensity in the Auger spectra in figure 7.2.

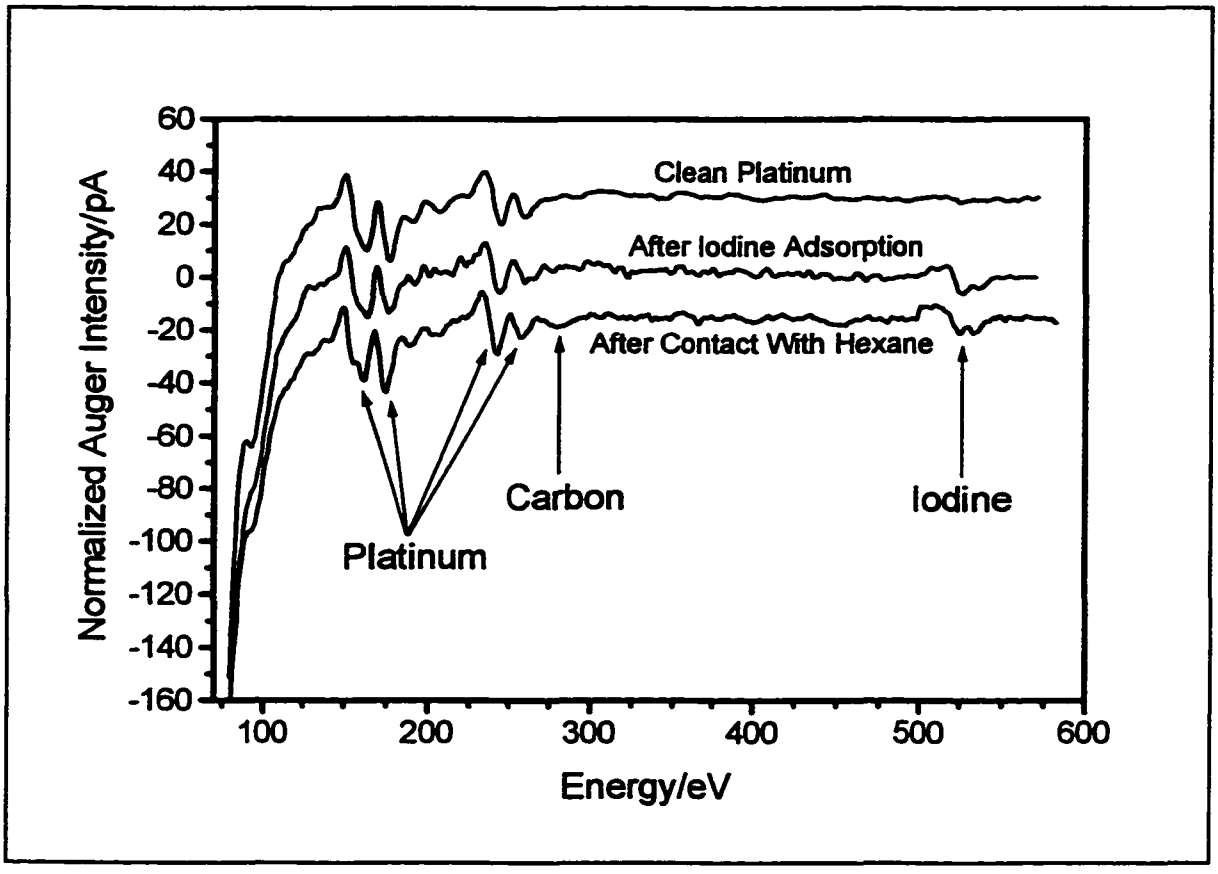

Figure 7.2-Iodine-Covered Platinum Before and After 30 Second Contact With Hexane

The (√7x√7)R19.1° -I structure also provides a useful reference for measuring the size of the dendrimer molecules. Monolayers of the dendrimers would be expected to have large real-space unit cells with correspondingly small unit cells in reciprocal space. The size of the reciprocal-space unit cell would be determined from the LEED pattern of the surface, which would be expected to consist of a superposition of the dendrimer pattern, the (√7x√7)R19.1° iodine pattern, and the platinum (1x1) pattern. At energies where the

platinum integral beams are visible (above 70 eV), the spots from the dendrimer pattern would be close together, making measurements of the unit cell size difficult. The $(\sqrt{7}x\sqrt{7})R19.1°$ reciprocal-space unit cell, approximately 2.5 times smaller than the platinum (1x1) unit cell, could be used as a calibration point for the dendrimer unit cells as it is visible at energies as low as 18 eV. At these lower energies, the dendrimer diffaction spots would be less-tightly spaced and easier to measure.

The final reason for the use of iodine is its high polarizabilty. Dendrimers **2** and **3** are both spherically symmetrical and would be expected to have no permanent dipole moment. Therefore, any attractive forces felt by the dendrimers would be expected to be governed by induced-dipole interactions. The strength of these interactions is proportional to the product of the polarizability of the two interacting species, as shown by the London formula:

$$V = \frac{3}{2r^6}\alpha_1\alpha_2\frac{I_1 I_2}{I_1 + I_2} \qquad (7.1)$$

In this equation, α is the polarizability, I is the ionization energy, and r is the dipole separation.

There are two significant induced-dipole interactions to consider. The interaction between dendrimer molecules is proportional to α_D^2, where α_D is the polarizabiltiy of the dendrimer molcule. The interaction between the dendrimer and the surface is proportional to $\alpha_D\alpha_S$, where α_S is the polarizabilty of the surface. If α_D can be lowered below α_S, the dendrimer should interact with the surface more than it does with other dendrimer molecules. This would favor the formation of a monolayer of dendrimer to the formation of dendrimer multilayers.

This situation can be achieved by lowering α_D and/or increasing α_S. Iodine is highly polarizable and is expected to increase α_S from the bare platinum value. The dendrimer's polarizability can be lowered by fluorinating the endgroups of the dendrimers, an effect well known in teflon surface chemistry.

The decrease in polarizability can be measured by comparing the refractive indexes (n_r) of the fluorinated and non-fluorinated dendrimers. Although no non-fluorinated analogue of dendrimer **2** was available, the refractive indexes of a number of non-fluorinated compounds have been measured [7.2]. All of these compounds had a refractive index of approximately 1.5 (±0.02). For example, $Si(CH_2CH_2{=}CH_2)_4$ has a refractive index of 1.49. The refractive index of a non-fluorinated analogue of dendrimer **2** would be expected to be in this range as well. The polarizability can then be calculated using the Clausius-Mossotti equation:

$$\frac{n_r^2 - 1}{n_r^2 + 2} = \frac{N\alpha}{3\varepsilon_0} \qquad (7.2)$$

where N is the number density.

The refractive index of dendrimer **2** was measured to be 1.42. Using the measured density of 1g/mL, the polarizability is 4.0×10^{-38} C^2m^2/J. As there is no density or refractive index data for the non-fluorinated equivalent of dendrimer **2**, it is difficult to estimate how much, if any, the polarizability has decreased. However, for similar compounds, if the refactive index decreases, the polarizability generally decreases.

In the above arguments, it is assumed that the dominating force affecting the dendrimer molecules is due to induced dipoles. But there are polar Si-F bonds around the

outside edge of the dendrimer molecule that can interact with the surface through a dipole/induced-dipole attraction. The interaction energy (V) is given by:

$$V = \frac{\mu^2 \alpha_S}{r^6 4\pi\varepsilon_0} \tag{7.3}$$

where μ is the dipole moment of the polar Si-F bond. When the dendrimers are in intimate contact with a flat surface, the surface does not 'see' a simple ball with an overall dipole moment of μ. The overall interaction energy is a summation of the interactions between the iodine layer and several different Si-F bonds. The surface interacts more with one side of the dendrimer 'ball', and the dipole/induced dipole interactions are stronger for these Si-F bonds because of the $1/r^6$ dependence of the interaction energy. As the iodine layer is highly polarizable, even a small effect of this type would be expected to strengthen the interaction between the dendrimer and the surface and help in the formation of a monolayer.

It should be mentioned that in some preliminary experiments, dendrimer 1 ($n_r = 1.50$), which is not fluorinated, was adsorbed onto the ($\sqrt{7}$x$\sqrt{7}$)R19.1°-I surface from the pure liquid. This produced a macroscopic drop on the surface that was stable at room temperature and a pressure of 1×10^{-8} mbar. The unusually low vapour pressure of dendrimer 1 is a clear indication of the strength of the interactions between dendrimer molecules that must be overcome for the formation of a monolayer.

7.4 Auger and LEED Analysis of the Adsorbed Fluorinated Dendrimers

Adsorption of dendrimers **2** and **3** onto the clean and iodine-covered platinum surface was carried out using the ambient-pressure transfer chamber of the UHV system, as described in the experimental section. The platinum surface was prepared in the usual manner for transfer experiments. After annealing, the clean platinum crystal was allowed to cool to ambient temperature and, in most cases, was dosed with iodine to form the $(\sqrt{7}x\sqrt{7})R19.1°$-I structure. As usual, the iodine coverage was followed using the change in work function and the $(\sqrt{7}x\sqrt{7})R19.1°$ structure was confirmed by LEED.

Adsorbing dendrimer **2** onto the $(\sqrt{7}x\sqrt{7})R19.1°$-I surface by contacting the surface with a 250 μM solution for thirty seconds produced a multilayer structure. The Auger spectrum of this multilayer, shown in figure 7.3, indicates a significant amount of silicon and carbon.

It is clear that the dendrimer multilayer attenuates the platinum Auger signals between 150 eV and 270 eV. The iodine signal at 530 eV is also attenuated by the dendrimer multilayer. The fluorine Auger signal at 675 eV has an inherently low intensity and is not visible in spectra of the dendrimer multilayers. Averaging a series of ten scans in the fluorine region did show evidence of a fluorine Auger transition. The fluorine signal is a doublet, as expected [7.4].

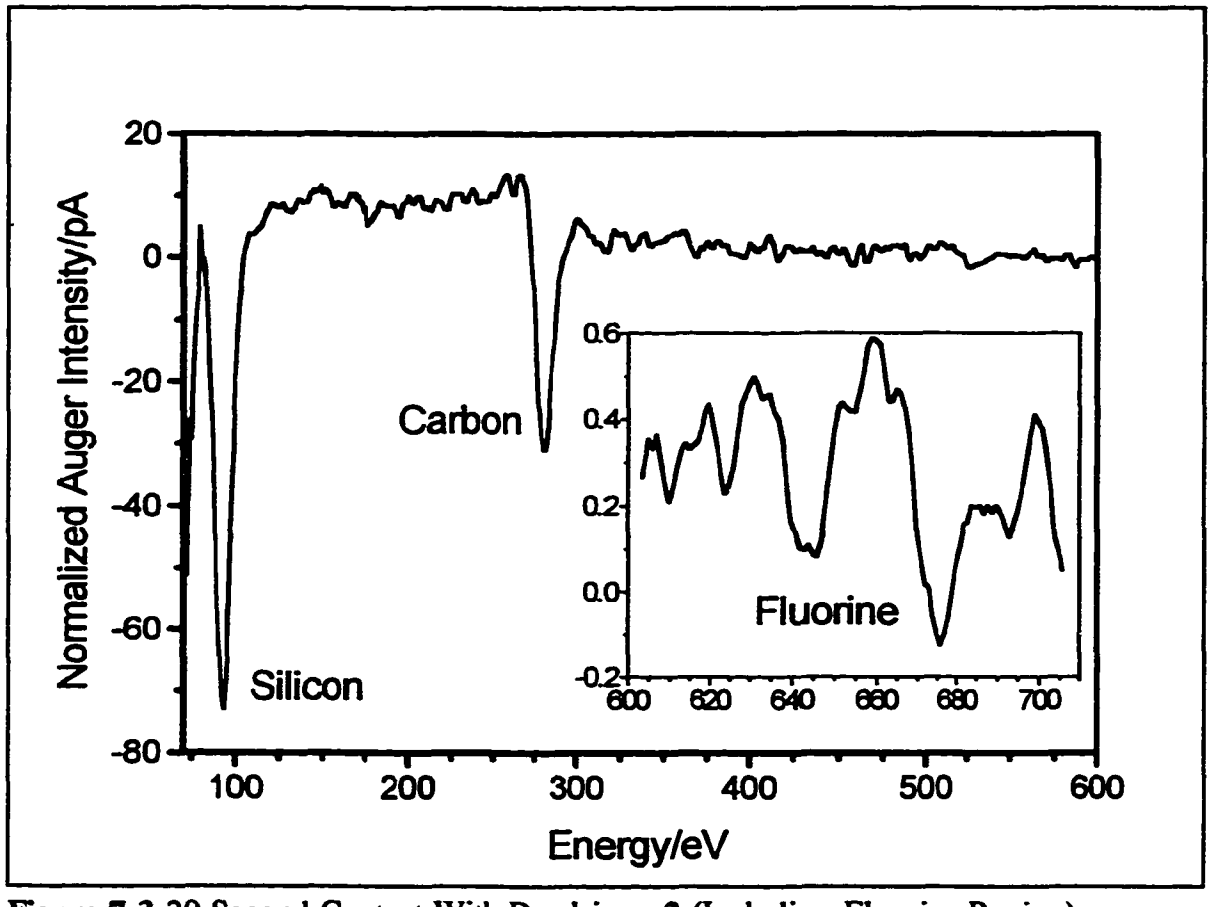

Figure 7.3-30 Second Contact With Dendrimer 2 (Including Fluorine Region)

Contacting the iodine-overed surface with the same 250 μM solution of dendrimer 2 for only one second also adsorbed a significant amount of dendrimer, as judged from silicon and carbon intensities in the Auger spectrum shown in figure 7.4. There appears to be little difference in the intensity of the carbon and silicon Auger intensities between the one second and thirty second contact-time experiments. However, while both the platinum and iodine Auger signals are completely attenuated in the 30 second experiment, both are visible in the one second experiment. These signal attenuations can be used to estimate the thickness of the dendrimer multilayer, as discussed in the next section.

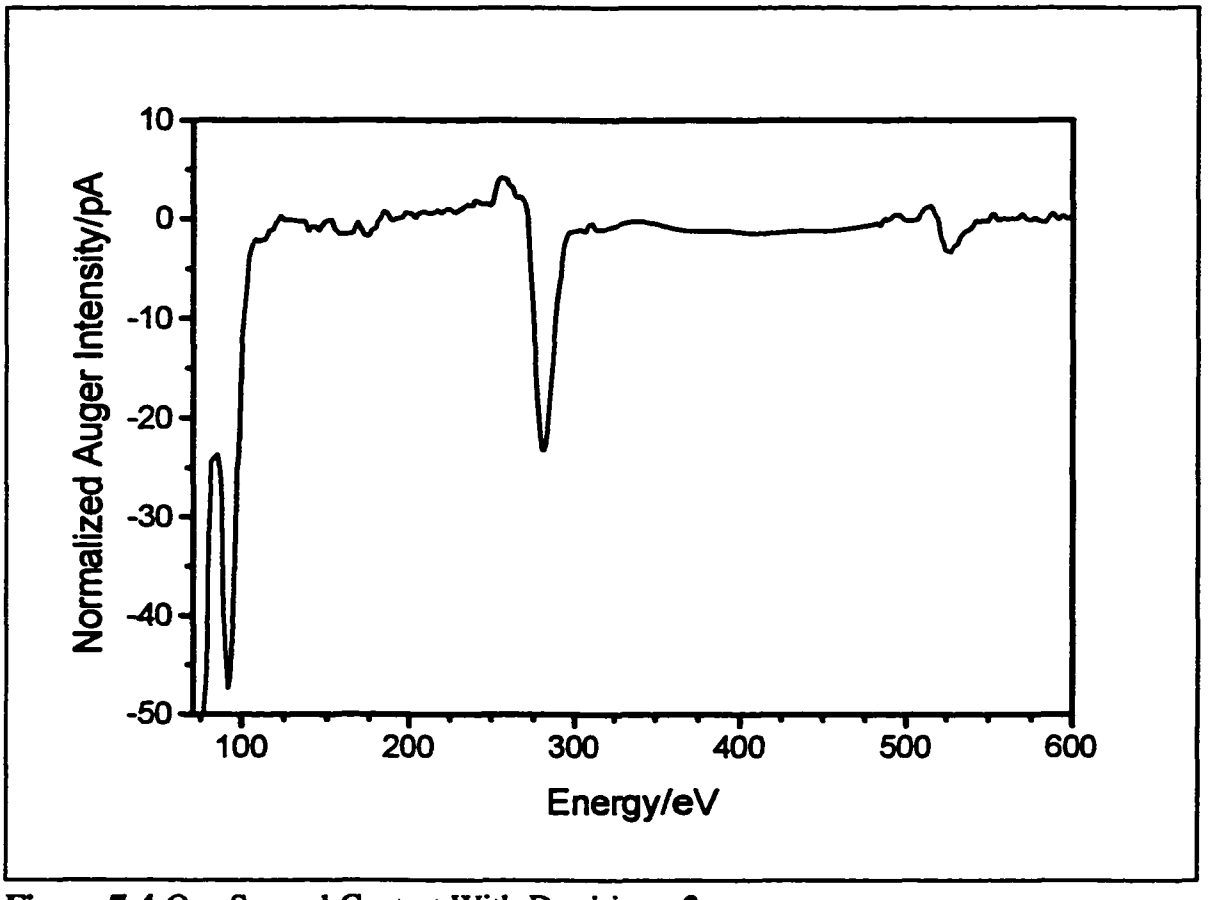

Figure 7.4-One Second Contact With Dendrimer **2**

The multilayers formed by these procedures were then studied by LEED. In the case of the thirty second contact, only a diffuse pattern was observed, indicating a disordered structure. The (1x1) diffraction beams from the platinum could not be seen, even at energies up to 400 eV. After contacting for only one second, the LEED was still diffuse but the platinum (1x1) and the iodine ($\sqrt{7}x\sqrt{7}$)R19.1° diffraction beams were observed at energies above 70 eV. The focussing of the electron gun had to be significantly altered before any diffraction beams were observed. In addition, as the crystal was moved so the electron beam would hit new regions of the surface, the focussing needed constant readjustment. This effect had not been observed in any previous

LEED studies using this set of electron optics and could be due to surface charging. The various iodine adlayers formed on platinum are known to be quite stable and are not susceptible to electron-beam damage. With the dendrimer overlayers present, beam damage was observed as the ($\sqrt{7}$x$\sqrt{7}$)R19.1° structure transformed to the ($\sqrt{3}$x$\sqrt{3}$)R30° structure during the LEED investigations. Exposing one area of the dendrimer-covered surface to the electron beam for more than five seconds caused the iodine to rearrange producing a mixed LEED pattern. Leaving the beam in one spot for several minutes caused the ($\sqrt{7}$x$\sqrt{7}$)R19.1° pattern to disappear and the ($\sqrt{3}$x$\sqrt{3}$)R30° pattern to become dominant.

Adsorbing dendrimer **2** onto bare platinum (with no iodine adlayer) by contacting with a 250 μM solution for 30 seconds also produced a structure with a diffuse LEED pattern. However, the Auger spectrum of this structure (figure 7.5) shows considerably less carbon and silicon than is found in figure 7.3. The notable absence of the silicon Auger peak will be discussed in the section 7.6. The platinum peaks between 120 and 250 eV are not attenuated, also indicating that there is considerably less adsorbed dendrimer on the surface. This clearly demonstrates that the dendrimer is more strongly attracted to the surface when the iodine layer is present and that the arguments made in the previous section about the influence of using a polarizable surface for the adsorption studies are atleast qualitatively correct.

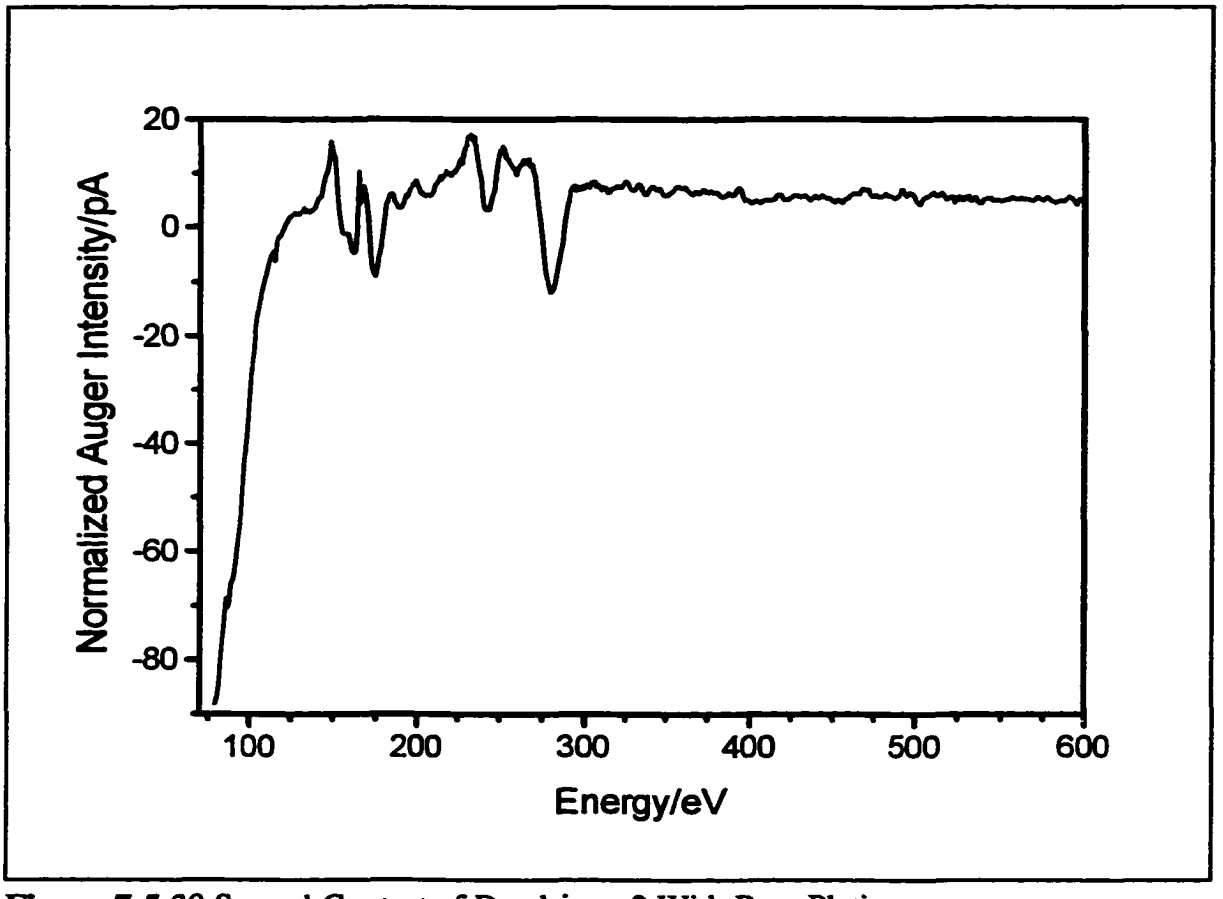

Figure 7.5-30 Second Contact of Dendrimer **2** With Bare Platinum

Contacting the iodine-covered surface with a 220 μM solution of the larger dendrimer **3** for thirty seconds again produced a diffuse LEED pattern. The Auger spectrum, shown in figure 7.6, is similar to that obtained from dendrimer **2**. The silicon and carbon Auger intensities are very strong while the platinum and iodine have only weak Auger intensities. The ratio of silicon to carbon atoms in dendrimer **3** is 1:3.53, while the ratio is 1:3.20 in dendrimer **2**. This means that in dendrimer **3**, there are more carbon atoms per silicon atom when compared to dendrimer **2**. Although simple ratios cannot be used to quantify Auger spectra, when the spectra of the two dendrimers are compared, the intensity of the carbon Auger transition (relative to the silicon signal) for dendrimer

3 is larger than from dendrimer 2.

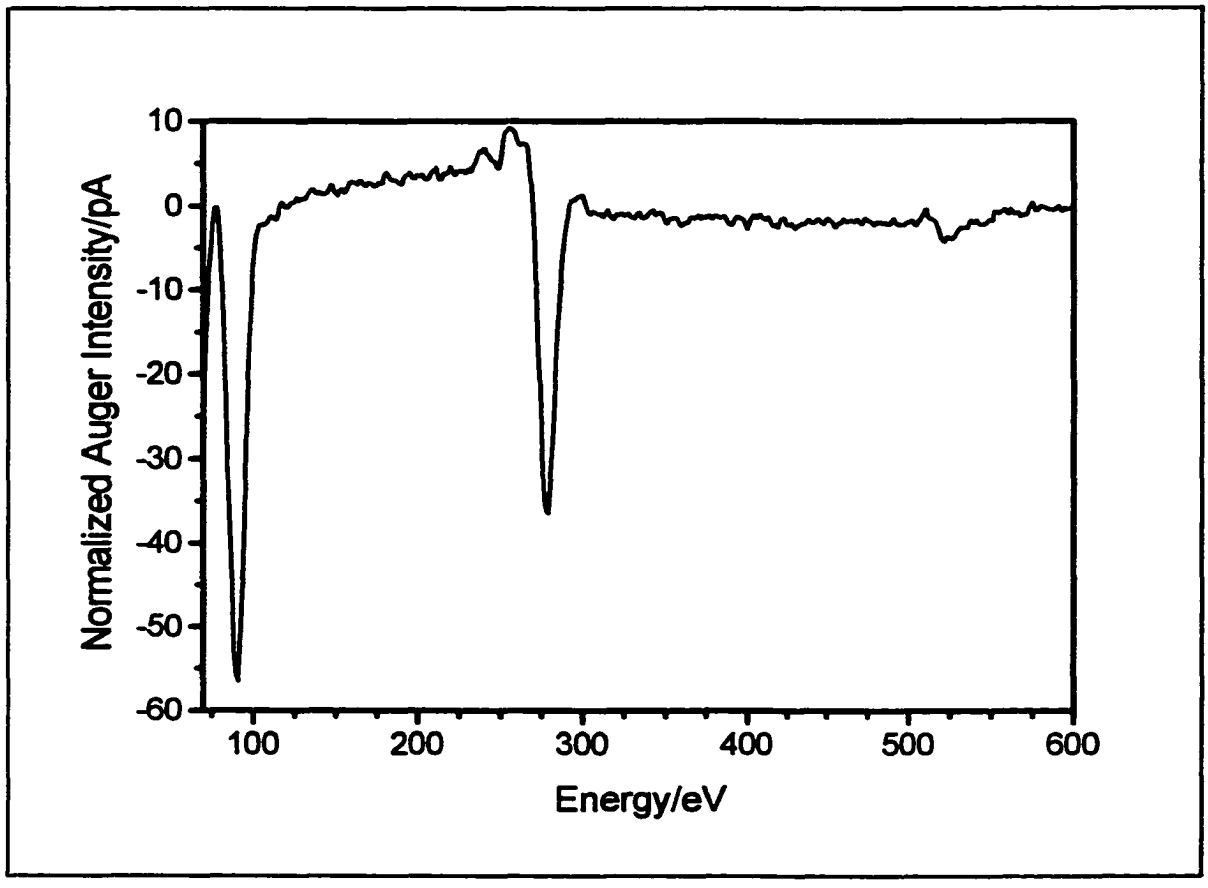

Figure 7.6-30 Second Contact With Dendrimer 3

Adsorbing dendrimer 3 onto only one section of the surface by tilting the crystal (see figure 7.7) before contacting with a 220 μM solution (for 30 seconds) produced a gradient in the thickness of the dendrimer overlayer. LEED analysis showed a very clear ($\sqrt{7}$x$\sqrt{7}$)R19.1° pattern at the end of the crystal that did not come into contact with the dendrimer solution. As the crystal was moved from the region with no dendrimer to the contact region, a diffuse background in the ($\sqrt{7}$x$\sqrt{7}$)R19.1° diffraction pattern steadily increased. The focussing of the electron gun had to be continually adjusted as the crystal

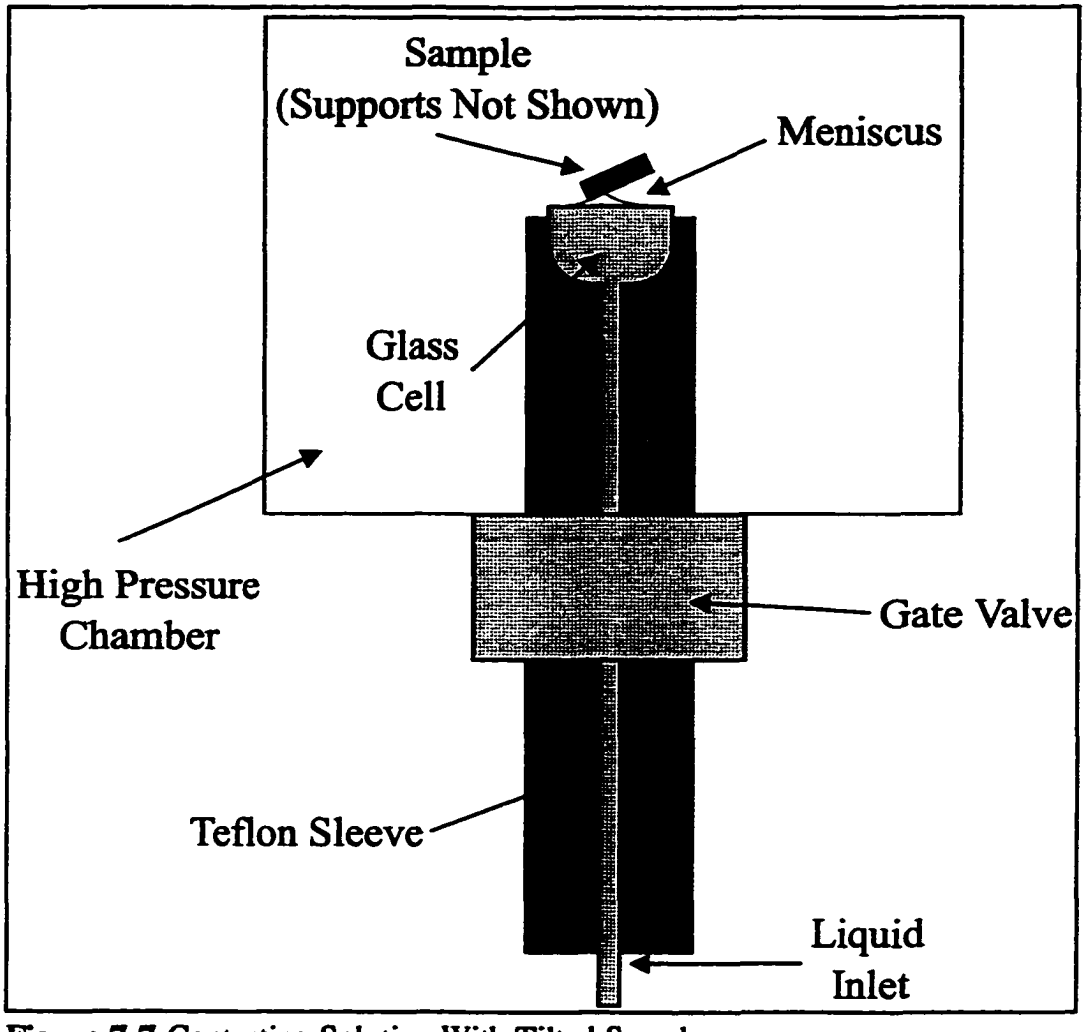

Figure 7.7-Contacting Solution With Tilted Sample

was moved. The direction of the focussing adjustment was constant as the crystal was moved, indicating the dendrimer was thicker closer to the contact region. As with dendrimer **2**, the $(\sqrt{7}x\sqrt{7})R19.1°$ pattern transformed to a mixed $(\sqrt{3}x\sqrt{3})R30°$ pattern under the influence of the electron beam. Eventually the electron gun could no longer be adjusted to yield a clear $(\sqrt{7}x\sqrt{7})R19.1°$ pattern. The (1x1) and $(\sqrt{7}x\sqrt{7})R19.1°$ diffraction beams lost their sharpness and finally disappeared as the diffuse background became dominant.

This experiment clearly indicates a gradient in the dendrimer thickness across the crystal and there was likely a region where the coverage was appropriate for the formation of a dendrimer monolayer. However, no ordered pattern, aside from the platinum and iodine diffraction beams, was observed. It seems likely from these experiments that simply adsorbing the dendrimer onto the surface cannot produce an ordered monolayer.

7.5 Quantification Of Auger Intensities

It is well known that for submonolayer coverages, the intensity of an Auger transition due to an adsorbate will increase linearly with coverage. Unfortunately, when the adsorbed layer becomes thicker than a monolayer, the Auger intensity does not increase linearly and quantification becomes more difficult. There are two main factors that must be addressed to properly analyze Auger intensity data from thick layers of adsorbates. These are the mean-free path of the electron (both incident and scattered) and the sensitivity factors for the Auger transitions of interest.

The Auger current reaching the detector can be thought of as being a sum of Auger currents that originate in different adsorbate layers. The adsorbate layers near the outer surface of the sample contribute the most to the measured Auger current. Deeper layers contribute less, the contribution falling to zero after a certain distance. Where the contribution becomes zero and how fast the Auger contribution drops off is dependent on the mean-free path of the electrons.

Electrons travelling through solids interact strongly with the atomic centres and can only travel a limited distance before an inelastic collision occurs. After each collision, the

electrons loose energy and eventually comes to rest within the solid. Some inelastically-scattered electrons do manage to escape the sample but all Auger information is lost in the scattering process. The probability that an electron will travel a distance d through a sample without having an inelastic collision is:

$$P = \exp(-d/\lambda) \tag{7.4}$$

where λ is the mean-free path of the electron. The mean-free path depends on the energy of the electron, the density of atomic scattering centres in the sample, and the magnitude of the energy-loss (E_l) that will deplete the electron's initial kinetic energy (E_p). From simple scattering theory, the mean-free path is given by [7.5]:

$$\lambda/\text{Å} = \frac{2.11674\,E_p}{E_l \ln(E_p/E_l)} \tag{7.5}$$

The energy loss is usually assumed to be due to plasmons, which fall in a narrow energy range (5-15 eV) for most solids. To account for the difference in the energy-loss mechanisms for organic layers, an alternative formula has been developed [7.6]:

$$\lambda/mg{\cdot}m^{-2} = 49(E_p/eV)^{-2} + 0.11(E_p/eV)^{1/2} \tag{7.6}$$

Once an estimate of the mean-free path for electrons travelling through the adsorbate layer has been made, it is then possible to make an estimate of the thickness of the adsorbate by measuring the attenuation of the substrate's Auger signals (platinum and iodine). The attenuation is given by the ratio of the Auger intensity from the surface with

the adsorbate (I_a) to the Auger intensity from the clean surface (I_c). The number of adsorbate layers (n) can be found from:

$$\frac{I_a}{I_c} = \exp(-(n-1)d/\lambda) \qquad (7.7)$$

where d is the thickness of one adsorbate layer.

The mean-free paths for electrons with different kinetic energies are given in Table 7.1. The λ_1 values were calculated (with equation 7.5) using the experimentally measured density of 1 g/cm^3 for dendrimer **2**. Mean-free paths calculated using equation 7.4 (λ_2-λ_6) used different values for the energy loss (E_l) that span the normal range of plasmon losses.

Table 7.1-Calculated Mean-Free Path Lengths (λ) For Different Auger Electrons

Element	Electron Energy/eV	Mean-Free Path Length/Å					
		λ_1	λ_2	λ_3	λ_4	λ_5	λ_6
		Eqn.7.5	E_l=2eV	E_l=5eV	E_l=10eV	E_l=15eV	E_l=20eV
Si	93	10.7	25.6	13.5	8.8	7.2	6.4
Pt	150	13.5	36.8	18.7	11.7	9.2	7.9
Pt	175	14.6	41.4	20.8	12.9	10.1	8.5
C	278	18.3	59.6	29.3	17.7	13.4	11.2
I	535	25.4	101.3	48.5	28.5	21.1	17.2

The Auger intensities of the main elements present (except fluorine) from the experiments described above is given in Table 7.2. The attenuation of different Auger signals by adsorbed dendrimer layers is given in Table 7.3.

The estimated thickness of a single layer of adsorbate is approximately 15Å for dendrimer 2 and 25Å for dendrimer 3. These estimates are based on simple models using C-C and C-Si distances of 1.4Å. Different values of the mean-free path from Table 7.1 were used to calculate the number of adsorbate layers, as given in Table 7.4.

Table 7.2-Auger Intensities For Adsorbate Systems

Surface Description	Auger Intensities/pA				
	Si(93eV)	Pt(150eV)	Pt(175eV)	C(278eV)	I(535eV)
Clean Platinum	1.3	29	22	0	0
Iodine/Platinum	0	26	17	0	11
30 s Contact of Dendrimer 2 With Pt/I	76	2.6	4.4	44	3.2
1 s Contact of Dendrimer 2 With Pt/I	71	1.6	1.6	27	4.6
30 s Contact of Dendrimer 3 With Pt/I	56	0	0	45	3.3
30 s Contact of Dendrimer 2 With Pt	0	19	16	25	0

From these results it can be seen that the calculated number of adsorbed dendrimer layers is relatively insensitive to the value of the mean-free path used in equation 7.6. There is also very little difference in the number of dendrimer layers that are adsorbed between the one second and 30 second contact times. As the two platinum Auger transitions below 200 eV are near the detection limit of the spectrometer (see figure 7.4), the usefulness of information extracted from the platinum attenuation data is limited. In fact, the number

of layers derived from the platinum attenuation data indicates that more dendrimer is present for the shorter contact time.

Table 7.3-Attenuation Of Auger Intensities

Surface Description	Auger Attenuation (I_s/I_c)		
	Pt(150eV)	Pt(175eV)	I(535eV)
30 s Contact of Dendrimer **2** With Pt/I	0.10	0.26	0.31
1 s Contact of Dendrimer **2** With Pt/I	0.06	0.09	0.44
30 s Contact of Dendrimer **3** With Pt/I	0	0	0.31
30 s Contact of Dendrimer **2** With Pt	0.67	0.73	-

The film thicknesses derived from the iodine attenuation data appear to be more consistent in that the longer contact times do appear to produce thicker layers. However, the noise in the Auger spectra limits the reliability of the estimates of dendrimer thicknesses. Fortunately, the calculated dendrimer thickness is also relatively insensitive to the Auger attenuation. In figure 7.8 the number of dendrimer layers is calculated over a wide range of attenuations and mean-free path lengths (assuming a thickness of 15Å per layer).

Table 7.4-Dendrimer Film Thicknesses From Auger Attenuations

Surface Description	Auger Energy	Number Of Dendrimer Layers (from equation 7.6)					
		λ_1	λ_2	λ_3	λ_4	λ_5	λ_6
30 s Contact of Dendrimer 2 With Pt/I	150 eV	3.1	6.7	3.9	2.8	2.4	2.2
	175 eV	2.3	4.7	2.9	2.2	1.9	1.8
	535 eV	3.0	9.0	4.8	3.3	2.7	2.4
1 s Contact of Dendrimer 2 With Pt/I	150 eV	3.5	7.9	4.5	3.2	2.7	2.5
	175 eV	3.3	7.5	4.3	3.0	2.6	2.3
	535 eV	2.4	6.6	3.7	2.6	2.1	1.9
30 s Contact of Dendrimer 3 With Pt/I	150 eV	-	-	-	-	-	-
	175 eV	-	-	-	-	-	-
	535 eV	2.2	5.7	3.2	2.3	2.0	1.8
30 s Contact of Dendrimer 2 With Pt	150 eV	1.4	2.0	1.5	1.3	1.2	1.2
	175 eV	1.3	1.9	1.4	1.3	1.2	1.2
	535 eV	-	-	-	-	-	-

The above calculations yield a dendrimer film thickness of only a few layers and demonstrate the insensitivity of applying this technique to relatively thin films. An alternative approach is to assume that the intensities of the Auger signals from the dendrimer layers do increase linearly with coverage. This is a much simpler calculation and should provide a lower limit of the actual coverage.

To make such an estimate, the Auger current from a standard sample with a known coverage must be available. The standard should be as chemically similar to the unknown as possible and the Auger spectrum should be acquired under similar experimental

conditions using the same energy analyzer and electron collector. Unfortunately, no such sample was available for our electron optics. However, there are several spectra published in the literature that are suitable for such a comparison.

It is usually not possible to directly compare Auger currents between two different spectrometers as the electron collection efficiency is usually different. A comparison can be made if the same, or similar, sample is run on both spectrometers and the ratio of two peaks within each of the spectra are measured. For the samples studied here, the ratio of the intensities of the platinum (150 eV) and the carbon (278 eV) Auger transitions are used for the comparison.

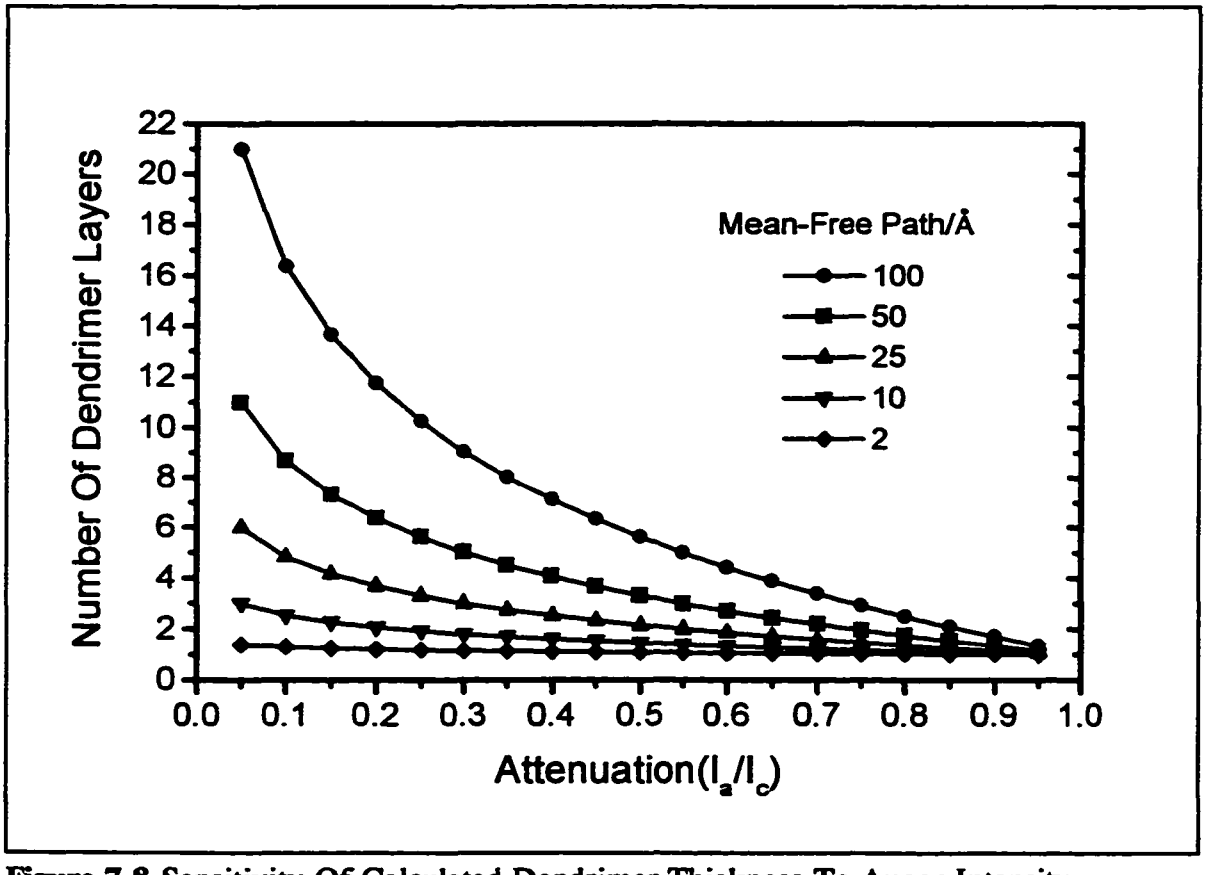

Figure 7.8-Sensitivity Of Calculated Dendrimer Thickness To Auger Intensity Attenuation and Mean-Free Path of Electrons

Fortunately, a reference Auger spectrum of a monolayer of ethylene adsorbed on Pt(100) is available [7.7]. The spectrum was collected using a retarding-field analyzer and the coverage of ethylene was accurately determined by coulometric oxidation to be $8.4x10^{14}$ atoms/cm^2. The ratio of the platinum to carbon Auger transitions is 1:0.939. If an Auger spectrum is acquired using any other retarding-field analyzer and the same carbon to platinum ratio is found, the carbon coverage will approximately be $8.4x10^{14}$ atoms/cm^2.

To make the comparison, an Auger spectrum of an unknown compound (taken from section 7.7) is used to make the comparison. The fact that the structure of the adsorbed layer is unknown does not affect the calculation. The spectrum, shown in figure 7.17, contains mostly platinum and carbon, with only a small amount of silicon present. The ratio of the platinum to carbon Auger intensities was found to be 1:0.849, with a carbon Auger intensity of 19 pA. This means there is 0.91 (0.850/0.939) times as much carbon in the sample from figure 7.17 as there is in the reference spectrum (ethylene on Pt(100)). The carbon coverage is therefore estimated to be $7.6x10^{14}$ atoms/cm^2. Assuming a linear calibration is appropriate, this procedure indicates that there are $4.0x10^{13}$ carbons atoms/cm^2 per pA of detected Auger current for the electron optics used in this thesis.

In the case of the 30 second contact with dendrimer **2**, which had a carbon Auger intensity of 44 pA, the carbon coverage is estimated to be $1.8x10^{15}$ atoms/cm^2. Assuming the dendrimer (containing 16 carbon atoms/molecule) is a 15Å sphere that forms a close-packed layer, each dendrimer layer contains approximately $8.2x10^{14}$ carbon atoms/cm^2.

This coverage corresponds to approximately 2 dendrimer layers. This is in good agreement with the values calculated in Table 7.4, considering that the linear calibration method is expected to yield lower coverages.

7.6 Desorption of Fluorinated Dendrimers

Heating the surface will often induce a monolayer to become ordered as the molecules on the surface gain enough energy to diffuse across the surface. This allows the molecules to reach their favoured thermodynamic positions, usually placing them in specific surface sites or in specific orientations. As no ordered structures were observed at ambient temperature, thermally producing a monolayer became the main focus of these studies.

One of the main problems with trying to thermally order adsorbates is the possibility of thermal decomposition. Mass spectral analysis of the thermal desorption products can be quite informative for monitoring the changes that occur at the surface. However, both dendrimers **2** and **3** have molecular weights that are out of range of the mass spectrometer (>320 amu). These dendrimers do fragment in the mass spectrometer when ionized, and these fragments can then be used instead of the parent ion to track the dendrimer desorptions.

A list of common fragments found for both dendrimers **2** and **3** is shown in Table 7.5. All of these fragments were detected when the dendrimer-covered surface was heated. The strongest signals were found for dendrimer fragments 81 and 84. All other fragments were much less intense and were not always detected during desorption of the

dendrimers. However, it was always observed that mass fragments 38, 40, 66, 109 and 123 tracked with mass 81. These fragments are considered to be due to fragmentation in the mass spectrometer. As seen in Table 7.1, these are all valid dendrimer fragments that could be formed by ionizing dendrimers **2** and **3**.

Table 7.5-Common Mass Fragments Seen During Dendrimer Desorption

Mass/amu	Fragment Identity
38	F_2
40	C_3H_4
66	SiF_2
81	SiF_2CH_3
84	$CH_2CH_2SiCH_2CH_2$
86	C_3H_3SiF
86	$CH_3CH_2CH_2CH_2CH_2CH_3$ (Hexane)
109	$CH_2CH_2SiF_2CH_3$
123	$CH_2CH_2CH_2SiF_2CH_3$
127	I
141	CH_3I

Mass 86 and mass 84 track each other, although mass 86 is much less intense than mass 84. These masses do not track with mass 81 and the other masses associated with the fragmentation of the dendrimer inside the mass spectrometer. The significance of these masses will be discussed below.

Mass 127 is due to the desorption of atomic iodine from the platinum surface. Mass 141 indicates that the iodine has picked up a methyl group from the dendrimer. This methyl transfer could happen either in the mass spectrometer or on the surface as the desorbing atomic iodine passes through the dendrimer layers. From the large number of iodine desorption experiments, described in Chapter 5, there is a constant residual amount of iodine present in the mass spectrometer. In one experiment where the dendrimer was adsorbed onto a clean platinum surface (with no adsorbed iodine), mass 141 was still observed during dendrimer desorption. This indicates that mass 141 is formed in the spectrometer. However, as with some of the other mass fragments, mass 141 was not consistently observed during the dendrimer desorption and the intensity of the 141 mass

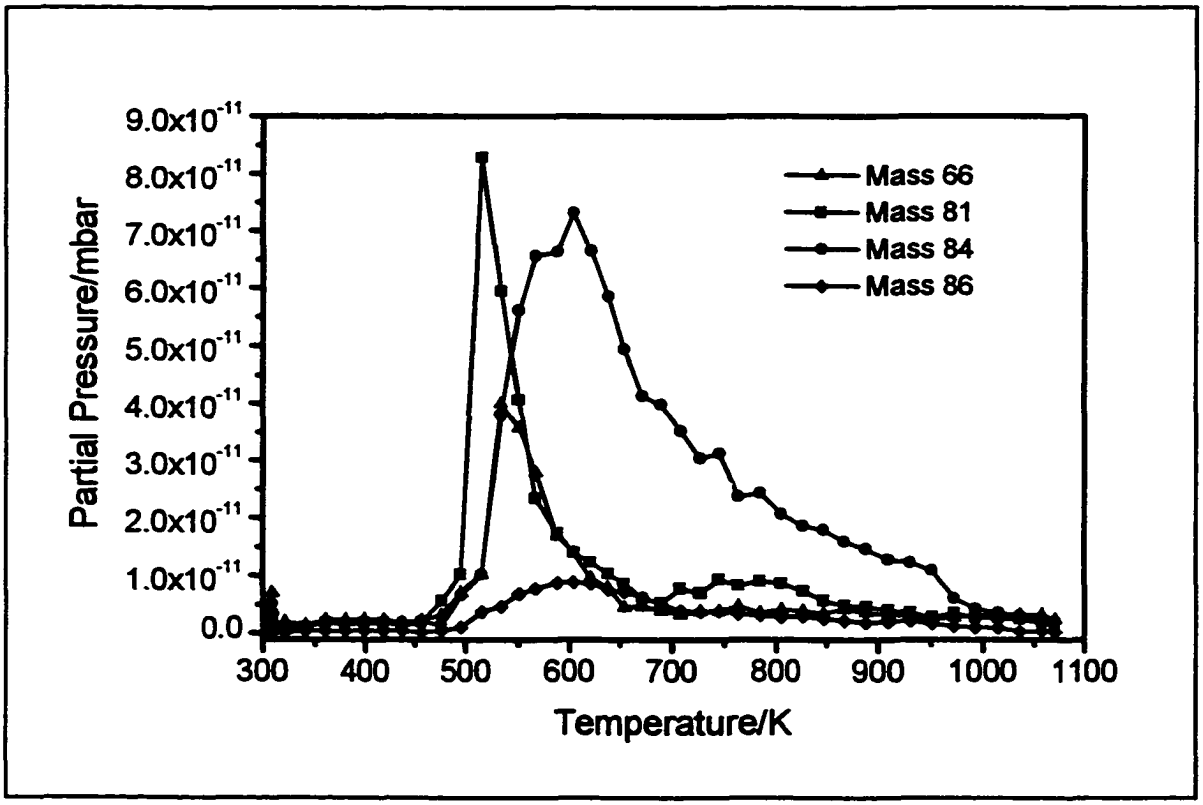

Figure 7.9-Desorption of Dendrimer 2 From Iodine-Covered Platinum After 30 Second Contact

fragment never exceeded the value obtained during the bare platinum experiment by more than a factor of three.

The iodine-covered surface that was contacted for 30 seconds with the solution of dendrimer **2** was heated at 1 K/s to 1100 K. The thermal desorption spectra for several masses are shown in figure 7.9. The desorption of iodine occurs at 500 K and is accompanied the desorption of some dendrimer, as indicated by mass 81. Presumably when the iodine desorbs it disrupts the dendrimer layer and causes some dendrimer to desorb as well.

The desorption of masses 81 and 84 after a one second contact with a dendrimer 2 solution is shown in figure 7.10. In contrast to figure 7.9, there is no desorption of mass

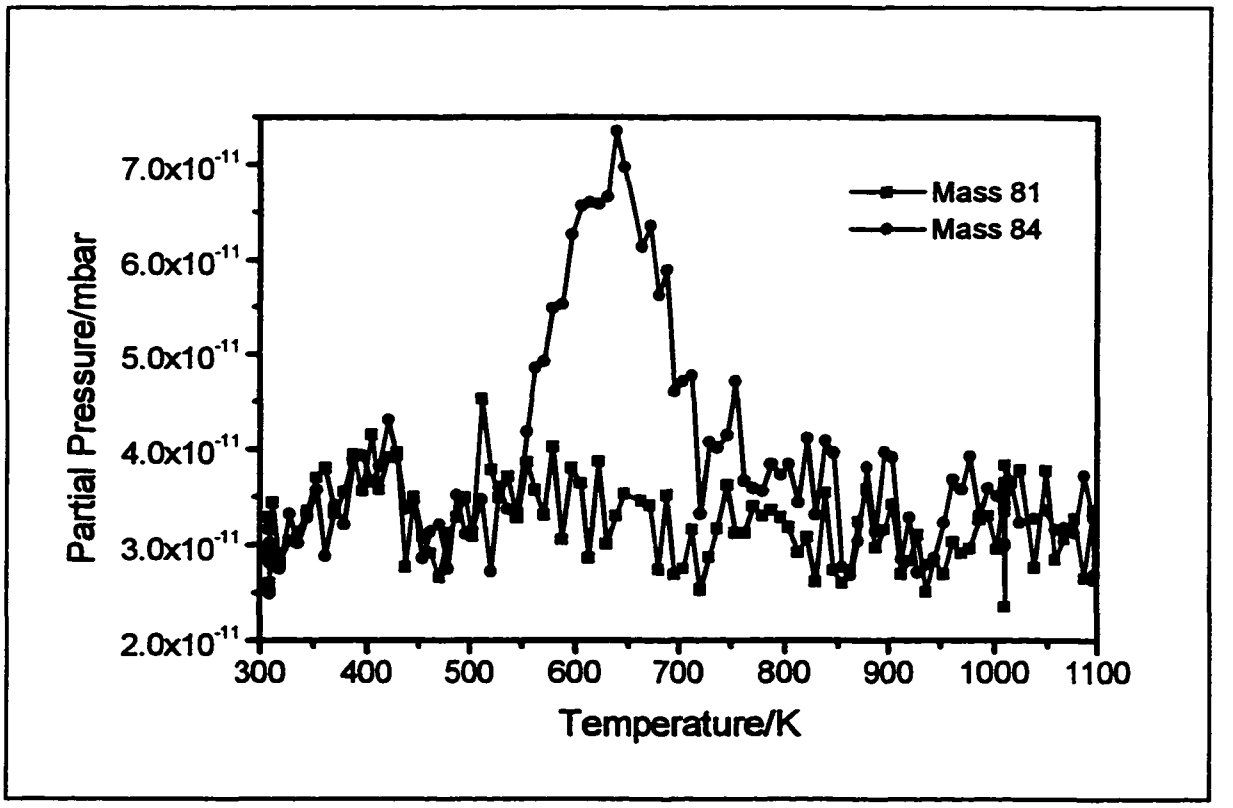

Figure 7.10-Desorption of Dendrimer **2** From Iodine-Covered Platinum After One Second Contact

81. Mass 84 appears to be approximately the same intensity and desorbs over the same temperature range.

The desorption of atomic iodine is also shown as it appears that mass 81 does not appear until the ($\sqrt{7}x\sqrt{7}$)R19.1°-I structure has been disrupted. One explanation is that mass 81 is associated with the decomposition of the dendrimer that occurs once the protective iodine layer is removed. This would allow the dendrimer to come in direct contact with the platinum, which is well-known to catalyze hydrocarbon decomposition. Masses 84 and 86 could also be associated with the fragmentation of an iodine complex formed when iodine atoms pass through the dendrimer layer after desorbing from the platinum substrate.

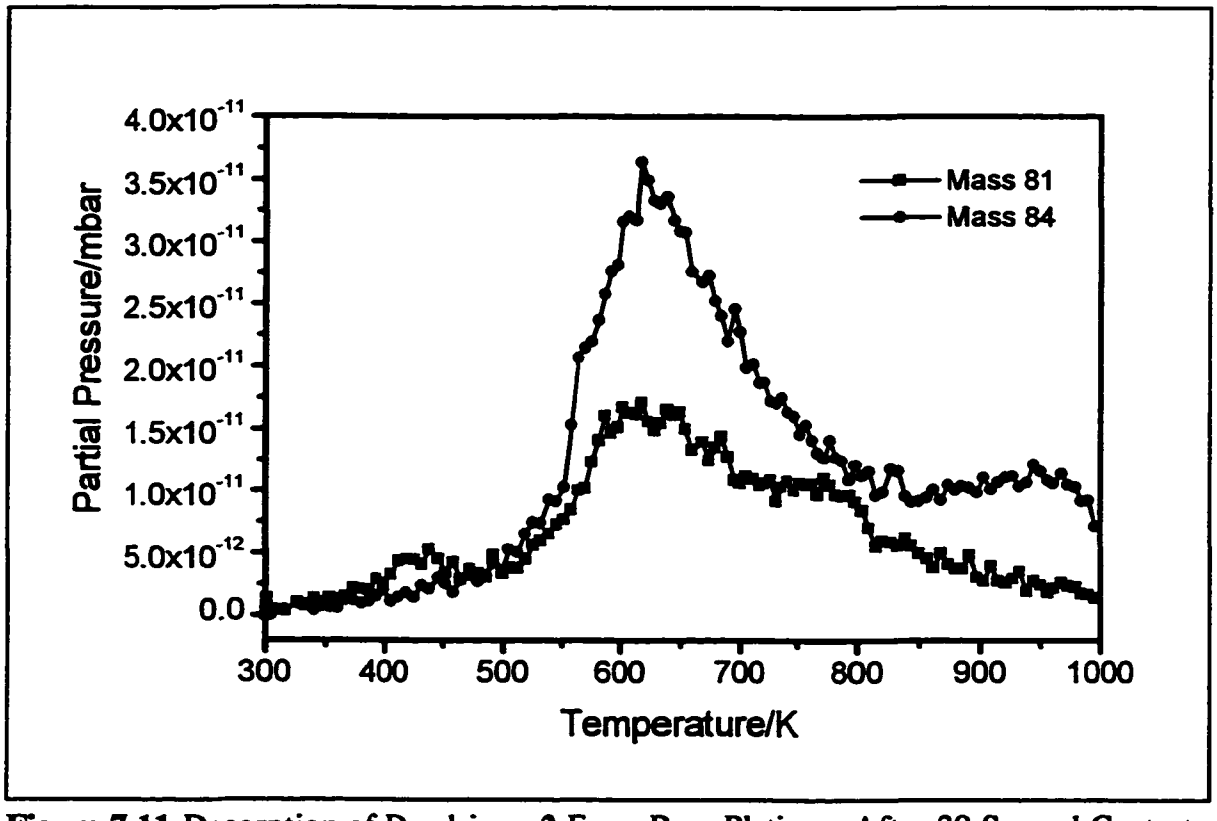

Figure 7.11-Desorption of Dendrimer 2 From Bare Platinum After 30 Second Contact

Desorbing the dendrimer after contacting the bare platinum for 30 seconds with a solution of dendrimer **2** produced the desorption spectrum in figure 7.11. It is known from the Auger analysis in the previous section that the amount of dendrimer adsorbed onto bare platinum is less than when the iodine layer is present. Mass 81 is reduced and mass 84 once again reaches a maximum desorption rate by 625 K. But mass 84 begins to appear at 300 K and steadily increases as the sample is heated. This is consistent with the hypothesis that mass 84 is due to the reaction of the dendrimer with the platinum as mass 84 did not appear in previous experiments until the iodine layer was disrupted.

Desorption experiments using dendrimer **3** produced similar results to those using dendrimer **2**. The desorption of masses 81 and 84 are shown in figure 7.12. Mass 81

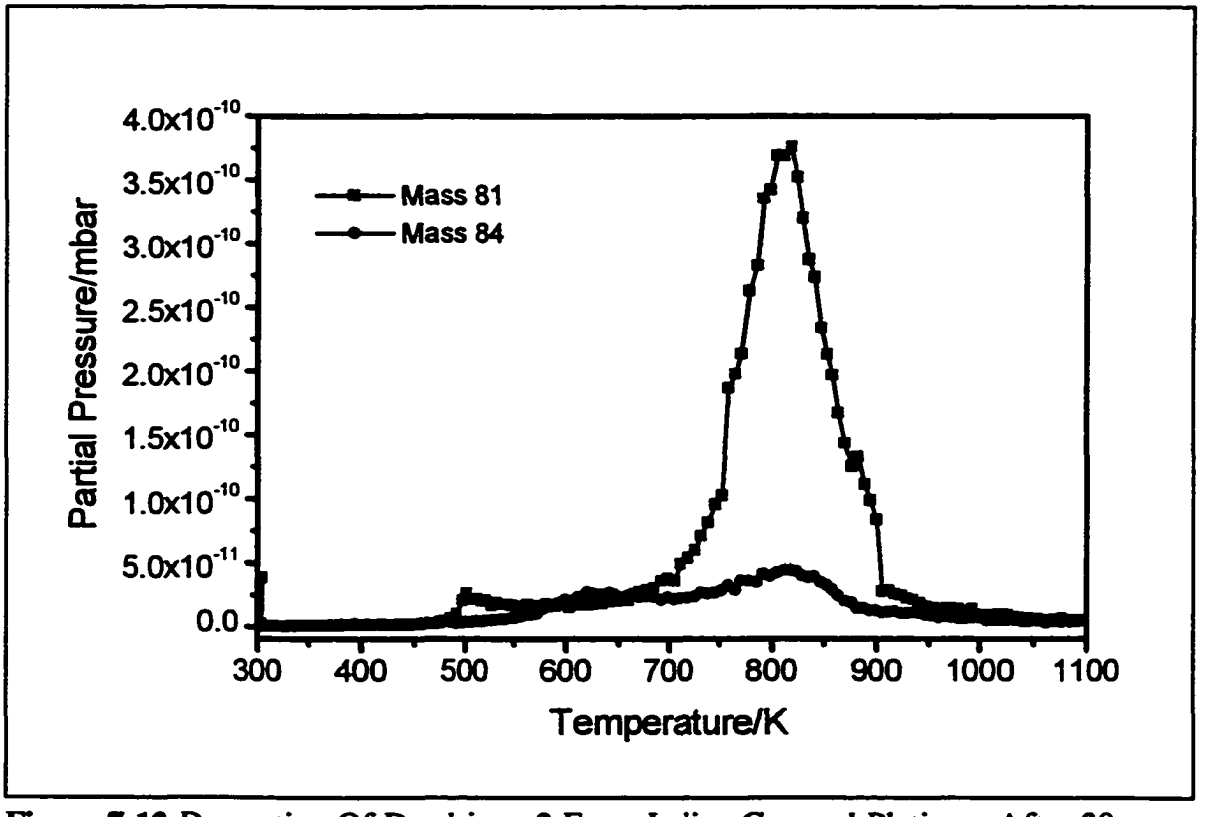

Figure 7.12-Desorption Of Dendrimer **3** From Iodine-Covered Platinum After 30 Second Contact

shows a disruption near the iodine desorption at 500 K that is similar to what is observed when using dendrimer **2** (see figure 7.12). Mass 84 begins to increase after the iodine desorption and has approximately the same intensity as in experiments using dendrimer **2**. However, at 800 K there is a significant desorption of mass 81. Mass 81 is associated with the terminating groups (SiF_2CH_3) on the dendrimers and dendrimer **3** has three times as many terminal groups as dendrimer **2**. The desorption of mass 81 is also seen near this temperature when using dendrimer **2**, but the desorption in figure 7.12 is much more intense and the peak has been shifted to higher temperatures.

After contacting the iodine-covered platinum with a solution of dendrimer **3** for 30 seconds, some of the adsorbed dendrimer was removed with a mild flow of hexane.

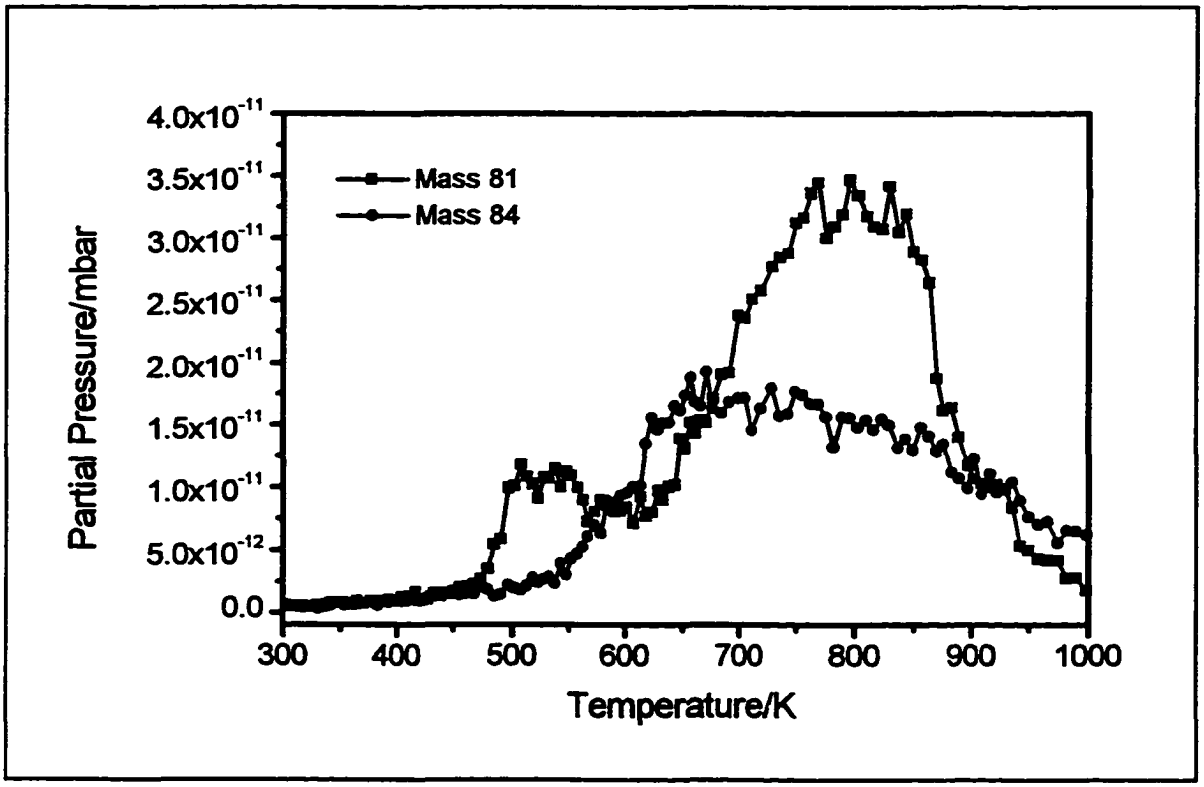

Figure 7.13-Desorption of Dendrimer **3** From Iodine-Covered Platinum After 30 Second Contact Followed by 30 Second Contact With Flowing Hexane

In figure 7.13, the desorption of the dendrimer shows that the peak in mass 81 near 825 K has been reduced while all other features appear unchanged. This would indicate that this desorption peak is from the multilayer dendrimer structure.

7.7 Thermal Production of an Ordered Structure

Several experiments were performed where the thermal desorption of dendrimer

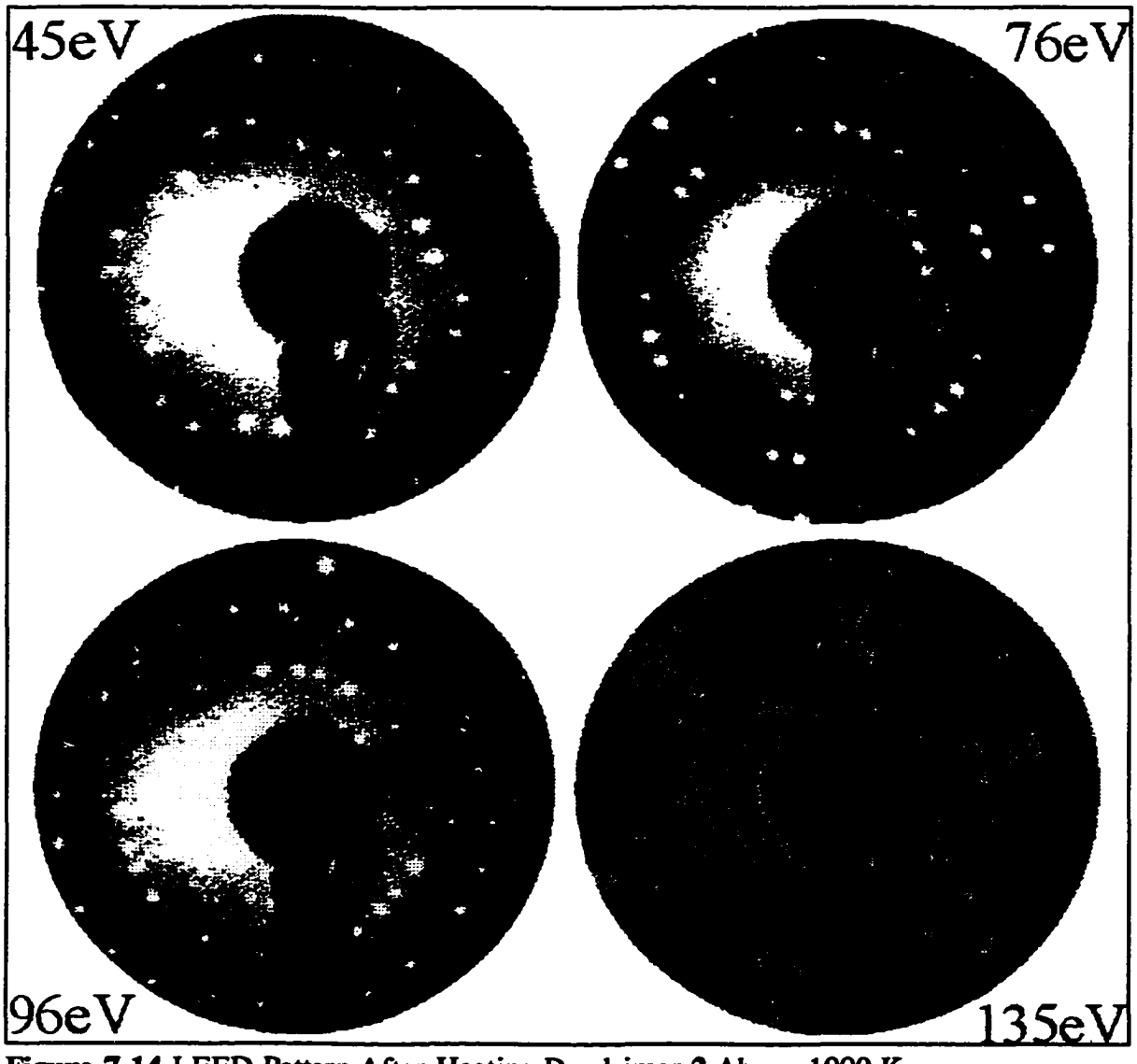

Figure 7.14-LEED Pattern After Heating Dendrimer 2 Above 1000 K

2 was interrupted at different temperatures and the crystal was cooled back down to 300 K. No extra diffraction patterns were observed using LEED. If the crystal was heated above 500 K, the ($\sqrt{7}$x$\sqrt{7}$)R19.1° diffraction pattern was no longer observed and only the (1x1) and ($\sqrt{3}$x$\sqrt{3}$)R30° patterns were seen. When the crystal was heated above 650 K, the ($\sqrt{3}$x$\sqrt{3}$)R30° pattern was no longer visible and only the (1x1) pattern remained.

Heating the platinum crystal above 1000 K and cooling back to 300 K did produce

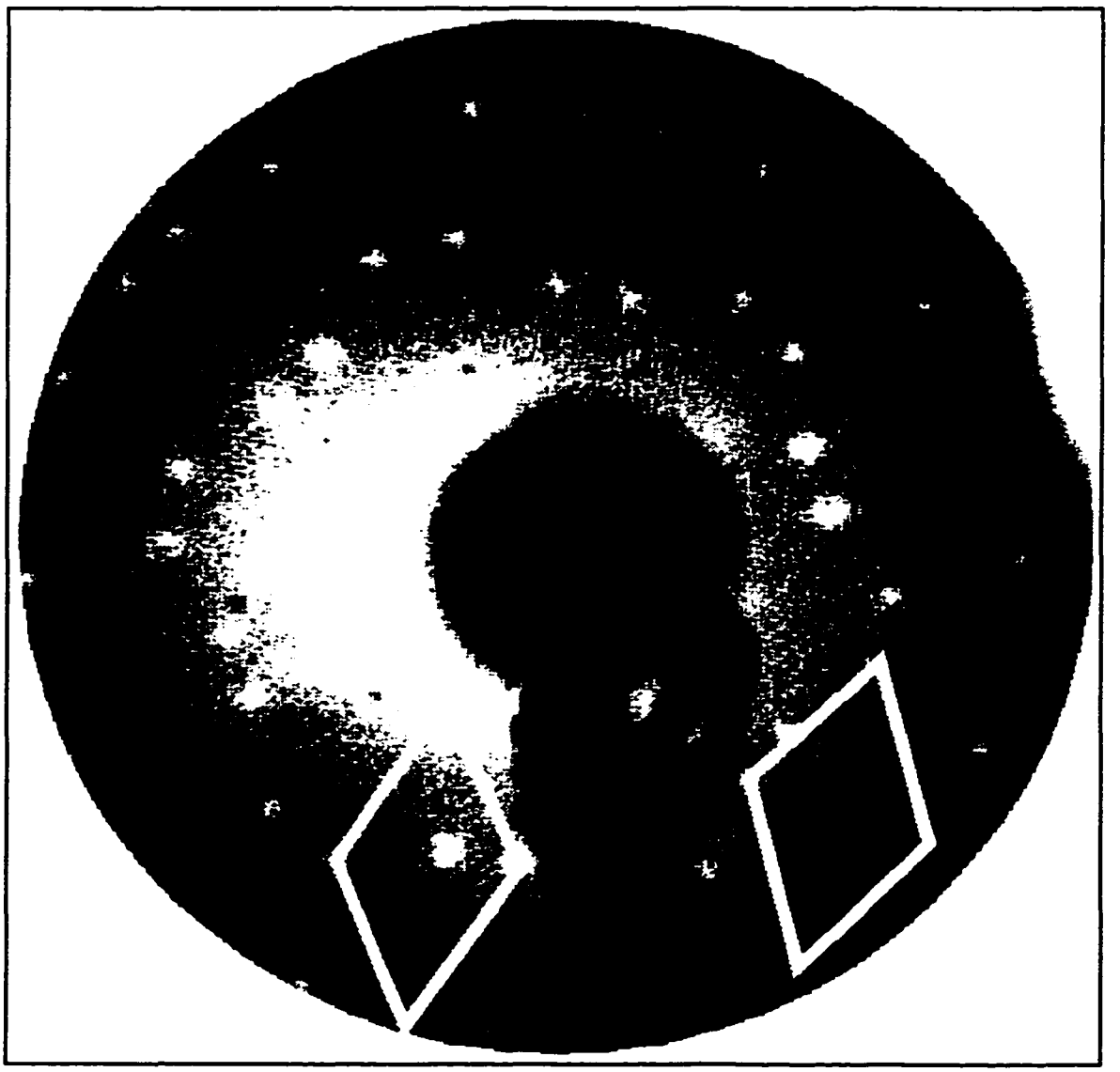

Figure 7.15-($\sqrt{19}$x$\sqrt{19}$)R23.4° LEED Pattern (45 eV) Showing Unit Cells of Domains

a new LEED pattern, shown in figure 7.14. This pattern has been assigned as two rotational domains of a ($\sqrt{19}$x$\sqrt{19}$)R23.4° pattern. The unit cells of the two domains are shown in figure 7.15. The platinum integral beams are still present in the LEED pattern indicating that the platinum surface has not reconstructed and that the ($\sqrt{19}$x$\sqrt{19}$)R23.4° pattern is due an adsorbed layer on the surface.

The real-space unit cell that corresponds to this LEED pattern is shown in figure 7.16. The size of this unit cell is close to the expected size of a unit cell that would contain one molecule of dendrimer **2.** Although it seemed unlikely that any organic molecule could remain intact while in direct contact with a platinum surface at 1000 K,

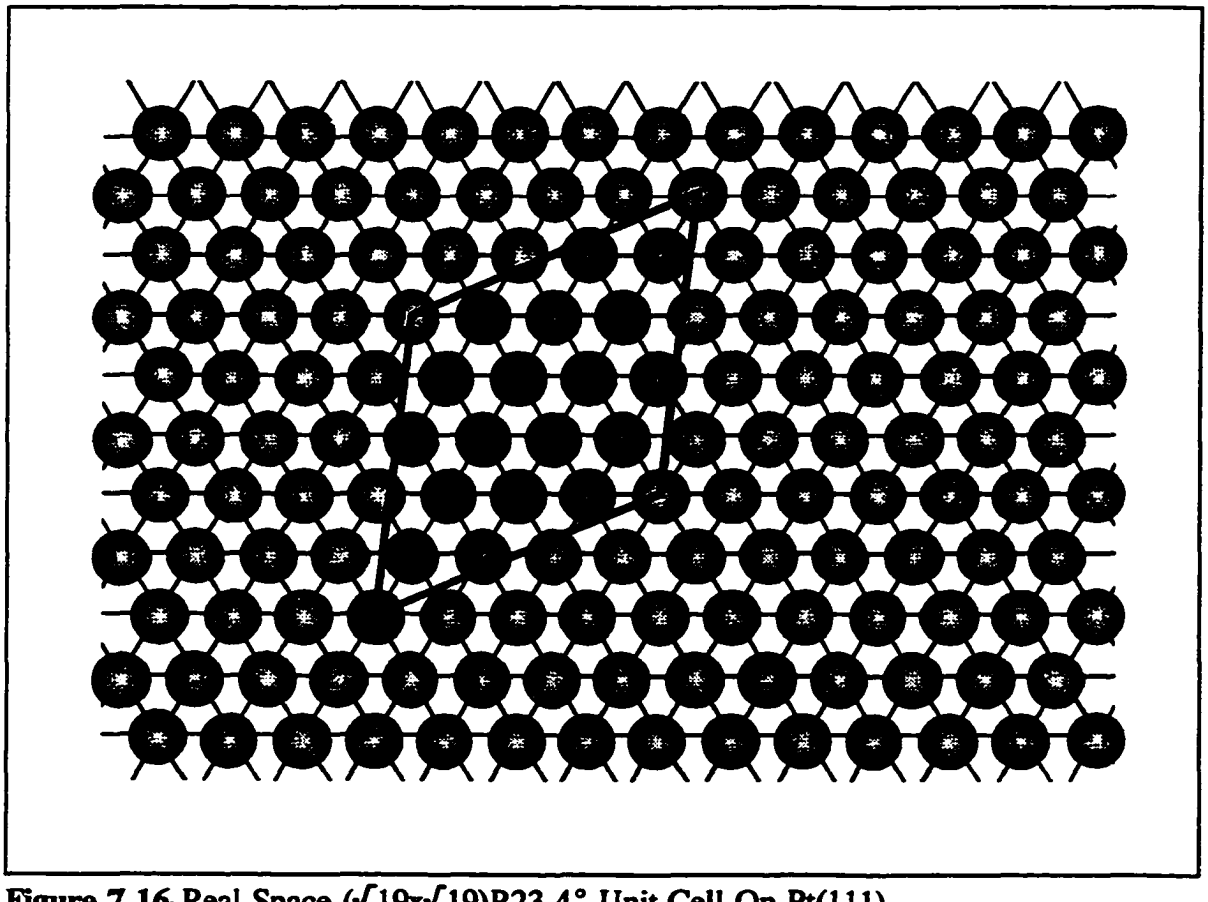

Figure 7.16-Real-Space ($\sqrt{19}$x$\sqrt{19}$)R23.4° Unit Cell On Pt(111)

it is difficult to prove that the ordered structure is not a layer of ordered dendrimer molecules using the surface techniques available.

The Auger spectrum of this new surface structure, shown in figure 7.17, indicates the presence of carbon with some evidence of silicon. The platinum signals are clearly visible and are only slightly attenuated (23/29=0.79) compared to the intensity from the bare surface. The carbon coverage was estimated in section 7.5 by comparing the platinum and carbon Auger intensities with a reference spectrum. The calculated carbon coverage was 7.6×10^{14} atoms/cm^2. As there are 1.5×10^{15} platinum atoms/cm^2 on the (111) face of platinum, this means there are approximately 2 platinum atoms per carbon atom

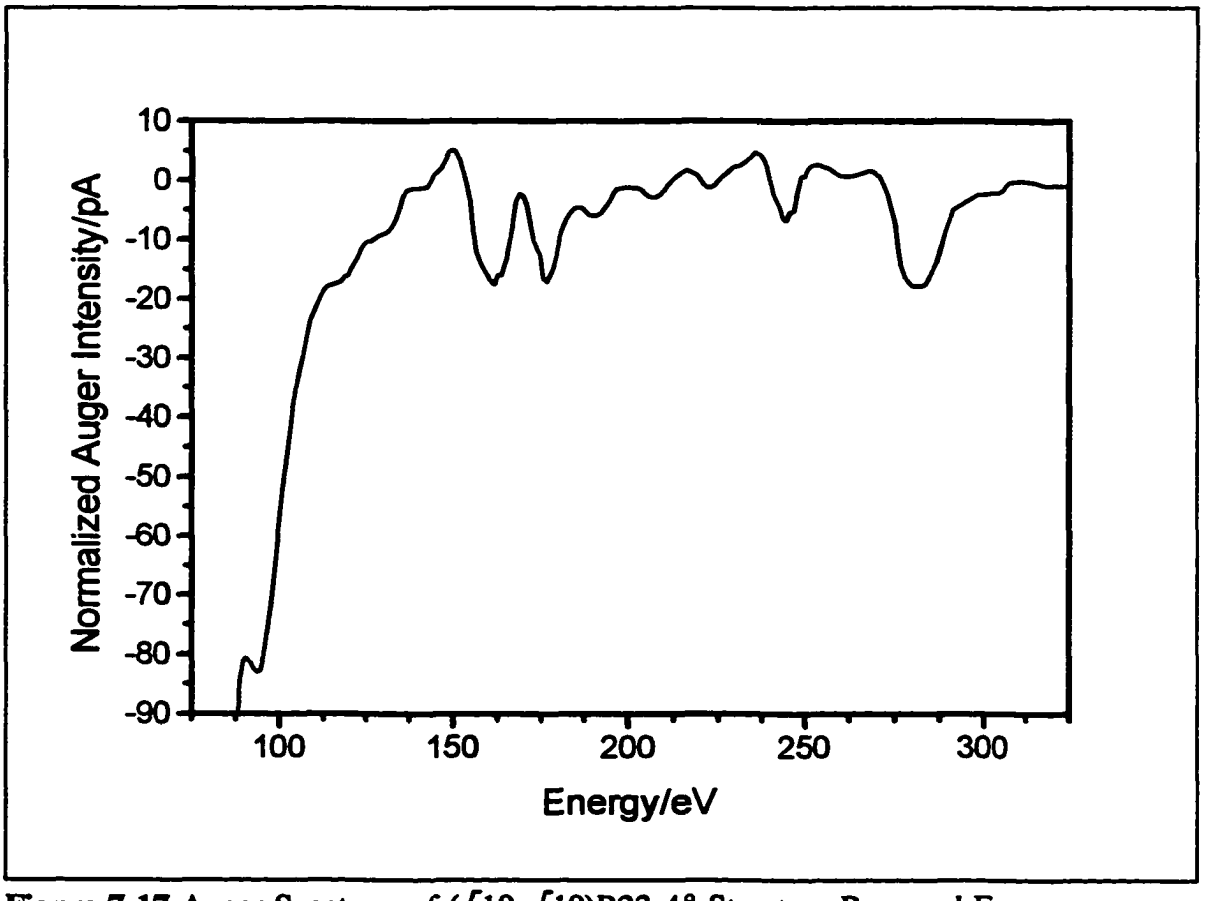

Figure 7.17-Auger Spectrum of ($\sqrt{19}$x$\sqrt{19}$)R23.4° Structure Prepared From Dendrimer **2**

on the surface.

The quantification of the silicon signal at 93 eV is difficult due to the overlap of a platinum Auger transition at 93eV and the fact that the Auger peak lies in a region of the spectrum where there is a large contribution from secondary electrons. The platinum transition at 92 eV is very weak, as can be seen in figure 7.3, and will be neglected to make an estimate of the silicon coverage. This is a poor approximation but the silicon coverage is quite low (see below) and the platinum Auger transition will be only slightly attenuated by the presence of the ordered structure.

The silicon coverage can be calculated by comparing the intensity of the silicon transition to the intensity of the carbon transition. The Auger yield for each element must be known before such a comparison can be made. The Auger yield determines how many Auger electrons reach the detector per ionization event and represents an overall cross section.

Calculation of the Auger yield (G) requires two parameters; the ionization cross section (Q) and the backscattering factor (S). The ionization cross section is a measure of how easily the core ionization that creates the Auger electron can occur. The backscattering factor determines how many extra ionization events will occur (aside from the ionization events from the primary electron beam) due to secondary electrons.

The Auger yield is given by:

$$G = Q\sec\theta_i + S \qquad \textbf{(7.8)}$$

where θ_i is the angle of incidence measure from the surface normal (0° for all experiments

described here).

The ionization cross section is given by the following empirical formula [7.7]:

$$Q/cm^2 = \frac{6.56x10^{-14}n}{E_p E_w}\left[\frac{(E_p/E_w)-1}{(E_p/E_w)+1}\right]^{3/2}\left[1+\frac{2}{3}\left(1-\frac{E_w}{2E_p}\right)\ln\left(2.7+\sqrt{\frac{E_p}{E_w}-1}\right)\right] \quad (7.9)$$

where n is the number of electrons in the ionized shell with binding energy E_w (eV). E_p (eV) is the energy of the primary electron beam (3 keV for all experiments here).

The backscattering factor for a number of elements has been calculated [7.7] and a simple relationship was found between S/n and the binding energy E_w. This relation is shown in figure 7.18. The backscattering factor for carbon has been determined [7.7] and the backscattering factor for silicon has been taken from figure 7.18. A summary of the results of these calculations is given in Table 7.6.

Table 7.6-Determination Of Auger Yield (3 keV)

Element	E_w/eV	n	$Q/10^{-19}$ cm^2	$S/10^{-19}$ cm^2	$G/10^{-19}$ cm^2
C	284	2	2.45	6.68	9.13
Si	100	6	28.1	6.48	34.6
I	685	10	3.01	3.66	6.67

The measured intensity of the silicon peak in figure 7.17 is 2 pA. Comparing this to the carbon signal and taking the different in Auger yields into account gives a silicon coverage of $2x10^{13}$ atoms/cm^2 (~1 silicon atom per 100 platinum atoms on the surface).

At the temperatures used to create the ($\sqrt{19}x\sqrt{19}$)R23.4° structure (>1000 K), silicon readily dissolves in platinum while carbon does not [7.8]. Upon cooling to 300 K,

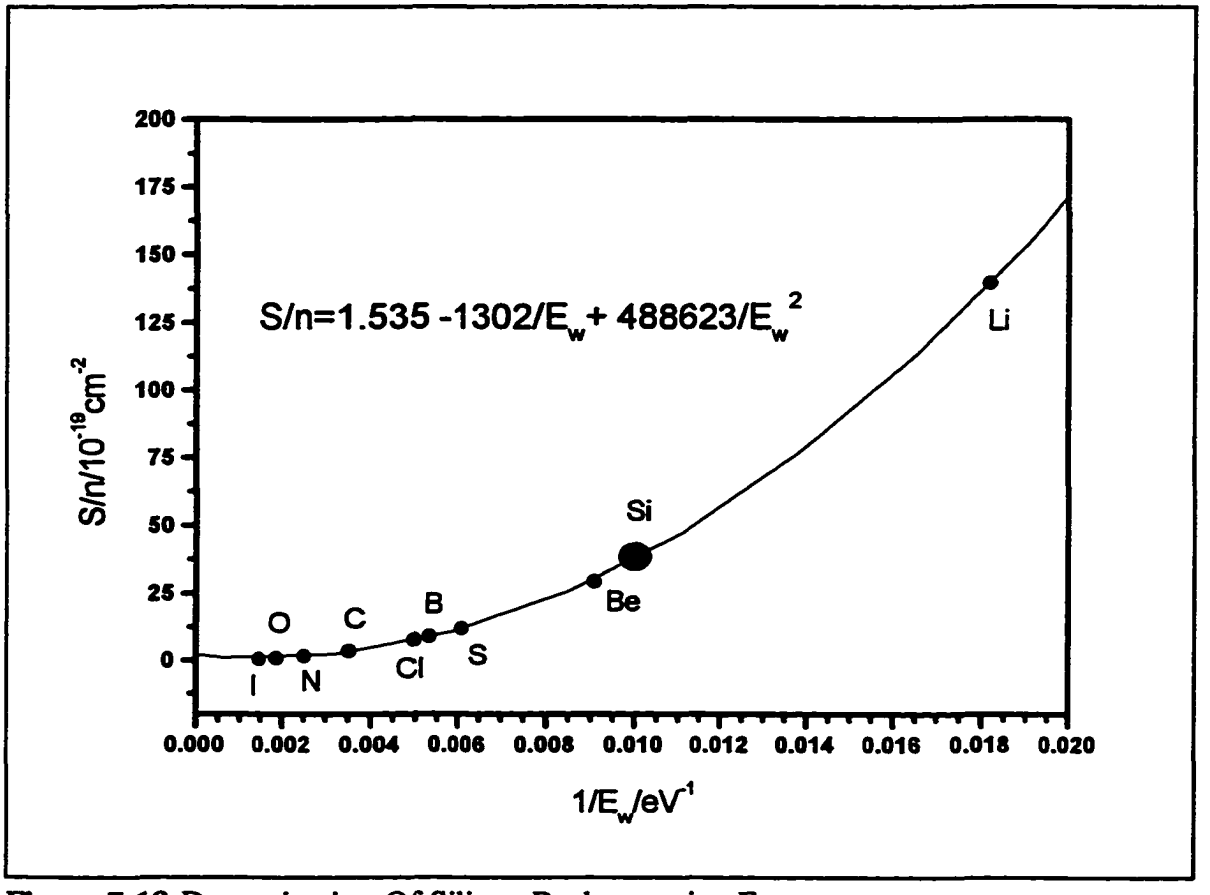

Figure 7.18-Determination Of Silicon Backscattering Factor

where the LEED and Auger measurements were made, the some silicon might segregate to the surface and be present as a surface impurity rather than an integral part of the ordered structure. At present, there is no way to determine whether the silicon is necessary to form the $(\sqrt{19}x\sqrt{19})R23.4°$ structure.

As a check of the calculations used to estimate carbon and silicon coverages, it is possible to compare the iodine and carbon Auger intensities and use the Auger yields in Table 7.6 to calculate the carbon coverage. The iodine Auger current from the $(\sqrt{7}x\sqrt{7})R19.1°$ structure is 12 pA with a coverage of $6.4x10^{14}$ atoms/cm^2. The carbon intensity of 19 pA would therefore give a coverage of $6.4x10^{14}$

$(19/12)(9.13/6.67)=1.4\times10^{15}$ atoms/cm^2. This is approximately twice the coverage estimated by comparison with a reference spectrum. Although the coverages are the correct order of magnitude, these calculations demonstrate the difficulties in gaining quantitative information from Auger spectra.

Heating the crystal with an adsorbed layer of dendrimer 3 to 1100 K and cooling to 300 K also produced the same ($\sqrt{19}\times\sqrt{19}$)R23.4° LEED pattern. This clearly indicates that both dendrimers are at least partially decomposing to yield the identical product on the surface. The Auger spectrum of the ($\sqrt{19}\times\sqrt{19}$)R23.4° structure obtained by heating dendrimer 3 to 1100 K is shown in figure 7.19. The quality of the ($\sqrt{19}\times\sqrt{19}$)R23.4° LEED pattern obtained from dendrimer 3 was not as good as that obtained from dendrimer 2. Also shown in figure 7.19 is the Auger spectrum of a ($\sqrt{19}\times\sqrt{19}$)R23.4° structure produced by adsorbing dendrimer 2 onto bare platinum and heating to 1100 K. Clearly the iodine is not required for the production of the ($\sqrt{19}\times\sqrt{19}$)R23.4° structure. The silicon Auger currents in these two spectra (7 pA and 18 pA) are larger than the silicon signal in figure 7.17 (2 pA). It seems that the amount of silicon on the surface does not affect the formation of the ($\sqrt{19}\times\sqrt{19}$)R23.4° structure. The carbon signals from all the Auger spectra of the ($\sqrt{19}\times\sqrt{19}$)R23.4° structure also vary, ranging between 19 and 27 pA. This variation could be due to the fact that there was no attempt to optimize the formation of the ($\sqrt{19}\times\sqrt{19}$)R23.4° structure in different experiments. The ($\sqrt{19}\times\sqrt{19}$)R23.4° structure was found to be stable over a range of approximately 200 K, disappearing if the sample was heated above 1200 K.

The position of the atoms within the unit cell of the ($\sqrt{19}\times\sqrt{19}$)R23.4° structure is

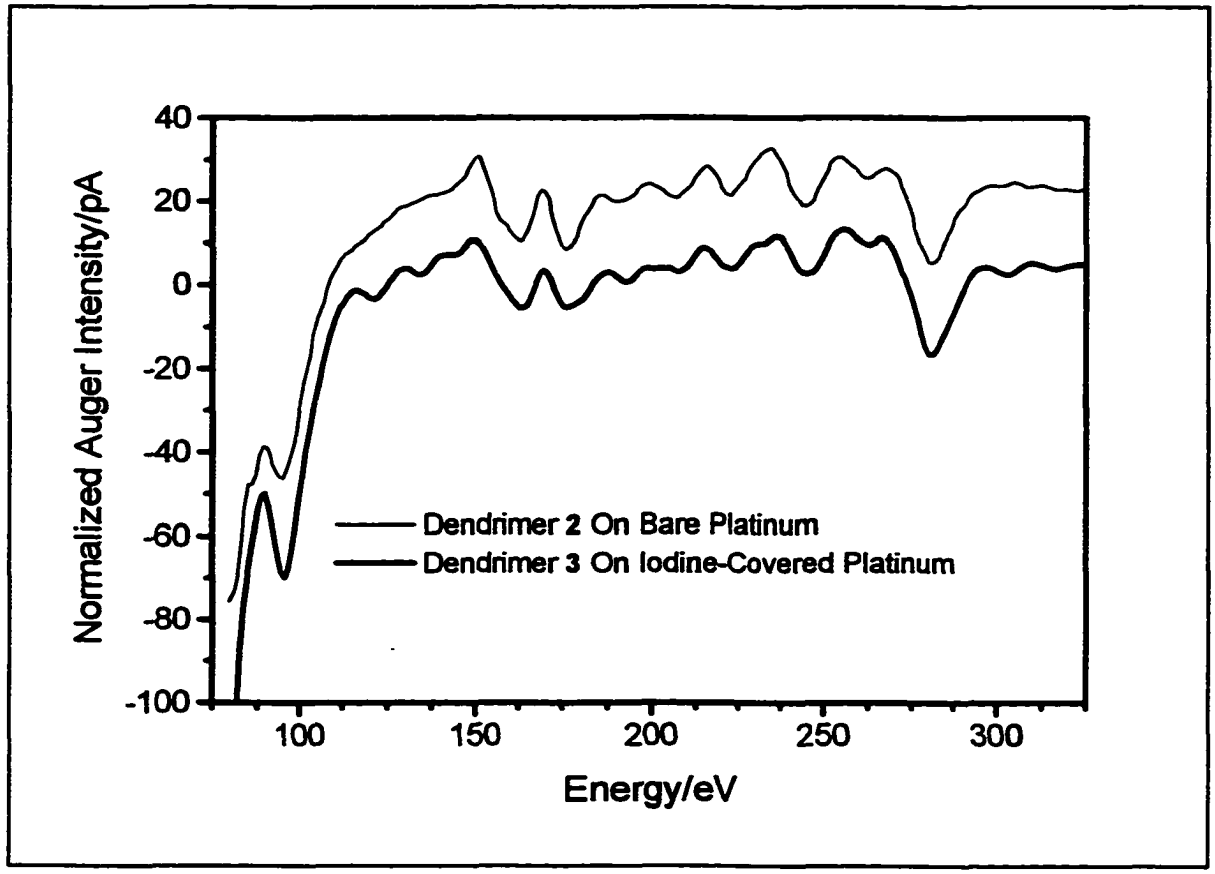

Figure 7.19-Auger Spectra of ($\sqrt{19}$x$\sqrt{19}$)R23.4° Structure Produced by Two Different Methods With Two Different Dendrimers

very difficult to determine. One possibility is that the dendrimers decompose to form graphite on the surface. The graphite structure does have a coincidental lattice match with the Pt(111) surface [7.9] corresponding to the ($\sqrt{19}$x$\sqrt{19}$)R23.4° structure, as shown in figure 7.20. The registry of the carbons atoms with respect to the metal is not known. Most simple organic compounds form graphite at elevated temperature on platinum surfaces [7.10]. In most cases, ring-like structures are observed [7.11] as the graphite sheets have a random rotational orientation. In some cases, diffraction spots have been observed but these have mostly been on stepped surface where the terraces help to orient the graphite layers [7.12]. In one case [7.9], there was a report of spots from a

($\sqrt{19}$x$\sqrt{19}$)R23.4° structure combined with rings. Unfortunately, the LEED pattern was not published and no comparison can be made. However, at no time during the course of these experiments were graphite rings ever observed and the sharpness of the diffraction beams (observed at energies as low as 32 eV) suggests a structure that is much more ordered than any previously observed graphite structure.

The carbon coverage of the graphite structure (75 atoms/($\sqrt{19}$x$\sqrt{19}$)R23.4° unit cell) would be expected to be 5.9×10^{15} atoms/cm^2. Although this is higher than the calculated carbon coverage (7.6×10^{14} atoms/cm^2), different forms of adsorbed carbon are known to have different sensitivity factors [7.13]. Any difference between the carbon

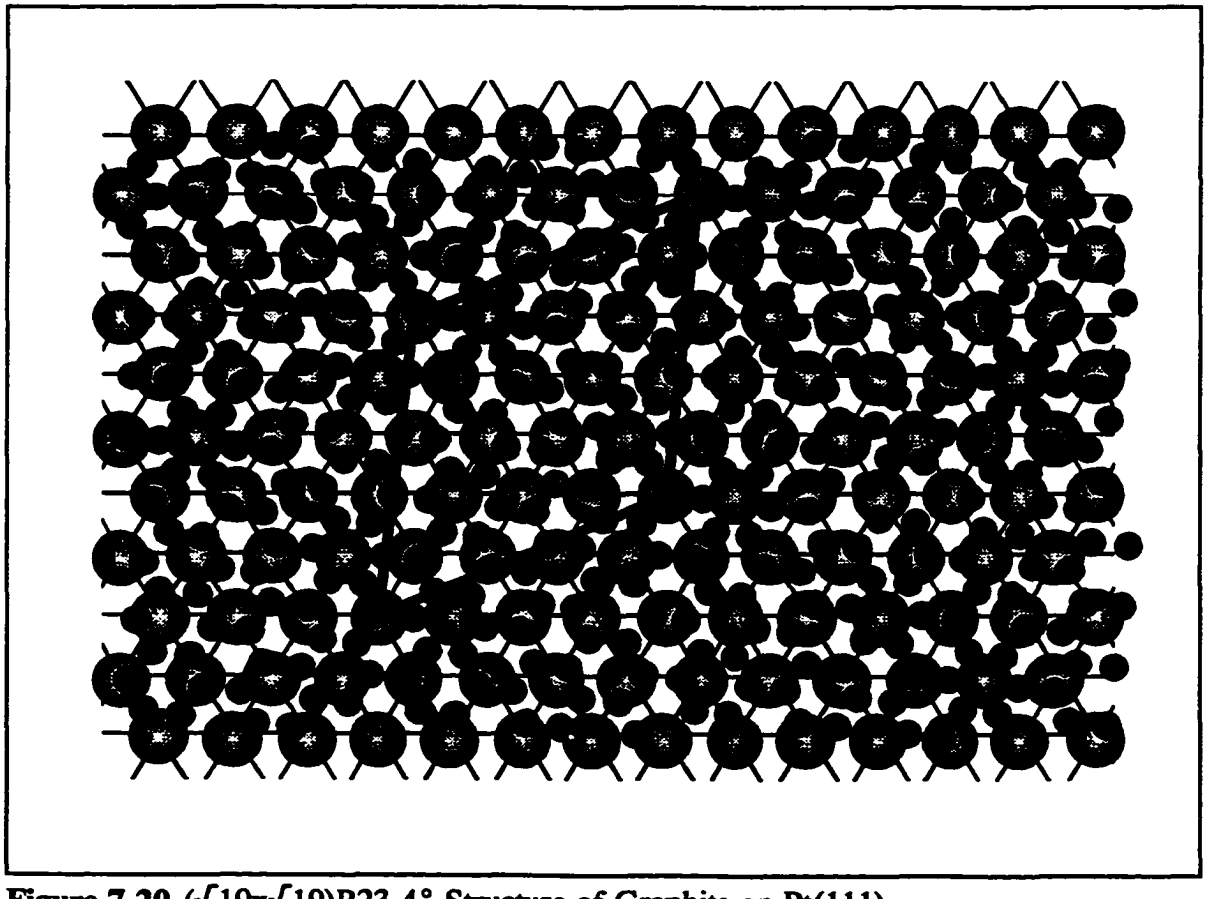

Figure 7.20-($\sqrt{19}$x$\sqrt{19}$)R23.4° Structure of Graphite on Pt(111)

sensitivity factors of adsorbed hydrocarbons and graphite would lead to errors in the calculation of the carbon coverage.

The form of the adsorbed carbon can be determined by analyzing the lineshape of the carbon (278 eV) Auger transition. This has been done for several forms of carbon including SiC, diamond, graphite, and metal carbides [7.14]. If the ($\sqrt{19}$x$\sqrt{19}$)R23.4° structure is not graphite, it is most likely to be platinum carbide and should be easily distinguishable from graphite.

To determine the carbon lineshape, the spectrum of the clean platinum surface was subtracted from the spectrum of the ($\sqrt{19}$x$\sqrt{19}$)R23.4° structure. The clean-surface

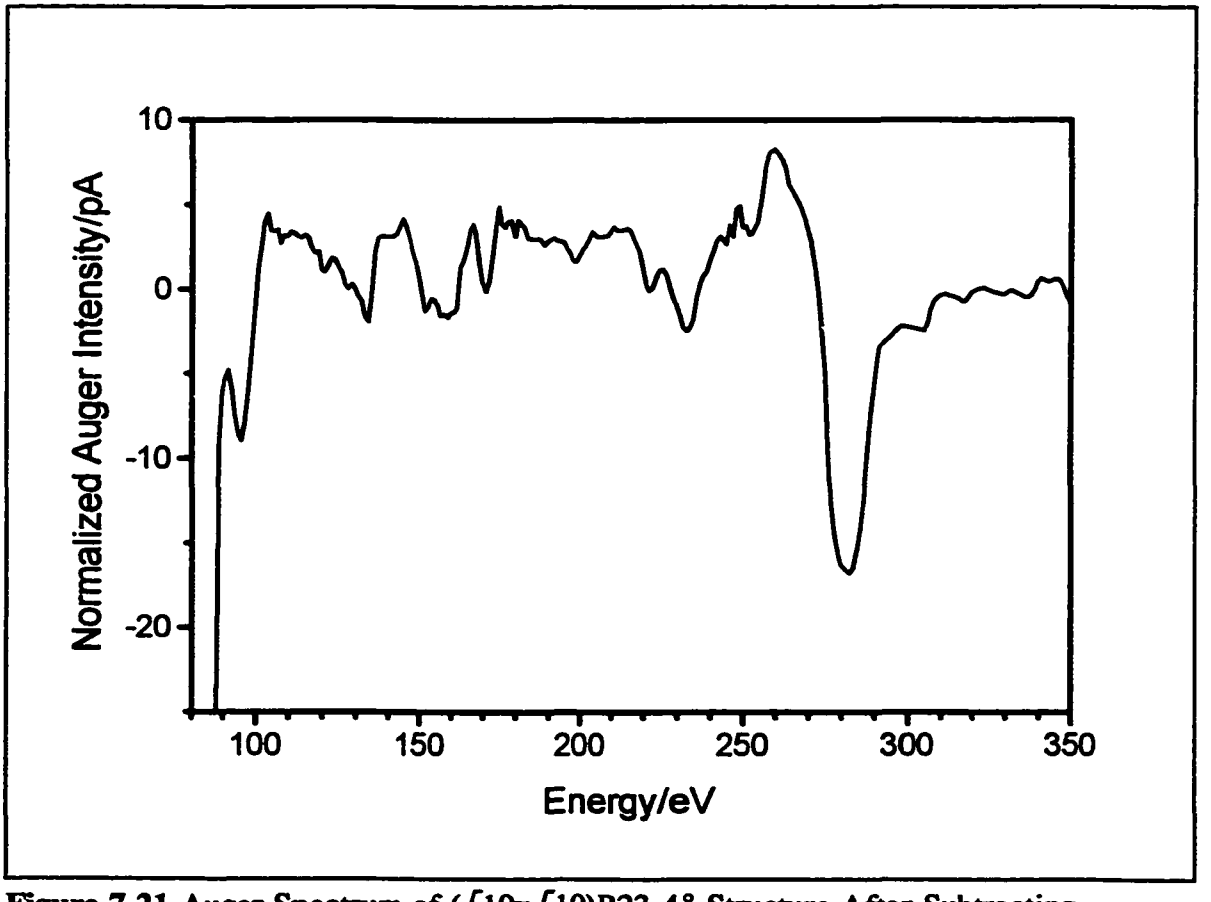

Figure 7.21-Auger Spectrum of ($\sqrt{19}$x$\sqrt{19}$)R23.4° Structure After Subtracting Spectrum of Clean Platinum

spectrum was multiplied by a factor of 0.8 to match the intensities of the platinum signals at 150 and 175 eV. This spectrum, shown in figure 7.21, is very close to the reference spectrum of graphite [7.14] and does not have features associated with metal carbides between 220 and 270 eV. However, the noise introduced into the spectrum (100-200 eV range) by the background subtraction is of the same order of magnitude as the feature at 230 eV that appears to be the same lineshape as graphite. Therefore, this spectrum cannot be used as proof that the ($\sqrt{19}$x$\sqrt{19}$)R23.4° structure is an ordered layer of graphite.

If the structure is graphite, then the Auger intensities must be reexamined. If we assume that the carbon Auger intensity corresponds to the coverage expected for graphite, the silicon coverage, originally estimated from the carbon coverage, would be different. As the carbon coverage is too low by a factor of 7.8, the silicon coverage would be estimated to 1.5×10^{14} atoms/cm^2. This corresponds to approximately 2 Si atoms per ($\sqrt{19}$x$\sqrt{19}$)R23.4° unit cell. If this structures is indeed a form of graphite, the small amount of silicon incorporated into the unit cell could help to 'pin' the graphite layer to a specific rotational orientation on the surface.

The only other choice would be the formation of silicon carbide, but the silicon content is too low for this to be considered. At present, there is no way to determine the structure of this ordered carbon layer. The formation of the ($\sqrt{19}$x$\sqrt{19}$)R23.4° structure has proven to be very reproducible, being readily produced by two types of dendrimers on clean and iodine-covered platinum. The purity of the dendrimer sample also seems to affect the production of the ($\sqrt{19}$x$\sqrt{19}$)R23.4° structure. On two occasions where dendrimers more than a few months old were used, no ordered structures were observed.

Two separate batches of freshly prepared dendrimer **2** easily produced the ordered structure. This suggests that the chemistry taking place is specific and not just a thermal decomposition.

There may be some interest in its catalytic activity as 'working' platinum catalysts are known to have a significant amount of carbon present at the surface [7.15]. As no carbon structures with this degree of order have been observed, it may be possible to provide information about the bonding of carbon to platinum through further study of this unusual structure.

7.8 Summary Of Results

The initial goal of these dendrimer investigations was to produce an ordered monolayer of dendrimer molecules on a platinum surface and to use LEED to estimate their size. This aspect of the project was unsuccessful as no ordered structure was ever observed that could be attributed to an intact dendrimer monolayer. However, several useful results were produced that may be of some use in future investigations.

The dendrimer layers adsorbed onto the surface were stable at UHV pressures when adsorbed onto an iodine-covered surface. The iodine layer appeared to be undisturbed by the dendrimer layer as the diffraction pattern from the iodine layer was visible through the dendrimer overlayer. There was evidence of beam damage as the iodine layer converted from the $(\sqrt{7}x\sqrt{7})R19.1°$ structure to the $(\sqrt{3}x\sqrt{3})R30°$ structure during LEED observations after dendrimer adsorption. It is not known at this time whether this was facilitated by the electron beam or if this transformation occurs spontaneously. This is the

only time the iodine layer has been reported to be susceptible to beam damage effects.

It does seem clear that using a highly polarizable substrate (the iodine adlayer) and a fluorinated dendrimer has increased the strength of the interaction between the dendrimer and the substrate. The fact that beam damage to the iodine layer is observed indicates that there is a significant interaction, although it is not known if the interaction has a chemical component or whether it is purely electrostatic. The other evidence for an increased dendrimer-substrate interaction comes from the variation of the thickness of the adsorbed dendrimer layer with solution contact time. Increasing the contact time from one second to thirty seconds did not cause an appreciable difference in the amount of dendrimer adsorbed. If the dendrimer molecules were more attracted to each other than to the surface, increasing the contact time should increase amount of dendrimer adsorbed.

The results from the thermal desorption experiments show that the iodine layer is essential as it protects the dendrimer from intimate contact with the platinum surface. Direct contact with the platinum seems to cause the dendrimer to decompose, a result not entirely unexpected. Contacting the dendrimer solution directly with the platinum surface with no iodine layer present causes this decomposition to occur immediately, indicating this decomposition is not thermally induced.

Quantification of the amount of dendrimer adsorbed on the surface is difficult as there are no standards to use for comparison. Using the attenuation of the iodine Auger current is the only method that can be used to estimate the thickness of the dendrimer layer. Fortunately, the calculated thickness is relatively insensitive to the mean-free path of the iodine Auger electrons.

The production of an ordered structure at elevated temperatures was unexpected. Most hydrocarbons decompose at temperatures well below the temperature where this ordered structure is produced. The fact that both dendrimers **2** and **3** produce the same ordered structure clearly shows that this structure is not due to intact dendrimer molecules that have been thermally ordered on the surface. The iodine is not essential for the production of the ordered structure as it was produced by adsorbing dendrimer **2** onto the bare platinum. The purity of the dendrimers used did seem to have an effect on the production of the ordered as no structures were observed using dendrimers that were more than a few months old. This implies that there is a specific mechanism for the production of the ordered layer.

The chemical similarity between the two dendrimer molecules suggests that the ordered structure is produced by a molecular moiety common to both dendrimers. The central core fragment seem most likely as the pendant arms are the main fragment seen in the mass spectrometer. However, this evidence does not provide direct proof and experiments involving other arms and cores would be needed to make such a conclusion.

The ordered $(\sqrt{19}x\sqrt{19})R23.4°$ structure could be graphite as graphite has a coincidental lattice match with the platinum substrate in this orientation. The Auger results do not directly support this structure as the carbon coverage is too low. However, the Auger results can be explained by assuming that the structure exists in islands with patches of bare platinum between the islands. This would reduce the calculated carbon coverage.

The presence of silicon is difficult to interpret as silicon dissolves readily in platinum at the temperatures where the structure is formed. Any silicon present in the

Auger spectrum could simply be due to silicon that has dissolved into the platinum at high temperatures and segregated to the surface during cooling to ambient temperature.

The possibility exists that the silicon is actually an integral part of the $(\sqrt{19}x\sqrt{19})R23.4°$ structure and is required for its formation. Graphite layers do not usually have a preferred rotational orientation, and the silicon atoms could help to pin the graphite to the surface in a specific orientation.

8

Conclusions

It is known that iodine forms several well-ordered surface structures when adsorbed on platinum (111). At temperatures above 300 K, the iodine is adsorbed in an atomic form that desorbs with first order kinetics. Lateral interactions between the adsorbed atoms cause a coverage-dependent activation energy for desorption from the threefold site. The activation energy changes from 253 kJ/mole at zero coverage to 196 kJ/mole at an iodine coverage of 1/3 ML. The frequency factor for the desorption from the threefold sites was determined to be 8.2×10^{13} s^{-1}. Desorption from the atop sites had an activation energy of 146 kJ/mole. The frequency factor for atop desorption was determined to be 4×10^{26} atoms cm^{-2} s^{-1} (assuming zero-order desorption kinetics). Simulation of thermal desorption spectra using the experimental rate parameters was only partially successful. The desorption temperatures and line shapes were in qualitative agreement with the experimental spectra. However, several features indicate the desorption to be more complicated than the models used in the simulation.

The desorptions at higher temperatures have interesting work function changes associated with them. The change in work function is coverage dependent and does not depend on the adsorption sites occupied. During the desorption from the atop sites, the work function change has been observed to be both positive and negative, depending on the coverage. The work function has always been observed to increase during desorption from the threefold sites.

The sign of the work function change due to iodine adsorption is opposite that expected based on the greater electronegativity of iodine. Iodine would be expected to withdraw electrons from the metal and increase the surface dipole. A decrease in work function means that electron density is being shifted back into the metal. A theoretical treatment of the work function was developed using translationally-symmetric Bloch wavefunctions to construct molecular orbitals. The coefficients of those molecular orbitals are used to calculate the hybridization dipole of both the metal and the iodine atoms. It was found that as the platinum-iodine bond became stronger (by moving the iodine atom closer to the surface) the hybridization dipole on the surface metal atoms decreased. This would be expected to decrease the work function. However, the iodine atoms develop an hybridization dipole during adsorption and this dipole becomes larger as the platinum-iodine interaction becomes stronger. Both dipoles have their negative end pointing away from the surface. The overall effect on the work function is a summation of the two dipoles. They tend to balance each other as an increase in one of the dipoles is accompanied by a decrease in the other. The work functions calculated using this procedure do not agree with the experimentally measured changes but this effect could be due to a poor choice of atomic positions.

Once the atomic positions have been determined (using tensor LEED), the calculation can be refined. Unfortunately the tensor LEED analysis was not complete at the time this thesis was prepared. The atomic charge on the metal atoms should be determined self-consistently, as was done for the iodine atoms.

Desorption of iodine at 200 K occurs in the molecular form with essentially zeroth order kinetics. Two desorption states are observed at low temperature. One of these desorption states (at 230 K) has a large work function change associated with it. This layer

is likely a loosely associated layer that is close enough to the surface to be polarized by the surface electric field. This work function change was also found to be coverage dependent as both positive and negative work function changes were observed for this transition.

The results from the dendrimer adsorption experiments show that the dendrimer begins to decompose when it contacts the bare platinum. The protective iodine layer is therefore essential for the dendrimer to remain intact on the surface. Increasing the dendrimer contact time with the surface from one second to 30 seconds did not significantly increase the amount of dendrimer adsorbed on the surface. Quantification of the Auger spectra was done by comparison with spectra of compounds with known surface coverages and by measuring the attenuation of other Auger signals (platinum and iodine). Estimating the mean-free path of these other Auger electrons allows the calculation of the thickness of the dendrimer layer. It was found that 3-4 layers of dendrimers were adsorbed on the iodine-covered surface. Contacting the dendrimer solution with bare platinum shows the presence of only 1-2 layers.

Thermal desorption experiments showed that a variety of mass fragments were produced when the sample was heated. All of the fragments observed were valid fragments of the dendrimers studied. There were two main masses observed that did not track each other. Mass 81 is associated with the fragmentation of the intact dendrimer molecule while mass 84 is associated with the decomposition of the dendrimer on the bare platinum surface.

Heating the dendrimers above 1000 K produce an ordered structure with a $(\sqrt{19}x\sqrt{19})R23.4°$ LEED pattern. Auger analysis showed the presence of carbon with trace amounts of silicon. Graphite has a coincidental lattice match with the platinum(111) plane that would have a $(\sqrt{19}x\sqrt{19})R23.4°$ structure. The measured carbon coverage is almost an order of magnitude too low for graphite structure. However, this can be explained by

assuming that the ($\sqrt{19}$x$\sqrt{19}$)R23.4° structure exists as islands on the surface.

Literature Cited

[2.1] S.B DiCenzo, G.K. Wertheim, and D.N.E. Buchanan, Surface Science, **121** (1982) 411

[2.2] H.H. Farrell, Surface Science, **100** (1980) 613

[2.3] R.Schennach, E. Bechtold, Surface Science, **380** (1997) 9

[2.4] E. Bertel, K. Schwaha, F.P. Netzer, Surface Science, **83** (1979) 439

[2.5] A. Neumann, K. Christman, T. Solomun, Surface Science, **287** (1993) 593

[2.6] R.G. Jones, Progress in Surface Science, **27** (1988) 25

[2.7] F. Lu, G.N. Salaita, H. Baltruschat, A.T. Hubbard, Journal of Electroanalytical Chemistry, **222** (1987) 305

[2.8] H. Baltrushat, U. Bringemeier, R. Vogel, Faraday Discussions, **94** (1982) 317

[2.9] Persistence Of Vision Ray Tracing Software downloaded from www.povray.org

[2.10] B.R. Schardt, S.L. Yan, F. Rinaldi, Science, **243** (1989) 1050

[2.11] S.C. Chang, S.L. Yau, B.C. Schardt, M.J. Weaver, Journal of Physical Chemistry, **95** (1991) 4787

[2.12] A. Wieckowski, B.C. Schardt, S.D. Rosasco, J.L. Stickney, A.T. Hubbard, Surface Science, **146** (1984) 115

[2.13] T. Mebrahtu, J.F. Rodriguez, B.G. Bravo, M.P. Soriaga, Journal of Electroanalytical Chemistry, **219** (1987) 327

[2.14] T.E. Felter, A.T. Hubbard, Journal of Electroanalytical Chemistry, **100** (1979) 473

[2.15] J.H. White, H.D Abruna, Journal of Physical Chemistry, **92** (1988) 7131

[2.16] R.F. Lane, A.T. Hubbard, Journal of Physical Chemistry, **79(8)** (1975) 808

[2.17] M.P Soriaga, Journal of Electroanalytical Chemistry, **240** (1988) 309

[2.18] F. Lu, G.N. Salaita, H. Baltruschat, A.T. Hubbard, Journal of Electroanalytical Chemistry, **222** (1987) 305

[2.19] A.T. Hubbard, E.Y. Cao, D.A. Stern, Electrochimica Acta, **39** (1994) 1007

[2.20] J.Y. Katekaru, G.A. Garwood Jr., J.F. Hershberger, A.T. Hubbard, Surface Science, **121** (1982) 396

[2.21] D. Zurawski, L. Rice, M. Hourani, A. Wieckowski, Journal of Electroanalytical Chemistry, **230** (1987) 221

[2.22] M. Wasberg, L. Palaikis, S. Wallen, M Kamrath, A. Wieckowski, Journal of Electroanalytical Chemistry, **256** (1988) 51

[2.23] G.A. Garwood Jr., A.T. Hubbard, Surface Science, **92** (1980) 617

[2.24] J.G. Gordon II, O.R. Melroy, G.L. Borges, D.L. Reisner, Journal of Electroanalytical Chemistry, **210** (1986) 311

[2.25] T. Solomun, A. Wieckowski, S.D. Rosasco, A.T. Hubbard, Surface Science, **147** (1984) 241

[2.26] S.B. DiCenzo, G.K. Wertheim, D.N.E. Buchanan, Physical Review B, **30** (1984) 553

[2.27] S.K. Jo, J.M. White, Surface Science, **261** (1992) 111

[3.1] M. Mundschau, R. Vanselow, Surface Science, **157** (1985) 87

[3.2] K. Griffiths, D. Bonnett, Surface Science, **177** (1986) 169

[3.3] H.P. Bonzel, A.M. Franken, G. Pirug, Surface Science, **104** (1981) 625

[3.4] H. Niehus, G. Cosma, Surface Science, **102** (1981) L14

[3.5] D. Briggs, M.P. Sean, "Practical Surface Analysis", 2nd edition, JohnWiley and Sons (Canada) Ltd, Rexdale, Canada, 1990

[3.6] C.J Davisson, L. H. Germer, Physical Review, **30** (1927) 705

[3.7] P. Auger, Academic Science Paris, **177** (1923) 169

[3.8] M.W. Roberts, C.S. McKee, "Chemistry of the Metal-Gas Interface", Oxford University Press, Oxford, 1978

[3.9] R.D. Armstrong, T. Dickinson, H.R. Thirsk, R. Whitfield, Electronanalytical Chemistry and Interfacial Electrochemistry, **34** (1972) 47

[3.10] A. Ponowski, J.Doneit, K. Junttner, W.J. Lorenz, G. Saemann-Ischenko, M. Breiter, Europhysics Letters, **9** (1989) 269

[3.11] S.A.Furman, D.A.Harrington, Journal of Vacuum Science and Technology A, **14** (1996) 256

[4.1] T.E. Felter, A.T. Hubbard, Journal of Electroanalytical Chemistry, **100** (1979) 473

[4.2] A. Wieckowski, B.C. Schardt, S.D. Rosasco, J.L. Stickney, A.T. Hubbard, Surface Science, **146** (1984) 115

[5.1] A. Wieckowski, B.C. Schardt, S.D. Rosasco, J.L. Stickney, A.T. Hubbard, Surface Science, **146** (1984) 115

[5.2] Z. Sidorski, I Pelly, R. Gomer, Journal of Chemical Physics, **50** (1969) 2382

[5.3] N.D. Lang, Physical Review B, **4**(12) (1971) 4324

[5.4] D.A. King, Surface Science, **47** (1975) 384

[5.5] M.W. Roberts, C.S. McKee, "Chemistry of the Metal-Gas Interface", Oxford University Press, Oxford, 1978

[5.6] P.R. Norton, K. Griffiths, Surface Science, **138** (1984) 125

[5.7] P.A. Redhead, Vacuum, **12** (1962) 203

[5.8] M. Golze, M. Grunze, W. Hirschwald, Vacuum, **31** (1981) 697

[5.9] F. A. Houle, W. D. Hinsberg, Surface Science, **338** (1995) 329

[5.10] S.B. DiCenzo, G.K. Wertheim, D.N.E. Buchanan, Physical Review B, **30** (1984) 553

[6.1] G. Gamow, "Biography of Physics", Huchinson and Co. Ltd., 1962

[6.2] C. Herring, M.H. Nichols, Reviews of Modern Physics, **21** (1949) 185

[6.3] S. Trasatti, Electronanalytical Chemistry and Interfacial Electrochemistry, **33** (1971) 351

[6.4] J.O'M. Brokris, S.D. Argade, Journal of Chemical Physics, **49** (1968) 5133

[6.5] L.Y. Firsova, V.N. Gramm-Osipova, Zhurnal Fizicheskoi Khimii, **52** (1978) 3166

[6.6] S. Trasatti, Electrochima Acta, **35** (1990) 269

[6.7] J. Holzl, F.K. Schulte, "Solid State Physics ", Springer, Berlin, 1979

[6.8] J. Cousty, C.A. Papageorgopoulus, Surface Science **223** (1989) 479

[6.9] Z. Sidorski, I Pelly, R. Gomer, Journal of Chemical Physics, **50** (1969) 2382

[6.10] E. Bertel, K. Schwaha, F.P. Netzer, Surface Science, **83** (1979) 439

[6.11] W. Erley, Surface Science, **114** (1980) 281

[6.12] F. Bloch, Z Physik, **52** (1928) 555

[6.13] C. Kittel, "Introduction to Solid State Physics", 7th edition, John Wiley and Sons, 1996

[6.14] J.R. Smith, Physical Review, **181**(2) (1969) 522

[6.15] E. Wimmer, A.J. Freeman, J.R. Hiskes, A.M. Karo, Physical Review B, **28**(6) (1983) 3074

[6.16] P.J. Feibelman, Surface Science, **299** (1994) 426

[6.17] R.C. Chaney, T.K. Tung, C.C. Lin, E.E. Lafon, Journal of Chemical Physics, **52**(1) (1970) 361

[6.18] L.G. Pettersson, P.S. Bagus, Physical Review Letters, **56**(5) (1986) 500

[6.19] P.S. Bagus, G. Pacchioni, M.R. Philpott, Journal of Chemical Physics, **90**(8) (1989) 4287

[6.20] C. Pisani, Physical Review B, **17**(8) (1978) 3143

[6.21] R.P. Messmer, Chemical Physics Letters, **11**(5) (1971) 589

[6.22] E. Shustorovich, R.C. Baetzold, Journal of the American Chemical Society, **102**(19) (1980) 5989

[6.23] E. Shustorovich, Journal of Physical Chemistry, **86** (1982) 3114

[6.24] R.C Baetzold, Journal of Physical Chemistry, **87** (1983) 3858

[6.25] A.B. Anderson, Journal of Chemical Physics, **62**(3) (1975) 1187

[6.26] P.J. Feibelman, D.R. Hamann, Surface Science, **149** (1985) 48

[6.27] G. Oxinos, A. Modinos, Surface Science, **89** (1979) 292

[6.28] J. Topping, Proceedings of the Royal Society (London), **A114** (1927) 67

[6.29] N.D. Lang, Physical Review B, **4**(12) (1971) 4234

[6.30] E. Wimmer, Surface Science Letters, **134** (1983) L487

[6.31] J.W. Gadzuk, J.K. Hartman, T.N. Rhodin, Physical Review B, **4** (1971) 241

[6.32] S.P. McGlynn, L.G. Vanquickenbourne, M Kinoshita, D.G. Carroll, "Introduction to Applied Quantum Chemistry", Holt, Rinehart, and Winston Inc, 1972

[6.33] B.E. Nieuwehhuys, D.T. Meijer, W.M.H. Sachtler, Physica, Stata, Solida A, **24** (1974) 115

[6.34] E. Shustorovich, Journal of Physical Chemistry, **86** (1982) 3114

[6.35] P.D. Ditlevsen, M.A. Van Hove, G.A. Somorjai, Surface Science, **292** (1993) 267

[7.1] H. Tokuhisa, R.M. Crooks, Langmuir, **13** (1997) 5608

[7.2] R. Hooper, "Synthesis, Characterization, and Group Modification of Carbosilane Dendrimers", PhD. Thesis, University of Victoria, 1997

[7.3] R.A.Gossage, "Phosphinoalkylsilyl Chemistry: Tripodal and Mesomolecular Complexation", PhD. Thesis, University of Victoria, 1997

[7.4] L.E. Davis, N.C. MacDonald, P.W. Palmberg, G.E. Riach, R,R, Weber, "Handbook of Auger Spectroscopy ", Physical Electronics Division, Eden Prairie, Minnesota.

[7.5] H. Ibach, "Electron Spectroscopy for Surface Analysis ", Springer-Verlag Berlin, 1977

[7.6] D. Briggs, M.P. Seah, "Practical Surface Analysis ", Second Edition, John Wiley and Sons, New York, 1990

[7.7] J.A Schoeffel, A.T. Hubbard, Analytical Chemistry, **49** (1977) 2330

[7.8] M. Mundschau, R. Vansleow, Surface Science, **157** (1985) 87

[7.9] B. Lang, Surface Science, 53 (1975) 317

[7.10] K. Baron, D.W. Blakely, G.A. Somorjai, Surface Science, **41** (1974) 45

[7.11] A.E. Morgan, G.A. Somarjai, Surface Science, **12** (1968) 405

[7.12] B. Lang, R.W. Juoyner, G.A. Somorjai, Surface Science, **30** (1972) 454

[7.13] T.W. Haas, J.T. Grant, G.J. Dooley, Journal of Applied Physics, **43** (1972) 1853

[7.14] S. Craig, G.L Harding, Surface Science, **124** (1983) 591

[7.15] J. Vetrone, J. Fan, M Terary, Surface Science, **314** (1994) 315